

THÈSE DE DOCTORAT

de l'Université de recherche Paris Sciences et Lettres
PSL Research University

Préparée à Observatoire de Paris, IMCCE

Search for planetary influences on solar activity

École doctorale n°127

ASTRONOMIE ET ASTROPHYSIQUE D'ÎLE-DE-FRANCE

Spécialité ASTRONOMIE ET ASTROPHYSIQUE

Soutenue par **Farida BAIDOLDA**
le 22 septembre 2017

Dirigée par **Jacques LASKAR**

COMPOSITION DU JURY :

Président: M Jacques Le Bourlot
Professeur Paris-VII, Obs. de Paris

Rapporteur: M Serge Koutchmy
DRCE CNRS, IAP

Rapporteur: Mme Anne Lemaitre
Professeur UN

Membre du jury:
M Sacha Brun DRCE CNRS, CEA

Membre du jury:
Leonid Chenin, DRCE AFIF

Membre du jury:
Jacques Laskar, DRCE CNRS, IMCCE

Dédié à celui qui est devenu mon père, Jacques Laskar.

Remerciements

Tout d'abord, j'aimerais remercier ce pays, la France, qui est devenu mon deuxième pays et où j'ai rencontré mes grands amis et mes proches pleins d'humanité et de sincérité et où j'ai aussi construit ma famille.

Je tiens à remercier tout d'abord Jacques Laskar pour m'avoir encadrée et conseillée tout au long de cette thèse. Je le remercie aussi de sa tolérance sans limite, de la confiance qu'il m'a témoignée et de son soutien pendant cette longue période. Jacques, tu es devenu non seulement mon mentor dans la science, mais aussi le père que je n'avais jamais eu. Ton mode de vie, ta créativité, ta façon de penser ont influencé la formation et le développement de ma vision du monde. Exemple d'humanité, tu m'inspires admiration, respect et le désir d'être comme toi orientée vers un but, avec mon propre jugement. J'en suis fière et infiniment reconnaissante. Mes remerciements chaleureux vont également à son épouse, Marie Postel, pour son hospitalité généreuse et sa grande richesse humaine qui m'a donnée l'élan nécessaire pour finir cette thèse. Je voudrais remercier Almas Chalabaev qui m'a conseillé d'étudier en France. Je souhaite remercier aussi Anne Lemaître et Serge Koutchmy pour leur lecture attentive du manuscrit, ainsi que Sacha Brun, Jacques Le Bourlot et Leonid Chechin pour l'intérêt qu'ils ont porté à cette thèse et l'honneur qu'ils me font en participant au jury. De grands remerciements à Jacques Le Bourlot et William Thuillot, Chingis Omarov pour le soutien administratif qu'ils apportent individuellement aux doctorant(e)s avec une grande compétence. Je remercie à centre 'Bolashak International Scholarship' qui a financé mon étude.

Je tiens à remercier Alain Chenciner de sa forte et solide amitié qui a fleuri et enrichi ma vie en France par diverses conversations notamment sur la littérature Russe. Merci pour tes livres et de m'avoir aidé à apprendre le français et aussi pour tes beaux dessins, qui décrivent la morale du jour. C'est en toute humilité et profonde amitié que je garderai précieusement ces valeurs dans mon âme. Je remercie Alain Albouy pour ses discours politiques et ses nobles pensées ainsi que pour ses actes remplis de sa personnalité morale exemplaire.

Je remercie Hervé Manche pour sa lecture attentive du manuscrit, pour ses conseils et ses précieuses explications notamment sur la déformation des corps due à l'effet de marée. C'est le plus gentil homme de France (à l'Observatoire de Paris en tout cas), terriblement gentil et attentionné avec les femmes, mais qui préfère le cacher avec ses anecdotes interminables. Grand remerciement à Didier et à Agnès Patu pour sa lecture attentive du manuscrit, ainsi que pour sa grande ouverture de cœur, amicale et d'esprit à mon égard, c'est la plus gentille et la plus douce femme de France (à l'Observatoire de Paris en tout cas).

Sincère merci à Mickaël Gastineau, qui trouve toujours une solution à chaque problème, pour ses nombreux conseils et dépannages informatiques et aussi à Frédéric Dauvergne qui s'est efforcé d'enrichir mon vocabulaire en mots français modernes. Je voudrais aussi adresser mes remerciements à Philippe Robutel (un écrivain de chansons), Gwenaël Boué (un peintre),

Nathan Hara (un musicien) et Jacques Féjoz (un musicien et un chanteur) pour leur disponibilité et leur engagement, qui nous ont permis d'organiser ensemble un grand évènement. Merci également à l'amitié de Timothée Vaillant qui, "walking encyclopædia", m'a raconté plein d'histoires politiques et culturelles de la France.

Je tiens aussi à remercier l'ensemble de l'équipe ASD pour son accueil et la chaleureuse ambiance de travail qui y règne. Rassemblement de personnalités possédant chacune une connaissance approfondie dans divers domaines, ASD est une grande équipe avec qui j'ai passé une période de joie que je garderai profondément dans mon cœur. Je voudrais aussi remercier tous les amis qui m'ont encouragé pendant mes études à l'Observatoire de Paris, Anatoliy Ivantsov, Maria Kudryashova, Siegfried Eggl, Lisseth Gavilan, Paola Modica, Jean-Baptiste Delisle, Jessica Massetti, Alexandre Pousse et tout les autres je ne suis pas oublié exprès.

Enfin, j'aimerais remercier ma famille, ma mère Dildagul, ma soeur Gulnur et mon beau-frère Thierry, mon frère Talant, mon beau-père Bill et ma belle-mère Jean, aussi mes amis Emelie et Romain pour leur présence et leur soutien tout au long de ces longues études. Un merci tout particulier à Peter pour sa patience, ses encouragements pendant ces dernières années et ses corrections d'anglais et à la petite Kunbibi Sophie qui m'a permis de travailler jusqu'à la veille de sa naissance et son frère Chingis Tom.

Contents

1	Introduction	1
2	Solar observations and its general physical characteristics	3
2.1	The history of Solar observations and surveys	3
2.1.1	Historical perspectives of the Sun	3
2.1.2	The origin of the Sun	6
2.2	Instruments and methods for observing the Sun	7
2.2.1	Some telescopes and other accessories	8
2.2.2	Recent and future Solar probes	10
2.3	The physical properties and structure of the Sun	11
2.3.1	The Sun as a star and its internal structure	11
2.3.2	The physics of Solar plasma	13
2.3.3	The outer layers of the Sun	13
3	Solar activity and sunspots	19
3.1	Sunspots and their general properties	19
3.2	The sunspot umbra and penumbra	24
3.3	Sunspot groups and models	25
3.4	Sunspot cycles radiance and irradiance models	28
3.5	Cycle characteristics of the activity and chaos	30
3.6	Solar cycle prediction	37
4	Solar variability and its data	43
4.1	Direct and indirect observational data's of Solar activity	43
4.1.1	Historical naked-eye sunspot records	43
4.1.2	Pre-telescope and early telescope sunspot records	44
4.1.3	Historical Auroral Observation	44
4.1.4	Some current measurements of solar activity	44
4.2	Solar datasets	48
4.2.1	International Sunspot Numbers (1610-Present)	48
4.2.2	American Relative Sunspot Numbers (1944-Present)	50
4.2.3	Group Sunspot Numbers (1610–Present)	50
4.2.4	Hemispheric Sunspot Numbers (1992-Present)	52
4.2.5	Predicted Sunspot Numbers (2009 – 2020)	52
4.2.6	Swiss-Wolf Sunspot Numbers (2011-Present)	52
4.2.7	Solar Cycle Parameters (1610-Present)	52
4.2.8	Ancient Sunspot Numbers (165 B.C.-1715)	53

4.3	Solar activity proxies and paleo records	53
4.3.1	Geomagnetic field measurements	53
4.3.2	Cosmic rays	54
4.3.3	Cosmogenic Isotopes ^{10}Be	54
4.3.4	Cosmogenic Radioisotope ^{14}C	55
5	The planetary theory of solar and climate change	57
5.1	Some empirical evidence of planetary forces acting on solar variation	57
5.1.1	Evidence in the short, mid and long term periodicity of the Sun	57
5.1.2	Approaches of the measurement of planetary alignments	61
5.1.3	Approaches based on the dynamical and physical mechanisms of the Sun	66
5.1.4	Climate and the changing Sun	67
5.2	Some classical objections of planetary hypothesis	68
5.2.1	Classical physics of planetary tidal forces	68
5.2.2	Exoplanet approaches of stellar activity	69
5.3	Estimations of planetary tidal perturbation and its influences on solar activity	71
5.3.1	Possible partial modulation of Solar variability by planetary tidal cycles	71
5.3.2	Some predictions of solar activity induced by planetary tidal motion	74
6	Search for quasi-periodicities in the solar activity records	77
6.1	The treatment method of used data series	77
6.2	Frequency Analysis	78
6.3	Quasi-periodic search of short and mid-term variation of solar activity indicators	79
6.3.1	Periodicity in sunspot number data	79
6.3.2	Periodicity in Group Sunspot Number Data	90
6.3.3	Verification of the QP variations of solar activity records	100
6.4	Secular and millennial variation of solar activity proxies	104
6.4.1	Periodicity in the isotope proxies of carbon ^{14}C	105
6.4.2	Periodicity of the solar activity indicators in beryllium ^{10}Be	105
6.4.3	Periodicity of the estimated solar activity indicators in carbon ^{14}C	107
6.4.4	Comparison of the physical based reconstruction of the solar activity proxies	110
6.5	Reconstruction of the long-term evolution of solar activity	113
6.5.1	Mid and long-term reconstruction of the direct observed solar activity variation	113
6.5.2	Verification of the reconstructed series	126
7	Approaches of the dynamical model of planetary influences	143
7.1	Physical model of planetary influence	143
7.1.1	Interaction between non-spherical and material bodies	144
7.1.2	Expression of the potential	144
7.1.3	The relation between 2^{nd} degree coefficients and coefficients of the inertia matrix	145
7.2	Deformation of extended body due to tidal effect	146
7.2.1	Solid tides	146
7.2.2	Harmonic degrees $n \geq 2$	147
7.2.3	2^{nd} degree deformation coefficients	148

7.2.4	Tidal effect	149
7.3	Estimation of the planetary effects	149
7.3.1	Analytical expression of the deformation coefficients	149
7.3.2	Secular part of the deformation coefficients	153
7.4	Data	156
7.4.1	The solar activity indices, its direct and indirect proxies	156
7.4.2	INPOP and La2004	157
7.4.2.1	The transformation of ICRF (INPOP) to J2000 mean equator	158
7.4.2.2	The passage of "nearly ecliptic" (La2004) to J2000 mean equator	158
7.5	Semi-analytical and numerical estimation of the deformation coefficients	159
7.5.1	Variation of the potential coefficients of the Sun due to the tidal effect of planets	159
7.5.1.1	Maximum values of the tide effect	159
7.5.1.2	Variation of the evolution of the Sun's deformations coefficients	160
7.5.2	Periodicities of ΔC_{20}	171
7.5.3	Comparison of potential coefficients of the Sun with solar activity records	172
7.5.3.1	QP reconstruction of SSN vs ΔC_{20}	172
7.5.3.2	QP reconstruction of estimated GSN vs ΔC_{20}	176
7.5.3.3	Physical based reconstruction of GSN vs ΔC_{20}	182
7.5.3.4	IntCal13 radiocarbon calibration curve ^{14}C vs ΔC_{20}	185
8	Conclusion and Perspectives	187
A	Expression of the potential	191
B	The deformation coefficients	193
C	The inertia matrix of the extended body	195
D	Analytical expression of the deformation coefficients	197
E	Reference frame	201
E.1	Transformation of references	201
E.2	Integration of direction	201
	Bibliography	203

Chapter 1

Introduction

The investigation on a possible link of planetary theory to long term solar activity variation has been well studied. It is also known that solar activity influences human living, navigation systems, the electrical power grid, oil tubes, satellite operation and the whole solar system environment. Many different methods use proxy based data to understand and to predict long term global climate change. According to many authors sunspot cycles are linked with planetary motion. Noyes (1982) showed the derivative acceleration caused by planets attraction and that it followed the pattern of solar maxima. The planetary induced torques acting on the Sun could have an influence on solar activity (Wood, 1972a; Zaqarashvili, 1997a; Wilson, 2013). Trellis (1966) published observations of the Sun, concerning the gravitational tides generated by planets. His full statistical results are ordered by follow concept: Jupiter as the most massive planet in the solar system; Venus as one of the closest planets to the Sun. The rest of planets are not practically detectable.

Major investigations to understand planetary influences on solar activity are based on coincidences of the alignments and orbital periods of the planets (Wolf, 1859a; Brown, 1900; Schuster, 1911; Wood, 1965; Bigg & Mulhall, 1967; Wood, 1972b; Fairbridge & Shirley, 1987; Blizard, 1981; Charvatova & Strestik, 1991; Juckett, 2003; Shirley, 2006). There are also many approaches designed to understand the Sun and planetary relationships. For example, the solar motion around its center of mass shows a 12 year periodicity related mainly to the period of Jupiter (Landscheidt, 1999). Jose (1965) pointed out that the 12 year period of Jupiter included effects of the other planets and has a correlation with the solar cycle. Many authors argued that according to the solar model, the origin of the solar cycle might be rooted in the solar core.

According to Eddy et al. (1976) planetary tidal effects are extremely small when compared to the Sun's own gravitation to have significant influence on solar activity (Callebaut et al., 2012). Planetary tidal effects would cause of a tide height of less than 1 micron on the Sun's surface and the amplitude of the tides would be about a few millimetres. It requires a deeper mechanism to understand a tidal effect on the long term solar activity.

Babcock (1961) outlined that convection in the subphotospheric convective zone of the Sun and its global rotation are considered as the basis of atmospheric dynamo theory of solar activity, which are insensitive to planetary influences and thus are irrelevant. Desmoulins (1995) showed a numerical calculation of planetary tides which is related with solar activity as the interaction of gravitational waves and magnetohydrodynamical processes in the solar core. Since the topic on the influences of planetary perturbation on solar variation has more scientific interest and its still open question because of its complexities.

In our research we attempted to investigate the relationship of the sunspot cycle and planetary tides. Our approach is based a purely dynamical model of the planets. In Sec.2 is outlined solar observation and is given the general physical background on the Sun. Sec.3 is devoted to the nature and the physical characteristics of solar activity. Solar activity data and its proxies are discussed in Sec.4. Stages of this investigation on planetary theory are classified in Sec.5. In Sec.6 frequency analysis was used to investigate the different periodicities of solar proxies based on the quasi-periodic approximation. Finally, in Sec.7 is given a dynamical model of the Sun-Planet interaction based on tidal theory. It also contains the analytical expressions of the tidal effect exerted by planets on the deformation of the non-spherical Sun's surface. The semi-analytical deformation coefficients of the solar surface were calculated to search for sunspot cycle like periodicities.

Chapter 2

Solar observations and its general physical characteristics

Those who will not study history are condemned to repeat it.

Karl Marx

The Sun is the central star of our solar system which provides all the energy for Earth's bio-system. The source of life, the origin and the existence of humankind, the whole of Earth's bio-system depends entirely on the steady inflow of light. Without it all life would perish and the Earth's surface would be reduced to a cold icy desert. The Sun is a hot rotating gas sphere with a radius of $R_{\odot} = 696300$ km and mass of $M_{\odot} = 1.989 \cdot 10^{30}$ kg. The average density of solar material is close to $\rho_{\odot} = 1.41$ g/cm³. In the Sun's center, the density reaches a value of 160 g/cm³ and the diameter is $D_{\odot} = 1390600$ km. In Earth's sky the Sun's angular diameter is about 0.5 degrees. The Sun belongs to a type of star called yellow dwarfs. The Sun has an absolute magnitude of +4.83, with a G-type main-sequence star (G2V) based on spectral class. G2's class means that the star has a surface temperature $T_{\odot} \approx 5780$ K, by producing heat and light by thermonuclear reactions taking place inside the core. In the observable universe of the stars, the Standart Hertzsprung-Russel (HR) diagrams show the "Temperature-Luminosity" as shown in Fig.2.1 where the Sun is located in the Main Sequence (MS). The Sun is immersed into a partially ionized local interstellar cloud and moves through an interstellar medium, with the velocity of 25 km/s. The speed of the Sun around the Milky Way galactic center is about 250 km/s. The Sun's rotational period around the galactic center is about 225 – 250 Myr. The regions of the Sun near its equator rotate once every 25 days and at its poles once every 36 days.

2.1 The history of Solar observations and surveys

2.1.1 Historical perspectives of the Sun

To fully realize the complexity of solar activity it is important to analyse the stumbling blocks faced by scientists in discovering its existence. In human history the Sun is the most investigated celestial body. Initially the most studied aspects of the Sun were its mysterious phenomena such as eclipses and sunspots. The importance of the Sun was realized centuries ago for civilized man and their livelihoods. Throughout human history, in global cultures,

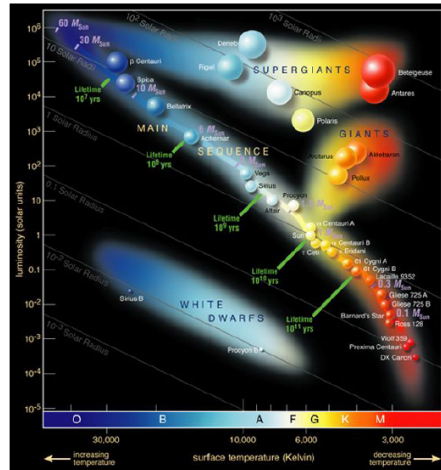


Figure 2.1 – Hertzsprung-Russell diagram of major stellar categories derived from correlation of luminosity with surface temperature. In the upper-left installed hot and bright stars, to the lower-right the cooler and less bright stars. In the lower-left is where white dwarfs are found, and above the main sequence are the subgiants, giants and supergiants. The Sun is found on the main sequence with the absolute magnitude of 4.8 and B-V color index 0.66, temperature 5780 K and spectral type of $G2V$. On the x- axis is indicated the conventional nomenclature for the various spectral classes, from ESO.

the Sun’s events have been utilized to predict its effects. The ancient records, such as Native American medicine wheels, the Egyptian Sun temples and aboriginal star lore. The Sun played a key role in orientation of Nomads during the nomadic seasons (eclipses, solstices, equinoxes, considering that the Sun rises in a different position every day). The installation and structure of Yurts were directly related to the relative position of the Sun, stars and other astronomical events around the world bare witness to mark special times of the year. In the early Aristotle epoch the Sun was considered most pure and without fault like God (Heath, 2014).

Appearances of the Sun’s effects such as its spots ((Schwabe, 1844)) have led to theories and speculations from various interpreters, e.g. the mountain top connects with climatic disasters. The regular surveillance of the Sun’s surface led to discovery of the 11 year cycle which governs the strength and abundance of sunspots. Moreover from carbon dated tree rings, it was estimated that an 11 year solar cycle persisted for a long time-scale, hence the solar cycle correlates with plants growth on Earth. Regularities of the sunspots have shown that the Sun rotates with differential rotation between poles and equator. R. Carrington determined the Sun’s rotational axis between the years 1851 – 1863. The results underline that stars rotate as a sphere of rotating gas with a dense core which is related to the Sun’s dynamo in its interior. The Sun’s energy source was estimated by the discovery of nuclear chain reactions where hydrogen transforms into helium under release of unprecedented amounts of energy.

Ancient eclipses and sunspot records. Let’s now review some remarkable solar eclipses and sunspot records, archived through ancient eras. Historical records contain around 300 unaided-eye measurements of the total solar eclipse’s (Stephenson, 1982). The recorded ancient pre-telescopic measurements are from different eras and cultures such as ancient Babylon (Steele et al., 1997; Richard Stephenson et al., 2004), ancient and medieval East Asia (China, Korean and Japan) (Wittmann & Xu, 1987; Yau & Stephenson, 1988), medieval Europe, and the medieval Arab word. There are also other Indian (Clegg, 1958; Malville & Singh, 1995)

sources, and some Occidental observations compiled in Sarton (1947). Among the above records, the Oriental historical sources (China and Korea), Europe and Arab dominions have long timescales. An interpretation of the ancient pre-telescopic and early telescopic sunspot observational records in solar activity from the centennial to millennial timescale has been published (Stephenson, 1990). There are various catalogues of naked-eye sunspot observations available from the ancient era until present. Updated research regarding new naked-eye records appeared in e.g. (Vaquero, 2007).

Babylonian records. One of the oldest records of solar and lunar eclipses containing around three thousand sightings is found in Western Asia, namely Babylon in the period of 1500 to 700 B.C.(Stephenson, 1978). In Western Asia the archaic records show two solar eclipses, and are particularly interesting for solar scientists. A solar eclipse was seen in the ancient city Ugarit, in Syria. The suggested year of occurrence was 1223 B.C. and was recorded on a clay tablet using a cuneiform alphabetic script (De Jong & van Soldt, 1989). Another eclipse was recorded in 763 B.C. where well established data was recorded in the Assyrian chronicle, during the period of 910 to 646 B.C.

Chinese records. The earliest naked-eye sunspot observations were reported in China over 2000 years ago (KANDA, 1933). A catalogue of the pre-telescopic sunspot records from the Orient is based on Chinese and Korean dynastic histories (Clark & Stephenson, 1978). The official histories and the systematic recording of naked-eye sunspots in China started to be compiled in the Han dynasty (206 B.C. to 220 A.D.). The sunspot observations covering the period from 165 B.C. to 1684 A.D. were collected in a catalogue (Wittmann & Xu, 1987) which contains fairly complete entries from both oriental and occidental history and some catalogues of pre-telescopic sunspot records complied with details (Wittmann & Xu, 1988). The accuracy of the records requires verification, as reliability of the archaic such as Chinese or Western Asian records were investigated and detailed in (Stephenson, 2008).

European records. In Europe the earliest naked-eye sunspot observations were recorded in 807 B.C. (Vaquero, 2007) and briefly investigated (Stephenson, 1978; Eddy, 1980; Eddy et al., 1989; Eddy, 1994). Solar auroral observation is one of the ancient indicators of solar activity. In (Bigg, 1967a). This data was collected from the ancient catalogue of the naked-eye auroras of the Sun. The first scientific study of sunspot observations through the telescope in the West, marked the beginning of astrophysics in 1609. After his observation in 1607 with the obscure camera, Kepler mentioned the observation of the transit of Mercury and then published his observations of the Mercury conjunction. In 1609 Kepler realized that it was a spot on the Sun surface. The greatest "sunspot" discoveries belonged to Johann Goldsmid in Holland, Galileo Galilei in Italy, Christopher Scheiner in Germany, and Thomas Harriot in England. David and Johannes Fabiricius (son and father) independently discovered sunspots in March, 1611, and used them to infer that the Sun must rotate. They published their observations in a pamphlet titled 'On the spots observed in the Sun and their apparent rotation with the Sun' in 1611 (see Schröder, 2009). After initially suspecting that the sunspots were due to some defect with his telescope, Scheiner was eventually convinced by their existence. Galileo, who in 1612 reported in three letters 'The Sunspot Letters' claiming the priority of discovery and giving an account of his own research. Finally, Thomas Horriot using one of the first telescopes reported his observation of sunspots, that described sunspot activity and included several drawings from his notebook during the year 1610 (see, for example, Seltman & Robert Goulding, 2007). Although there is still controversy about when and who first observed sunspots through the telescope, the implication of this discovery is still a topic of interest to historians of science

(see, e.g. Drake, 1957, 2001; Galilei & Drake, 1990a; Bray, 1967; Kunitomo, 1980; Judit Brody, 2002). It is known that the solar activity during the 17th century i.e. its cycles have been discussed (Link, 1977). During the Maunder Minimum (1654 – 1714) around 750 reports of sunspots are presented from Europe (Stephenson, 1990).

Examples of sunspots were believed to be transits of the planets. For instance, transit phenomena was observed in 1811 by German pharmacist Samuel Heinrich Schwabe. The official observation reports were registered by Schwabe between 1825 – 1867 (Arlt, 2011). Schwabe showed variability of the solar activity for 18 years between 1826 – 1844 (Schwabe, 1844). Schwabe expected to find a single intra-mercurial planet, but discovered that the cycles of an average number of visible sunspots on the Sun increased and decreased, with a period that Schwabe originally estimated to be 10 years. This solar cycle discovery acted as an impetus to investigation of the most important things such as the Sun's rotation and its variation between the pole and the equator (Carrington, 1859, 1858), which plays an important role in understanding the solar dynamo and the Sun's interior physics.

Earth stored records. In solar physics one of the most focused subjects is the Sun's activity. The observational sunspot data were systematically recorded during the last 400 years, as well as indirect sources involving meteorites, ice cores and tree rings. The long history of the Sun forms from processes on a human timescale and with human significance. Such terrestrial data provides evidence of solar variation and its internal physical dynamics. One of the pioneer of estimation of the sunspots from terrestrial records made by Schöve (1955) for a solar minima from 649 to 2000. To understand the Sun's physical characteristics it is natural to study what induces solar activity such as sunspots, sunspots area, total solar irradiance (TSI), magnetic field, geomagnetic activity, flares and coronal mass ejection (CME), galactic cosmic ray fluxes, the 10.7cm radio flux, radioisotopes in tree rings and ice cores that vary in association with solar activity namely sunspots. The correlation of the solar cycles with cosmogenic isotopes such as ^{10}B -beryllium concentration in polar ice and ^{14}C -radiocarbon concentration in tree rings shows that this cycle may have persisted for at least 700 Myr (Schulz, 2012). The proxy of solar activity is formed by the data on above cosmogenic radio nuclides, which are produced by cosmic rays in the Earth's atmosphere (e.g. Stuiver & Quay, 1980; Beer et al., 1990; Bard et al., 1997; Beer, 2000). The other cosmogenic nuclides, which are used in geological and paleo magnetic dating are generally less suitable for studies of solar activity (see e.g., Beer, 2000; Beer et al., 2012) as shown in the remains of the meteorites in the Earth's core. The age of the meteorite isotopes indicates a structure of the Sun of at least 5 billion years (Satya Narayanan, 2013). The prediction and reconstruction of the geomagnetic inducers and radio proxies nuclides have been investigated (for more see Steinhilber et al., 2008; Steinhilber & Jürg, 2011; Steinhilber et al., 2012a) during Medieval minimum to the little ice age from TSI.

2.1.2 The origin of the Sun

The first approaches to investigate stellar evolution were made by William Herschel (Herschel, 1811). The astronomers in planetary cosmology have two assumptions on the origin of the Solar System.

Origin of solar nebula. The first and most natural stage is the formation of a protoplanetary disk of astar from a substance (matter) of the cloud of dust and gas called the solar 'Nebula', through nuclear processes or by experiencing the destructively powerful ending to a

star, called a supernova. Briefly, dust particles of solar nebula, were coated with an elemental icy compound. Due to gravity, these icy particles tend to move toward the center of the nebula, then create an increasing gravity-induced density and pressure in the central region, the co-proto-Sun. In the center of the proto-Sun, the temperature begins to rise due to compression between atoms, hence the Helmholtz contraction takes place. Precisely the process in which gravity's energy heats matter, thus due to angular momentum or rotation of the solar nebula gives rise to a passing shock wave from a nearby supernova explosion. Finally the pressure and temperature resulting from the contracting gas and particles cause the new proto-Sun called 'Ignite' which begins to glow. The temperature and pressure cause hydrogen atoms to fuse together forming helium, with a portion of the Sun's mass being released as energy, fuelling the solar furnace. The solar nebula is composed of numbers of elements including hydrogen, helium, carbon, nitrogen, oxygen, neon, magnesium, silicon and sulfur. Present but not in abundance are nickel, calcium, argon, aluminum, and sodium. Hydrogen and helium make up around 98% of the mass of the Sun, the other elements originated in the interiors of early stars and were dispersed throughout the Milky Way, via exploding supernova. Hence (Patterson, 1956) estimated that the oldest iron of chondritic and achondrite meteorites's, was aged 4.55 ± 0.07 Gyr. Estimation of isotopic composition of meteoroids revealed the dynamical evolution of the nebula in the environment of the proto-Sun (Simon et al., 2011).

Standard Solar Model. The second assumption on the formation of the solar system is based on the implications of the Standard Solar Model (SSM), for which helioseismology now provides corroboration, e.g. a numerical model of the solar interior, for testing the physical inputs and providing a detailed map of the Sun's structure. The five-minute oscillations of the Sun were discovered (Leighton et al., 1962), then this progressed into a powerful tool for probing the helioseismology studies to provide the information about static and dynamic properties of the Sun's interior (especially on its core and convection zone). The accuracy of the SSM is assessed using the observed spectrum of five-minute oscillations, which was evolved with precision from 10000 solar models (Bahcall et al., 2006). According to SSM, each second around $6 \cdot 10^8$ tons of hydrogen are converted, hence the solar energy output will be expended in 5 billion years.

In the cases of origin of solar nebula and the SSM, however, the formation of the proto planetary disk was directly related to the formation of the most important characteristics of the Sun as a star (age, chemical composition, etc.). Eynar Hertzsprung in 1911 and Henry Norris Russell in 1913 (herein H-R) from collected observational and theoretical data produced statistical analyses by comparing the spectral type and luminosity of stars (see Fig. 2.1). According to the H-R diagram, the full evolutionary life of the stars can be traced. Interpretation of the diagram, and indeed the allocation of stars to their individual places. They hinge on a number of assumptions, notably the links between spectral type and temperature.

2.2 Instruments and methods for observing the Sun

In this section our attention was focused to revise some of the solar telescopes and observations from the depth of the outer of the tenuous Sun's layer, such as the helioseismology, the chromosphere and the corona at solar eclipses. The solar activity indicators such total solar irradiance (TSI), sunspots etc have been reviewed along with general instruments and observatories both on the ground and space based. Thus some amateur's solar instruments have also been reviewed.

2.2.1 Some telescopes and other accessories

Research of solar activity phenomena on short and long timescales has the potential to provide information on the issues frequently encountered in the context of space weather, e.g., solar activity elements such as flares, filament eruptions, and CMEs, magnetic field and fine structure of the solar atmosphere, etc. Observation of the Sun's induced activity, active regions, magnetic structure and evolution provides understanding of the triggering, and underlying physics, which are available with high-resolution observations that are rich in detail and highly dynamic. The observation with a high temporal, spatial, and spectral resolution as well as with sufficient magnetic sensitivity helps to investigate the solar activity phenomenon, its effect on the Earth and on the near-Earth environment. Some of the instrumentation listed below provides data from ground and space-based observatories, this data ensures accuracy of theoretical Solar activity models.

Ground-Based Solar Observations. Physics of the Sun can be carried out from ground based solar observatories equipped with large aperture telescopes using high-angular resolution. Furthermore at ground level the instruments are easier to operate, maintain and have long-term potential to adjustment, repair, and upgrade. The angular resolution of a circular aperture telescope is dependent on its diameter according to the Rayleigh criterion:

$$\theta_{min} = 1.22 \frac{\lambda}{D}$$

where θ is an angle of resolution, λ is wavelength and D is diameter of circular opening.

The Dunn Solar Telescope (DST, 76cm) at the National Solar Observatory and Sacramento Peak (NSO,SP) has an angular resolution of 0.15", the Swedish Solar Telescope (SST, 1m) has an angular resolution of 0.12". 3D structures in the photosphere and the resolve of fundamental features are provided with angular resolution down to 0.1" e.g. the large-aperture telescopes. Some example include: the GREGOR telescope in Spain (1.5m), the New Solar Telescope (NST, 1.6m) at BBSO, the Advanced Technology Solar Telescope (ATST, 44m) led by the National Solar Observatory. All these telescopes provide data to investigate the basic processes of solar activity events at infrared wavelengths to resolve the fundamental issues on the surface of the Sun i.e. in the photosphere and chromosphere. The Spectral Ratio Technique, Speckle Masking Imaging, Two-Dimensional Imaging Spectrometer are used for the purpose of high quality reconstruction of images.

Space-Based Solar Observations. Satellites such as NASA's Orbiting Solar Observatories (OSO), Solar Maximum Mission (SMM), the European Space Agency/NASA Ulysses probe, Japan /US /UK Yokohama (also called Solar-A), the Solar and Heliospheric Observatory (SOHO), the Transition Region and Coronal Explorer (TRACE), the Reuven Ramaty High Energy Solar Spectroscopic Imager (RHESSI), as well as recent efforts of Solar-B now named Hinode (Japanese for 'Sunrise'), Solar Terrestrial Relations Observatory (STEREO), and Solar Dynamics Observatory (SDO) launched in to near space are used for the purpose of solar observation. The basic scientific goals of these satellites are: the formation and the heating of the solar corona; understanding the physical process of coronal material into the expanding solar wind; investigation of the fundamental causes of activities observed on the solar surface, to infer the interior structure of the Sun. SOHO studies the structure and evolution of the longitudinal component of magnetic and velocity fields by continuously taking full-disk data. TRACE observes the Sun in multi-wavelengths and EUV ranges that are formed in the chromosphere, transition region, and lower corona. RHESSI observes in hard X-rays to investigate the high-energy solar physics including particle acceleration and energy release mechanisms during solar flares. Indeed, the observations from space contribute in advancing

solar physics studies related to solar activity events and space weather.

Solar observational instruments. Various kinds of solar instruments can be equipped with monochromatic filters, spectrographs, spectroheliographs, magnetographs, which are used for photospheric, chromospheric, coronal and magnetic field observations. Amateur astronomers use three kinds of telescopes refractors, reflectors and catadioptrics (or Compound telescopes).

Solar telescopes. Solar telescopes are synoptic instruments with apertures ranging from a few centimeters to four or more meters. The purposes of the telescopes are to make helioseismology measurements view, solar activity and the Sun's disk at different wavelength bands, or for magnetograms. Among the large number of solar telescopes, three of the large-aperture telescopes such the Dunn Solar Telescope (DST, Sunspot, New Mexico, 1969), the German Vacuum Tower Telescope (VTT, Tenerife, 1987), and the Swedish 1-meter Solar Telescope (SST, La Palma, 2002) have higher possible spatial resolution and have a longer focal length of the primary mirror or lens. A list of large optical telescopes erected after 1960 are shown (Hellwege & Madelung, 1975). The multiple focal lengths, various combination of mirrors, lenses, spectrographs, cameras, coronagraphs and tubes for the instruments provide a high performance of solar observation. Numerous works are devoted to solar telescopes and instrumentation (Fineschi & Gummin, 2003; Keil & Avakyan, 2003; Navarro, 2012; Schmidt, 2000, 2008). Fig. 2.2 shows the optical schematic layouts of the three simple types of solar telescopes.

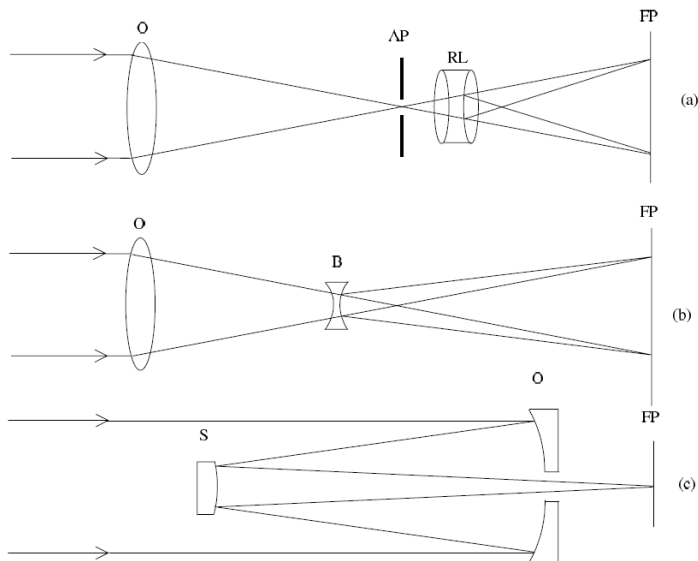


Figure 2.2 – Optical layout of 3 simple type of solar telescopes, (a) Relay lens RL used to enlarge the image, the image is limited by an aperture stop AP, (b) Solar image enlarged by a negative Barlow lens B, (c) Reflecting Cassegrain telescope with hyperbolic secondary (Antia & A. Bhatnagar, 2003).

Refracting telescopes were invented in the era of Galileo Galilei. It has a lens as the primary optical component to gather and focus light. Refracting telescopes have an achromatic and an apochromat objective lens according to the number of the lens elements with a focal ratio $f/12 - 16$ or greater.

Reflecting telescopes designs are utilized for reflecting optics. The classical Newtonian

reflector is devised with improvement known as Dobsonian Solar Telescope (DST), it uses a plate glass one way mirror, which is indented for a low-power view of the Sun's white light. DST allows for sunspot counting and to trace the solar disk. The refractors and reflectors with long focal lengths are used more, which produce large solar images, in addition to the requirement of light gathering power, magnification and optical quality.

Compound telescopes such as Cassegrain, Maksutov, and the Schmidt telescope utilize a combination of several mirrors or a mirror/lens to form an image at the eyepiece with plenty of back focus.

Spectrographs, in the case of coronagraphs, special purpose solar telescopes are dedicated for monochromatic observations, such as the twin 25-cm aperture telescopes of Big Bear Solar Observatory and the Udaipur Solar Observatory's 25-cm refractor. A spectrograph is the most important instrument for astrophysical work and especially for the purposes of solar studies. A typical spectrograph consists of a slit, onto which the solar image is focused. The spectroheliograph was invented by Henri-Alexandre Deslandres (1853 – 1948) and George Ellery Hale (1868 – 1938) in 1891 – 1890, G.H. Hale also invented the spectrohelioscope in 1924 – 1929 and discovered the magnetic fields of sunspots. In Fig2.3 and Fig2.4 are shown the spectroheliographs obtained at Meudon and Mount Wilson observatory. Narrow birefringent

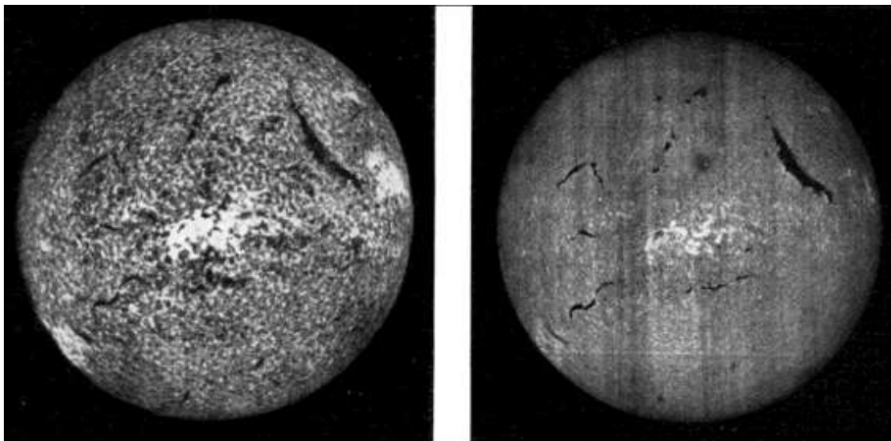


Figure 2.3 – Spectroheliographs obtained at Meudon observatory: Calcium (left) and H-alpha (right). March, 21, 1910, (Hale, 1929).

filters with passbands of 0.25\AA or narrower are used for photospheric lines to study the solar features of a flare, mass ejections and a variety of chromospheric phenomena, and to study the magnetic and velocity field measurements.

2.2.2 Recent and future Solar probes

Some of the recent probes sent into space are intended to investigate the Sun and the solar environment, to predict its impact on our planet. Tab. 2.2.2 lists some of employed solar missions.

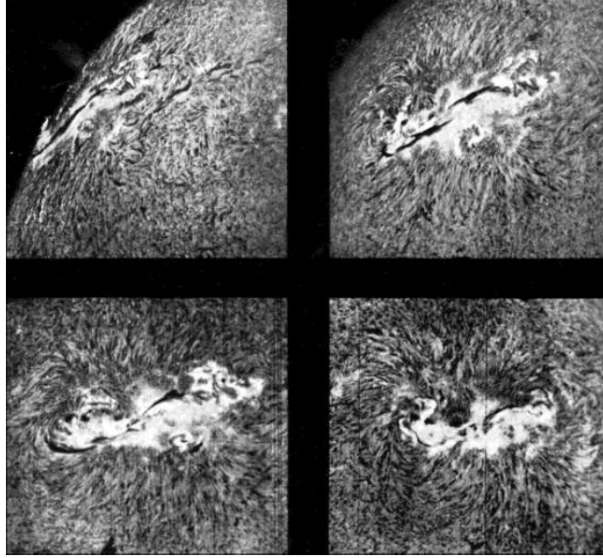


Figure 2.4 – Spectroheliograph images (H -alpha). Mount Wilson observatory, August, 3, 5, 7 and 9, 1915, (Hale, 1929).

2.3 The physical properties and structure of the Sun

Investigation of the closest stars to Earth helps us to understand the evolution of the stars, while it is an actual goal for testing atomic and nuclear physics, high-temperature plasma physics and magnetohydrodynamics, neutrino physics, general relativity, etc. The much more significant aspect is its impact on the planet's environment, namely the influences on the Earth's biosphere during the different short and long timescales. In this section has been provided information regarding the Sun's physical properties.

2.3.1 The Sun as a star and its internal structure

Equations of mechanical and thermal equilibrium are required to test the theories of important relevance, which is provided by observations of its physical properties (i.e. mass, radius, luminosity and surface chemical composition etc). The theoretical solar models were tested with the observational parameters of the Sun as its mass, radius, luminosity and ratio of chemical abundances by mass, Z/X . The SSM allows the estimation of temperature T , density ρ , pressure P , speed of sound, adiabatic index Γ_1 , hydrogen abundance X and helium abundance Y . Hence, it is shown that, the pressure and density falls off monotonically with increasing radius, also at the core's T is 14.5 million $^{\circ}C$ decreasing towards a surface about 5.778K, hence the speed of sound also has a minimum at the temperature minimum. The main physical properties are presented in Tab.2.2 with its radiation (Antia & A. Bhatnagar, 2003).

According to the SSM, our Sun contains several regions which depends on the physical properties that transfers energy towards the surface. The interior layers of the Sun are its core, radiative and convection zone (see Table 2.3). The solar radiation originates from its atmospheric layers, i.e. the photosphere, chromosphere, transition region, corona and its solar wind (see Table 2.3.1). The flux sent from the Sun to the Earth's atmosphere at the mean distance of d_{\oplus} , from electromagnetic radiation by a surface perpendicular surface to the rays

of sunlight is called the solar constant (Prša et al., 2016):

$$S = \frac{L_{\odot}}{4\pi d_{earth}^2} = 1.361 \cdot 10^3 W m^{-2}, \quad (2.1)$$

The solar luminosity which is given by Stefan-Boltzmann law with its constant of $\sigma_S = 5.67 \cdot 10^{-8}$ is:

$$L_{\odot} = \sigma_S T_{eff}^4 \cdot 4\pi R_{\odot}^2, \quad (2.2)$$

where the effective temperature of the Sun is (Benestad, 2002):

$$T_{eff} = 5800K. \quad (2.3)$$

Core. The innermost and the hottest part of the Sun is called the core which is extended out to around $0.25R_{\odot}$, temperature of ~ 14.5 million $^{\circ}C$, and density of $150g/cm^3$. Its pressure is estimated to be $2.5 \cdot 10^{11}$ atmospheres (1atm= 1013hPa) at the center (see Tab.2.2). In the core of the Sun, nuclear energy is generated. In this nuclear cauldron atoms of hydrogen are fused into atoms of helium due to compression from gravity. Mass is turned into energy providing light and heat toward the surface of the Sun. It is estimated that every second $6 \cdot 10^8$ tons of hydrogen are transformed into helium and 4 million tones of mass into radiation and neutrinos.

Radiative zone. The temperature reduces along its radius, in a statistical radiative zone, hence there is not sufficient heat for nuclear fusion and a slow heat flow diffusion takes place. The photons need millions of years to cross the radiative zone, then the process of transfer by an emitting change to a more effective convective transfer. On the way to the surface, for the absorbed atoms a single photon is re-emitted. They form two or more quanta, according to the law of conservation their total energy is saved. The energy of each quanta is reduced, so the quanta acquire less energy. Powerful gamma-quanta will give rise to less energetic photons of the electromagnetic bands first X-ray, then an ultraviolet (UV), a visible (or optical) and finally infrared radiation (Peter Foukal, 1990), most of the energy is radiated in the optical band, where a human eye is sensitive (see Tab.2.2).

Convective zone. The absorbed radiation induce to form gas which is unstable and leads to convection. The layer between the radiative and convective zone is a thin layer called the tachocline with mean properties that are established from helioseismic data. Physical characteristics of this tachocline have been discussed by many authors due to its dynamo interests (for example Charbonneau et al, 1999; Charbonneau, 2010, 2013b; Dikpati & Gilman, 2001a,b). The falling and rising convective elements are measured by Doppler shift. Passing along the way, about equal in size, the convective elements seem to dissolve in the surrounding environment, creating new heterogeneity. The flow of the heat plasma rises upward, hence heat will spread to all the environments, then the plasma gas moves down. It means that the solar substance boils and mixes, however by inertia the heat flow permeates the photosphere from the deeper layers of convection. This granulation (the visual effect of boiling convection currents on the surface of Sun) is a clean manifestation of convection. The unstable solar interior is its convective zone, its mean physical characteristics presented in the Table 2.3. The solar atmosphere provides a study into the distribution of energy in the observed spectrum, as well as to find the abundances of elements and boundary conditions for the solar interior model. Moreover the standard solar model (SSM) involves the variation of the temperature and the turbulent velocity parameters, to describe the solar phenomena. The equation of

energy transfer, equation of hydrostatic equilibrium and the equation of state (including the conditions of local thermodynamic equilibrium) allows the estimation of the parameters such as absorption coefficients, ionization, pressure, excitation etc (Abhyankar, 1977). The solar atmosphere gives a continuing challenge to solar physicists and its mean parameters are presented in Fig. 2.5.

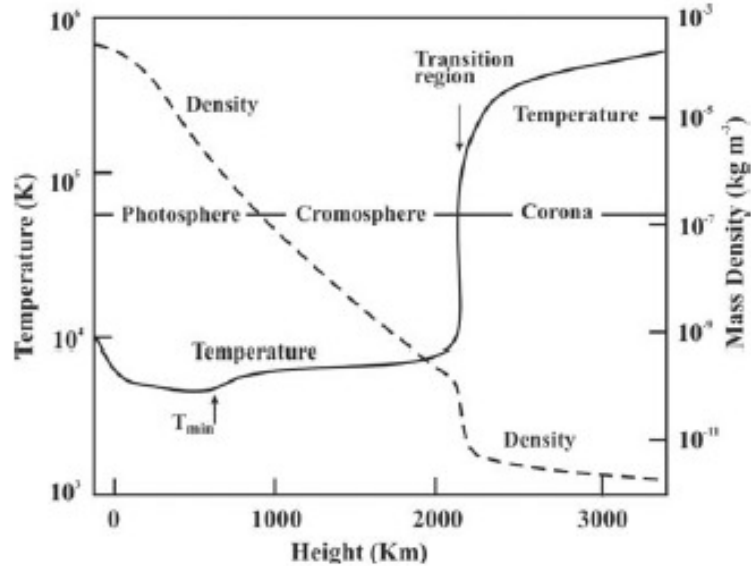


Figure 2.5 – Variation of temperature and density in the solar atmosphere (Athay, 1976).

2.3.2 The physics of Solar plasma

The magnetic field of the Sun is involved in a complex interaction with the plasma. The solar magnetic field is believed to be generated by a hydromagnetic dynamo process operating in the Sun's interior, hence in the convective zone, due to the strongly turbulent environment, the flow-field interactions release at the Sun's surface and then disperse into the spatial environment. The turbulent electromotive force, the dynamo saturation problem, and the flux transport dynamo have been studied (Charbonneau, 2013b,a). The solar activity event occurs over the whole of the solar atmosphere by causing phenomena such as: sunspots in the photosphere, the faculae near the sunspots and overlying plagues in the chromosphere, activation and eruption of the prominence and filaments in the corona. The indication of magnetic activity of the Sun is also given by its flares and the coronal mass ejection (CME) which eject the coronal matter into space. The magnetic field of the Sun is related by the solar dynamo action (Larmor, 1919; Cowling, 1933) in the convective zone, through an interaction with the differential rotation, the helical convective motions and the north-south meridional circulation (Dikpati & Gilman, 2009).

2.3.3 The outer layers of the Sun

Photosphere. The photosphere is the deepest layer of the solar atmosphere visible to the naked-eye (C. J. Durrant, 1988), where most of the Sun's energy is radiated out. This is not a solid surface, as the Sun is totally gaseous, the rotation rate is different for each

layer of the Sun. The flow is rising from the center of the granulation cells, cools down while it floats horizontally out toward the darker layers where it sinks down again. Features such as dark sunspots pores, sunspots (see for more Sec.3), bright faculae, granulation and super granulation are observed at the photosphere. The photosphere emits a continuous spectrum, hence it allows measurements of large flows and a pattern of waves and oscillations.

Granulation. The granulation is observed at the photosphere. This bright rounded area produces the Sun's surface granules, and its whole structure-granulation. Typical granules have around 5 – 20 min of lifetime before dissipating (Bahng & Schwarzschild, 1961) and diameters on the order of 1500 km, after which they are divided by the appearance of new granular structures. The visible granules are explained by convective motion. The entire Sun is covered with small granulations. The granulation flows can have supersonic speeds, which may produce sonic "booms", also waves at the Sun's surface.

Super granulation. Another kind of granulation occurs below the photosphere, it is called the super granulation which is between 20000 – 40000 km in diameter with lifespans of between 20 – 48 h. Several thousands of the super granulations cover the Sun's surface. The observational data of the SOHO's Michelson Doppler Image (MDI) helped to understand the movement and structure of plasma at the surface and deeper in the interior. Moreover analysis of the MDI's data showed that the super granulation has a pattern of activity which is moving across the solar surface in waves (Tom Duvall, NASA).

Faculae. The solar faculae is the bright edge of the solar disk, a measurement of the visible faculae can be achieved with a spectroheliogram at the wavelengths of hydrogen or ionized calcium vapour. The appearance of faculae over the sunspots makes the Sun brighter during the sunspot cycles, being that the faculae is hotter than its surroundings, therefore looks as bright spots at the photosphere.

Chromosphere. The observable outer layers of the Sun above the photosphere constitute its chromosphere. One of the interests in the feature of the chromosphere is that temperature rises with height. A possible explanation is related to the magnetohydrodynamic waves. The chromosphere erupts as a narrow, bright red ring ambient in its corona. The chromosphere is the coldest part of the Sun's atmosphere which allows for the existence of carbon monoxide and water as indicated in absorption spectra (Solanki et al., 1994). The chromosphere's spectrum exhibits numerous emission and absorption lines (Abhyankar, 1977), such as helium and Ca II, helium becomes partially ionized (Hansteen et al., 1997a). The mean physical characteristics are shown in Tab.2.3.1. The chromosphere is a place of activity, hence filament eruption, flow of materials are observable over the chromosphere. Besides the ejection of materials to the corona with high speed, in the chromosphere events such as polar solar flares and prominence take place. At the outline of the chromosphere are super granules with magnetic field branches in the super granulation (Narayanan, 2012).

Transition Region. Between the cooler chromosphere and the hot corona is the irregular narrow transit region. From this region the energy emitted onto the coronal region is dominated by ionized carbon (IV), oxygen (V) and silicon (I) with stripped electrons (Benestad, 2002). Due to the full ionization of helium in the thin transit region the temperature increases, hence the reduction of the radiative cooling of the plasma will take place (Hansteen et al., 1997b). This highly variable zone is not easy to observe from the Earth, however it is visible from space by sensitive instruments to the extreme ultraviolet (Dwivedi, 2003). The ions emit light in the ultraviolet region of the spectrum and can be studied by TRACE and SOHO solar mission's. The energy in the transition region is supplied from the corona as heat or as

potential energy of the elevated material which can then be radiated away or carried in the solar wind.

Corona. The corona is visible during a solar eclipse like the chromosphere, as the Sun covers up the photosphere, the white corona around the dark moon appears (Golub et al., 2010) and it is a collection of gases. The Sun's extended atmosphere starts at its corona, with a larger volume than that of whole Sun's photosphere. Mechanical energy dissipates while the flow moves into interplanetary space the radiation flux and the solar wind (Russell, 2001). Thus the loss of the total energy in the Sun's corona can be carried out through the solar wind and the radiation flux. By thermal conduction and the enthalpy flow, the energy loss from the corona appears in the transition region and upper chromosphere. Due to ions with electrons from the plasma state, the corona has a high temperature. The atoms collide with sufficient energy to eject electrons, causing the ionization process to take place, in strong solar activity at temperatures from 1.3 million K to 3.6 million K (Narayanan, 2012).

Coronal mass ejection. Important events taking place in the corona is its mass ejection (CME). The CME's have an effect on the physical conditions of the interplanetary medium. The CME's are huge clouds of ionized gas that contain 10 billion tons of material carried with the typical speed of 1000 km/s into space from the Sun, by disrupting the flow of the solar wind (Vázquez & Hanslmeier, 2005). CME's were detected as a magnetic cloud that often exhibits a three part structure, the bright active regions, the dark elongated regions in the north-south direction, which are then followed by surrounding regions. The observation of the Interplanetary Scintillation (IPS) have showed the detection of the CME on the Sun Earth environment (Manoharan et al., 1995).

Prominence. One inducer of solar activity is its prominence. The solar activity causes such activity as flares and sunspots. Prominence is measurable data of Sun, which can be achieved by ground based telescopes and spacecraft such as SOHO. The solar outer layers from the solar photosphere to corona exhibit events such as coronal mass ejection, flares, granulation, super granulation and faculae.

Solar wind. The source of the solar wind is the Sun's corona which extends out into interstellar space (Meyer-Vernet, 2007). As it pours out in to space it amounts to $10^{-4}M_{\odot}$ over the Sun's age over 10^9 years. The spacecraft Ulysses has made a complete orbit of the Sun and mapped the speed of the solar wind, the magnetic field strength, direction and particle composition. This solar mission established that the solar wind is uniform in all directions and that the streams in the solar corona can often be used to identify the solar poles. The solar wind is not only the source of the solar mass loss, as there are other sources such as by electromagnetic waves. The interaction between Earth's geomagnetic field and the solar wind produces storms in Earth's magnetosphere, also seen as northern or southern lights (aurora borealis and aurora australis). The solar variability and its rotational evolution are partially linked with the magnetism. These solar magnetic field lines carry the solar wind which allows researchers to study planetary magnetospheres. These magnetic fields are frozen in the flow of the solar winds because of the high electromagnetic conductivity of the solar wind, which expands from the Sun towards space. Depending on the differential rotation of the Sun, the magnetic field links in a low latitude near to the solar equator with a slow speed and a fast wind originates in high latitudes near to the Sun's pole.

The role of the coronal magnetic fields and the rotation of the Sun, and the sources of the solar wind is still an actual outstanding issue in solar physics which is a complex astrophysical goal.

CHAPTER 2. SOLAR OBSERVATIONS AND ITS GENERAL PHYSICAL CHARACTERISTICS

Table 2.1 – List of some future solar missions.

Name	Mission	Launch date and country	Instruments papers
Yohkoh (sunbeam- Formerly Solar-A)	Spacecraft studied high-energy radiation from solar flares	30 August 1991, Japan/USA/England	(Ogawara et al., 1991; Acton et al., 1992)
Ulysses	Spacecraft is an international project to study the poles of the Sun and interstellar space above and below the poles	6 October 1990, USA and Europe	Wenzel et al. (1992)
Wind	A spin stabilized spacecraft and placed in a halo orbit around the L1 Lagrange point, more than 200 Re upstream of Earth to observe the unperturbed solar wind that is about to impact the magnetosphere of Earth.	in November, 1994 US	(Acuña et al., 1995)
SOHO-Solar and Helispheric Observatory	The main scientific purpose of SOHO is to study the Sun's internal structure, and Sun's corona and that gives rise to the solar wind, using imaging and spectroscopic diagnosis of the plasma in the Sun's outer regions coupled with in-situ measurements of the solar wind.	21 December 1995, USA	Domingo et al. (1995)
Genesis	The primary objective of the Genesis mission was to collect samples of solar wind particles and return them to Earth for detailed analysis.	8 August 2001, USA Solar Wind Sample Return	Lo et al. (2001)
ACE-Advanced Composition Explorer	A robotic spacecraft and explorers program Solar and space exploration mission to study matter comprising energetic particles from the solar wind, the interplanetary medium, and other sources.	25 August 1997, NASA	Stone et al. (1998)
TRACE-The objective of the Transition Region and Coronal Explorer	The space telescopes satellite was to explore the three-dimensional magnetic structures which emerge through the visible surface of the Sun, the photosphere and define both the geometry and dynamics of the upper solar atmosphere, the transition region and corona.	1 April 1998, NASA	Handy et al. (1999)
RHESSI-Ramaty High Energy Solar Spectroscopic Imager	The overall objective is to explore the basic physics of particle acceleration and explosive energy release in solar flares.	5 February 2002, NASA	Lin et al. (2002); Hurford et al. (2002)
Hinode sunrise- Formerly Solar-B	Was planned to explore the magnetic fields of the sun. It consists of a coordinated set of optical, extreme ultraviolet, X-ray instruments to investigate the interaction between the Sun's magnetic field and its corona	22 September 2006, Japan Aero space Exploration Agency Solar mission with USA and UK	(Kosugi et al., 2007; Culhane et al., 2007; Golub et al., 2007; Tsuneta, 2008)
10 STEREO-Solar Terrestrial Relation Observatory	Solar Terrestrial Probes program, it employs two nearly identical space based observatories-one ahead of Earth in its orbit, the other trailing behind-to provide the first-ever stereoscopic measurement to study the Sun and the nature of its coronal mass ejections.	26 October 2006, NASA	Kaiser et al. (2008)
IRIS-Interface Region Imaging Spectrograph	The mission to study the crucial region by tracing the flow of energy and plasma through the chromosphere and transition region into the corona using spectrometry and imaging.	Operating, 27 June 2007, NASA	De Pontieu et al. (2014)
PICARD	PICARD takes simultaneous measurements of the Sun's irradiance, solar flares, magnetic fields and diameter/shape, studying the link between solar cycles and temperature changes on earth.	Operating, 15 June, 2010, CNES, France	Meftah et al. (2014)
SDO-Solar Dynamics Observatory	SDO records the Sun's dynamic solar activity to understand how it affects life on Earth.	2 November 2011, NASA	Pesnell et al. (2012)
SOLAR/SMO - Solar Monitoring Observatory	SOLAR is mounted on the Columbus module of the International Space Station. It measures the irradiance received from the Sun, contributing to solar and stellar physics research, as well as improving atmospheric modeling, atmospheric chemistry and climatology models.	7 February 2008, NASA	Schmidtke et al. (2006)
Solar Probe Plus	Solar Probe+ will explore what is arguably the last region of the solar system to be visited by a spacecraft, the Sun's outer atmosphere or corona as it extends out into space. Solar Probe+ will study the coronal heating and of the origin and evolution of the solar wind.	Development, July 2018, NASA	Fox et al. (2015)
DSCOVR (The Deep Space Climate Observatory)	The Deep Space Climate Observatory (DSCOVR) will maintain real-time solar wind monitoring capabilities critical to the accuracy and lead time of the National Oceanic and Atmospheric Administration (NOAA) s space weather alerts and forecasts.	Launch vehicle on 11 February 2015, NOAA, USA	Cash et al. (2012)
Aditya-1	The mission of Aditya is to study the Sun's coronal mass ejections and magnetic field structures.	Development, 2019 – 2020, India, ISRO	Sankarasubramanian (2013)
Solar Orbiter-SolO	Sun-centric 25 degrees solar inclination, 0.28 AU SolO is an ESA mission to study how the Sun creates and control its heliosphere.	Lanced date is the, Planned to be lanced in October 2018, in Florida	Gandorfer et al. (2011); Woch & Gizon (2007) to be add the papers
Solar Sentinels	Solar Sentinels contains six spacecraft (with three separated group) that will study the sun during solar maximum of solar cycle 24, that provide to understand the solar storms and the deadly radiation of a solar maximum, researching energetic particles, coronal mass ejections and interplanetary shocks in the inner heliosphere.	NASSA, Planed in 2015, 2014, 2017	

Table 2.2 – Observational and calculated (from SSM) physical characteristics of the Sun, (Satya Narayanan, 2013).

Properties	Values
Radius R_{\odot}	696.000 km
Mass M_{\odot}	$1.988 \cdot 10^{30}$ kg
Volume V_{\odot}	$1.41 \cdot 10^{27} m^3$
Average density ρ_{\odot}	$1.408 kg/m^3$
Surface gravity	$273.95 m/s^2$
Equatorial rotation	25.4 days
Polar rotation	36 days
Temperature at surface T_{\odot}	5.785 K
Escape velocity at surface	$2.223 \cdot 10^6$ km/h
Hydrogen abundance X	73%
Helium abundance Y	25%
Heavy elements Z	2%
Luminosity L_{\odot}	$3.846 \cdot 10^{33}$ erg/s

Table 2.3 – Physical properties of the solar interior (Wilson, 1994).

Zone	Radius in R_{sun}	Density [g/cm^3]	Temperature [K]
Core	$0 \sim 0.25(R_c)$	$150 \sim 20$	$1.5 \cdot 10^7 \sim 7 \cdot 10^6$
Radioactive zone	$0.25 \sim 0.70$	$20 \sim 0.2$	$7 \cdot 10^6 \sim 2 \cdot 10^6$
Tachocline	$R_c/R_{\odot} = 0.693$	~ 0.2	$\sim 2 \cdot 10^6$
Convective zone	$0.7 \sim 1.0$	$\sim 0.2 \cdot 10^{-6}$	$2 \cdot 10^6 \sim 7 \cdot 10^3$

Zone	Extension	Temperature [K]	Density [g/cm^3]
Photosphere	400km	7000 – 4500	$\sim 10^{-7}$
Chromosphere	$\sim 10^4$ km	10^4	10^{-12}
Transition Region	~ 100 km	from 20.000 to $2 \cdot 10^6$	
Carone	R_{\odot}	10^6	10^{-17}
Solar wins		from $1.6 \cdot 10^6$ to $8 \cdot 10^5$	from $10^8 cm^{-8}$ to $10 cm^{-3}$ (Schwenn, 1990)

Chapter 3

Solar activity and sunspots

We are living in the Sun's corona.

Sydney Chapman (1957)

Increased solar activity (SA) causes extreme ultraviolet and X-ray emissions from the Sun that produce effects in Earth's upper atmosphere owing to atmospheric heating increasing the temperature and density at spacecraft altitudes. Energetic particles accelerated from the Sun, increase of solar flares and CME's cause damage to sensitive instruments in the space environment. Photospheric and chromospheric phenomena such as sunspots, prominences, and coronal disturbances, as well as solar magnetism are all associated with solar activity. The fine structures of the sunspots are presented by many authors e.g. (Rubio, 2010). There is some evidence that variation of solar activity causes changes to Earth's climate (Haigh, 2007), and that the variability of the Sun has had a significant impact on global climate (Bard & Frank, 2006). The origin and cause of SA is still uncertain, but there are dynamo models that predict the SA is magnetic in nature and is produced by solar dynamo processes (Charbonneau, 2005). In general two processes are used in the theory of the Sun's dynamo models as the Ω effect-shearing and the α effect-helical motions. The structure and formation of sunspots are briefly recollected in historical sequence as outlined in Sec.2.1. In this section it was briefly summarized the general nature of solar activity and its physical characteristics, i.e. their sizes, lifetimes, brightness, evolution, Wilson depression, magnetic field and physical structure. The modern observational data are discussed in this section.

3.1 Sunspots and their general properties

The active regions of the Sun have an intense photospheric magnetic field, the magnetic flux loops into chromosphere, transition region and corona. These are manifested in different wavelengths and in different layers of the Sun's atmosphere. Dark cooler regions in the photosphere of the Sun were named "sunspots" in Galileo's era.

General characteristics of sunspots. Sunspot groups have a high magnetic field which has two parts, the leading sunspot in a sunspot group will have a north magnetic pole, while the trailing sunspot group will have a south magnetic pole (Thomas & Weiss, 2008; Moreno-Insertis, 1992; Minasyants & Minasyants, 2013). Sunspots move to the opposite polarity by roughly aligning east-west i.e. rotational direction of the Sun. The magnetic field lines emerge from a spot with one polarity and re-enter another one of opposite polarity. The gaseous

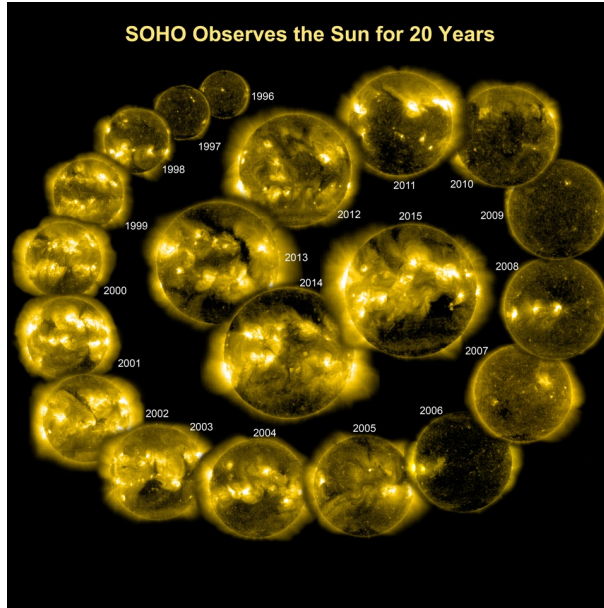


Figure 3.1 – The evolution of the active regions of Sun through almost two complete solar cycles. The collage of images taken in the 284 Angstrom wavelength of extreme ultraviolet light. Abated from ESA and NASA/SOHO.

regions do not rotate with the same rate, hence at the equator the Sun rotates once every 25 days which is where the solar maximum takes place. At regions 30° above and below from the equator it takes 26.5 days to rotate to the start of a sunspot cycle i.e. sunspot numbers are at a minimum on the equator. Regions at 60° from the equator take up to 30 days to rotate due to regions of strong magnetic field sunspots and the switched poles will linger in total for 22 years. The small sunspot pores link with the weaker magnetic fields which are long lived in a dark region without a penumbral structure. Generally the spot pore vanishes after typical lifetimes shorter than one month, then the advance stage of pores will have acquired a penumbra forming the sunspots (Thomas & Weiss, 1992).

Sunspot cycle. Schwabe (1844) first in 1843 mentioned the periodic nature of sunspots where the records of sunspot observation varied between minima and maxima with a periodicity of 10 years. The maximum number of spots was as high as 250 per month but no sunspots may appear during the solar activity minimum which is known as the Schwabe cycle. The standard 11 year length of the solar cycle was established by Wolf in 1852 and that the length of the individual cycles vary between 9 and 12 years. The 11 year period of the active regions vary in rising size, number, latitude and solar activity level by reflecting magnetic field strength tracing almost similar behavior in each 11 year period. The strongest flattening of the corona takes place two years before the sunspot minima, while the weakest takes place two years before sunspot maxima. This explains that during the solar activity maximum corona is blown out in all directions and why the coronal mass ejections are observable during sunspot maximum. The Extreme Ultraviolet (EUV) and X-ray image observations show that the brighter active regions begin from the transition region which extend to the corona. The active regions of the Sun during a solar maximum and minimum are illustrated in Fig.3.1. The brighter areas in the extreme ultraviolet correspond to areas of strong magnetic fields. The strongest magnetic concentration on the Sun's surface provides evidence of sunspots with

a dark central part of umbra and its radial, filamentary structure surrounding of penumbra. The fine structures of the umbra and penumbra are observed in high resolution. Observed features such as umbral dots, light bridges, penumbral grains and dark cores are important events for sunspot model patterns.

Sunspot classification. Sunspots are classified by various methods such as the Wilson classification which shows α, β, γ and δ types (see Tab.3.1). The magnetic δ class is the most interesting type of sunspot structure due to its high solar activity. The δ group is the biggest and 90% of the sunspots have reversed polarity with a high activity level. During the big solar flare eruptions they emit strong H-alpha emissions because of a strong magnetic gradient. The quantification of magnetic activity estimated via sunspots was initially developed by Rudolf Wolf and a recent review of sunspot numbers and solar cycles is outlined in (Minasyants & Minasyants, 2013; Hathaway, 2015).

Table 3.1 – General different classifications of the sunspot structure

The type	Structure and Location
α	A unipolar sunspot group.
β	A sunspot group that has a positive and a negative polarity (or bipolar) with a simple division between the polarities.
γ	A complex region in which the positive and negative polarities are so irregularly distributed that they can't be classified as a bipolar Sunspot group.
$\beta - \gamma$	A bipolar sunspot group but complex enough so that no line can be drawn between spots of opposite polarity.
Δ	The umbrae of opposite polarity in a single penumbra.
$\beta - \delta$	A sunspot group with a general beta magnetic configuration but contains one (or more) delta sunspot.
$\beta - \gamma - \delta$	A sunspot group with a beta-gamma magnetic configuration but contains one (or more) delta sunspot.
$\gamma - \delta$	A sunspot group with a gamma magnetic configuration but contains one (or more) delta sunspot.

SSN and GSN. There is physical understanding of solar activity events. The physical parameters e.g its inertial structure, velocity, magnetic field and thermal properties have been well investigated. The dynamical aspects and the sunspot morphological features, i.e., umbra, penumbra and light bridges according to the physical processes acting on and within sunspots are part of the solar activity. The systematic daily observations counting the sunspot number (herein SSN) and introduction of the sunspot relative number i.e. Zurich number or Wolf number invented by Rudolf Wolf. The group sunspot number (herein GSN) is estimated from the SSN (Hoyt & Schatten, 1998). The SSN is a common useful parameter in quantifying the level of solar activity which is synthetic, rather than a physical index. The GSN is calculated

from visual observation of each individual SSN on the solar surface. The sunspot activity is estimated also by the area occupied by the sunspots, it gives approximately similar results to the Wolf number. A relationship between the monthly mean sunspot number R_z and area A_{spot} is $A_{spot} \approx 16.7R_z$.

Location and evolution. Sunspots are located in active regions with a bipolar magnetic structure by restricting the activity belts reaching up to high latitudes of 25° to 35° (but they have been observed at 75° from the equator). This corresponds to a new solar cycle on each side of the solar equator. The latitude of the sunspots varies with the solar activity cycle. During the solar maximum the spots are located at a lower latitude of $15^\circ - 20^\circ$ for between 4 and 7 years after starting the solar cycle. In the most active period features such as flares and CME's occur frequently and powerfully. Large sunspot timescale formation varies from a few hours and several days. The formed sunspots begin to decay with linear and quadratic decay laws, which have different consequences for the theory underlying sunspot decay (Solanki, 2003). New spots that are fewer in number and have lower activity drift to the equator. These are located within $\pm 10^\circ$ near the end of Sun's minimum cycle. The reversed magnetic polarities of the new solar cycle starts in a similar manner, namely the magnetic polarities of sunspot pairs by Hale. One sunspot cycle to the next, the magnetic polarities of sunspot pairs undergo a reversal in each hemisphere (Hale & Ellerman, 1918). The latitudinal distribution within a cycle shown in Tab. 3.2.

Table 3.2 – Latitudinal variation of the sunspot belt over a sunspot cycle (Bray & Loughhead, 1979).

Time from minimum (years)	Average latitude (\pm°)
0	28
2	21
4	16
6	12
8	10
11	7

Sunspot groups have an oval region whose major axis is slightly inclined with respect to the parallax of latitude. The preceding spots i.e. west p-spot is referred to as the leading spot with a lower latitude than the following east f-spot. This is according to the differential motion of the Sun caused by impacting the dynamical behaviour of the magnetic flux loops attached to the sunspots.

Brightness, magnetic and dynamic structure. The brightness signature of sunspots is composed of the umbra and penumbra. The umbra radiates roughly 20 – 30% of the wavelength-integrated flux of the quiet Sun. The penumbra radiates 75 – 85% of the quiet Sun's energy flux. The umbra is 1000 – 1900 K cooler than the quiet Sun, while the penumbra is 250 – 400 K cooler also with respect to the quiet Sun. Over a sunspot, the magnetic field strength in the photosphere is 1000 – 1500G. It varies gradually at the umbra between 1800 – 3700G and at the penumbra between 700 – 1000G. The magnetic field strength also decreases with height in the atmosphere. At the same time the field fans out very rapidly. Approximate magnetic configuration of a regular sunspot is similar to that produced by a vertically oriented magnetic dipole buried below the solar surface (Solanki, 2003).

The size of sunspots. Sunspots have wide varieties of sizes and the largest of them have diameters of 60000 km or more, while the smallest sunspots are roughly 3500 km in diameter, and have the largest pores of 7 km. Generally, the ratio of total sunspot area A_{tot} to umbral area A_u :

$$r_A = \frac{A_{tot}}{A_u} \quad (3.1)$$

which gives a value of $r_A = 5.9 \pm 1$ in (Tandberg-Hanssen, 1956). Physical characteristics of r_A , depend on other parameters such as sunspot size, age, phase of the solar cycle etc.

Lifetimes. Sunspots exist in general for a time span of hours to months but existence for up to half-a-year has also been observed. The lifetime increases linearly with maximum size, following the so-called Gnevyshev-Waldmeier rule:

$$A_0 = WT \quad (3.2)$$

where A_0 is the maximum size of the sunspot, T is its lifetime and $W = 10.89 \pm 0.18$ MSH day^{-1} which is the Micro Solar Hemisphere. Most sunspots exist for less than a day, some have a lifetimes around day, and a few exist longer than a week. The timing is difficult to measure because of interruptions of the observations due to nightfall or the passage of the sunspot to behind the solar limb through solar rotation (Solanki, 2003). Essential topics such as the nature and evolution of sunspots have been covered by review in (Solanki, 2003). The small pores grow with penumbrae in pairs that develops over a large area with several spots with different intensities, sizes and shapes. Detailed descriptions of sunspot development is given in (Bray & Loughhead, 1979). A brief description of the development of large sunspot groups is described as follows (Antia & A. Bhatnagar, 2003):

1st day: The reaches of the magnetic flux on the photosphere identified by a small bright faculae in white light near the limb, or a small arch system in $H\alpha$, near the disk center.

2nd: At at the western edge of the faculae appears a small preceding p sunspot that increases in size, brightness with a rising magnetic field.

3th: The area of the faculae increases and with opposite polarity to the first spots appearance. Some following f spots at the eastern edge of the faculae appear.

4th: Large spots form from the dissolution and coalescence of small spots thus the western preceding p -spot of the group forms a penumbra with a bipolar magnetic field.

5 – 13th day: The eastern f -spot forms a penumbra then the p and f spots appear until the maximum size of group is extended. The brightness and the plages increase, if the magnetic field strength and the shear of field lines are optimal. During this phase the flare activity is higher on the sunspots group's development.

14 – 30th day: By dividing into smaller areas the $H\alpha$ plage brightness decreases, thus with opposite polarity the dark $H\alpha$ filaments appear in the active region. All spots disappear except for the residual p -spot.

30 – 60th day: The p spots have a tendency to shrink and disappear and the $H\alpha$ brightness plages will continue to decrease thus the $H\alpha$ filaments increase in length and may divide the active region into two halves of opposite polarity.

60 – 100th day: Almost all $H\alpha$ plages disappear but the photospheric faculae may persist. The filament reaches it's greatest length and lies almost parallel to the equator.

100 – 250th day: The CME forms from the broken sections of filament or the filament may erupt as a whole.

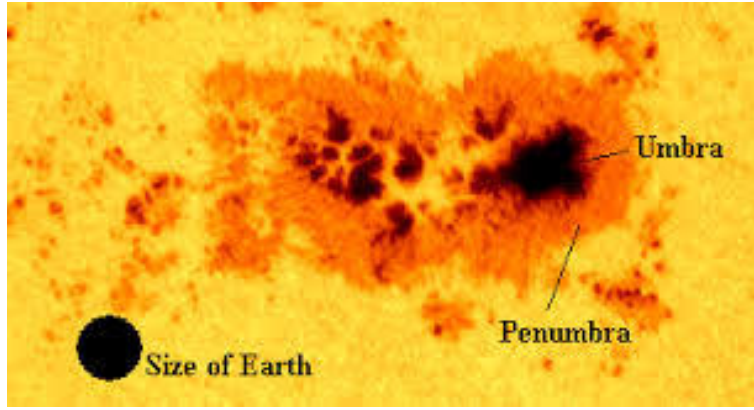


Figure 3.2 – Photograph of sunspot showing the structure of a large sunspot with umbra and penumbra. Image from SOHO/MDI consortium, a project of international cooperation between ESA and NASA.

3.2 The sunspot umbra and penumbra

The study of solar activity is related with many solar features such as: a magnetic inhibition of convection, the conjecture of a flat penumbra, the stratification beneath the umbra, the observable magnetic profile, the Evershed effect, the cooling by Alfvén waves, variation of the umbra brightness with the phase of the sunspot cycle, structure of the penumbra and the inclination of its field etc. The structure and physics of sunspots have been largely studied by many authors (Bray & Loughhead, 1979; Thomas & Weiss, 1992; Schmieder, 1997; Strassmeier, 2002; Minasyants & Minasyants, 2013) and sunspots and its historical observation was reviewed in (Zwaan, 1981; Schmidt, 1991; Judit Brody, 2002; Vaquero, 2007; Galilei & Drake, 1990b; Stix, 2003; Vaquero, 2007), while physics of the periodicity properties have been outlined in (Grant, 1979; Schöve, 1983b; Hathaway, 2015) and its records throughout history are archived in (Vaquero & Vázquez, 2009; Frédéric et al., 2015).

Sunspot umbra. The inner, dark, cool region of the sunspots which harbors dynamic inhomogeneities were called umbral dots by Danielson in 1964. The intensity of the umbra has been measured for about 125 years. The direct evidence of the umbral convection is its granulation. There the convection is most effective in the upper 1500 km. In the umbra region the gas pressure is lower than outside. The magnetic field in umbral dots is weaker than in its surroundings. The variable magnetic field lines have flux tubes with the electric currents due to induction. The number of dark umbral regions is approximately the same as the total sunspots number i.e. $R_{umbra} \approx R_{spot}$. The umbra and penumbra of the sunspots are illustrated in Fig.3.2. The main characteristics of the fine structure of the Sun are presented in Tab.3.3.

Sunspot penumbra. The manifestation of small-scale light filamentary structures around the umbra is called penumbra (Thomas & Weiss, 1992). These have an average lifetime of 2 hours, a length of 5000 km, and width of around 300 km. The configuration of the magnetic field in the penumbra models during the last 15 years has been explained with Evershed flows (1909). A distinctive gas flow as a radial motion but irregular tangential motion has also been observed. The Evershed flows heats the penumbra very efficiently by creating radial motion, which reproduces observational features such as dark-cored penumbral filaments. The magnetic field in the dark region is horizontal, while the brighter filaments have vertical

Table 3.3 – Umbral and penumbral timescales (Bray & Loughhead, 1979).

Penumbra filaments	$\approx 2h$
Penumbra bright region	30min
Umbral granules	15min-2hours
Faculae granules	2hours
Photospheric granules	7 – 10min

magnetic fields. The Wilson depression occurs when the radiation from sunspot penumbrae and umbrae emerge from a deeper layer than in the quiet photosphere. The intensity of the fine structure of the Sun has been reviewed (Rubio, 2010). The intensity of the penumbra does not depend on the size of the sunspots, while the penumbral temperature increases from the interface between the umbra and penumbra toward the edge of the photosphere (Benestad, 2002). The relationship between the sunspot decay rate D_{spot} and the ratio of umbra to whole spot area U/W established by Hoyt & Schatten (1998) is as follows:

$$D_{spot} = 63.3 - \frac{(6.0 \pm 0.4)}{\overline{U/W}}, \quad (3.3)$$

The ratio of umbral decay rate D_{umbra} to sunspot area D_{spot} lasting N days is:

$$\overline{U/W} = \frac{2U_0 - (1 + N) D_{umbra}}{2W_0 - (1 + N) D_{spot}}. \quad (3.4)$$

The decay rate of the umbra is constant and the penumbra rate is variable. The umbra regions disappear before the penumbra then the penumbra structure is involved in the final stage of sunspot life.

3.3 Sunspot groups and models

The group sunspot number (GSN) is an alternative indicator of solar activity which counts only the sunspot groups by disregarding the number of spots in each group.

Counting methods of GSN. The GSN is based on a weighted average of all observations for a given day, hence its reconstruction is included for all available ancient and archival records from 1611 – 1998. This was first introduced by Hoyt & Schatten (1998) who performed an extensive archive search of R_g data. The new series of the solar activity GSN's period from 1611 – 1818 are more reliable than R_g . The daily GSN R_g is defined as follows:

$$R_g = \frac{12.08}{n} \sum_i \kappa'_i G_i. \quad (3.5)$$

where G_i is the number of sunspot groups recorded by the i th observer, κ' is the observer's individual correction factor, n is the number of observers for the particular day, finally 12.08 is a normalization number scaling R_g to R_W (relative Wolf GSN) for the period of 1874 – 1976. R_g is based on the easily identified sunspot groups either and R_g covers the known minima and maxima of solar activity evolution. Although, the systematic uncertainty of R_g before

1640 has been estimated about 10%, it is less than 5% during the periods of 1640 – 1728 and 1800 – 1849, 15 – 20% from 1728 – 1799, and about 1% since 1849 (Hoyt & Schatten, 1998).

Table 3.4 – Magnetic classification of sunspot groups (Bray & Loughhead, 1979).

Classification of SPG	Description
α	Unipolar, symmetrical faculae preceding and following the group
αp	Unipolar, followed by elongated faculae
αf	Unipolar, preceded by elongated faculae
β	Bipolar, preceding and following members almost equal area
βp	Bipolar, preceding member is the principal feature
βf	Bipolar, following member is the principal feature
$\beta\gamma$	Bipolar, characteristic but lacks well marked division between region of opposite polarity
γ	Complex
Zurich classification of SPG	
<i>A</i>	Single pore or group of pores showing no bipolar configuration
<i>B</i>	Group of pores showing a bipolar configuration
<i>C</i>	Bipolar group with one spot possessing a penumbra
<i>D</i>	Bipolar group whose main spots have penumbra and a least one spot has simple structure length of group $> 10^\circ$
<i>E</i>	Large bipolar group with two main spots having penumbra length of group $> 10^\circ$
<i>F</i>	Very large bipolar or complex group length of $> 10^\circ$
<i>G</i>	Large bipolar group containing no small spots between main spots length of group $> 10^\circ$
<i>H</i>	Unipolar, spot with penumbra and diameter $> 2.5^\circ$
<i>J</i>	Unipolar spot with penumbra and diameter $> 2.5^\circ$

A fully updated reconstruction series of new GSN (Hoyt & Schatten, 1998) estimated by SIDC including the currently available sources and archives is shown in Fig.3.3. The series of relative GSN is the longest homogeneous global indicator of solar activity. Constituted by direct solar observations with an accuracy controlling technical method. The RSN is defined by Wolf (1859) as R_W :

$$R_W = \kappa(10G + N). \quad (3.6)$$

where G is the GSN (including solitary spots), N is the total number of all individual groups visible on the solar disc, while κ denotes an individual correction factor depending on an instrument parameters, observatory location, and details of the counting method, $\kappa = 1$ is used. Only larger spots are counted and the smallest spots are ignored. Current methods count even the smallest spots, attributing a higher weight (i.e., $f > 1$) to spots with a penumbra, depending on their size and umbral structure. Different counting methods and the determination of R_W were discussed in (Hoyt & Schatten, 1998; Hathaway, 2010). The value of R_W is

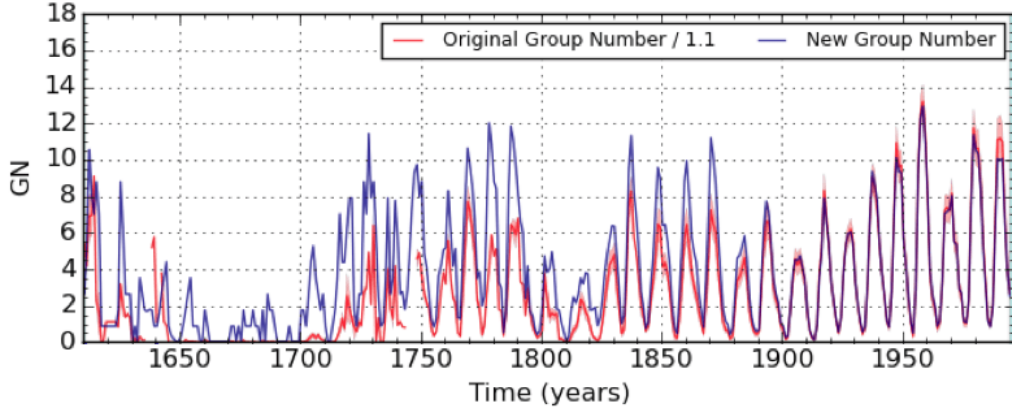


Figure 3.3 – The comparison of observed old and new undated group sunspot numbers (Clette et al., 2015).

calculated for each day e.g. the primary observers were Staudacher (1749 – 1787), Flaugergues (1788 – 1825), Schwabe (1826 – 1847), Wolf (1848 – 1893), Wolfer (1893 – 1928), Brunner (1929 – 1944), Waldmeier and Koeckelenbergh (1945 – 1980). Since 1982 the production of the R_w terminated, then international sunspot number R_i is updated and is computed like in Eq. 3.6. The whole new R_i are based on average data of more than 20 approved observers. R_i are estimated by the hemispheric sunspots numbers i.e. in the northern R_N and in the southern R_S sunspots numbers for the purpose of studying the north and south asymmetry:

$$R_i = R_N + R_S. \quad (3.7)$$

The models of estimation of the GSN are the most studied issue in solar observation. The main source of observational archives regarding sunspot number data is known from various institutions: Sunspot Index Data Center, recently renamed Solar Influences Data Analysis Center (SIDIC), AAVSO and available from the National Geophysical Data Center, the Kislovodsk Sunspot Number from the Pulkovo Observatory. Estimations of the cycle amplitudes are varied by up to 6 – 7% from the SIDC values, NOAA numbers being consistently lower, while Kislovodsk numbers show no such systematic trend. To propose long term changes of solar activity, the annual mean values are used. These are estimated as the first and last months which are given half the weight of other months hence the R - sunspot numbers is:

$$R = \frac{1}{24} \left(R_{m,-6} + 2 \sum_{i=-5}^{i=5} R_{m,i} + R_{m,6} \right), \quad (3.8)$$

where $R_{m,i}$ being the main monthly value of R_W for i th calendar month counted from the present month. There are also some known alternating sunspot series R_{\pm} and non-linear transformed indexes R' . The strongly peaked and asymmetrical sunspot cycle profiles are strongly deviated from a sinusoidal profile. The constructs of the sunspot number (Petrovay, 2010) are arbitrary. The long-lived sunspot group lifetimes are related to the maximum group area according to the "rule-of-thumb" $T \approx 0.1A_{max}$, where A_{max} is measured in millionths of the visible hemisphere.

Magnetic classification. Often the sunspot groups contain individual spots with the same magnetic field structures, where the spots are in the group leading or following the Sun's

rotation. Generally, the observed sunspot groups are classified depending on their polarity, state of umbral and penumbral structures, and area covered. Among the various classifications are the Waldmeier Classification which takes account of the polarity, the number of spots and number of groups, the formation of penumbrae and the longitudinal extent. The modified version of Waldmeier's is the McIntosh's classification in which the 'active' and 'inactive' varieties of sunspot groups are described, including the correlation with the complexity of the group and X-ray flares. Mount Wilson magnetic classification with Unipolar- α , Bipolar- β , and complex- γ classes are also used. This is based on the magnetic complexity of the sunspot group using magnetic field data (see Tab.3.4). GSN starts from type A by evolving through the various states during their life cycle, i.e. from A to E, spending most of the time in G to J where the lowest flare activity slowly disappears. The highest flare activity tends to be associated with classes D, E to H. Small groups like A-B-C-B-A tend to have symmetrical development, whereas large groups like A-C-C-D-C-H-J-A have the symmetrical development. The sunspots spend most of their life in a decaying phase, after rapidly growing.

GSN models. The understanding of solar activity, and formation of sunspots require physical insight into the processes taking place in the Sun. The hypotheses based on dynamo processes with different mechanisms revealed the involvement of magnetic interactions with turbulent flow and electric conduction. According to a different interpretation of α -effect (negative or positive) the classification of the recent solar dynamo models are: overshoot layer models, distributed wave models, co-spatial transport models, and distributed transport models (Petrovay, 2010). One of the hypothesis regarding to sunspot rises is the convective or hydrodynamical sunspot model. This explains the origin of the sunspots as being due to an initial cooling and subsequent intensification of the magnetic field. A second hypothesis is magnetic cooling which suggests that the sunspots are formed as a result of regional intensification of the magnetic fields. Colder and darker material on the surface of the Sun is produced by the magnetic fields inhibiting the convection in the sunspots, which can be explained by a dynamo theory similar to the geomagnetic field model (Petrovay, 2010). Extensive summaries of the current standing of solar dynamo theory are given in a review by Charbonneau (2010). There are also some models known which predict the solar cycle 24 on the basis of dynamo models with a high confidence. For example the flux transport dynamo model which is an advection-dominated model (Dikpati & Gilman, 2006).

3.4 Sunspot cycles radiance and irradiance models

Space-born measurements of the total spectral irradiance (TSI) have been measured since the 1970s. The relationship between solar activity and total electromagnetic energy output from the Sun are provided by space based measurements of the total spectral irradiance. Thus, the data from TSI observation and the solar cycle are correlated with variations of the total solar luminance of the order 0.1%. The TSI database provides an accurate record for investigating models of solar variation used to study the relative significance of natural and anthropogenic forcing climate change. The TSI database has a correlation between the non-overlapping components which includes the maxima and minima of three solar cycles. This database is comprised of the observations of some independent experiments: Nimbus7/ERB (Hoyt & Schatten, 1998; Hoyt et al., 1992), SMM/ACRIM1 (Willson & Hudson, 1991), ERBS/ERBE (Lee et al., 1995), UARS/ACRIM2 (Willson, 1997; Willson & Mordvinov, 2003), SOHO/VIRGO (Frohlich et al., 1997), ACRIMSAT/ACRIM3 (Willson, 2014),

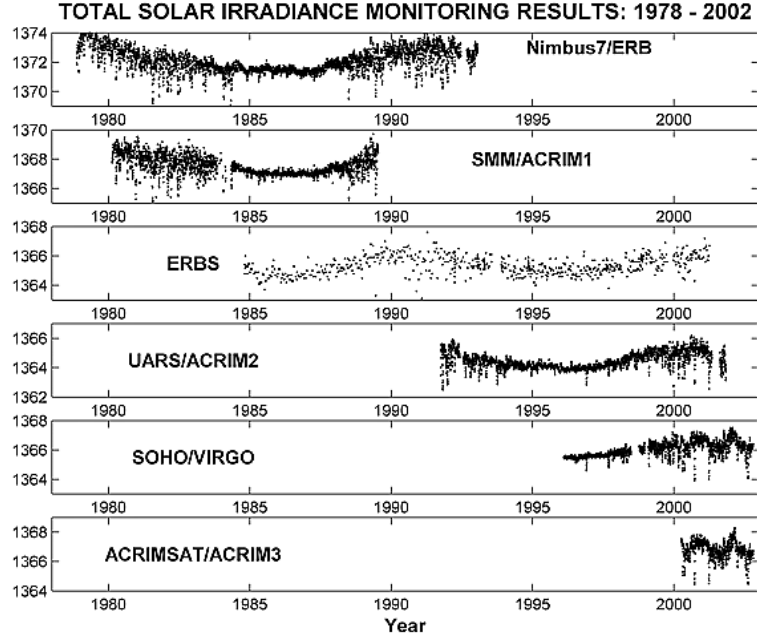


Figure 3.4 – TSI observations by satellite experiments: 1978 – 2002 (units of W/m^2 at 1 A.U.) plotted on each experiment’s "native scale" (Willson & Mordvinov, 2003).

SORCE/TIM (Kopp et al., 2005), and PREMOS/PICARD (Schmutz et al., 2013).

The data sets of satellite TSI monitoring results are shown in Fig.3.4 and Fig.3.5. The TSI database experiment was compared with the solar cycle minima. It was experimentally proved that during the a period of fewer sunspots the measurements of the TSI dropped. Over a short timescale of the Sun’s rotation the TSI was dominated by the darkening effect, while the faculae brightening and plages were more strong by impacted to the TSI in (W/m^2) over longer 11 year timescales, as the network faculae emission varied with the overall solar activity cycle.

$$TSI = S = 1365.7445 + 0.0055R_Z, \quad (3.9)$$

or another similar relationship is known as, in W/m^2 :

$$S = 1366 + 7.71 \cdot 10^{-3}R_W, \quad (3.10)$$

where R_Z and R_W are Zurich and Wolf relative sunspot number respectively. A simple relationship between the solar activity component of the irradiance and sunspot number:

$$\Delta S = 0.001R_Z. \quad (3.11)$$

The variation of the TSI is associated with a Schwabe cycle and is only $\sim 1W/m^2$ between a solar minimum and maximum, but the temperatures in the Northern Hemisphere show a variation to this small-scale variability. The observational database of space-based solar monitoring show the larger amplitude solar total radiative output changes of 0.24% relative to the Maunder Minimum.

Solar total and ultraviolet irradiances were reconstructed. There has been $0.27^\circ C$ warming since 1900, $0.12^\circ C$ since 1970 where a climatic sensitivity of $\Delta S = 0.1233\Delta R_Z$ was used (Lean & Rind, 1998a). The variation of the irradiance caused by the outer solar layers to thermal or

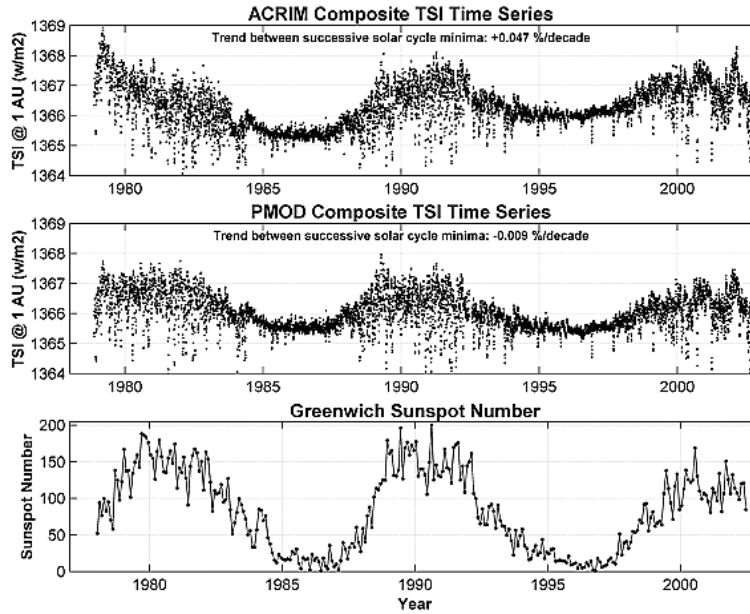


Figure 3.5 – Comparison of the ACRIM and PMOD (Fröhlich, 2003) composite TSI time series with the Greenwich Sunspot Number, (Willson & Mordvinov, 2003).

magnetic processes on the convection zone, where the photospheric features such as sunspots and faculae are generated by the same mechanism. Although correlation of the solar radiance to solar activity is related for a timescale longer than one solar cycle, it was suggested that the solar output is linked to the length of the solar cycle.

3.5 Cycle characteristics of the activity and chaos

Usually, the solar activity is considered as a superposition of Fourier components, e.g. (Wolf, 1859b), who suggested monthly sunspot numbers reconstruction formula was based on the orbits of Venus, Earth, Jupiter, and Saturn to fit Schwabe’s data for the years 1826 to 1848. The determination of the periods and the amplitudes of the SSN is based on the estimation of the dates of the solar minima cycle, which generally used a monthly average of SSN with the 13 month running mean smooth. The minima and maxima cycles have been studied by many authors. The variation of observation data over last 300 years is shown in Fig.3.6. The reconstruction of the SSN covering the last 11,400 years based on the dendrochronologically dated radioisotope concentrations are shown in Fig.3.7. Variations of the solar cycles are not only 11 years, but can also have shorter or longer cycles. Generally the maxima and minima values of solar cycles are more useful and informative to study the nature of the cycle, which is identified by applying mathematical methods. The maximum and minimum solar cycles can be determined not only on sunspot number but also by using the sunspot areas, and 10.7cm radio flux as listed in Tab.3.5. Here the data and values for a maximum period used the 13th-month running mean on activity indicators. The determination of the maxima and minima cycles from the activity records are a more complex subject, thus solar activity has trends of short and long term variability which requires more improved variations of smoothing mathematical methods. The uses of methods and techniques of data are discussed in the next section.

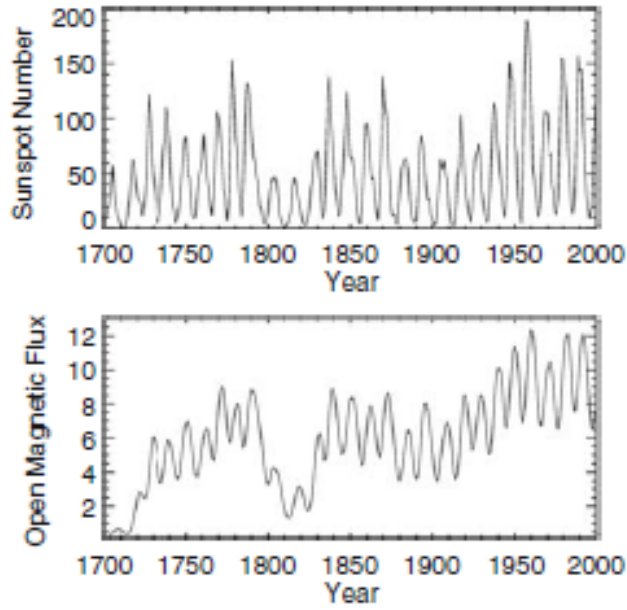


Figure 3.6 – The variation of the closed magnetic field (CMF), indicated by the sunspot number on the top and the variation of the open magnetic flux (OMF) calculated by Usoskin (2013).

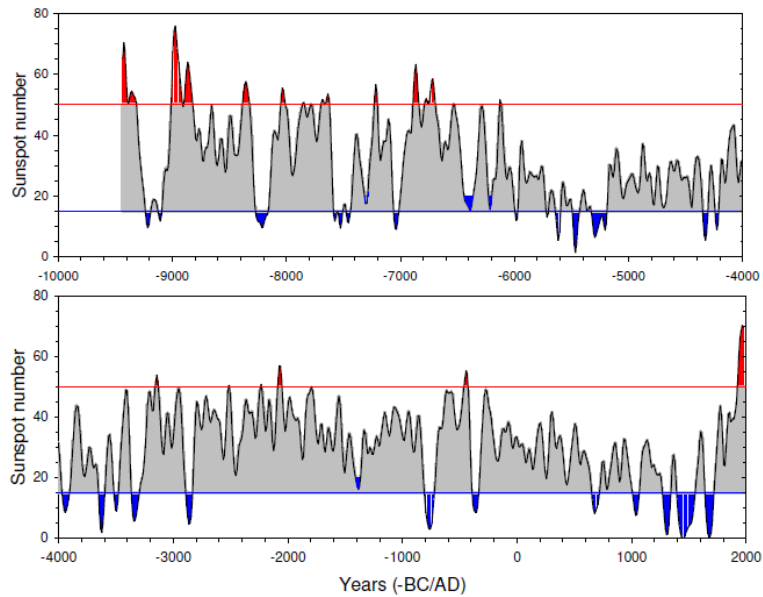


Figure 3.7 – Sunspot activity throughout the Holocene, reconstructed from ^{14}C using geomagnetic data. Blue and red areas denote grand minima and maxima, respectively, (Usoskin, 2013).

Cyclic period. One of the characteristics of solar cycles is its cyclic period, which is estimated as the elapsed time from solar cycle minimum to maximum. Generally the determination of the average cycle period depends upon the cycles and the methods used to determine the minima. In Fig.3.8 are shown the 24-month Gaussian smoothed ISN for 1 – 23 cycles,

Table 3.5 – Data and values of the maxima and minima using the 13-month mean of International Sunspot Number (ISN), Sunspot Area data and 10.7cm Radio Flux data which are estimated only for cycle maxima (Hathaway, 2015).

Cycle	13-month ISN Cycle Date	mean Maximum Value	13-month Sunspot Data Value	mean Area R-	13-month 10.7cm Date Value	mean Ray Flux R-	13-month ISN Cycle Date	mean Minimum Value
1	1761/06	86.5					1755/02	8.4
2	1769/09	115.8					1766/06	11.2
3	1778/05	158.5					1775/06	7.2
4	1788/02	141.2					1784/09	9.5
5	1816/05	49.2					1798/04	3.2
6	1816/05	48.7					1810/08	0.0
7	1829/11	71.5					1823/05	0.1
8	1837/03	146.9					1833/11	7.3
9	1848/02	131.9					1843/07	10.6
10	1860/02	98.0					1855/12	3.2
11	1870/08	140.3					1867/03	5.2
12	1883/12	74.6	1883/11	88.3			1878/12	2.2
13	1894/01	87.9	1894/01	100.4			1890/03	5.0
14	1906/02	64.2	1905/06	75.4			1902/01	2.7
15	1917/08	105.4	1917/08	93.0			1913/07	1.5
16	1928/04	78.1	1926/04	92.3			1923/08	5.6
17	1937/04	119.2	1937/05	133.3			1933/09	3.5
18	1947/05	151.8	1947/05	166.5			1944/02	7.7
19	1958/03	201.3	1957/11	216.5	1958/03	201.2	1954/04	3.4
20	1968/11	110.6	1968/04	100.9	1970/07	109.6	1964/10	9.6
21	1979/12	164.5	1982/01	156.0	1981/05	159.4	1976/03	12.2
22	1989/07	158.5	1989/06	158.5	1989/06	168.0	1986/09	12.3
23	2000/04	120.7	2002/02	126.7	2002/02	152.3	1986/09	8.0
24	2014/04	81.9					2008/12	1.7

GSN for 4 – 2 cycles minima dates and these cycles periods.

Amplitude. Another characteristic of the solar cycle is its amplitude which depends on the activity index used and the methods of smoothing. Systematic differences between the ISN and the GSN are shown in Fig.3.9 and 3.10 with the determination of maxima by a 13-month mean. The mean amplitude of ISN from 1 – 13 cycles is given as 114 in (Hathaway, 2015) with a standard deviation of 40. GSN 4 – 23 is given a mean amplitude 90 with a standard deviation of 41 which is shown in Fig. 3.11. The elapsed time from minimum to maximum is almost always shorter than the elapsed time from maximum to minimum. For ISN 1 – 23 an average cycle takes about 48 months to rise from minimum to maximum and about 84 months to fall back to minimum again (Hathaway, 2015).The observed cycle data have double peaks,

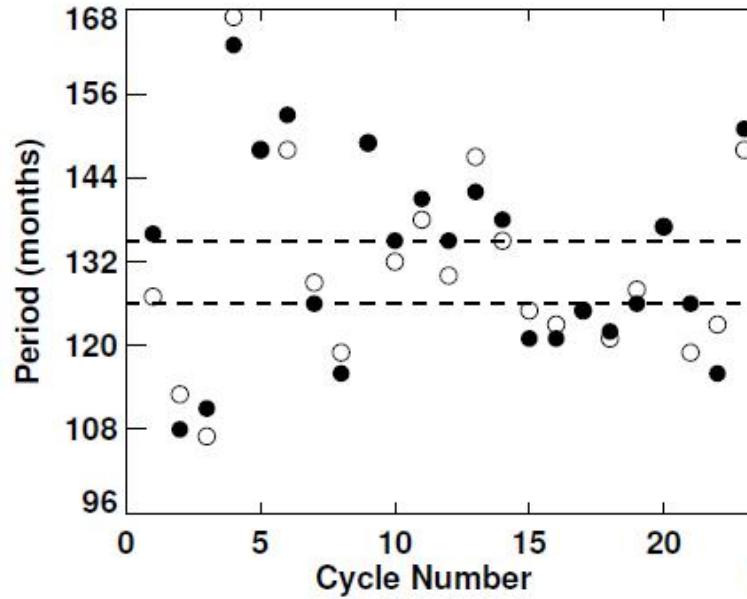


Figure 3.8 – The cycle periods as functions of Cycle Number, where filled circles give periods determined from minima in the 13-month mean, while open circles give periods determined from the 24-month Gaussian smoothing, the with dashed lines is the Wilson Gap also from the 13-th month mean which is a mean period of both with a standard deviation of about 14 months (Hathaway, 2015).

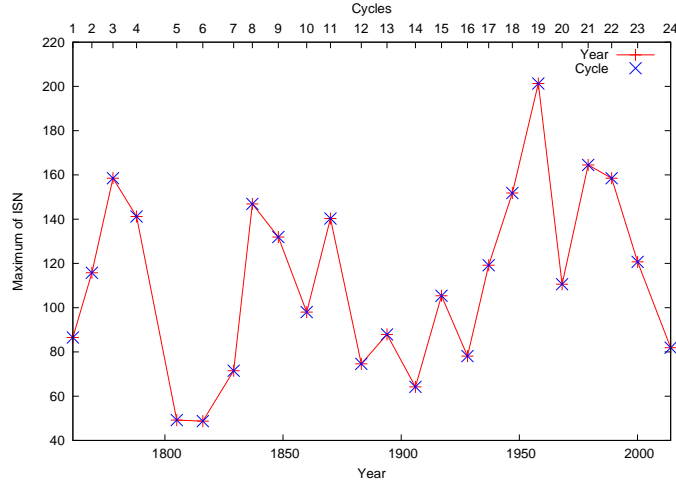


Figure 3.9 – Cycle maxima from GSN determined by the 13-month mean. The Group values are systematically lower than the International values prior to cycle 12. The data are taken from (Hathaway, 2015).

which suggests a north, south asymmetry in solar activity, and is called as the Gnevyshev Gap. The Waldmeier Effect is one of the effects showing the relationship of the sunspot cycle characteristics, i.e the rise time (R_{time} in month) SSN from minima to maxima is inversely

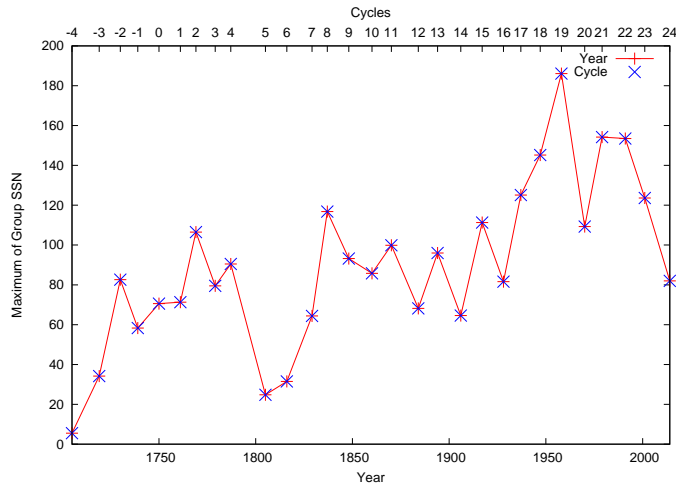


Figure 3.10 – Cycle maxima from ISN determined by the 13-month mean. The ISN values are systematically higher than GSN values prior to cycle 12 (Hathaway, 2015).

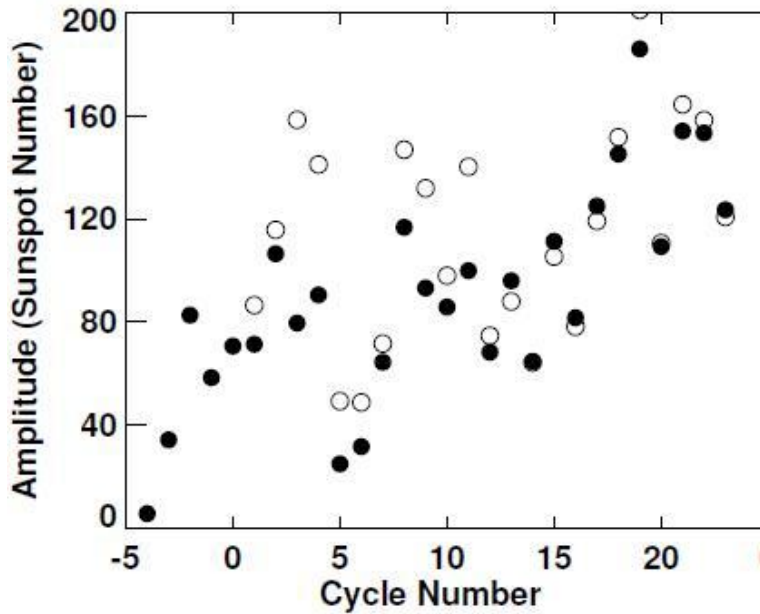


Figure 3.11 – The cycle amplitudes as functions of cycle number. The filled circles show the 13-month mean maxima with the GSN while the open circles show the maxima with the ISN (Hathaway, 2015).

proportional to the cycle amplitude (A , in SSN):

$$R_{time} \approx 35 + \frac{1800}{A}. \quad (3.12)$$

A significant relationship between a cycle period and the amplitude of the following cycle was studied (Hathaway et al., 1994; Solanki et al., 2002). Hathaway (2015) argued that a fairly

strong correlation of $r = -0.68, r^2 = 0.46$ at the level of 99%, and a weaker correlation of $r = -0.37, r^2 = 0.14$. A relationship between cycle maxima and the previous minima was correlated as $r = 0.56, r^2 = 0.31$ at a significant 99% level (Hathaway et al., 1999). That is the variation of the active latitude according to the Sporer's law. The variation of the active latitude (Hathaway, 2011) found a fit with an exponential function:

$$\bar{\lambda}(t) = 28^\circ \exp[-(t - t_0)/90], \quad (3.13)$$

where $\bar{\lambda}$ and t are the active latitude and time respectively, and t_0 is the starting time which is measured in months. At the maximum the sunspot zones have higher trends in the large cycle than in the small cycle (Waldmeier, 1955; Becker, 1954). In Li et al. (2003) the high latitude was found as 35° . In Fig.3.12 is illustrated the latitudinal widths of the sunspot zones where the active latitude bands are narrow at the minimum. They migrate to a maximum width at the time of maximum, then finally narrow with the declining phase. Fig. 3.12 shows that the large amplitude has a tendency to reach the solar maxima quicker than the medium or small amplitude cycles according to the Waldmeier Effect. That is why the sunspot zone latitude at the maximum of a large cycle will be higher.

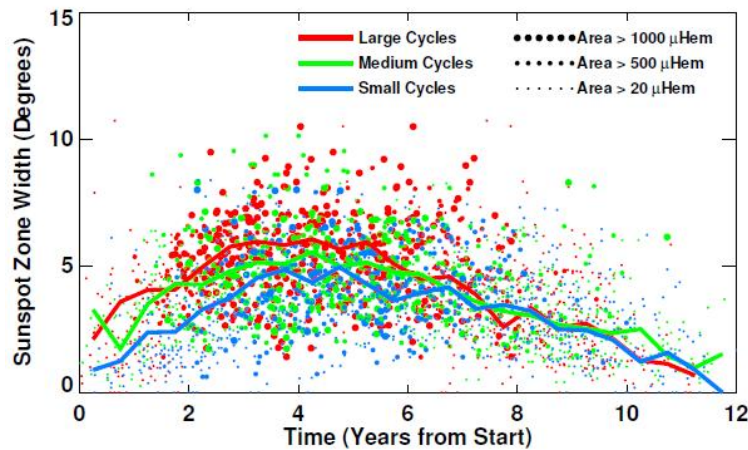


Figure 3.12 – Latitudinal widths of the sunspot area centroid in each hemisphere for each Carrington Rotation as functions of time from cycle start. Three symbol sizes are used to differentiate data according to the daily average of the sunspot area for each hemisphere and rotation. The centroids of the centroids in 6-month intervals are shown for large amplitude cycles (red line), medium amplitude cycles (green line), and small amplitude cycles (blue line), (Hathaway, 2015).

Northern and southern asymmetry. The variation of the sunspot areas on each different hemisphere provides changes in phase, i.e. the phase relationship between northern and southern sunspot areas, see Fig.3.13. As shown, the cycles 17 – 19 have the south leading the north, but then suddenly from cycle 20 the north leads the south. Using sunspot area data (Donner & Thiel, 2007) concluded that at a period of 10.75 years, the north and south hemispheres never shifted out of phase by more than ± 10 months or 10% of the cycle period. Studies of the activity in each solar hemisphere have long shown significant asymmetries and the natural characteristics of this asymmetry were recently investigated by Yang et al. (2015).

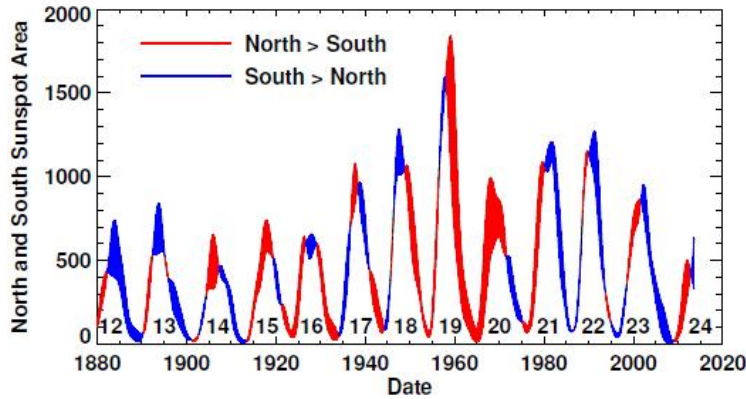


Figure 3.13 – Variation of smoothed monthly sunspot areas for northern and southern hemispheres separately. The difference between the two curves is filled in red if the north dominates or in blue if the south dominates, (Usoskin, 2013).

In (Nagovitsyn & Kuleshova, 2015) for 2000 years of low-latitude auroras reconstructed with time variations in the north-south asymmetry of solar activity. They determined that it was the north-south asymmetry that has quasi-periodic variations of the Schwabe cycle of 8 – 16 years, the Bruckner cycle of 30 – 50 years, the Gleissberg cycle of 65 – 110 years, the Suess cycle of 150 – 210 years and the Link cycle of 380 – 420 years. More investigations on the north and south sunspot asymmetry are outlined by other researchers (Javaraiah, 2015; Leussu & Ilya G. Usoskin, 2016; Muraközy, 2016; Javaraiah, 2016; Latyshev & Olemskoy, 2016).

Tilt of active regions. The next important characteristic of the sunspot cycle is the tilt of active regions. The tilt of the active region starts systematically in each cycle on higher latitudes with the opposite charge by following the polarity magnetic flux toward the leading polarity magnetic flux. The flux transports poleward and at the cycle maximum the polar field reverses, then it will be built up of new polar fields during the declining phase of each cycle (Charbonneau, 2010). Due to the observation the tilt of the active region of the latitude varies, as the measurements of the magnetograms indicate higher values of $4 - 5^\circ$ for each 10° of latitude (Stenflo & Kosovichev, 2012). The measurements of the white-light images indicate lower values of 2.5° for each 10° of latitude (Sivaraman et al., 1999). Recently, Ivanov & Miletsky (2016) studied the characteristics of sunspot group latitude distribution in two catalogues: the extended Greenwich (1874 – 2014) and Schwabe’s data (1825 – 1867). They suggested both data sets reveal similar links between latitude and amplitude characteristics of the 11 year cycle. More results of research and higher resolution observational data of the activity induces suggested the extension of the solar cycle, which indicated a latitude range of $\sim 30 - 60^\circ$ for the first bipoles in a cycle and extended cycle durations of $\sim 14 - 16$ years. The equatorward migration of sunspots during a given solar cycle can be extended to higher latitudes than indicated by the sunspot zones (Cliver, 2015). Fig.3.14 shows the monthly averaged sunspot numbers from 1750 to 2016, the data is from the Solar Influences Data Analysis Center in Belgium.

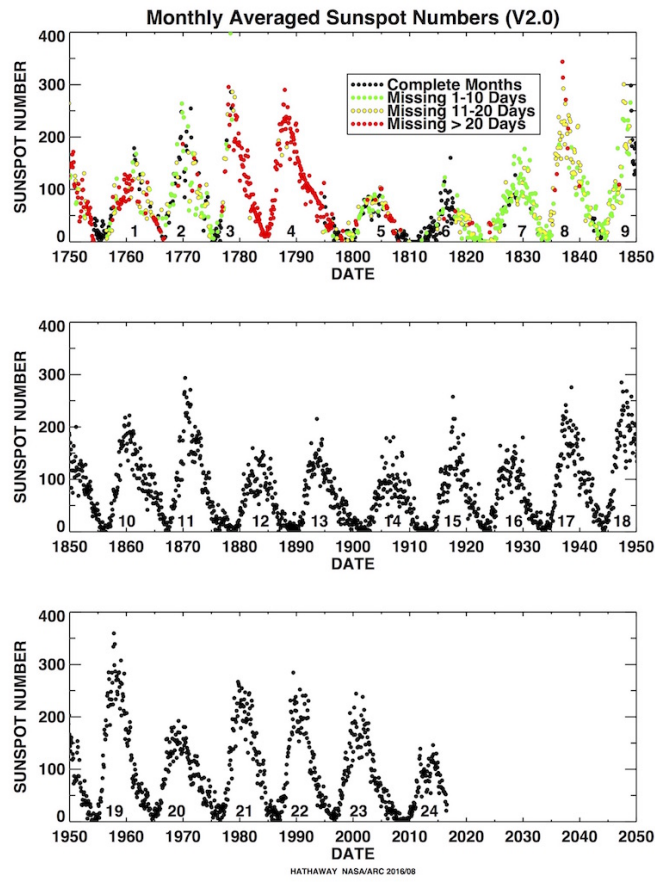


Figure 3.14 – The monthly averaged sunspot numbers from 1750 to 2016, based on observational data of the Solar Influences Data Analysis Center in Belgium, (Hathaway, 2010).

3.6 Solar cycle prediction

One of the important subjects in solar terrestrial physics is to predict the peak amplitude of the sunspot cycle. Predictions of the solar cycles are based on various observational data, which are then treated with different techniques over different timescales, i.e a short term for day-month-year, while a long term view in solar activity considers data on centennial or even millennial scale. Due to the changes of cycle's amplitude, variations in the cycle length and shape, this is why it is a complex subject to research. A monograph on the solar activity prediction was presented by Vitinskij (1973). In a recent review Petrovay (2010) overviewed different methods of solar cycle prediction and its models based on prediction. Pesnell (2008, 2012a) presented the analysis of more than 75 predictions of the amplitude of solar cycle 24 and these predictions were compared to the climatological average. Hathaway (2009) proposed solar cycle forecasting using auto-regression and curve fitting techniques. Numerical solar activity phenomena forecasting employed by numerous methods with often no physical basis. Often are used well-established mathematical techniques, and precursor methods based on a physical basis.

Precursor methods. Empirical predictions have two methods. Firstly as a statistical

method that is based on the long term variation of the sunspot number. Secondary the physical proprieties of solar activity used by statistical analysis for treatment to extract and exploit for forecasting. The precursor methods are based on the properties of the current solar cycle mode and are predictive for the next cycle. At a specified time to predict the amplitude of the solar minimum the precursor method is used with any observational proxy, value e.g. the activity data. Each numbered solar cycle is a consistent unit in itself, while solar activity seems to consist of a series of much less tightly intercorrelated individual cycles (Petrovay, 2010). Predicting techniques can be based on the characteristics of the preceding cycle as indicators of the size of the next cycle and periodicities in the cycle amplitudes. This technique is used to predict future cycle amplitudes based on cycle statistics (Wilson et al., 1998; Ahluwalia, 1998a; Javaraiah, 2007). In general, three precursor types are used for prediction, namely the polar field precursors, geomagnetic precursors and characterization of interplanetary magnetic field strength or open flux. One of the most simple approaches of sunspot cycle prediction is correlating the amplitudes of consecutive cycles, which are related to secular variations in solar activity. The correlation between the R_{min} minimum activity level and the amplitude of the next R_{max} maximum is a linear relationship, with a correlation coefficient of $r = 0.72$ given as:

$$R_{max} = 67.5 + 6.91R_{min}. \quad (3.14)$$

In Fig.3.15 is illustrated this correlation of R_{max} and R_{min} using the observed value of 1.7 for the sunspot number in the recent minimum (by the minimax method) cycle 24 is predicted to have a value of 80 (Petrovay, 2010). For cycle 24, Petrovay (2010) suggested the correlation

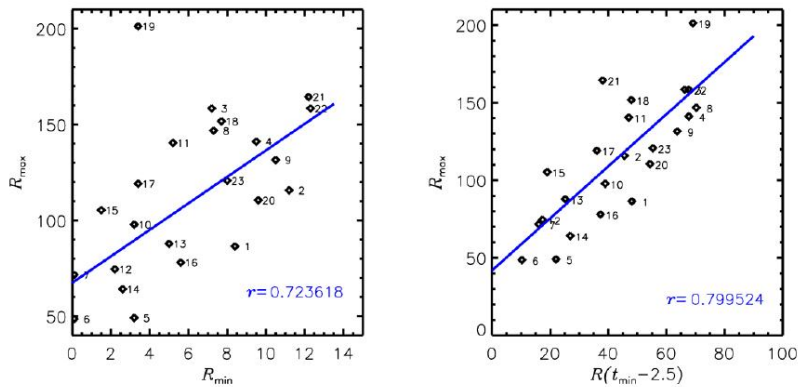


Figure 3.15 – Comparison of the monthly smoothed sunspot number of R_{max} at cycle maximum and R_{max} at the previous minimum (left), 2.5 years before the minimum (right) with labeled cycle number, linear regression, and corresponding correlation coefficients (Petrovay, 2010).

coefficient corresponds to a time shift of 2.5 years, hence point out the linear regression with a value predictor of 16.3 at the epoch of minimum t_{min} :

$$R_{max} = 41.9 + 1.68R(t_{min} - 2.5). \quad (3.15)$$

A minimum in the solar polar magnetic field is an indicator of the level of activity at next maximum. Prediction of future cycle amplitudes are based on polar field methods which show better results than the extrapolation methods (Babcock, 1961; Schatten & Sofia, 1996;

Schatten, 2002; Svalgaard & Schatten, 2008; Hathaway & Upton, 2016a). A minimum in the geomagnetic activity is also an indicator of the level of activity at next maximum. The geomagnetic precursors are based on the precursor signal of the high-speed solar wind streams from low latitude coronal holes late in a cycle. The minimum amplitudes of the smoothed geomagnetic aa index are well-defined and are well correlated to the amplitude of the following sunspot number maximum, where the ratio of R_{max} to the minimum geomagnetic index of aa_{min} gives:

$$R_{max} = 7.95aa_{min} \pm 18. \quad (3.16)$$

Prediction of the solar cycle is based on a geomagnetic precursor and has been studied (Thompson, 1993; Wang & Sheeley, 2009a). In Tab.3.6 is listed the errors of the different geomagnetic precursor predictions, here Ohl’s and Feynman’s methods show more accurate results. Another method of predicting future cycle amplitudes is based on flux transport dy-

Table 3.6 – Prediction method errors for 19 – 23 solar cycles, (Hathaway, 2010).

Prediction method	Cycle 19	Cycle 20	Cycle 21	Cycle 22	Cycle 23	RMS	Reference
Mean Cycle	-97.4	-1.6	-55.4	-46.7	6.9	54.4	Wilson (1987)
Even-Odd	-60.1		-26.7		61.4	52.0	Gnevyshev & Ohl (1948)
Maximum-Minimum Amplitude-Period	-109.7	24.9	-18.6	-8.1	5.2	51.2	Waldmeier (1939)
Secular Trend	-75.3	18.4	-73.5	-25.6	15.0	49.6	Hathaway et al. (1994)
Three Cycle Sawtooth	-96.4	14.6	-40.6	-25.4	18.9	49.3	Wilson (1988a)
Gleissberg Cycle	-96.5	14.6	-38.5	-25.4	18.8	49.0	Ahluwalia (1998b)
Ohl’s Method	-64.8	48.0	-36.9	-31.8	-0.9	42.1	Gleissberg (1939a)
Feynman’s Method	-55.4	-5.9	2.3	-9.1	10.5	28.7	Ol’ (1978)
	-43.3	-22.4	-1.0	-14.8	25.9	28.6	Feynman (1982)

namos. Recently, in (Hathaway & Upton, 2016a) the amplitude and hemispheric asymmetry of 25th solar cycle was predicted using the surface flux transport method. The flux transport emerges in active regions by differential rotation, poleward meridional flow, and cellular convective motions, namely the horizontal flows in the Sun’s near-surface shear layer.

Extrapolation methods. One of the frequently used methods which was first described for predicting solar activity is the regression technique, which now uses an auto-regression, time series analysis assumed to be homogeneous. The daily-monthly-yearly observed data of the sunspot numbers is extrapolated toward future time series for the prediction of the remainder of the cycle. Time series analysis is more reliable for long term data sets like

cosmogenic radionuclides with the variation of secular and millennial. Time series analysis methods can be used successfully because of its century long observed records, as the sunspot number series is a uniquely homogeneous in terms of long term variation. The treatment of data on basis of time series analysis methods are quite various, from simple linear regression to the most complex spectral methods. The simple extrapolation method is based on the auto regression technique which is known as the Auto Moving Average model. The idea is that at a given time series, the value at time t has a linear combination of values at time $t - \Delta t$, $t - 2\Delta t, \dots, t - p\Delta t$, with p order of auto regression and some random error e_n in n points. Taking the errors from the previous q points, so in point n the R value is expressed:

$$R_n = R_0 + \sum_{i=1}^p c_{n-i} R_{n-i} + e_n + \sum_{i=1}^q d_{n-i} e_{n-i}, \quad (3.17)$$

where c_n and d_n are weight parameters, R_n is a linear regression in point n . The prediction based ARMA method used in (Brajivia et al., 2009a), suggesting that cycle 24 starts around 2012 with an amplitude of 90 ± 27 , and the following minimum will occur in 2017. Using precursor methods (Brajivia et al., 2015) researched the modified minimum-maximum method which is based on a linear relationship between the smoothed monthly relative sunspot number in the minimum R_{min} and in the maximum epoch R_{max} of solar cycles. For the observed data set (1749 – 2015) they found a good agreement value of $R_{max} = 83$, while the observed ISN is $R_{max} = 81.9$. The prediction of Hiremath (2008a) using physical parameters of previous 22 solar cycles with an auto regressive method predicted the amplitude of 110 ± 11 and period of 9.34 years for cycle 23 with a starting time of around May-September 2008. Using the same method they predicted timings of another fifteen future solar cycles.

Spectral forecast methods. Spectral forecast methods belonging to Fourier analysis of the sunspot time series can be used to determine its frequencies whose amplitudes are conserved or have a simple time dependence. Using one or more periods of the solar activity the spectral analysis reconstructs a long term modulation of the data series by superposition of genuflections forming an orthogonal basis. Spectral analyses used various means of harmonic analysis, Fourier analysis, the maximum entropy method and singular spectrum analysis.

Another model of the spectral analysis uses wavelet-based forecasts of solar activity cycles. Ochadlick et al. (1993) used the yearly sunspot series extracted by this approach and found the Gleissberg cycle in their wavelet analyses. The spectral models also used include the dynamo model equation which is based on non-linear time series analysis. To conclude, harmonic analysis provides the most confident and optimum forecasts if the quasi-periodic, non-periodic i.e., chaotic or stochastic (as grand maxima and minima behaviour of solar activity) components have been taken into account of the treatment. As the spectral methods used for very long-term forecasts, the prediction of cycle-to-cycle allowed by identifying the physically peculiar periodicity (as described in Sec.3.5) which potentiality could have an impact on solar cycle prediction. The nonlinear methods are based on the attractor analysis with phase space reconstruction.

Neural networks. The neural network algorithms described by a step function, i.e. a large number of the small interconnected neurons where each of them is able to provide a simple non-linear operation on an input signal by accounting their non-linear relationships (Maris & Oncica, 2006a; Uwamahoro et al., 2009a; Tebabal Yirdaw et al., 2015; Tebabal & Damtie, 2015).

Dynamo model forecasts. Some dynamo model forecasts are based on physics models which are produced by integrating conservation equations. Dikpati (2008) and Choudhuri

et al. (2007a) have completed models to predict high and low solar activity, respectively. The overview details and prediction of the solar cycles are based on a dynamo model outlined in (Svalgaard et al., 2005a; Cameron & Schüssler, 2007; Dikpati et al., 2008; Choudhuri et al., 2007b). Generally a flux transport dynamo includes a rotation profile, a meridional and polar flow based on helioseismical observations. Extreme solar activity fluctuations and the occurrence of the solar grand minima and grand maxima events which are well-established and observed features of the solar cycle, but the physical mechanism is still unclear. Scafetta (2016b) proposed the forecast of grand solar minima and maxima using a three-frequency dynamo model based on Jupiter-Saturn tidal frequencies, where it was argued that the solar and climatic oscillations are related to planetary motion and discussed the possible decadal, secular and millennial forecasts. The prediction catalogues could be extended larger, as the climatological forecasts are based on the statistical properties of the past, where further the maximum of the solar cycle can be estimated.

Finally to summarize this section, in Fig.3.16 is illustrated the analysis of the 75 predictions of the recently passed solar cycle 24 estimated using the different catalogues of predication methods namely climatology, dynamo model, spectral, neural network, geomagnetic and solar polar precursor which are based on the corresponding solar activity data. In Fig.3.16, the standard deviation within the category is drawn as a coloured box, and the range within the category is drawn as an error bar. A dashed line is drawn at $R(24) = 115$, showing that almost all of the categories include R_{ave} in the predictions (Pesnell, 2012a). The observed maxima of cycle 24 on April of 2014 determined by the 13 month mean with the ISN and the GSN are estimated at 81.9 and 82.0 respectively (SILSTO). Li et al. (2001) and Kane (2008) discussed

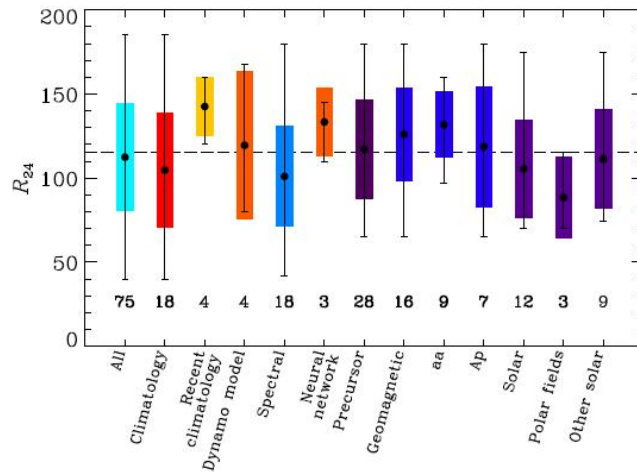


Figure 3.16 – The categorized predictions of solar cycle 24. The dot shows the average prediction in each category, the color bar is drawn at the 1σ error limits, and the error bars show the range of each category. The number of predictions in each category is written under the symbols. A dashed horizontal line is drawn at $R(24) = 115$ (Pesnell, 2012a).

the various forecast methods, Pesnell (2012a) analysed the predictions for the amplitude of the solar cycle 24. Tab.3.7 from Petrovay (2010) presents a collection of forecasts for the amplitude of cycle 24.

Table 3.7 – Prediction methods used for 24th cycle’s amplitude. The columns show 1: The used prediction method, 2: Peak amplitude, 3: Difference of observed international and predicted sunspot numbers, 4: Reference.

Category	A_{max}	$ R_{pred} - R_{obs} $	Reference
Precursor methods			
Minimax	80 ± 25	1.9	Brown (1976); Brajivia et al. (2009b)
Minimax3	69 ± 15	12.9	Cameron & Schüssler (2007)
Polar field	75 ± 8	6.9	Svalgaard et al. (2005b)
Polar field	80 ± 30	1.9	Schatten (2005)
Geomagnetic (Feynman)	150	68.1	Hathaway & Wilson (2006)
Geomagnetic (Ohl)	93 ± 20	11.1	Bhatt et al. (2009)
Geomagnetic (Ohl)	101 ± 5	19.1	Ahluwalia & Ygbuhay (2009)
Geomagnetic (interpl.)	97 ± 25	15.1	Wang & Sheeley (2009b)
Field reversal	94 ± 14	12.1	Tlatov (2009)
Extrapolation methods			
Linear regression	90 ± 27	8.1	Brajivia et al. (2009b)
Linear regression	110 ± 10	28.1	Hiremath (2008b)
Spectral (MEM)	90 ± 11	8.1	Kane (2007)
Spectral (SSA)	117	35.1	Loskutov et al. (2001)
Spectral (SSA)	106	24.1	Kuzanyan et al. (2008)
Attractor analysis	87	5.1	Kilcik et al. (2009)
Attractor analysis	65 ± 16	16.9	Aguirre et al. (2008)
Attractor analysis	145 ± 7	63.1	Crosson & Binder (2009)
Neural network	145	63.1	Maris & Oncica (2006b)
Neural network	117.5 ± 8.5	35.6	Uwamahoro et al. (2009b)
Model based methods			
Explicit models	167 ± 12	85.1	Dikpati & Gilman (2006)
Explicit models	~ 80	1.9	Choudhuri et al. (2007c)
Explicit models	~ 85	3.1	Jiang et al. (2007a)
Truncated models	~ 80	1.9	Kitiashvili & Kosovichev (2008)

Chapter 4

Solar variability and its data

The tally of splotches on our Sun tells us what it's up to. It's a pity no one can agree how to count them.

Brian Owens

Official continuous daily observations of sunspots began during the year 1849 at the Zurich Observatory. The SSN was calculated by first counting the number of sunspot groups and the number of individual sunspots. The kind of observational data used to calculate solar activity includes: sunspots, sunspot areas, 10.7 cm solar flux, total irradiance, magnetic field, ephemeral regions, flares and coronal mass ejections, geomagnetic activity, radioisotopes in tree rings and ice cores. In this section has been briefly listed the solar activity data, and most attention was given to the sunspot numbers that have been analysed.

4.1 Direct and indirect observational data's of Solar activity

The methods of the various observational data of solar activity have two types of measurement both physical and synthetic. Physical data records are directly measurable values of real physical observable events (i.e radioflux). The synthetic data are calculated using a special algorithm from the observed data. The direct and indirect data of the solar activity are quantitative measures of solar variability effects, which reveal the Sun's impact on terrestrial, interplanetary, geomagnetic and heliospheric, environments.

4.1.1 Historical naked-eye sunspot records

Sunspots are usually too small to be visible to the naked eye, although some sunspots reach a size large enough to be visible without a telescope with suitable viewing conditions. Historical records are used as a qualitative indicator of sunspot activity. Comparison of Oriental naked-eye and European telescopic data showed important discrepancies (Usoskin & Mursula, 2004) although with quantitative interpretation. Naked-eye sunspot historical records have been reconstructed in arbitrary units (Vaquero, 2007). Naked-eye records are not useful for the study of long-term solar activity from 200 B.C. to A.D. 800. Solar historical events occur in the records too. In many ancient chronicles and short chronologies evidence can be found of

spots being observed on the solar disc during the 4 century B.C. The earliest known drawing of sunspots is dated from December 8, 1128. Rich Oriental sources of naked-eye sunspot records are known (Richard Stephenson et al., 2004; Wittmann & Xu, 1987), while from official Chinese and Korean chronicles the record covered the period from 165 B.C. to 1918 A.D. Since antiquity from Occidental and Oriental sources the Sun's aurora was recorded, first from March 12, 567 B.C. from Babylon (Richard Stephenson et al., 2004).

4.1.2 Pre-telescope and early telescope sunspot records

During the pre-telescopic era, instrumental solar data was based on regular observation of the Sun by drawings or counting of spots. Using optical instruments such as the telescope of Galileo begun in the 17th century. Hoyt & Schatten (1998) initially reconstructed the sunspot group number. In terms of observations aided by instrumentation the camera obscura provided relatively good solar images and served to define the Sun's position (Vaquero & Vázquez, 2009). The earliest drawing of a solar observation using a camera obscura came from Frisius (1545) who observed the 1544 solar eclipse from Louvain, which corresponded to the spotless period of the Sporer Minimum. Small camera obscuras in astronomical observations were used during the 17th and 18th centuries, meridian lines in cathedrals in Bologna, Rome, Florence, and Paris for solar observation. Some further details on this topic have been reviewed in Sec.2.1.

4.1.3 Historical Auroral Observation

Various historical auroral observation records were collected by Eddy et al. (1976), it was postulated the existence of a solar minimum which was then referred to as the Maunder Minima. The oldest known auroral citing was written in 2600 B.C. in China. In 1570 A.D., a drawing of the aurora depicted candles burning above the clouds and then in 1619 A.D., Galileo Galilei coined the term 'aurora borealis' after aurora, the Roman goddess of morning. In 1790 Henry Cavendish made quantifiable observations of the aurora and estimated that the aurora light is produced around 100 – 130 km in altitude. In 1902 – 1903 Kristian Birkeland stated that auroral light was caused by currents flowing through the gas of the upper atmosphere and it is the modern-day explanation of how neon lights work.

4.1.4 Some current measurements of solar activity

Sunspot Number. Solar activity records i.e. individual sunspots and sunspot groups are calculated without reference to preceding days. The records were combined together from earlier regular and fragmentary solar observations. Johann Rudolph Wolf's technique of estimation of the daily sunspot number is still used today. In this technique the total number of spots visible on the Sun are counted as well as the number of groups into which they cluster, because neither variable alone satisfactorily measures sunspot activity. This Wolf (relative) sunspot number (WSN) series can be calculated as follows:

$$R_w = \kappa(10G + N) \quad (4.1)$$

where R_w is the relative sunspot number, G is the number of sunspot groups, N is the number of individual sunspots in all groups visible on the solar disc and κ denotes the individual correction factor. The sunspot number can be given in daily figures, monthly averages,

yearly averages, smoothed numbers and its standard smoothing is a 13-month running average. Therefore in this data set the maxima and minima solar cycle are indicative. The official records of sunspot data compiled by the National Oceanic and Atmospheric Administration (NOAA) in the US since 1977 and the Solar Influences Data Analysis Center (SILSO-SIDC) in Belgium since 1981. Generally it is noted that the three sunspot number databases such as the International Sunspot Number (ISN) R_I compiled by SILSO-SIDC, where the data is treated from more than 25 observing international network stations, and the averaged total daily, monthly and 13 month mean sunspot numbers are calculated by a straightforward technique. The next is the Boulder Sunspot Number (BSN) derived from the daily Solar Region Summaries which is about 55% larger than the ISN. Finally, the sunspot number data recorded by the American Association of Variable Star Observers (AAVSO), which is referred to as the American Sunspot Number (ASN) and has published the sunspot number data since 1944.

Flare Index. Flare index is a synthetic index of the solar activity which reveals the solar flare activity and records measured since 1947 (Oggusc, 2003). The daily flare activity is calculated as a product of the flare's relative importance I in the $H\alpha$ -range with duration t , the measure of the total energy emitted by the flare $Q = It$. The X-ray solar flux has been measured from space since 1975 by NOAA, with Geostationary Operational Environmental Satellites (GOES). Its observation is given in a typical level of A and B on a logarithmic scale, while C, M, and X levels are estimations of increasing of flaring activity, but X class flares can be observed in any phase of the sunspot cycle.

Coronal Mass Ejection. Coronal mass ejections (CMEs) also show a solar cycle dependence, even though it can occur in the absence of a flare. CMEs observations are measured with the Solar Maximum Mission and continue with SOHO. Routine CME observations began with the Solar Maximum Mission. This variation data is also correlated with sunspot number depending on the different used method (Webb & Howard, 2012), the relationship and periodicity of the magnetic flux emergence, solar flares and CMEs. The time series was studied by many others as by Choudhary et al. (2014), which found for the 23rd and 24th solar cycles the flux emergence represented by sunspot area had multiple periodicities. However flares and CMEs did not occur with the same period as the flux emergence.

F10.7cm Solar Flux. The more frequently used physical index of solar activity (which is more reliable than the sunspot number) is measured from the radioflux, i.e., the flux of solar radio emission in the 10.7cm (in solar flux units, $1\text{sfu} = 10^{-22}\text{Wm}^{-2}\text{Hz}^{-1}$) wavelength. The F10.7 solar flux index is measured as a result of the nonradiative heating of coronal plasma over active regions. It is a reliable and simple index of solar activity without directly relating to sunspots (Tapping & Charrois, 1994). Since 1946 the Canadian Solar Radio Monitoring Program, Ottawa area and Pentagon provide daily measurements. The relationship of 10.7cm radio flux $F_{10.7}$ to ISN R_I is shown in Fig. 4.1 with correlation of $r = 0.995$, $r^2 = 0.990$ before 1997 and is given as follows:

$$F_{10.7} = 67 + 0.97R_I + 17.6(\epsilon^{-0.035R_I} - 1) \quad (4.2)$$

Shaltout et al. (2008) proposed the 10.7cm radio flux is better correlated with the solar activity than the sunspot numbers. The 10.7cm radio flux is used to study the long-term evolution of the solar cycle.

Coronal index. A basic optical index of solar activity i.e. the coronal index (Rybansky et al., 2005) is measured from the irradiance of the Sun. The coronal index is based on the observation of green coronal intensities with FeXIV emission line at 530.3nm wavelength and

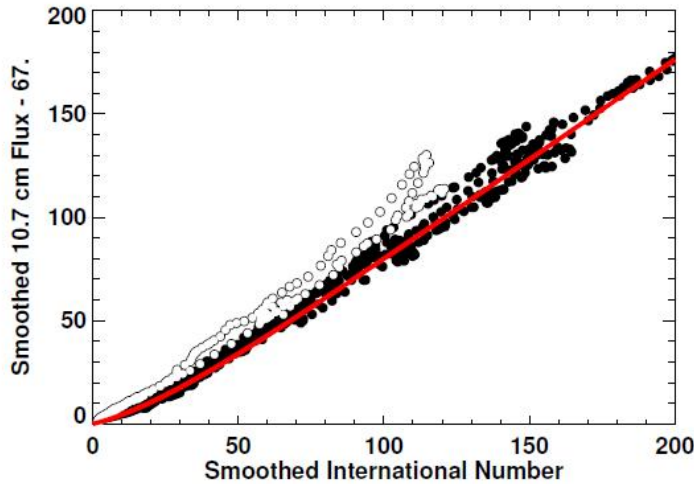


Figure 4.1 – 10.7cm radio flux vs. International Sunspot Number with correlation of 99.5% for the period of August 1947 to January 2014. Data obtained prior to cycle 23 are shown with filled dots while data obtained after 1997 are shown with open circles. The Eq.4.2 relates the radio flux to the sunspot number and is shown with the solid red line, (Hathaway, 2010).

has been recorded since 1943. The coronal index of solar activity is the averaged daily power of the green corona emitted from the Sun's visible hemisphere. The coronal index changes relates with the solar activity and is used to study the short, intermediate and long term variability of the Sun. The analysis of the coronal index and the magnetic field for the period of 1966 – 1988, showed the same periodicity which was proposed to use the coronal index as a global index of solar activity (Mavromichalaki et al., 2005).

Sunspot Area. Calculation of the total area of visible spots on the solar disc are achieved from daily photographic images of the Sun. The indexes give a sunspot area and are correlated with the solar magnetic flux emerging at the sunspots. The sunspot area is counted by employing an overlay with a number of circles and ellipses in different areas. This index was reported between 1874 and 1979 (Balthasar & Schuessler, 1983) by the Royal Greenwich Observatory (RGO), using measurements from photographic plates recording the umbral and sunspot areas (in units of millionths of a solar hemisphere μHem). The sunspot areas and the ISN are correlated with $r = 0.994$, $r^2 = 0.988$ as shown in Fig.4.2.

Accordingly, since 1977 the USAF/NOAA have recorded the same sunspot area data and its comparison with ISP and RGO are presented in Fig.4.3. The combination of RGO and the US Air Force (USAF/NOAA) datasets are available on-line. The butterfly diagram of Maunder (1904) illustrates the distribution of sunspot area with latitude, where the sunspots appear in each hemisphere at latitudes above about $20^\circ - 25^\circ$ from the equator then migrate toward the equator as the cycle progresses.

TSI. The solar magnetic variability affects the total and spectral irradiance variations of the Sun, and have a huge impact on the solar-terrestrial environment (Solanki et al., 2000). The accurate recent measurements of the TSI are based on space based instrument observations such as: Upper Atmosphere Research Satellite (UARS) ACRIM-II, ACRIMSAT, ACRIM-III, SOHO/VIRGO and SORCE/TIM. The measurements of these instruments show the drops of TSI caused by the formation and disc passages of large sunspot groups, which are impacted by

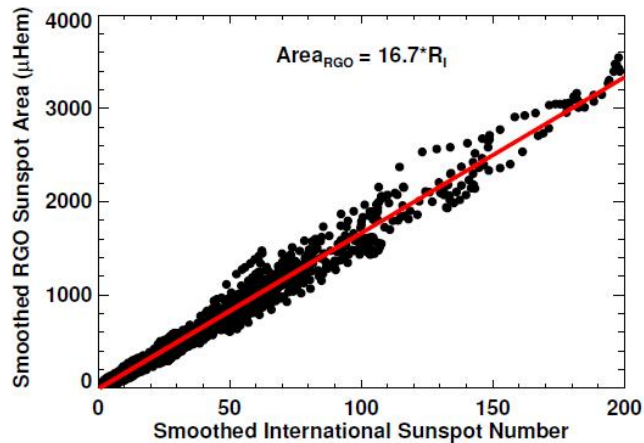


Figure 4.2 – Smoothed RGO Sunspot Area vs. the International Sunspot Number at monthly intervals from May 1874 to December 1976, demonstrating a 99.4% correlation level with a proportionality constant of about 16.7, (Hathaway, 2010)

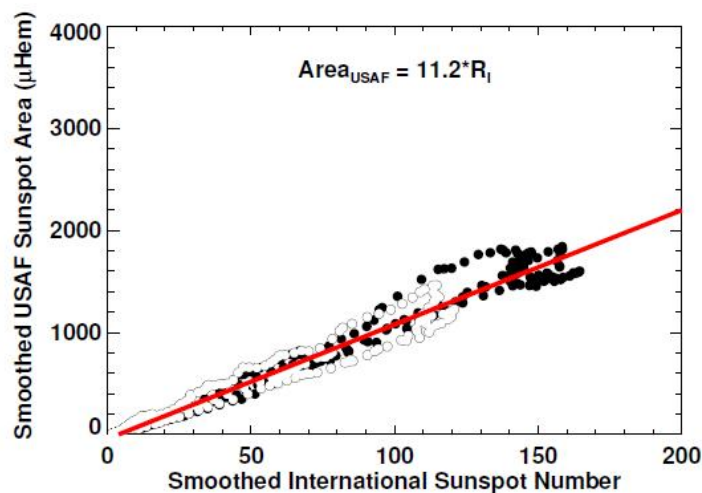


Figure 4.3 – Smoothed USAF/NOAA Sunspot Area *1.49 factor vs. the International Sunspot Number at monthly intervals from January 1977 to August 2014 with a correlation level of 99.1% with a proportionality constant of about 11.2. Data obtained prior to cycle 23 are shown with filled dots, while data obtained after 1997 are shown with open circles, (Hathaway, 2010).

solar cycle variation. The TSI have been discussed very briefly in Sec. 3.4. The solar activity indexes provided by spectral observation such as CaII-K (Foukal, 1996), or the space-based MgII core-to-wing ratio (Snow et al., 2005). There are also many indices that exist, the above examples are most used and are more or less correlated to sunspot numbers in the solar cycle. They also reveal different variations on short or long term time-scales as listed.

Magnetic Flux. Measurements of the solar wind or the magnetic field in interplanetary space are provided with heliospheric indices, such as open solar magnetic flux. Heliospheric

indices also link with galactic cosmic ray intensity, which is recorded in natural terrestrial archives. Thus, for the purpose of long time-scale evolution of solar activity and its contribution to climate change the natural terrestrial archive is important. The natural archived record can be used as a reconstruction of the millennium scale sunspot number (Usoskin et al., 2003). Magnetic field measurements provide a good representation of the solar cycle for example the Sun's polar fields change polarity as the Sun's field reverses that occur at about the time of the cycle maximum. The Sun's daily measurements have been available since 1970 from the Wilcox Solar Observatory, the National Solar Observatory (NSO), Synoptic Optical Long-term Investigations of the Sun (SOLIS), Michelson Doppler Imager (MDI) and Solar and Heliospheric Observatory (SOHO) mission. These measurements demonstrate butterfly wings describing Joy's Law and Hale's Law (Hale & Ellerman, 1918).

Ephemeral regions. Another index with a number of ephemeral regions is also related with the sunspot cycle. The ephemeral regions have a small size bipolar magnetic zone between one and two day's lifetime observed by space based magnetographe, with SOHO/MDI instruments. The variation of the small ephemeral regions tends to be anti-phased with the sunspot cycle (Hagenaar et al., 2003) and its emergence in unipolar regions was found (Hagenaar & Cheung, 2008). In the following section are listed the different sources of sunspots and group numbers. Some of these data sets were used in the main research of this thesis.

4.2 Solar datasets

Here were briefly listed the main SSN and GSN observational data. The study of the different solar observational data is important to select the most suitable data for further investigation. The reliability of the data can be verified for example with a long term historical data and cosmogenic indices.

4.2.1 International Sunspot Numbers (1610-Present)

Description: Prior to 1981 the daily Zurich (Wolf) relative sunspot number observation based at Zurich and its two branch stations in Arosa and Locarn, Switzerland. From January 1, 1981, the Zurich relative sunspot number program was replaced by the Solar Influences Data Analysis Centre SILSO-SIDC in Belgium where data from more than twenty-five observatories constitute an international network of stations. Monthly and yearly averages of the daily SSN are calculated using a straightforward method. The sunspot record is a direct reference retracing solar activity back over more than 400 years. It is the most used solar data set with around 100 publications per year and provides data for uses in many areas of science. Its count methods and records have been created by Rudolph Wolf in 1849. Hoyt & Schatten (1998) innovated the new sunspot index group number. The sunspot and group of sunspot numbers which are in two parallel series, reveal strong differences hinting at strong inhomogeneities in either series or both. Since July 1st, 2015, the World Data Centre SILSO presented the new sunspot data series with full revisions of the two series and improved verification which is now available in the data centre of SILSO-SIDC. This 400 year solar cycle has been revised in (Clette et al., 2014). Fig. 4.4 illustrates the change between the original and new sunspot number series. Daily mean, monthly mean, and smoothed monthly sunspot number for the last 13 years with their two different 12 monthly predictions of the monthly smoothed sunspot number are displayed in Fig.4.5 from SIDC.

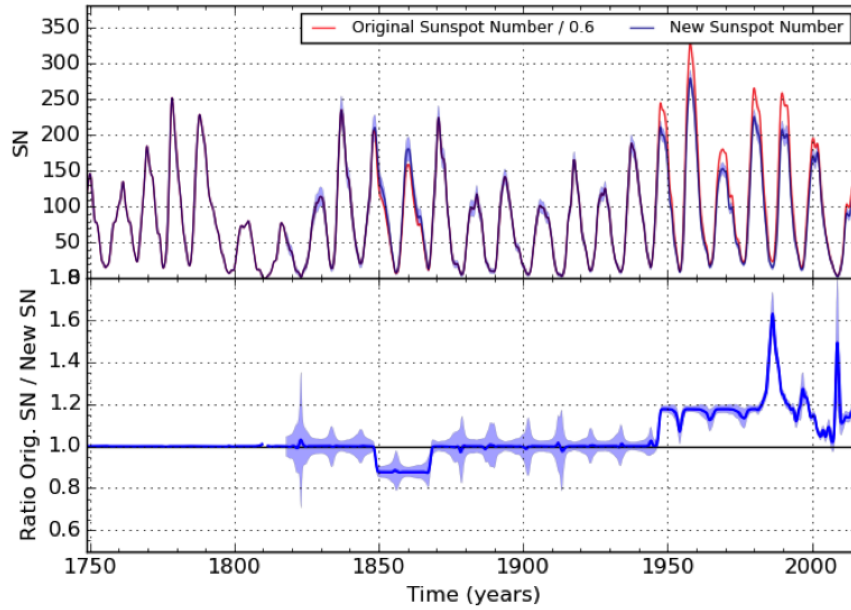


Figure 4.4 – Comparison of old and the new sunspot and group sunspot number series after correction and representation of SILSO-SIDC.

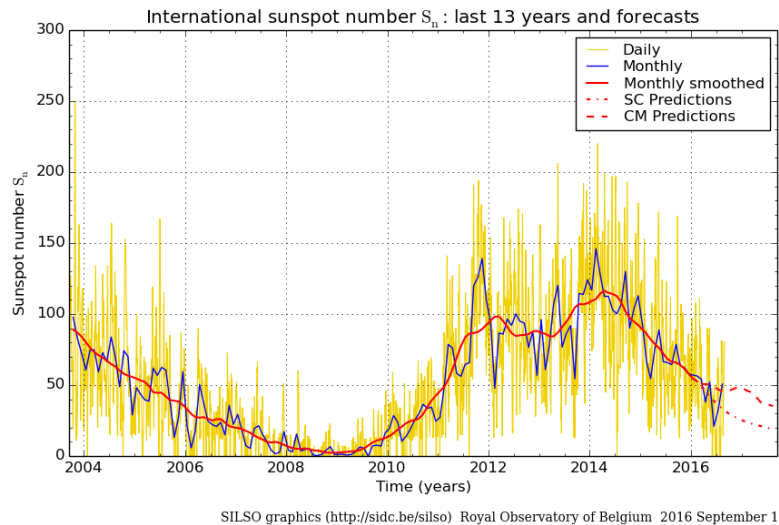


Figure 4.5 – Daily sunspot number (yellow), monthly mean sunspot number (blue), smoothed monthly sunspot number (red) for the last 13 years and one year ahead predictions of the monthly smoothed sunspot number: SC (red dots)- prediction method based on an interpolation of Waldmeier’s standard curves, only based on the sunspot number series; CM (red dashes)-method combining a regression technique applied to the sunspot number series with the aa geomagnetic index used as a precursor, SILSO-SIDC

Dataset Provider: Solar Influences Data analysis Centre (SILSO-SIDC), Royal Observatory of Belgium, in Brussels Belgium (POC: Frederic Clette).

- Daily total sunspot numbers from 01.01.1818 to present

- Monthly mean sunspots number from 01.01.1749 to present
- 13-month smoothed monthly total sunspot number from 01.01.1749 to present
- Yearly mean total sunspot number from 01.01.1749 to present
- Daily Estimated Sunspot Number.

Dataset Status: Active Revised and updated in 2015.

4.2.2 American Relative Sunspot Numbers (1944-Present)

Description: The American relative sunspot number are archived in the American Association of Variable Solar Observers (AAVSO) dataset. The tables and listings give the relative sunspot numbers RA before 1951. After 1951 less solar observations were required by using a new high quality procedure combining into RA' .

Data Provider: American Association of Variable Solar Observers (AAVSO), Cambridge, USA. (POC: Rodney Howe).

- Monthly Bulletin-Bulletin from 1964 to present
- Daily relative sunspots number from 1944 to present
- Monthly mean sunspots number from 1944 to present
- Yearly mean sunspots number from 1944 to present.

Dataset Status: Active, after the changes in 1951 the new data series RA' proposed.

4.2.3 Group Sunspot Numbers (1610–Present)

Description: The sunspot group is an isolated cluster of sunspots and consists of one or a large number of spots depending on their size, which are from 10 or more square degrees of the solar surface down to the limit of resolution. Each isolated cluster of sunspots is termed a sunspot group, this Wolf sunspot number has a lower quality before 1850 and had unreliable data before 1750, hence more reliable sunspot data set was required. For this purpose (Hoyt & Schatten, 1998) produced a new series of sunspot group activity. The group sunspot numbers (GSN), are based on the more easily identified sunspot groups disregarding the number of individual spots, R_g daily sunspot group is defined as follows:

$$R_g = \frac{12.08}{n} \sum_i^n \kappa'_i G_i \quad (4.3)$$

where G_i is the number of sunspot groups recorded by the i th observer, κ'_i is the observer's individual correction factor, n is the number of observers for the particular day, and 12.08 is a normalization number scaling R_g to R_w values for the period of 1874 – 1995. The GSN is hardly available after 1995. For the period of 1874 – 1976 the GSN vs ISN is shown in Fig.4.6.

Data Provider: Hoyt & Schatten (1998).

- Daily and means values from 1964 to present
- Standard deviations from 1610 to 1995
- Daily input data files from 1610 to 1995
- Number of observers from 1610 to 1995
- Documentation files from 1610 to 1995.

Dataset Status: Inactive. Recently, Svalgaard & Schatten (2016) developed a backbone-based group number, Usoskin et al. (2016c) proposed a new group number series, Cliver &

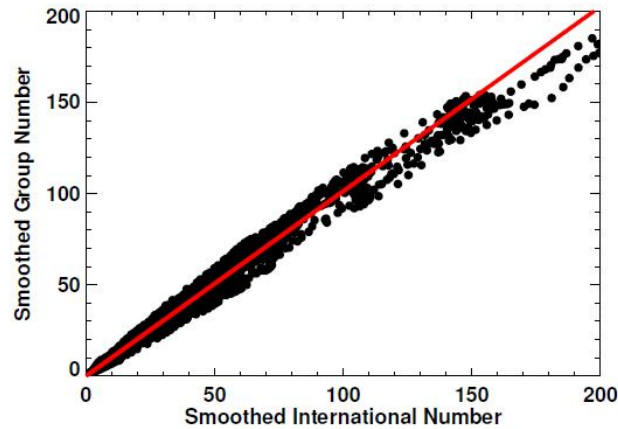


Figure 4.6 – Group Sunspot Number vs. the International Sunspot Number at monthly intervals from 1874 to 1995. The average ratio of the two is 1.01 which is shown in the solid line, (Hathaway, 2010).

Ling (2016) suggested a provisional group number series and in Clette et al. (2016) corrected the ISN number. Finally, Cliver (2016) compared these new four series of sunspot group numbers with the old sunspot group numbers, and showed inconsistency from Usoskin et al. (2016c) series. The series of four reconstructions are compared in Fig.4.7 (Cliver, 2016).

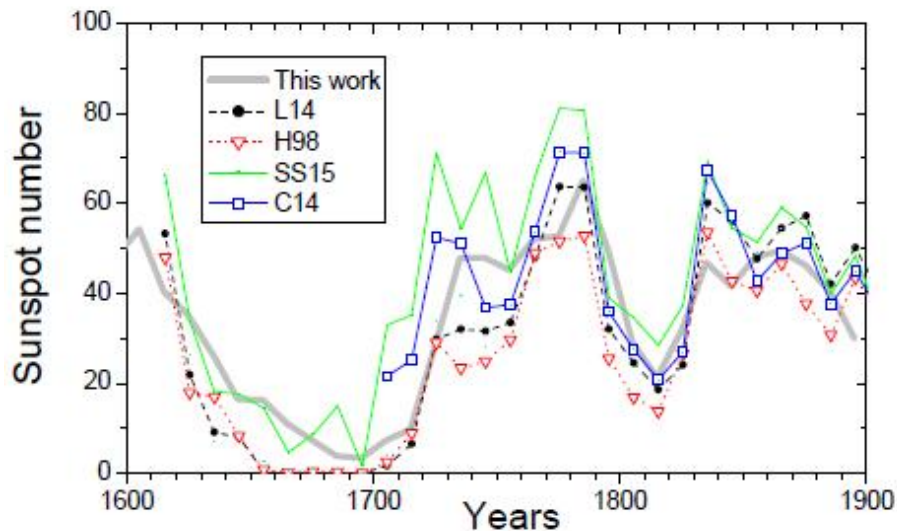


Figure 4.7 – Decadally averaged sunspot numbers for the period 1600 – 1900 A.D. The thick gray curve represents this work (uncertainties are not shown). Other curves correspond to sunspot number series: L14-(Lockwood et al., 2014), H98-(Hoyt & Schatten, 1998), SS15-(Svalgaard & Schatten, 2016), and C14-(Clette et al., 2014) international sunspot number (v.2) scaled with a factor 0.6, (Usoskin et al., 2016a).

4.2.4 Hemispheric Sunspot Numbers (1992-Present)

Description: Daily total and hemispheric sunspot numbers are derived by the formula: $R = 0.6(N_s + 10N_g)$, where N_s is the number of spots and N_g the number of groups counted either over the entire solar disk, the Northern hemisphere or Southern hemisphere based on the sunspot group heliographic latitude where 0.6 is the scaling factor. The Northern and Southern numbers are always normalized to the total number, due to the global scaling reference.

Dataset Provider: Solar Influences Data analysis Center, Brussels Belgium. (POC: Frederic Clette).

- The production of the R_n northern and R_s southern hemispheric numbers together with the international total sunspot number from 1992 to present.

Dataset Status: Active.

4.2.5 Predicted Sunspot Numbers (2009 – 2020)

Description: The traditional McNish-Lincoln technique is used to predict the future smoothed sunspot numbers of a solar cycle. The technique compares the amplitude of a cycle in the month to predict the amplitude of the mean cycle at the same epoch. That being the same month as measured from the preceding sunspot minimum. Then this difference is used in amplitudes to predict the cycle amplitude in future months. A review of other predictive techniques are discussed in (Hathaway et al., 1999) and comparison of different predictions of the 24th cycle have been reviewed (Pesnell, 2012b) and the different methods of its uses outlined by Petrovay (2010).

Dataset Provider: NOAA National Geophysical Data Centre, Boulder (POC:Justin Mabie).

- This data was predicted to forecast the solar modulation based on direct observation data predictions from 2009 to 2020.

Dataset Status: Active.

4.2.6 Swiss-Wolf Sunspot Numbers (2011-Present)

Description: The Rudolf Wolf Society seeks the continuation of Rudolf Wolf previous observations from the 19th century. The observations are realised using Wolf's original method and has been published from 1992.

Dataset Provider: Rudolph Wolf Society, POC (TBD).

- Swiss-Wolf SSN-Bulletin from 2011 to present.

Dataset Status: Active.

4.2.7 Solar Cycle Parameters (1610-Present)

Description: A number of the parameters of the solar cycle are described and characterised. When observations permit, the date selected for either the cycle minimum or maximum are based in part on an average of the times extremes are reached. Two more measures are used at the time of the sunspot minimum: the number of spotless days and the frequency of occurrence of 'old' and 'new' cycle sunspot groups.

Data Provider: NOAA National Geophysical Data Center, Boulder (POC:Justin Mabie).

- Minima and maxima of smoothed sunspots number from 1610 to present.

Dataset Status: Active.

4.2.8 Ancient Sunspot Numbers (165 B.C.-1715)

Description: A catalogue of naked-eye sunspot observations and large sunspots compiled from 165 B.C. to 1684 A.D. In (Wittmann & Xu, 1987) estimated the annual mean sunspot number, R , and in (Eddy, 1976) from 1610 to 1715.

Data Provider: Wittmann & Xu (1987), Eddy (1983).

- Eddy's reports of annual mean sunspot numbers from 1610 to 1715 .
- Wittman's naked-eye sunspot observations and large sunspot catalogues from 165 B.C. to 1684 A.D. American ancient data from 1610 to 1715 where this data has been estimated.

Dataset Status: Inactive.

4.3 Solar activity proxies and paleo records

The reconstruction of the solar activity data is based on the paleo proxies such as ^{10}Be and ^{14}C . The proxies provide evidence of some maxima and minima solar phenomena. The reconstruction of solar activity proxies from geomagnetic, palaeoclimatic and glaciological have long time-scales (i.e., ^{10}Be span the last 800 kyr, while the lunar and meteoritic record of solar history extends over several Gyr). Flares, CMEs and other explosive events on the Sun caused isotopes to be produced by solar interaction with galactic cosmic ray flux. This factor allows us to derive changes in solar activity from isotopic proxies even when the solar factor is not easily isolated.

4.3.1 Geomagnetic field measurements

The impacts of solar variability on different environments such as terrestrial, geomagnetic, heliospheric and interplanetary are also one of the indirect measured solar activity indexes. The interaction of the solar wind and the magnetosphere causes the appearance of geomagnetic activity indices. These indices provide good proxies of solar wind properties (Svalgaard & Cliver, 2007). Geomagnetic indices quantify different effects of geomagnetic activity which are caused by solar variability, mostly by variations of solar wind properties and the interplanetary magnetic field. Geomagnetic activity indices of the Sun are measured and detected by the global network of magnetic observatories which are achieved with different indices due to their localization and their measured time interval.

Various geomagnetic indices. The geomagnetic indices require the detection of charged particles from the Sun toward the Earth's magnetosphere, which is measured with different resolutions and thus used to derive various indexes with specific physical characteristics. For instance, the ap index is a measure of the range of variability in the geomagnetic field with three hour intervals from a global network of about 13 high latitude stations. The average of eight daily ap values is Ap the daily amplitude. The index Dst is the disturbance storm time, derived from measurements obtained at four hour equatorial stations. The K index is measured on the solar particle flux through its effect on the geomagnetic field. The aa -index defined the three-hour time resolution's as an average of K geomagnetic indices corresponding to the time it takes for the solar wind to reach the Earth's magnetosphere. The geomagnetic effects of solar activity have been outlined (Pulkkinen et al., 2007).

4.3.2 Cosmic rays

Cosmic rays hitting the Earth are modulated by the solar cycle and considered to be constant in the Solar system environment. In the Earth's upper atmosphere the cascading showers of particles are measured with neutron monitors at high-altitude observation sites. These galactic cosmic rays consist of electrons and bare nuclei that are accelerated to GeV energies. Cosmic rays in the Earth's atmosphere are modulated by the variation of solar magnetic activity, this variation affects the 11 year cycle with an inverse relationship to solar activity. These results in a time delay of around from a month but up to two years with respect to sunspots. The data from the cosmic rays is treated by charge dependent drift mechanism noted in the 22 year periodicities. These short term fluctuations are related by interplanetary transients caused by solar eruptive events e.g. flares or coronal mass ejections. The overall level of cosmic rays depends on the variation in the centennial and millennial time-scales (Usoskin et al., 2003).

Modulation potential ϕ . The parametrisation of the galactic cosmic rays is characterised by a modulation potential ϕ . The spectral index allows the reconstruction of the cosmogenic isotope proxy to study the solar activity changes in the historical past. The ϕ parameter describes the differential cosmic ray intensity in the time variability, which is interpreted as the averaged rigidity (i.e., the particle's momentum per unit of charge) loss of a cosmic ray particle in the heliosphere (Usoskin, 2011).

Isotopic records. Past information of solar activity or climatic variations can be provided by using proxies from the isotopic records such as isotopic ratios in air bubbles trapped in ice-cores, calcite shells, limestone or carbon atoms in coal and wood (Wagner et al., 2001). These galactic cosmic ray proxy records are obtained from beryllium-10 (^{10}Be) trapped in polar ice caps and carbon-14 (^{14}C) in trees. The reconstruction of proxies of ^{10}Be and ^{14}C , are formed by the interaction of galactic cosmic rays with atmospheric molecules and can be measured by mass spectrometry (Matthiä et al., 2013). The cosmic rays are modulated by solar activity and Earth's magnetic field intensity, while the ^{10}Be production is inversely related to the intensity of these two parameters. Usoskin et al. (2009) suggested that the ^{10}Be and ^{14}C based records are consistent with each other over a wide range of time intervals. The most reliable and useful proxy of long-term solar activity are cosmogenic radionuclides produced by cosmic rays in the atmosphere of Earth (Stuiver, 1980; Beer et al., 1990; Bard et al., 1997; Solanki et al., 2004a). Some of properties of cosmic isotopes are discussed in the next section.

4.3.3 Cosmogenic Isotopes ^{10}Be

^{10}Be cosmogenic isotope records are measured from ice core data and used as a long term indicator of solar variability. The details of the ^{10}Be series and their comparison with each other has been outlined (Beer, 2000; Beer et al., 2013). The cosmogenic isotopes are produced in the atmosphere by the interaction of primary and secondary galactic cosmic ray particles with nuclei of nitrogen, oxygen and argon. Two chronologically long ^{10}Be cores have been recorded at high latitudes, in the Greenland Ice Core Project (GRIP), ice core at Summit (Vonmoos et al., 2006) and EPICA Dome C core in Antarctica (Cauquoin et al., 2013). ^{10}Be has a half life of $1.5 \cdot 10^6$ years. The dating potential of ^{10}Be is thus at least 4 Myr. The influence of solar activity on radioisotopes and reconstruction of sunspots is based on the ^{10}Be isotope concentration measured in ice cores from Antarctica and Greenland and has been reviewed

by Usoskin & Mursula (2004). The authors suggested that the century scale Gleissberg cycle and a number of shorter quasi-periodicities give a fluctuation in the millennium time scale. Finding a relationship between cosmic ray variations and the heliospheric parameters (i.e. the open solar magnetic flux, the tilt angle of the heliospheric current sheet and the polarity of the large scale solar magnetic field) it has been calculated that the ^{10}Be , correlates with the ice core records from Greenland NGRIP, which also have an agreement with each other over the 20th century records (Asvestari & Usoskin, 2016). Bard et al. (2015) have reported a new ^{10}Be record from a dated ice core of Dome C in Antarctica, and the reconstruction of the proxy suggested that the sum of the solar minima had an extended period of low volcanicity between 1700 and 1800 years.

4.3.4 Cosmogenic Radioisotope ^{14}C

The ^{14}C isotope is generated in the Earth's atmosphere under the influence of cosmic rays and by climatic factors. The concentration of ^{14}C in tree rings carries information on the past solar activity evolution. Kudryavtsev et al. (2013) studied the possible correlation between variations in the ^{14}C atmospheric content and the Earth's global temperature. It was suggested that variations in global temperature may produce some change in the atmospheric content of ^{14}C and thus would have an impact in reconstructions of past solar activity deduced from the ^{14}C records. The spectral analysis of ^{14}C isotope ratios in (Lean & Rind, 1998b) identified variations with time-scales of 88 years as known the Gleissberg cycle and other cycles such as 210, 2300 and 2500 years. In (Solanki et al., 2004a; Usoskin et al., 2009; Usoskin et al., 2003) suggested that an increase of ^{14}C production is related to lower temperatures, also that the minima cycles such as Sporer (1450 – 1550) and Maunder (1645 – 1715) were identified, but without events of the Little Ice Age and the Medieval Warm Period. The ^{14}C is related to the deep ocean, ocean mixed layer, biosphere, and atmosphere. Comparison of the reconstructed sunspot number derived from ^{14}C to the observed sunspot number has a correlation of 0.83 ± 0.07 counting for a 20 year timespan. The reconstruction of the ^{14}C for the whole Holocene are presented in (Reimer, 2013) and the results provided the quantitative information for studying solar activity variations over several millennia.

Chapter 5

The planetary theory of solar and climate change

The best physical explanation is not, I believe, a delayed tidal effect, but..., some non-tidal factor contributing to the formation of sunspots.

Wood, K.D.

Generally, climate change evolution has been studied by different approaches such as ocean currents, anthropogenic global warming, cloud formation and albedo, greenhouse gases, biot thermostat, planetary motion and solar variability. In this chapter we discuss some global view's of climate change in terms of solar variability which is induced by planetary theory based on gravitational and magnetic oscillations.

5.1 Some empirical evidence of planetary forces acting on solar variation

Empirical approaches that solar activity and radiation variability are linked with gravitational forces of planets is still an open question. This is the case in spite of huge efforts by scientists and significant progress into the subject since first proposed by Wolf (1859a), where he suggested that solar dynamics is partially driven by planetary tides.

5.1.1 Evidence in the short, mid and long term periodicity of the Sun

Estimations of periodicities of solar activity vary due to the length of treated and used records, thus the cycle varies in amplitude and duration. Although, there are well determined solar activity periodicities which are confirmed either by the observational data set or by spectral analysis of the reconstructed data series of solar activity proxies. The temporal variation of solar activity is characterized by four time-scales: the short term cycle over several weeks which is caused by solar rotation and the evolution of active regions; intermediate (mid) term variations over several months caused by major activity events or long lived active regions; long term solar cycle variation (Donnelly et al., 1986) and super-secular cycles.

Search of short term periodicities. Periodicities are determined in solar activity time-scales in effects such as the solar rotation for periods of less than 27 days (Ma, 2015; Tan & Cheng, 2012).

Search of mid term periodicities. Numerous results reported the solar mid term periodic behaviour, e.g. Kilcik et al. (2010) used analysis of the solar flare index that determined a period of 53 days. A periodicity of about two years from cycle maximum exists from the analysis of a poloidal magnetic field by Benevolenskaya (1995). Wang et al. (2015) determined other periodicities including 85 days, 152 days, 248 days, 334 days and 683 days etc. Lean (1990) analysed the signal in the sunspot area data and found a 155 day periodicity that occurs in patches around the epochs of sunspot cycle maxima with a drifting frequency. The analysis of gamma-ray flare activity was demonstrated over 154 day periodicities (Rosen, 1984), while this signal in proton flares was confirmed by Bai & Cliver (1990). Ballester et al. (2002) found a 160 day signal in the Mt. Wilson sunspot index.

Wang & Sheeley (2003) determined quasi-periodicities of about 1.3 years where the Sun's dipole magnetic moment and open magnetic flux revealed multiple peaks. Multiple, significant peaks of power are seen intermittently at periods between 1 and 3 years i.e. quasi-biennial oscillations (known as mid-term quasi-periodicities) and are most prevalent at the time of cycle maxima. Hence, that is why a double-peak or triple-peak structure in the solar maximum phase occurs (Bazilevskaya et al., 2000; Howe et al., 2007).

Search of long term periodicities. The geomagnetic and auroral data indicate the variation from monthly to annual time-scales (Lockwood et al., 2016; Georgieva et al., 2013). The spectral analysis of the reconstructed proxy series defined a number of distinct periodicities at the multi-decadal, multi-secular and multi-millennial time-scales (Frick et al., 1997a,b; Bard et al., 2000; Bond et al., 2001; Abreu et al., 2012; Ogurtsov et al., 2002; Inceoglu et al., 2015) and (Inceoglu et al., 2016a).

Search of secular long term periodicities. Observations of the Sun and the Earth's climatic records reveal an ≈ 11 year variation with complex dynamics of monthly, annual and decadal oscillations. A number of the observed and reconstructed solar activity variations has demonstrated the 11 year cycle periods as in TSI (Willson & Mordvinov, 2003; Fröhlich, 2006; Wu et al., 2016) (see Fig5.1), in magnetic flux records (Ball et al., 2012), and in the variation of reconstructed cosmic isotopes (Steinhilber et al., 2012b; Beer et al., 2012) (see Fig.5.2).

The long periodicities of solar cycles are provided by their systematic variation. Periods of greatly depressed solar activity are referred to as grand minima. One of last grand minimum which was observed by direct solar observation was the Maunder minimum from 1645 – 1715 with a 70 year period of extremely low activity (Eddy et al., 1976). Since then there has been a gradual increase in cycle amplitudes as a secular trend (Wilson, 1988b) of the solar activity variation. The multi-cycle periodicities derived in sunspot cycle amplitudes, i.e. (Gleissberg, 1939b) showed a periodicity of seven or eight cycles from 1750 to 1928 and these had a 80 – 90 year duration. Ogurtsov et al. (2002, 2015) suggested that the cycle consists of two different components, one with a 90 – 100 year period and a second with a 50 – 60 year period and they also proposed a 60 – 120 year period.

A two-cycle variation with odd-numbered cycles higher than the preceding even-numbered cycles is known as the Gnevyshev-Ohl Rule or Even-Odd Effect. Other long-term modulations have been noted in the past from the cosmogenic isotope data. Observations of solar activity revealed the grand maxima and minima events. The analysis of solar proxies reveals that the Sun spends about 1/6th of its current life in a grand minimum phase and about 1/10th in a

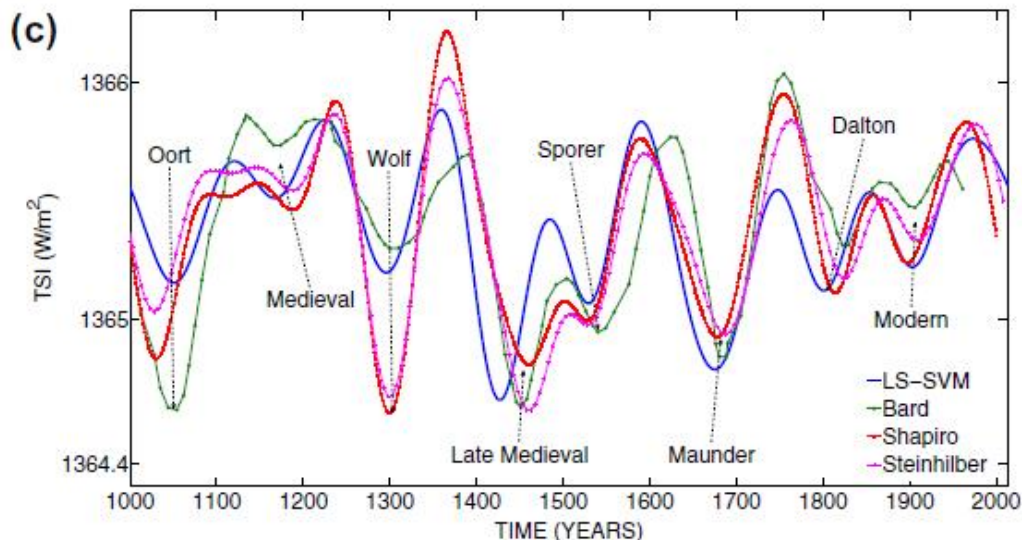


Figure 5.1 – Comparison of the LS-SVM filtered reconstruction PMOD-based model (blue line), with calibration and filtration of TSI reconstructions (Bard et al., 2000, green line), (Shapiro et al., 2011, red line), and (Steinhilber et al., 2009, pink line), (Velasco Herrera et al., 2015).

grand maximum state. The 205 – 210 year period is a prominent feature, observed in various cosmogenic data sets in the reconstructed radioisotope series and it shows correlation with the four observed sunspot records (Ma & Vaquero, 2009). This period is referred to as the Suess or Vries cycle. Reconstruction of isotopes shows evidence for the Sporer grand minimum around 1450 – 1550, the Wolf grand minimum around the 14th century and the Dalton grand minimum (ca. 1790 – 1820).

Using spectral analysis applied to different solar activity records different solar activity periodicities such as the following were found: a 51.5 year period for the interval of 1700–2009, an 103 year secular cycle (Tan, 2011), a 53 year period for the interval from 1725 to 1850 in (Le & Wang, 2003), a 80 – 90 year period, known as the Gleissberg cycle (Gleissberg, 1971). The analysis based on Krylov-Bogolyubov’s approach to the description of weakly non-linear oscillatory processes in (Nagovitsyn, 1997) determined 65 – 130 year quasi-periodic secular cycle. A cycle period of about 100 years has also been mentioned (Frick et al., 1997a; Tan, 2011; Le & Wang, 2003).

A double century cycle of 160 – 270 years was proposed by Schöve (1979, 1983c) and a 203 year Suess cycle was found on the radiocarbon record in tree rings (Suess, 1980). The long term cycles within the range of 80 – 100 years and 170 – 180 years were found from the non-integer technique of power spectral analysis of the sunspot series (Otaola & Zenteno, 1983). There are unnamed cycles around 350 years, 500 years and 710 years for further examples see (Steinhilber et al., 2012b). Longer cycles are studied using cosmogenic isotopes.

Search of millennial long term periodicities. Recently with the multi-proxy approaches using singular spectrum analysis based on the reconstructions of ^{14}C and ^{10}Be records, the geomagnetic field, the archeo and paleointensity database, show a dominant 2400 year quasi-periodicity. This periodicity so-called the Hallstatt cycle which is related to solar activity over the past nine millennia (Usoskin et al., 2016b) (see e.g., Fig.5.3). The reconstruction of

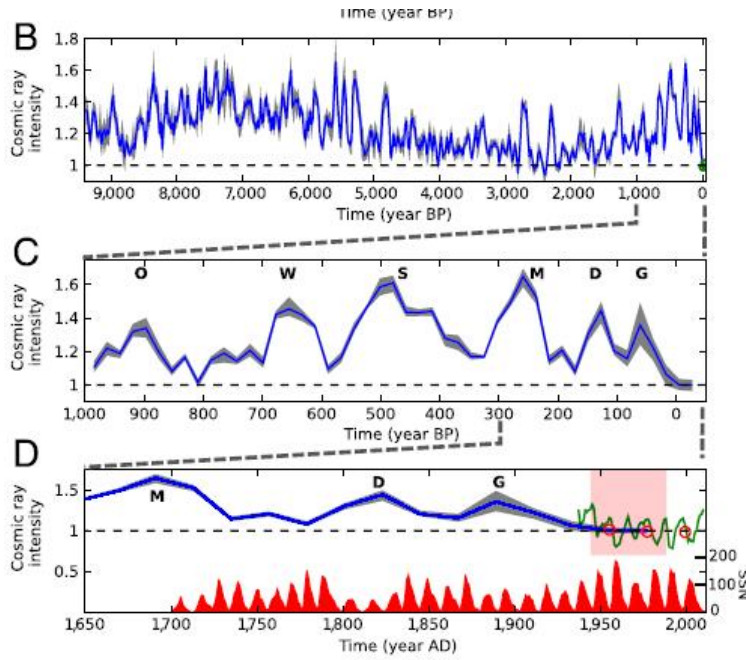


Figure 5.2 – (B): Cosmic radiation based on the first principal component of several radionuclide records, the gray band represents the standard deviation of the individual radionuclide records, the black dashed line represents the average cosmic ray intensity for 1944 – 1988 AD. (C) Same as (B) with a zoom-in of the past millennium. Capital letters mark grand solar minima: O: Oort, W: Wolf, S: Sporer, M: Maunder, D: Dalton, G: Gleissberg. (D) Same as (C), with a zoom-in of the past 350 years, the red circles and the green line represent 22 year averages and yearly averages of cosmic ray intensity respectively. At the bottom in red the annual sunspot number is plotted, (Steinhilber et al., 2012a).

TSI during the Holocen in (Vieira et al., 2011b) and (Krivova et al., 2016) indicates long term variability of solar activity in the past. Variations occur with a characteristic time of between 600 – 700 years or between 1000 – 1200 years, which is known as the Eddy 1000 year cycle (Usoskin et al., 2003).

Other known longer cycles of solar activity which have been studied by the cosmogenic radionuclide data analysis, showed that $\approx 71\%$ of grand minimum during the period from 6600 B.C. to 1650 A.D. were followed by a grand minimum and 47% of the grand maximum follow a grand maximum (Inceoglu et al., 2016b).

The analysis of Usoskin et al. (2016a) from new reconstructed sunspot proxy series dated between 7000 B.C. and 2000 A.D. shows the domination of a common ≈ 2400 year quasi-periodicity referred to as the Hallstatt cycle. This periodicity was mentioned in (Vitinskij et al., 1986; Sonett & Finney, 1990; Dergachev et al., 2000; Steinhilber et al., 2012b; Usoskin et al., 2016a). The decadal sunspot number components reconstructed from the ^{14}C and ^{10}Be data are shown in Fig.5.3 covering three millennia (Usoskin et al., 2014). Here are noted the sunspot numbers from ^{14}C and ^{10}Be as SN-14C and SN-10Be, respectively by Usoskin et al. (2016a). There has been 20 grand minima with a total duration of 1460 years ($\approx 17\%$ of time) and 14 grand maxima with a total duration of 750 years ($\approx 8\%$ of time). It should be noted that the above listed grand maxima and minima events have not necessarily been independently confirmed.

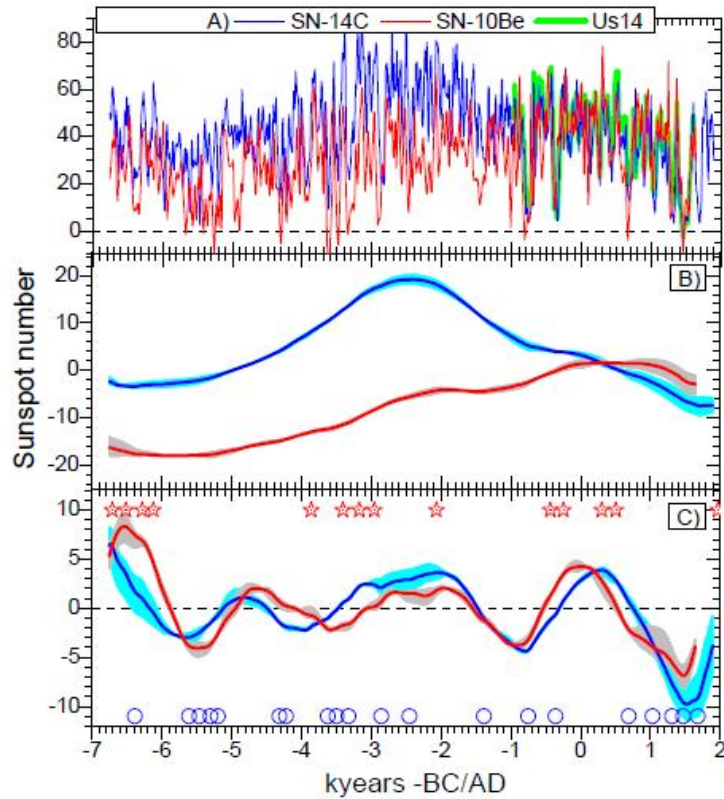


Figure 5.3 – Panel A): Raw reconstructions of sunspot numbers (mean curves). Sunspot number reconstruction from SN-14C (blue) and SN-10Be (red), compared to the recent three kyr reconstruction (green). Panel B): First component of the singular spectrum analysis for SN-14C (blue) and SN-10Be (red) series. Panel C): Same as in panel B), but for the second SSA components of the SN-14C (blue) and SN-10Be (red) series. The large dots and red stars denote times of the grand minima and grand maxima, respectively, (Usoskin et al., 2016a)

5.1.2 Approaches of the measurement of planetary alignments

Approaches of alignments of the planets are based on frequency matching between solar and planetary harmonics. These are achieved by adapting alternative physical functions of the orbits of the planets, assuming the existence of a physical link between planetary orbits and solar activity, without necessarily specifying the exact physical mechanisms involved in the process. Thus the variation of dynamical parameters of the planets as angular momentum, velocity and distance, as well as orbital elements have been proposed as a partial relationship to the periodicities of solar activity.

Tidal period. Generally, planetary theory approaches are based on several major empirical assumptions i.e., the well defined ≈ 11 year cycle between the spring tidal period of Jupiter and Saturn (median ~ 9.93 year) and 11.86 year tidal sidereal period of Jupiter which is correlated with the Schwabe frequency (11 year period) band and falls between two primary tidal cycles. The average planetary frequencies might also be synchronized to a quasi 11 year sunspot solar cycle. Because, the alignments of Venus, Earth and Jupiter have a quasi 11.07 year cycle. In addition, reversal of polarity of the sunspot cycle is known as the Hale duplex cycle of ~ 23 years, nearly half the triple Jupiter-Saturn-Uranus synodic cycle with a variation

of between 42 – 45 years.

Edmonds (2015) suggested that an 88 day periodicity is associated with a Mercury-Sun interaction, as the time variation of sunspot area is either exactly in-phase or exactly in anti-phase with the variation of tidal effect. Thus the author claimed that the motion of Mercury and the periodic emergence of sunspots provides some evidence of a link. The magnetic surface waves were matched to the sub harmonic periods associated with Mercury and triggering of sunspot emergence by the waves was observed. The solar activity proxies such as the aurora and sunspots seem to present planetary harmonics and suggest gravitational, electromagnetic and luminosity links between astronomical and climatic records (Scafetta, 2014).

Bendandi (1931) observed that a 11.07 year period appeared due to the tides of Venus, Earth and Jupiter. Wood (1965) observed that a solar-jerk function presented a period of 11.08 years which is induced mostly by Mercury and Venus. Jose (1965) proposed a correlation of a 178 year cycle and that the Wolf number maxima and the rate of change of solar angular momentum are based on the outer planets. The tidal effect due to the planets is calculated as the tidal potential generated by a planet on a point at the Sun's surface (Cartwright, 1999, e.g.):

$$U(r_s, \varphi) = \left(\frac{GM_p r_s^2}{R_{ps}^3} \right) (3 \cos^2 \varphi - 1), \quad (5.1)$$

where G is the gravitational constant, M_p is the mass of all planets, r_s is the radius of the Sun or the distance from the Sun's center to a point on Sun's surface, R_{ps} is the distance between the planet and the Sun's center, φ is the angle horizontal (east or westward) from the direction of the planet to a point on the Sun's surface. The horizontal g_h and vertical g_v (upward) components of the tide at the Sun's surface and on a point F (see Fig.5.4) are respectively given:

$$g_h = \frac{1}{r_s} \frac{\partial U}{\partial \phi}, g_v = \frac{\partial U}{\partial r_s}, \quad (5.2)$$

and

$$g_h = -\frac{3}{2} \left(\frac{GM_p r_s}{R_{ps}^3} \right) \sin(2\phi), g_v = \frac{3}{2} \left(\frac{GM_p r_s}{R_{ps}^3} \right) \left(\cos(2\phi + \frac{1}{3}) \right). \quad (5.3)$$

Non-linear planetary harmonic models. Using a non-linear processed model of planetary harmonics (Scafetta, 2016c) proposed that the major beat periods occur at about 61, 115 and 130 years, plus a quasi-millennial large beat cycle around 983 years. The equivalent synchronized cycles of cosmogenic records have been used to reconstruct the solar activity in proxy climate records throughout the Holocene for the last 12000 years. The model forecasts a new prolonged solar minimum during 2020 – 2045, which would be produced mostly by the combinations of minima of both the 61 and 115 years reconstructed cycles. These results seem to provide some indication that both solar and climatic oscillations are linked to planetary motion. Their timing can be reasonably hindcast and forecast for decades, centuries and millennia.

Using a simple solar model based on generic non-linear coupling between planetary and solar harmonics the spectral peaks of 103 and 150 years from the cosmogenic records of ^{10}Be and ^{14}C are covered in the Holocene. Spectral coherence of planetary, solar and climatic oscillations attempt to identify from the periods 5.2, 5.93, 6.62, 7.42 and 9.1 years may be caused by the main lunar tidal cycle. The 10.4 year period may be related to the 9.93 –

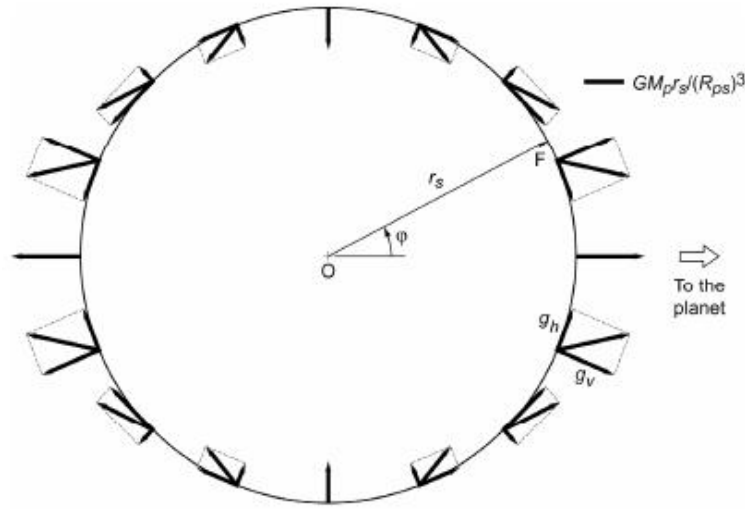


Figure 5.4 – Magnitude and direction of tide driving gravities with their horizontal vertical components (g_h and g_v) at different positions on the Sun's surface and the tide producing planet is off to right of figure, Hung (2007).

10.87 – 11.86 year solar cycle harmonics, possibly as well as 13.8 – 15.0 years, ~ 20 year, ~ 30 year, ~ 61 year, 103 year, 115 year, 130 year, 150 year and about 1000 year (Scafetta, 2014a).

Calculating the planetary harmonics Scafetta & Willson (2013) found that the most important period involves the four major tidal planets: Mercury, Venus, Earth and Jupiter. This was based on the spectral analyses of the TSI and satellite observations that indicated planetary forces are likely to modulate solar activity and also that both magnetic and gravitational coupling are involved.

Planetary position. Grandpierre (1996) attempted to explain the origin of the solar cycle by planetary theory claiming that sunspot formation is controlled by the relative positions of Jupiter, Venus, and the Earth. The well observed and defined planetary position of Venus, Earth and Jupiter ephemerides reveals a 11 year planet alignment cycle similar to the solar cycle. Thus raising the suggestion that the sunspot cycle could be exerted by resonance and beat between the solar tidal cycles. Takahashi (1968) and Wood (1972a) suggested that there is a possible resonance between the sunspot cycle and the planet alignment which might relate to the measured cycle of Venus, Earth, and Jupiter with an alignment period of 11(22) years. The combined alignments of these planets with the configuration Ea-Ve-Sun-Jp or Sun-Ve-Ea-Jp repeats with a period of approximately 22 years, and the correspondent half tidal period is calculated as:

$$P_{VEJ} = \frac{1}{2} \left(\frac{3}{P_V} - \frac{5}{P_E} + \frac{2}{P_J} \right)^{-1} = 11.07y, \quad (5.4)$$

where the sidereal period of planets are:

$$P_V = 224.701 \text{ day};$$

$$P_E = 365.256 \text{ day};$$

$$P_J = 4332.589 \text{ day.}$$

The observation of increased radio and X -ray emissions correspond to the phases when the planets are aligned during a two month period leading to large sunspot groups and major solar flares (Blizard, 1968). This assumes that the mechanism of the thermal effect modulates the tides on the solar surface. According to Smythe & Eddy (1977) the cycle is 10.4 years due to planet alignment and 11.87 years due to tidal potential. The planetary configuration is more precisely calculated for spanning decades to millennium as well as the solar magnetic activity proxies with a relatively high quality. It also allows the application of empirical approaches to study the evidence of planetary influences on solar behaviour. The calculation of alignment indexes for the Venus, Earth and Jupiter planet system with the FFT of planetary alignments indicate a cycle period of 11.07 years (Okal & Anderson, 1975; Scafetta, 2010a).

McCracken et al. (2014) compared the periodicities of the ^{10}Be and ^{14}C radioisotopes throughout the past 9400 years with planetary configurations that suggested a probability as low as $< 10^{-5}$ of occurring by chance. This suggested that paleo cosmic ray (PCR) records are strongly correlated with the motion of the Jovian planets as: the PCR periodicities at 87, 350, 510 and 710 years, which closely approximate integer multiples of half the Uranus and Neptune synodic period. The correlation of the calculated torques observed in the PCR, the maxima of the long term PCR variations are coincident with syzygy (alignment) of the four Jovian planets. PCR intensity decreases ~ 172 years and increases ~ 112 years which seems to be associated with barycentric anomalies in the distance between the Sun and the center of the barycentre.

Okhlopov (2014) used the heliocentric longitudes of Venus, Earth and Jupiter to compare with solar activity, and proposed a periodicity of 22 years at the linear configuration i.e. at conjunctions of these planets. According to Lun (2015), Jupiter, Saturn and Pluto's combined alignment will take place in 2020 which corresponds to the start of solar cycle 25, to peak in 2024. In 2014 the end of the 34 year Saturn-Pluto cycle occurred, which suggests the cooling is already beginning (see Fig.5.5).

Planetary motion. The discovery of an approximately 11 year sunspot cycle by Wolf (1859a) suggested that the observed solar variability could be synchronized with orbital movements of Venus, Earth, Jupiter and Saturn. The potential impact of planetary motion on solar activity was then expanded by Brown (1900) as a possible explanation of the sunspot period. Bigg (1967b) proposed that the relative sunspot number variation contains small but consistent periodicity at the sidereal period of Mercury. Many attempts were taken to correlate features of solar activity with the motion of the planets in the solar system. For example, the high tide displacement of the solar surface was calculated each day from the positions, masses and the distances of neighbouring planets (Bigg & Mulhall, 1967). This study was extended by many others (Okal & Anderson, 1975; Cionco & Compagnucci, 2012; Cionco & Soon, 2015; Charvatova & Strestik, 1991; Charvatova & Hejda, 2013; Leal-Silva & Herrera, 2012; Landscheidt, 1999).

The search of periodicities of the solar indices using spectral analysis and comparison with planetary harmonics has taken attention of other researchers. For example, Tan & Cheng (2013) investigated the solar quasi-periodic cycles of the observed relative sunspot number with multi time-scales and compared them with planetary motions. They proposed the classification of three cycles as a planetary-like cycle (PLC): the strong PLC which is related strongly with planetary motions, including nine periodic modes with relatively short periods ($P < 12$ years) related to the motions of the inner planets and of Jupiter. The

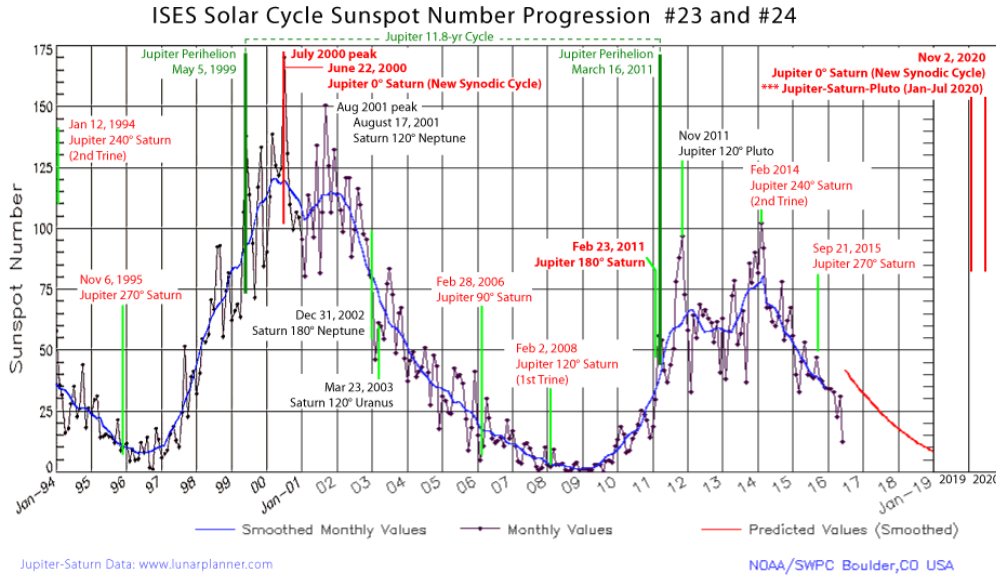


Figure 5.5 – Jupiter-Saturn and Solar Cycle Correspondences, from NOAA, Boulder, Colorado, USA (Lun, 2015).

weak PLC, which is related weakly to planetary motions, including two periodic modes with relatively long periods ($P > 12$ years), and possibly related to the motions of outer planets. The non-PLC shows no clear evidence for a relationship with any planetary motion.

Chowdhury et al. (2016), studied the spectral analysis of the CaII-K plage index of the Sun and displayed the periodicities correlated with the planetary motion as follows: short periodicities 2 to 4 months and 83.4 days is Mercury’s orbital period of 88 days; intermediate quasi-periodicities of 4 months to ~ 1 year. These periodicities correspond to the spring tidal periods of Mercury ~ 155.4 and Venus 144.56 days. Also other intermediate periodicities ~ 1 year to ~ 5 years are determined. These quasi-periodicities seem to lie in the range close to one or more planetary periodicities i.e., orbital, or spring tidal, or heliocentric conjunction frequency.

Sun’s and solar system motion. According to Juckett (2003), research of temporal variations of low-order spherical harmonic representations of sunspot group patterns suggests evidence for solar spin-orbit coupling. The intermediate time scale contains evidence that solar activity is modulated by the Sun’s motion around the solar system barycenter.

Positions of sunspots. Schuster (1911) and Okhlopkov (2014) suggested a correlation of the position of sunspots and the heliocentric longitude of Mercury, Venus, and Jupiter. While in (Dingle et al., 1973) no correlation was found between solar flares and the heliocentric longitude of Venus or Jupiter. However these approaches are not supported by Callebaut et al. (2012). They computed that the solar tide is not significant because the driven gravitational tide is too small to affect solar activity.

5.1.3 Approaches based on the dynamical and physical mechanisms of the Sun

Solar-planet interaction studies are devoted to different physical and dynamical mechanisms based on solar inertial motion, planetary alignments and physical parameters such as orbital angular momentum (or planetary torque), potential energy, barycentric motion, interplanetary shock impacts, dynamo models of Sun etc. (Wolf, 1859a; Brown, 1900; Wood, 1965; Fairbridge & Shirley, 1987; Charvatova & Strestik, 1991; Grandpierre, 1996; Landscheidt, 1999; Javaraiah, 2005; Wolff & Patrone, 2010; Cionco & Soon, 2015).

Dynamical mechanisms. Dynamical mechanisms consist of a working mechanism linking solar orbital dynamics with the internal dynamics of the Sun, including raising of the tides due to planets which are supposed to produce sporadic or cyclical modifications on solar magnetic activity (Takahashi, 1968; Wood, 1972a). In (Wood, 1965; Fairbridge & Shirley, 1987; Charvatova & Hejda, 2013) it was suggested that the variation of velocity and acceleration of the solar motion may induce solar activity, as well as orbital angular momentum (planetary torque) and its derivatives (Jose, 1965; Shirley, 2006; Perryman & Schulze-Hartung, 2011). These dynamical approaches have been proposed as the Sun is not a perfect sphere, hence are effected by torque of the planets. According to Javaraiah (2005) there may be evidence of spin-orbit coupling (as an observed precessional effect) in the Sun. Also, Wolff & Patrone (2010) proposed a new mechanism for the modification of stars interior's planetary gravity. This is due to potential energy per unit mass created in a cell, inside of a rotating star with orbiting planets.

Charvatova & Strestik (1991) computed the periodicity of Jovian planets as 13.7 years for Jupiter-Uranus, 12.8 years for Jupiter-Neptune and 9.9 years for half of the Jupiter-Saturn period. These periodicities are all close to the solar cycle of 11 years. Cionco & Compagnucci (2012) showed the variation of orbital angular momentum of the Sun as it evolves. They also found inclination of the solar barycentric orbit as varied during the epochs of orbital retrogressions and that this is effected during the grand solar maxima. Abreu et al. (2012) and Wolff & Patrone (2010) proposed that the planetary tides could exert a varying torque on a non-spherical tachocline. The perturbation of the solar dynamo and modulation of the long-term solar magnetic activity have shown that the torque signal presents numerous harmonics on the secular and multi-secular timescale. This seems to be similar to the long-term solar proxy models as well as the Venus-Earth-Jupiter spin-orbit coupling model (Wilson, 2013).

Physical mechanisms. The physical mechanism is based on force or momentum balance (between the solar atmospheric pressure, the field of gravity and magnetic field) on the plasma. The solar corona has looping magnetic field lines. These are potentially disturbed by tides and may result in magnetic field reconnection, solar flares and solar storms (Scharf, 2010a). The variation of magneto-acoustic heating and dynamo action could be caused by internal solar feedback i.e., resonances and synchronization mechanisms due to physical forcing (Cuntz et al., 2000).

The mechanism of the planetary tides raises the gravitational energy to the Sun which may trigger slight nuclear fusion rate variations by enhancing solar plasma mixing. Under gravitational perturbations electrons and protons may drift in opposite directions perpendicular to the gravitational forces generating micro currents in the plasma (Scafetta, 2010b). The wave signal can be transported from the core to the tachocline in a few weeks, this causes perturbation of the Sun's core which may expand and contract. The harmonic signal emerges from the radiative zone, forcing the convective zone to operate the solar dynamo i.e. neutrino pro-

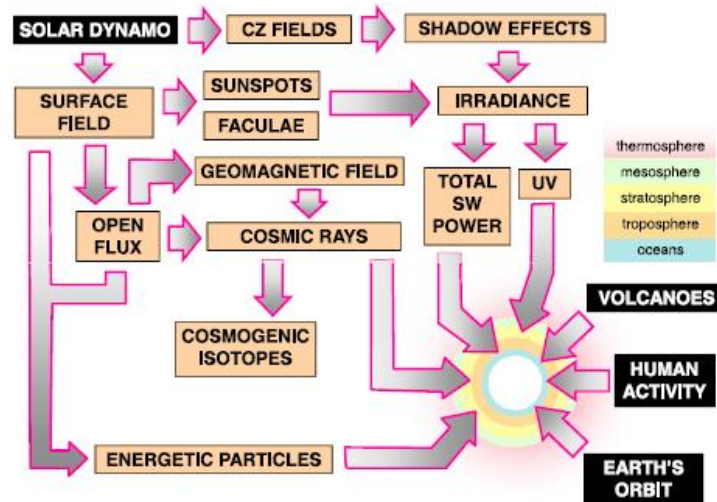


Figure 5.6 – Illustration of solar variability (irradiance and corpuscular radiation) impact to Earth’s atmosphere changing the climatic environment, (Gray et al., 2010).

duction. The resonances and synchronization of outputted solar luminosity by gravitational planetary motion, is about 0.005 – 0.05% of the luminosity variation (Scafetta, 2012,a).

Another approach is to find common frequency sets between the solar activity records and the theoretical planetary harmonics which are observed in total solar irradiance (TSI) satellite observations on monthly-to-annual timescales (Scafetta, 2009; Scafetta & Willson, 2014) (for more see Sec. 3.4).

5.1.4 Climate and the changing Sun

The relationship between solar variation and planetary climate change is a vast subject, requiring knowledge in several fields such as astronomy and astrophysics, atmospheric dynamics, geophysics, paleoceanography and glaciology. Milankovitch (1920) developed the theory of orbital cycles and their impact on climate (Roe, 2006, e.g.). This theory was verified and accepted only after using available data from isotope measurements (Hays et al., 1976). This ice age theory is interesting for our problem as it shows that a strong climatic change can cause a weak forcing.

The variability of the Sun may have an influence on the Earth’s climate as reported in (Herschel, 1801; Maunder, 1894), and followed by a great number of papers (Eddy et al., 1976; Hoyt & Schatten, 1997; Svensmark & Friis-Christensen, 1997; Ogurtsov et al., 2003; Damon & Laut, 2004a). However, the correlations between solar variability and climatic parameters were criticised by others e.g. (Pittock, 1978). The reason for the disapproval was due to the lack of extension of the time-frame required to establish statistical significance. Some of the suggested mechanisms by which solar variability might influence the climate have been carried out (Bard & Frank, 2006; Gray et al., 2010; Bard et al., 2015) and possible correlation has been shown in Fig. 5.6. Bard & Frank (2006) found that satellite observation of TSI data over short periods provides a small range of solar forces, e.g. 1% of TSI over the 11 year activity cycle.

Scafetta (2016a) studied the spectral coherence between climatic and astronomical records (planetary harmonic) with their statistical confidence. The research concluded that the cli-

matic system is partially modulated by astronomical forces of gravitational and solar origin. He writes that astronomical harmonics at 20 and 60 year periods were found in the analysis of global climate records. The climate proxy records covering several centuries and millennia were compared with global temperature records for the 6570 year cycle (Schlesinger & Ramankutty, 1994). They suggested a 95% confidence level using high resolution coherence analysis methodology and therefore concluded that the climatic system could be partially modulated by astronomical forces of gravitational and solar origin. Bianchini et al. (2016) analysed the spectral frequencies of the global temperature variation and conjectured that the global temperature is partially modulated by planetary harmonics that may also influence solar activity. This suggestion was based on the solar and climatic record variations related by planetary harmonics from the monthly to the millennial time-scales.

Scafetta (2014b) considered the solar system to be a resonator induced by a main harmonic planetary mechanism which affects the Sun's activity and the Earth's climate for a 60 year cycle of atmospheric circulation.

Mörner (2015) illustrated the cyclic alternations between solar maxima and minima which are correlated with periods of acceleration and deceleration in the Earth's rate of rotation. The variations in solar activity may have strict periodic variations correlated and driven by the planetary beat. The possible consequences of climate change include multiple effects of the interaction of solar wind with the magnetosphere and Earth's rate of rotation.

Another proposal is related to the formation of cloud cover on a global scale as a function of cosmic ray flux (Svensmark & Friis-Christensen, 1997), although in (Damon & Laut, 2004b) the results were questioned due to the data used.

5.2 Some classical objections of planetary hypotheses

The planetary hypothesis of the solar cycle has a long traditional evolution. The gravitational influence of the planets is assumed to have a negligible effect on the causes of the solar magnetic cycle. In this section we discuss some of general objections of planetary theory on solar variability.

5.2.1 Classical physics of planetary tidal forces

A general critic given by Smythe & Eddy (1977) was based on a presumed geometrical incompatibility between the dynamics revealed by planetary tidal forces and the known dynamical evolution of solar activity. They concluded that planetary tides could not influence solar dynamics due to Jupiter and Saturn's planetary tides occurring during the solar minimum presenting indistinguishable patterns. Hence, the solar secular activity variations were not present in the planetary cycles. This critic was discussed and rebutted by Scafetta (2012), explaining that the major observed solar activity and climatic records changed from the 11 year solar cycle to the quasi-millennial cycles such as the Oort, Wolf, Sporer, Maunder and Dalton minima. Thus, solar cycle throughout the Holocene can be reproduced by a model based on the frequencies and timings of the two major Jupiter and Saturn planetary tides.

Jager & Versteegh (2005) and Callebaut et al. (2012) presented the physical analysis of solar variability due to Newtonian attraction by the planets and calculated the forces exerted on the tachocline. They calculated from magnetic buoyancy and to the Coriolis force the sum of the tidal accelerations of planets a_{int} , Jupiter a_{Jup} and the accelerations a_{dyn} by convective motions

in the tachocline. At the tachocline for six planets $a_{Jup} = 2.8 \cdot 10^{-10} \text{m/s}^2$ is obtained, while the combined acceleration due to Mercury, Venus, Earth and Jupiter is about $7.8 \cdot 10^{-10} \text{m/s}^2$, with respect to the solar centre of $\sim 31 \cdot 10^{-10} \text{m/s}^2$, $a_{int} = 5 \cdot 10^{-10} \text{m/s}^2$ and $a_{dyn} = 6 \cdot 10^{-10} \text{m/s}^2$. Callebaut et al. (2012) concluded that planetary influences are too small to induce the solar cycle because the planetary tidal accelerations at the tachocline level are about 1000 times smaller than the accelerations of the convective motions. This work was discussed by Scafetta & Willson (2013) who argued that the planetary forcings may modulate solar activity only if internal solar mechanisms greatly amplify their effect. This suggests that the Sun works as an amplifier of gravitational disturbances, as it is a generator of energy controlled by gravity and even a small perturbation is sufficient to influence the solar dynamo.

Classical objection in the theory of stellar structure over the Kelvin-Helmholtz time-scale have been also studied. Mitalas & Sills (1992); Stix (2003) proposed an explanation was given that the very slow diffusion of photons from the core to the tachocline would smooth out any luminosity variation signal occurring in the core before the signal could reach the convective zone. The Kelvin-Helmholtz time-scale for the Sun is $\sim 10^4 - 10^5$ years. This objection and was discussed in (García et al., 2007; Wolff & Patrone, 2010). They postulated a fast acoustic-like or g-wave transport mechanism, which provides the energy variation signal from the core to the tachocline and takes a time scale of a few weeks. Bradley W. Carroll (2001) argued that classical physics alone cannot explain how the Sun works. The conventional view of solar science assumes that solar magnetic and radiant variability are driven by internal solar dynamics alone, characterised by hydromagnetic solar dynamo models (Tobias, 2002; Charbonneau, 2002; Jiang et al., 2007b). Strugarek (2017) argued that the magnetic cycle period is inversely proportional to the Rossby number, which quantifies the influence of rotation on turbulent convection. The trend relies on a fundamentally nonlinear dynamo process and is compatible with the Sun's cycle and those of other solar-type stars. Other important evidence of planetary motion based on the observational data of solar like stars, the magnetic and tidal interaction of planet stellar systems is discussed in the next section.

5.2.2 Exoplanet approaches of stellar activity

An intersection between the strength of planetary and stellar magnetic fields is identified as the Alfvénic surface (i.e., where the stellar wind flow velocity is subcritical). Cohen et al. (2009) concluded that the stellar and planetary interaction of the magnetosphere's produces a magnetic stress resulting in reconnection and reconfiguration phenomena events.

Scandariato et al. (2013a), conjuncted that the rotational modulation of the star would induce evolution of chromospheric and coronal activity, without any signature related to the orbital motion of the planet. However, a fraction of the chromospheric and coronal variability would be modulated with the orbital period of the planet, or the stellar-planet beat period.

In the case of star planet interactions the induced stellar activity was studied by numerous groups (e.g., Shkolnik, 2005; Scharf, 2010b; Matter et al., 2016). They proposed that the presence of a hot Jupiter with a 9.2 year circular orbit with radius of 4.2 AU and with a star of quasi 9 year activity cycle would have a macroscopic effect. Shkolnik (2010) performed photometric, spectroscopic and spectropolarimetric studies on a hot Jupiter short period ($< 0.1 \text{AU}$) orbiting its star within a distance of 10 stellar radii. This demonstrated that a planet can induce some activity on the upper atmosphere of its host star by tidal and magnetic star planet interactions. Due to the intersection of the location on the Alfvén radius the host star

provides a magnetic interaction with the stellar surface. Accordingly, the stellar rotation rate and the global stellar activity are increased by the tidal influence of a host Jupiter.

A configuration, where the planet is within the stars Alfvén radius, results in an extended system and may even propagate against the inflowing stellar wind with possible consequences for the stellar activity (Riouisset et al., 2015). Poppenhaeger (2015) outlined that the observed data of the stellar system indicates that star-planet interactions are not a strong factor during the period of planet-hosting stars. Although for some observed systems where the planet and star are close to each other, the interactions would have a relevant effect.

Figueira et al. (2016) used the HARPS-N spectrograph of the HD 80606 system with an eccentricity of 0.93 and an orbital period of 111 days during the planetary periastron passage. They analysed the activity close to periastron and found no evidence for a variation in the activity level of the star as a function of the planetary orbital distance. However magnetic and tidal interactions were found by Canto Martins et al. (2011). Spectrograph observation by Maggio et al. (2015) of the system HD 17156 in X-ray detection (with a transiting Jupiter mass planet of $\sim 3.2M_J$ on a 21.2 day period orbit with the eccentricity of $e = 0.68$ and semi-major axis of $a = 0.16\text{AU}$) presented two possible scenarios for the activity enhancement as magnetic reconnection and flaring or accretion onto the star of material tidally stripped from the planet.

Interpretation as a stellar planetary interaction linked with magnetic origin has been proposed by Shkolnik (2005). He showed results based on observations of variable chromospheric emission of CaIIH&K line cores that were modulated by the orbital period of a close planet. This evidence may be explained as a tidally induced effect of hosting planets with low eccentricity which modulates twice per orbital period (as on the opposite sides of the stellar surface the two tidal bulges). The 23 solar analogues with X-ray coverage used for the study for a statistically significant correlation by considering four different potential interactions, where L_X and L_X/L_{bol} are activity indicators, versus M_P/a^2 and $1/a$ as interaction-strength proxies as shown in Fig.5.7. They correspond to probabilities of 78%, 83%, 67%, and 73% (Miller et al., 2015) that show no correlation.

Stellar planetary interaction acts through a transfer of angular momentum from the planet to the star (Poppenhaeger & Wolk, 2014). This increases stellar rotation and activity and would give rise to enhanced X-ray emissions. Pillitteri et al. (2015) proposed that stellar planetary interaction leads to X-ray and FUV (far ultraviolet) variability phased with the planetary motion. The magnetic variation induced by stellar rotation affects short-term activity evolution (Scandariato et al., 2013b). The observations of X-rays of stars with a hosting Jupiter are statistically brighter than stars without hot a Jupiter (Kashyap et al., 2008). The X-ray luminosity of the host star and the planetary mass have been correlated (Scharf, 2010a).

Although Poppenhaeger & Schmitt (2011) concluded that stellar planetary interaction induces quite small effects which are measurable only in particular systems. Correlation of relative velocity between the coronal and planetary magnetic can be fields obtained using analytical models to study. Using this method Lanza (2009) developed periodic chromospheric enhancements as factor of a flare like magnetic reconnection. Lanza (2012) presented research that host sunspots phases are not caused by planetary motion.

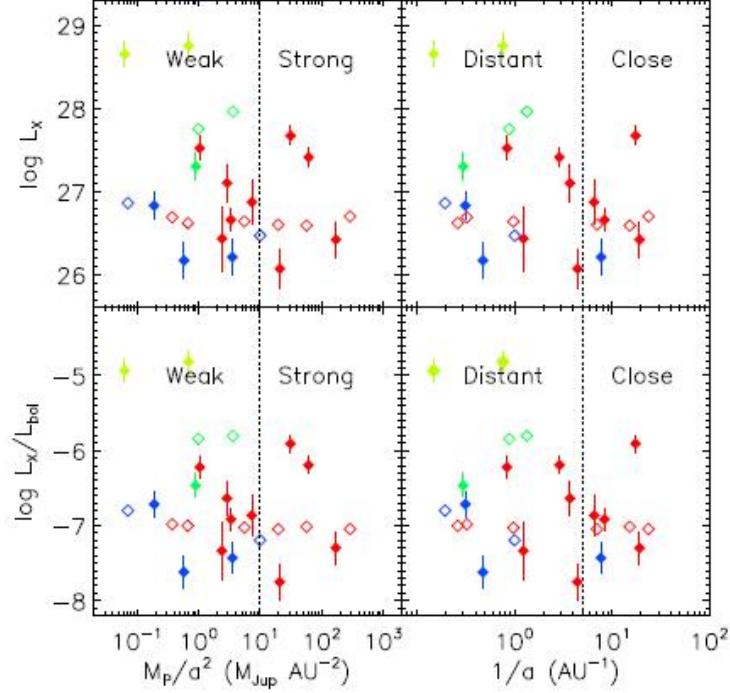


Figure 5.7 – Distribution of coronal activity vs. two proxies for interaction strength for the subsample of solar analogs. Red, blue, and green colors mark Chandra, XMM-Newton, and ROSAT measurements (the light-green points are excluded as atypically active). Filled symbols are X-ray detection and open symbols are upper limits. Vertical dashed lines delineate weakly vs. strongly interacting systems at $M_P/a^2 = 10M_{Jup} \text{ AU}^{-2}$ and close vs. distant planets at $a = 0.2 \text{ AU}$, (Miller et al., 2015).

5.3 Estimations of planetary tidal perturbation and its influences on solar activity

The partially exerted planetary perturbation on solar variability modulation has been largely investigated and is supported by various results based on empirical, physical and mathematical approaches.

5.3.1 Possible partial modulation of Solar variability by planetary tidal cycles

Studying the correlation between the orbital period of planets and solar variation assumes that the interaction of the forces of gravity (tidal force) and magnetism along with the thermodynamic principles generate the internal dynamics of the Sun. The approaches such as comparing sea level rise and global temperature change with sunspot variations reveal the phase (also phase reversal) (Mörner, 2012). The planetary beat generates a sensitive solar tachocline zone which controls the solar irradiance. Solar wind emission affects the Earth environment and the Earth-Moon system directly via tidal forces and angular momentum has been discussed by Mörner (2012). Cionco & Compagnucci (2012) argued that the giant planets quasi alignments repeat every ~ 170 years which only corresponds to the start of Maunder

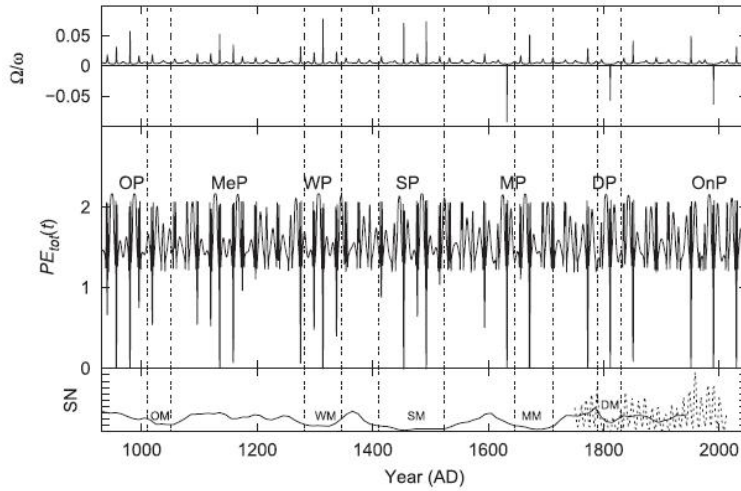


Figure 5.8 – Top panel: Translational-rotational parameter Ω/ω ratio; Middle panel: PE_{tot} -potential energy, stored in the Sun at three key locations; Bottom panel: SN-proxy sunspot numbers, reconstructed by Usoskin et al. (2014) in solid lines and the SN yearly observed data in dashed-line from 1749 – 2013, indicated with the corresponding known grand solar events, (Cionco & Soon, 2015)

and Dalton minima (Javaraiah, 2005).

Recently, Cionco & Soon (2015) proposed that the maximum storage of potential energy and the occurrences of grand minima are correlated. They explained that there is a connection between the planetary energy minima is the minima of the Sun's position relative to the barycenter. Fig.5.8 shows the pulses of potential energy PE_{tot} minima that are produced by the closest approaches of the Sun to the barycentre. At these epochs, the Ω/ω ratio has its maximum values and the solar grand minima events from solar activity proxies are indicated. The names of the pulses of the PE_{tot} minima between Oort Minimum and Wolf Minimum (MeP) and the related ongoing prolonged minima (OnP) are also labelled as well as those corresponding directly to historical grand minima events.

The estimation of the planetary tidal induced TSI oscillations at 1 AU, where the function $I_P(t)$ is numerically determined for each planet and displayed in Fig.5.9 and 5.10 (Scafetta & Willson, 2014). It is shown that the observed oscillations induced by elliptical orbits of the planets where the maximum is located at the aphelion. Jupiter produces the largest effect both in average and in the amplitude of the oscillation, then Venus, Earth, Mercury and Saturn follow in descending order.

Wolff & Patrone (2010) proposed that by planetary gravitational forcing a mass flow inside the Sun which carries fresh hydrogen fuel to deeper levels increased the solar nuclear fusion rate. This effect leads to observable variations in the orbital parameters which may partially perturb the operation of the solar dynamo (Zaqarashvili, 1997b). In the zone between the bottom of the convection zone and the top of the radiative zone is the buoyancy period that matches the tidal period (Goldreich & Nicholson, 1989). Below the convection zone is located the tachocline (Spiegel & Zahn, 1992) leading to a transition between the differently rotating convection zone and the almost rigidly rotating radiative interior. This is why the tachocline plays a fundamental role in the generation and storage of the toroidal magnetic flux which gives rise to solar activity cycles. Hence the net tidal torque is generated in this small region,

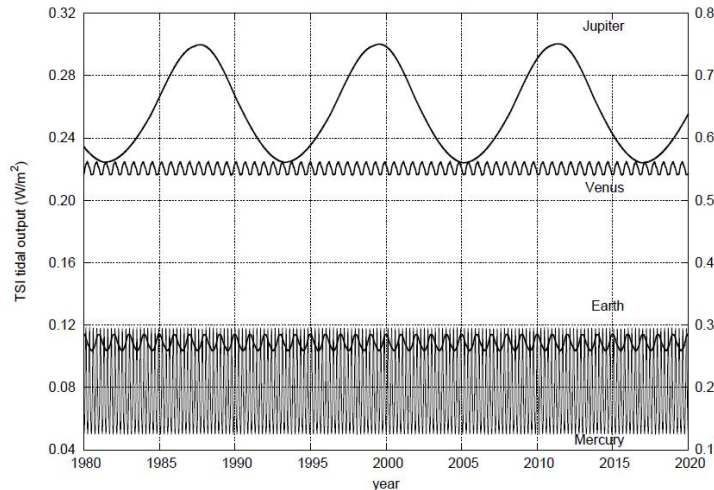


Figure 5.9 – Total tidal induced irradiance estimation for Jupiter, Venus, Earth and Mercury. The left scale refers to the Love number $3/2$ and the right scale to $15/4$, (Scafetta, 2012b).

as a possible coupling mechanism of planetary torques exerted on a non-spherical tachocline. This should exhibit features and periodicities close to those of solar activity variation.

Other approaches also studied a physical model for describing the time dependent torque exerted by the planets on a non-spherical tachocline (Abreu et al., 2012). It was found that the periodicities in the secular and multi-secular timescales obtained from the power spectrum using the proxy record reconstruction showed a correlation of solar and planetary harmonics, that is not based on exact physical mechanisms. This approach was criticised by several arguments, Cameron & Schüssler (2013) suggested that the agreement between the periodicities in proxies records and planetary torques is statistically insignificant, thus indicated no evidence for planetary influence on solar activity. Cauquoin et al. (2014) presented results of spectral analysis based on the simple mechanism of Abreu et al. (2012) that do not support planetary influence on solar activity. Finally Abreu et al. (2012) results have been questioned by Poluianov & Usoskin (2014), who recalculated the procedure and the results of Abreu et al. (2012). Poluianov & Usoskin (2014) compared the torque and the heliospheric modulation potential to show that peaks in the long-period range of the torque spectrum are artefacts, hence coherence between them becomes insignificant and concluded that this hypothesis is not based on solid ground.

Mörner et al. (2013) presented a tidal torque model to describe the chaotic characteristic time cycles of solar activity, admitting that the driving factor of solar variability may emerge from gravitational (exerted from planets) and inertial effects on the Sun based on planetary solar terrestrial interior. Charvatova & Hejda (2013) suggested possible responses of ordered (trefoil) and disordered intervals (types) of solar inertial motion. It is known that the Sun returns to the trefoil intervals always after 178.7 years. During intermediate intervals the Sun moves along chaotic (disordered) lines. Thus the calculation of solar inertial motion variation fits the same pattern to the long-scale reconstructed solar proxies records revealing the main grand minima events.

Salvador (2013) proposed a mathematical model of sunspots based on tidal torque theory aspects and Jovian magnetic field interactions. The model represents the solar cycle covering

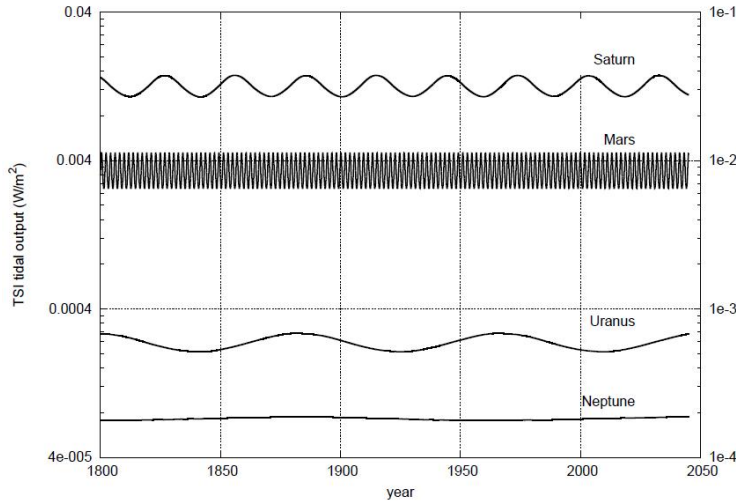


Figure 5.10 – Total tidal induced irradiance estimated for Saturn, Mars, Uranus and Neptune. The left scale refers to the Love number $3/2$ and the right scale to $15/4$, (Scafetta, 2012b).

1000 years indicating the known grand minima and maxima events describing the chaotic system. Wilson (2013) studied the torque tidal theory based on features of the combination of an Earth-Jupiter spin orbit coupling model and the gear effect. A physical theory of planetary impact, that may provide solar variability which is possibly caused by spin-orbital coupling between Venus, Earth and Jupiter (VEJ). The Jovian and Terrestrial planets may perturb bulk motions in the convective layer of the Sun. Shepherd et al. (2014) results are based on the comparison of spectral analysis of the solar background magnetic field (SBMF) and the sunspot magnetic field. This has two principal components (PCs) of SBF with opposite polarities. The variation is based on two PCs in SBF and seems to suggest a resemblance to the average number of sunspots in cycles.

5.3.2 Some predictions of solar activity induced by planetary tidal motion

The variation of solar activity tends to be characterised by multiple physical mechanisms such as: phasing of sunspot cycles, the cyclic observations over the past millennium, the cyclic pattern of cosmogenic radio nucleotides in natural terrestrial archives, the motions of the Sun with respect to the centre of mass, the planetary spin-orbit coupling, the planetary conjunction history and general planetary-solar-terrestrial interaction. Here are summarised some of the predictions for the coming 25th solar cycle. The 25th solar cycle is predicted to start in 2020, peaking in 2025 and is expected to be smaller than the current 24th cycle that peaked in 2013.

A purely mathematical model of the sunspot cycle based on a tidal-torque model is presented in (Salvador, 2013; Mörner, 2015). Their prediction for the next century and over the last 4000 years are shown in Figs. 5.11 and 5.12. They assumed that variations of the planetary beat reveal the main grand maxima and minima events with comparison of dTSI reconstructed radio isotopes proxies (Steinhilber et al., 2012a). They found an extended low up to the year 2160 with the lowest values reached within the period between 2028 – 2042 as occurrences

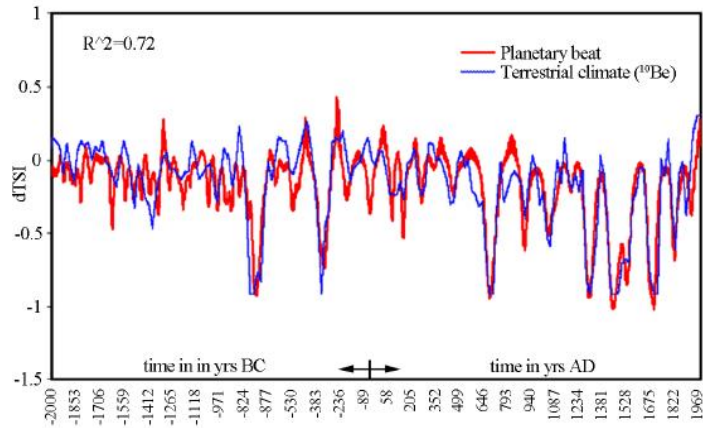


Figure 5.11 – Comparison over 4000 years between planetary beat according to the VEJ SOC Solar System Resonance Model based on the VEJ theory and the dTISI as calculated from terrestrial ^{10}Be variations, (Mörner, 2015).

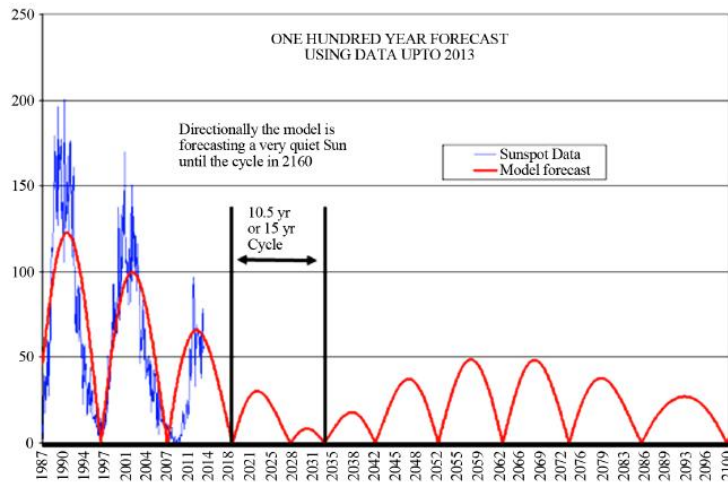


Figure 5.12 – A comparison of monthly sunspot numbers from 1987 to 2013 (in blue) with the absolute value of the correlation model (in red), derived using data up to 2013 and the extended forecast, (Salvador, 2013).

of a new grand solar minima. The known grand minimum periods are associated with less irradiation from the Sun and cold climatic periods on the Earth. Spectral analysis studies by Yndestad & Solheim (2016) were based on the deterministic properties of a model of the TSI ACRIM data series. The results suggested the identification of three grand Maunder type periods and two Dalton type periods in a thousand year period. The climate of Earth will cool due to these new Maunder or Dalton type periods from about 2018 to 2055, 2015 to 2071 and 2047 to 2068. This possible new grand solar minima during the years 2030 – 2040 is also mentioned by Mörner (2015).

Roshchina & Sarychev (2015) used empirical parameters of functions by approximating the solar activity cycle of 8 – 23 which shows the position of the cycle on the time axis and shape. They found statistical connections between two shapes of parameters of the solar cycle. These are an extension of the cycle growth branch and the start time of the following cycle. Thus from this model they estimated that the 25th cycle, with the smoothed sunspot number of 116,

is expected to take place in March/April 2026. A prediction of the axial dipole moment during the upcoming activity minimum was computed using surface flux transport simulations, hence the 25th cycle's expected value for the dipole moment should be around $2020(2.5 \pm 1.1G)$ with a lower amplitude than the current cycle (Cameron et al., 2016).

Hathaway & Upton (2016b) suggested that the solar activity records such as magnetic field measurements, polar faculae counts and geomagnetic field measurements strongly indicate the strength of Sun's poles at the cycle minimum. They also determined the strength of the following cycle, and the polar fields produced by the horizontal flows, poleward meridional flow, and cellular convective motions. Using advective flux transport code, they predicted that the 25th cycle will be similar in strength to the current cycle with an expected maximum sunspot number of 100 ± 15 . Javaraiah (2015) researched the spectral analysis of the combined Greenwich and Solar Optical Observing Network sunspot group data. They determined that the long periodicities in these parameters may provide prediction of the 25th cycle amplitudes to be 50 ± 10 . At the same time Li et al. (2015) used the featured parameters of solar cycle profiles to predict the maximum amplitude of the next upcoming, solar cycle and its timing. They suggested that cycle 25 will start in November 2019 with a maximum amplitude of 109.1 in October 2023. Other predictions for the 25th solar cycle are listed in Tab. 5.1.

Table 5.1 – Predictions for the next 25th solar cycle

Reference	Average Maximum SN	Time of Solar Maximum
Chistyakov (1983)	121	2028.5
Kontor et al. (1984)	117	2024
Du (2006)	102.6 ± 22.4	
Du & Du (2006)	111.6 ± 17.4	
Quassim et al. (2007)	116	2020
Hiremath (2008a)	110 ± 11	2023
Pishkalo (2008)	112.3 ± 33.4	2023.4 ± 0.7
Rigozo et al. (2011)	132.1	2023.3
Helal & Galal (2013)	118	2022 – 2023

It must be noted that we do not support neither refute any of outlined theories and assumptions. In this section it was attempted to overview the current known interpretation of planetary theory.

Chapter 6

Search for quasi-periodicities in the solar activity records

The investigation of the nature of the solar activity mechanism and its prediction forecasts require an accurate observed long-term data series which is not directly available from solar activity. There is therefore a need to reconstruct the activity based on the measurement of various sources through its properties. The search of periodicities in the observed solar activity data is based on several approaches such as extrapolation using the statistical properties of the daily, monthly and annual records of direct observation during the last 400 years (also included are examples of naked-eye sunspot viewings or sightings of aurorae records) without being based upon any physical characteristics of the solar activity process. It provides an ~ 11 year frequency and/or multi harmonic properties of the observed data series, extrapolating back over a long timescale. It is used in (Schove, 1955; Nagovitsyn, 1997; Rigozo et al., 2001; Echer et al., 2004; Rigozo et al., 2011), although the extrapolation based model provides only the periodicities in which the extrapolation is based. Other approaches are based upon measured archival proxies of solar activity such as cosmogenic isotopes of ^{10}Be and ^{14}C concentration provided in an ad-hoc fashion by the inverse relationship between solar activity and sunspot number (Beer et al., 1990; Bard et al., 1997; Usoskin et al., 2003; Solanki et al., 2004a; Damon & Laut, 2004a; Usoskin et al., 2005; Usoskin et al., 2009; Beer et al., 2012; Steinhilber et al., 2012). Radionuclide based models allow for the reconstruction of the activity from decade to multi-millennial time-frames providing a natural correlation with the Sun's variation. In this section are presented the uses of these two approaches for short-term and long-term variation of solar activity records.

6.1 The treatment method of used data series

The reconstruction and prediction of long-term solar activity indicators rely on data such as sunspot numbers, sunspot areas, 10.7 cm solar flux, total solar irradiances, radioisotopes, revised sunspot numbers, ephemeral region flares, coronal mass ejections, geomagnetic activity, cosmic rays, radioisotopes in tree rings and ice cores. The sunspot data has been analysed here as it's the most studied data indicative of the solar activity with four centuries of observations. One of the main purposes is to investigate the nature of the solar activity and to understand the possible link to long-term evolution of solar activity indicators. Thus, among the various methods a precursor is used to predict the amplitude of the following solar

maximum and for its reconstruction. For example the precursor may be any proxy of solar activity or other indicator of solar and interplanetary magnetism. Solar activity indicators are used for time series analysis or the regression method. One or more points are required to identify the trends that can be used to extrapolate the data for prediction of the future. This mathematical method relies on the assumption that the series is homogeneous. For example, cosmogenic radionuclides make realistic candidates for time series analysis. There are good reasons to consider the homogeneity of solar activity data on the scale of the solar cycle, as in dynamo models the solar magnetic fields have an osculation between poloidal and toroidal configuration.

The sunspot data are homogeneous and has long data sets collocated over centuries which represent a more tested method with a time series analysis (Tong, 1990; Wei, 2005; Box et al., 2015). There are also physical models based on the dynamo theory of the Sun (Charbonneau, 2005; Koestler & Dürrenmatt, 2008; Jones et al., 2010). Generally, observational data contain some missing data days. One of the general methods to fill in this missing data is linear interpolation, this can be applied to the treatment of the sunspot data. For example, every P, Q segment will interpolate independently as follows:

$$P(t) = (1 - t)P + tQ, \quad (6.1)$$

where $t \in [0, 1]$, t varies from 0 to 1, we will get the all intermediate points between P and Q , therefore $P(t) = P$ for $t = 0$ and $P(t) = Q$ for $t = 1$. For values of $t < 0$ and $t > 1$ result in extrapolation, where we get point on the line defined by P, Q outside the segment (P, Q) .

6.2 Frequency Analysis

In order to find the properties of solar cycles from the observational data series, we will use the frequency analysis method. Frequency analysis is a numerical method developed by Laskar (1999, 2003), based on refined numerical research of an approximation of the quasi-periodical solution of finite period. If $f(t)$ is a function with complex values, obtained numerically in a finite period $[-T : T]$ the algorithm of frequency analysis consists in the search of the quasi-periodical approximation for $f(t)$ with a finite number of periodic terms:

$$\tilde{f}(t) = \sum_{k=1}^N a_n e^{i\sigma_k t}. \quad (6.2)$$

The frequencies σ_k and complex amplitudes a_k are found with an iterative scheme. The determination of the first frequency σ_1 is obtained by a search of the maximum amplitude of:

$$\phi(\sigma) = \langle f(t), e^{i\sigma t} \rangle, \quad (6.3)$$

where the scalar product $\langle f(t), g(t) \rangle$ is defined by:

$$\langle f(t), g(t) \rangle = \frac{1}{2T} \int_{-T}^T f(t) \bar{g}(t) \chi(t) dt, \quad (6.4)$$

and where $\chi(t)$ is a weighting function, which is a positive function with:

$$\frac{1}{2T} \int_{-T}^T \chi(t) dt = 1. \quad (6.5)$$

If $f(t)$ is a quasi-periodic function:

$$f(t) = \sum_{k=1}^{\infty} \alpha_k e^{i\nu_k t}, \quad (6.6)$$

where α_k are decreasing in amplitude, the approximation of $f(t)$ is $\tilde{f}(t)$ obtained by frequency analysis which is very similar to the original function $f(t)$. This means that the a_k and σ_k are very similar to α_k and ν_k . For regular solutions and when coefficient α_k decreases rapidly, the algorithm provides a very accurate determination of the frequencies of greater amplitude. Using the above described methods such as interpolation, smoothed by average and frequency analysis we studied the periodicity of solar variation which is based on daily, monthly and annual observed activity data. Firstly, some data is interpolated if there is missing observational data. Secondly, some daily and yearly data is smoothed by a chosen average for the purpose of obtaining a corresponding timescales series to be compared with cosmogenic proxies. Thirdly, using frequency analysis the quasi-periodic approximation of the observational data was searched to calculate its mid and long-term reconstructions. Finally, these reconstructed series were then compared with the radio nuclide proxies to verify reliability of the reconstructed series.

6.3 Quasi-periodic search of short and mid-term variation of solar activity indicators

The solar activity numbers present a quasi-periodic (QP) oscillation with variations of short and long periods. Used from observational solar activity this indicates pronounced QP behaviour of both solar change (Gelfreikh et al., 2006; Schmidtke et al., 2006; Komitov et al., 2010; Vieira et al., 2011a; Chowdhury et al., 2016) and proxies of radio isotopes (Usoskin & Mursula, 2004; Tan & Cheng, 2012, 2013). The activity cycle varies in both amplitude and duration. In this section we investigate the QP behaviour of temporal solar activity variation reconstructed on short, mid and long timescales by frequency analysis. The similarity between long-term variations of all these solar activity indicators seems to present some correlation. Thus these series can be taken as evidence for the reliability of the chosen proxies. The main aim here is to analyze the spectral content of the solar activity and its evolution in time using frequency analysis. The quasi-periodic series were then compared with the different smoothed data to verify and to chose the most reliable approach for use in long-term reconstruction series.

6.3.1 Periodicity in sunspot number data

There are two official sunspot and group of sunspot numbers records. These are reported as the International Sunspot Number which is compiled by the Solar Influences Data Analysis Center (WDC-SILSO) at the Royal Observatory of Belgium, Brussels (which has been revised in July of 2015(Clette et al., 2015), and by the US National Oceanic and Atmospheric Administration (NOAA) (for more see Sec.4). In our analyses we used the SILSO data records, and its daily, monthly and yearly variation of sunspot data is displayed in Fig.6.1. Daily total sunspot number estimated with the method as described in Sec. 3.3 with the number of spots and the number of groups counted over the entire solar disk. Monthly means and yearly means

for all years before 1818 were compiled by R. Wolf. Monthly and yearly mean total sunspot number obtained only since 1749. This is based a simple arithmetic mean of the daily total sunspot number over all days of each calendar month and year respectively. Yearly mean total sunspot number are obtained by taking a simple arithmetic mean of the daily total sunspot number over all days of each year. Before 1749, the yearly means were computed on only a fraction of the days in each year because on many days, no observation was available. The SILSO (see for more Sec.4.2.1) data was used as it is the most recently updated and has systematic observational data records from the last four centuries.

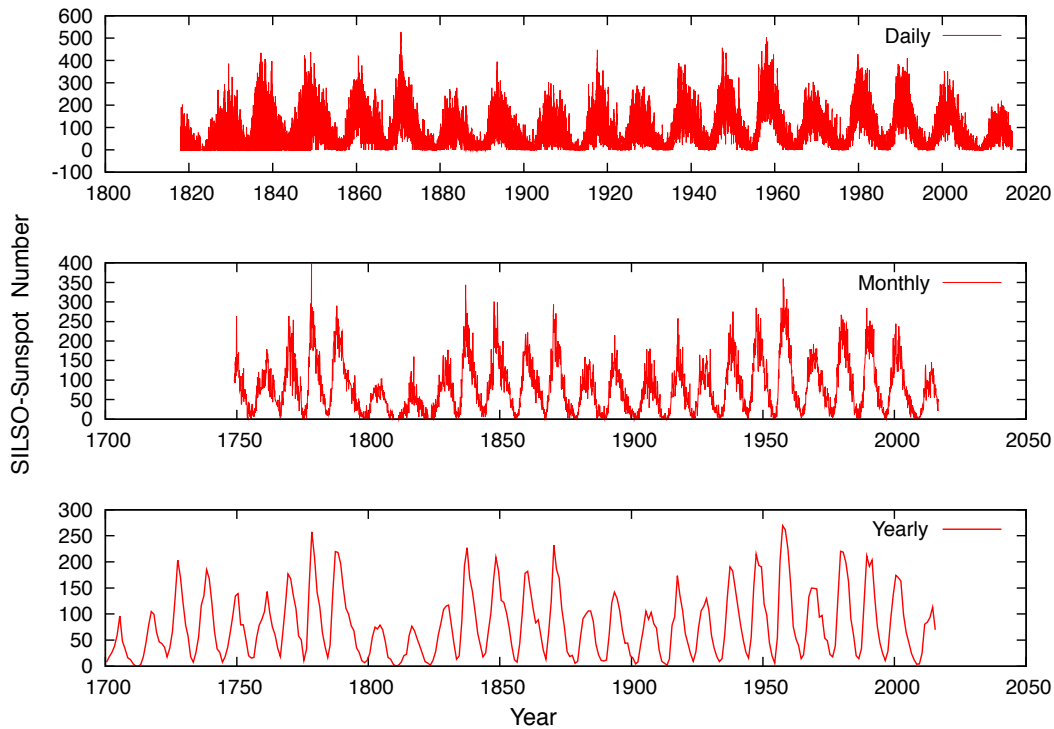


Figure 6.1 – Observational daily (for 1st of January 1818 to 30th of September, 2016), monthly (from January 1749 to September, 2016) and yearly (from 1700 to 2015) sunspot data, recorded by SILSO.

Interpolation of SSN's data. The SILSO observational records have missing data days. In the daily SSN data " - 1 " indicates that no data is available, while by interpolation the missing value can be calculated, which is important for analysis of data e.g. for reconstructions of series. Applying linear interpolation to a sequence of SSN, results in a polygonal line where each straight line segment connects two consecutive SSN's of the sequence. The interpolated curve of SSN using different averages are studied here.

In Fig.6.2 is plotted the original observed SSN containing the missing values of daily sunspot number DSN (in red) and it is interpolated without the missing values of daily sunspot number DSN_{int} (in green). As shown in Fig.6.2 the missing data days marked in red (i.e. " - 1 ") are contained in the period between 1818 – 1850 years. This DSN_{int} interpolated data was used to study its QP approximation series.

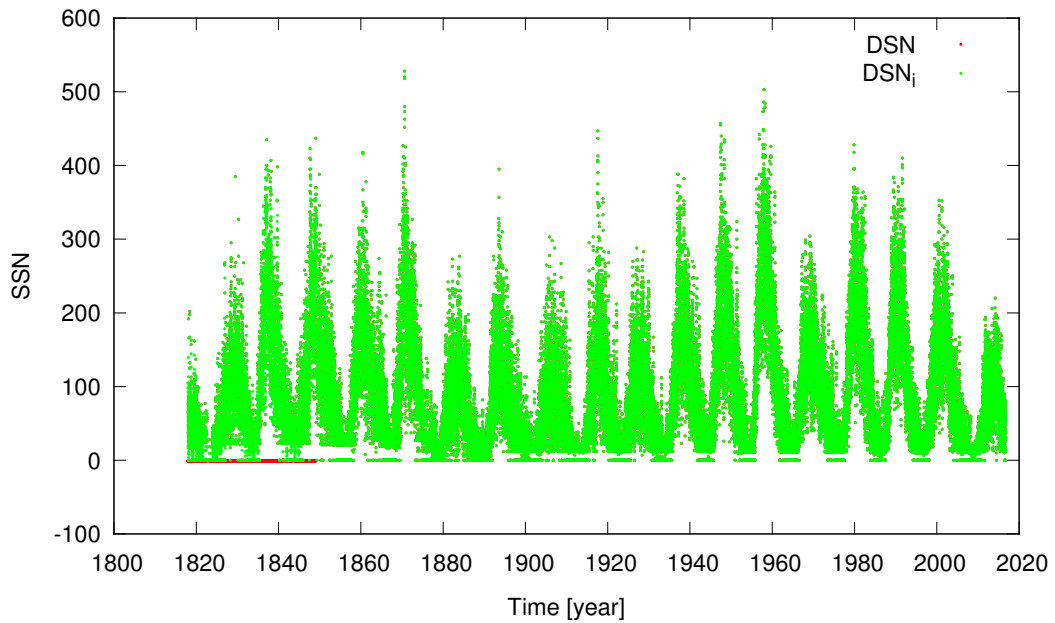


Figure 6.2 – Comparison of the daily observed data of sunspot number (in red) from WDC-SILSO, Royal Observatory of Belgium, Brussels with its interpolated variation (in green). The two series are the same except for missing observational DSN data during 1818 – 1850.

Smooth of SSN's data. To search the main properties in the observational SSNs data records we have used the simplest smoothing algorithm i.e. the "weighted sliding-average smooth" method. This method replaces each day in the data with the averages of DSNi400 and DSNi365 adjacent days, where 400 days and 365 days are the smoothed widths respectively. The threshold between average smoothing of the short-term and longer-term cycles depends

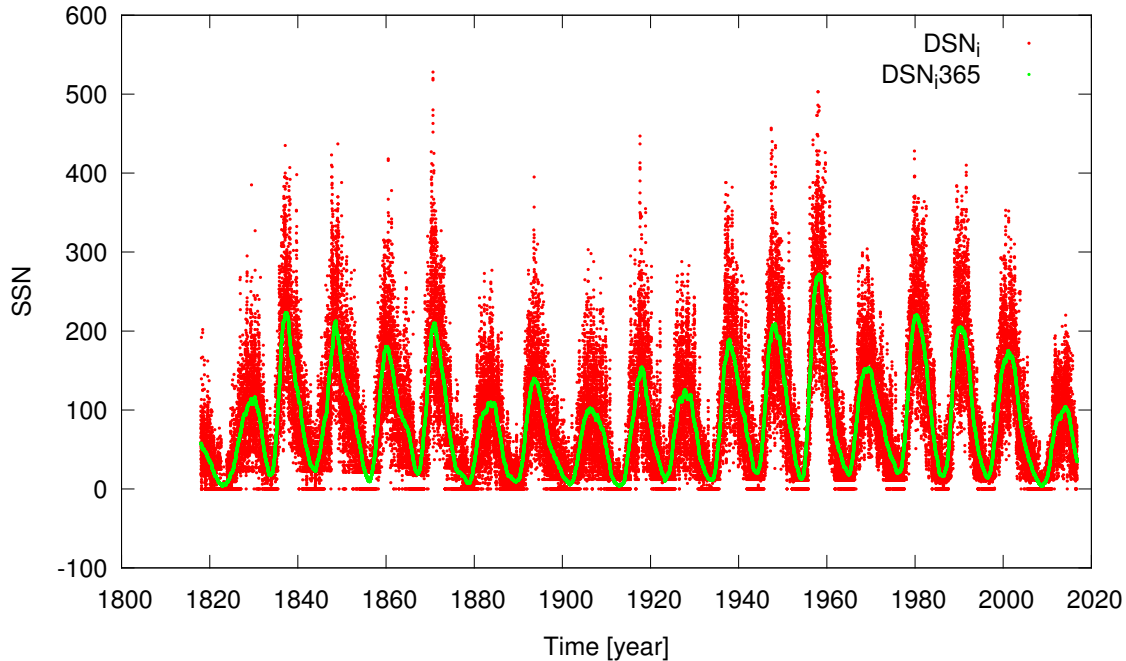


Figure 6.3 – The comparison of the interpolated daily observed DSNi data from the 1st of January 1818 to 30th June 2015 (in green) and its 365 days smoothed series (in blue).

on the applications and parameters of the average smoothing which will be set accordingly. The smoothing of the SSN is to create an approximating function to find important patterns in the SSN data. In Figs.6.3 and 6.4 are presented the SSN data with smoothed widths of 365 days (DSNi365) and 400 days (DSNi400), with its observational SSN's comparisons. After using the average smoothing technique from Fig.6.3 the variation trend of values show some correlation with the observed results. The variation of DSNi are aligned with its mean variations of DSNi365 and DSNi400 curves. One year averaged and interpolated series of SSN data have similarities, except the original SSN's series yield the "-1" missing observational data as shown in Fig.6.2 in red. These DSNi365 and DSNi400 series require a verification before being used as one of the principal data series of reconstruction.

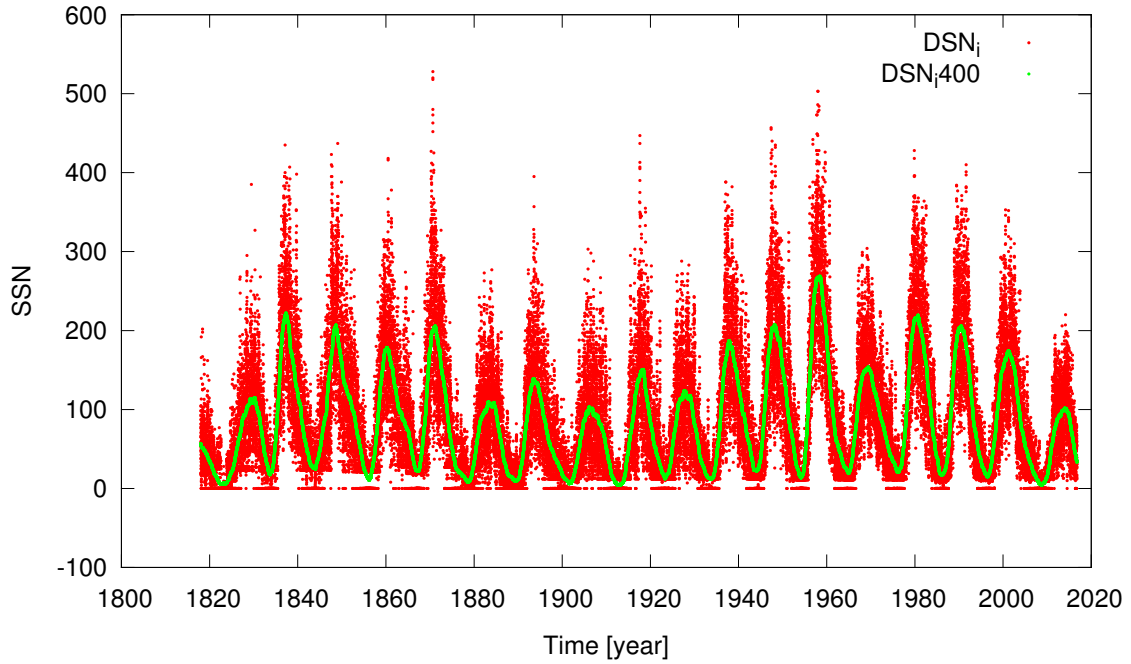


Figure 6.4 – The comparison of the interpolated daily observed DSN_i data from the 1st of January 1818 to 30th June 2015 (in green) and its 400 days smoothed series (in blue).

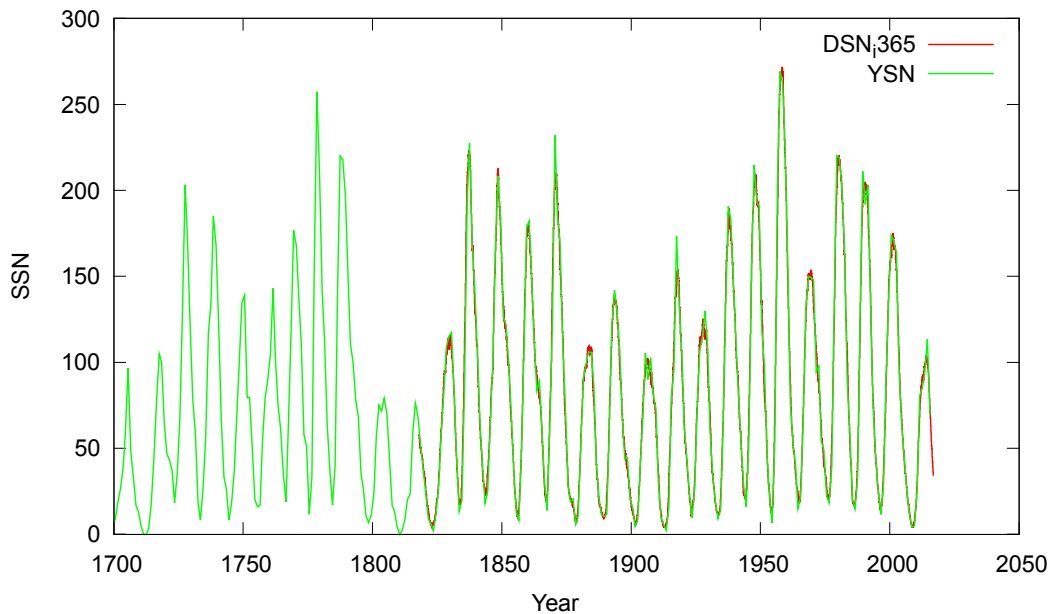


Figure 6.5 – DSN_{i365} is interpolated 365 days smoothed daily sunspot numbers data of WDC-SILSO for the period from the 1st of January 1818 to 30th September 2016 (in red), and YSN is yearly observed WDC-SILSO sunspot numbers data (in green).

Verification of the interpolated and smoothed SSN's series. Before studying the quasi-periodic (QP) approximations of the interpolated and smoothed series of observed SSN's data, it is necessary to verify the reliability and accuracy of these series. For this purpose in

Fig.6.5 are plotted interpolated 365 days smoothed values of daily series with the yearly observed sunspot numbers. This result demonstrates an excellent correlation between the interpolated-smoothed series and observed data which allows us to study its frequency analysis. The frequency components are used to identify and understand variation of SSN's series. Thus DSN_i and DSN_i365 series can now be used to study the QP properties which are based on a long-term reconstruction of solar activity series.

QP approximation of SSN's series. Before estimating the frequency analysis, the interpolated and smoothed series are averaged by reducing mean values to get rid of constants i.e. $DSN_i365 = 84.85$. The QP approximation method described in Sec.6.2 was used for DSN_i365 and DSN_i400 series. In Figs.6.6 and 6.7 are presented the variation of DSN_i365 and DSN_i400 with their QP approximation of QPDSN_i365 and QPDSN_i400 functions, where smoothed weights are 365 and 400 days respectively. From DSN_i365, the main 36 and 20 additional frequencies (by analysis of the series residues) with conjugations are found. In total there are 57 terms including a constant term. From DSN_i400, the main 34 and 40 additional frequencies (by analysis of the series residues) with conjugations are found. In total there are 75 terms including a constant term.

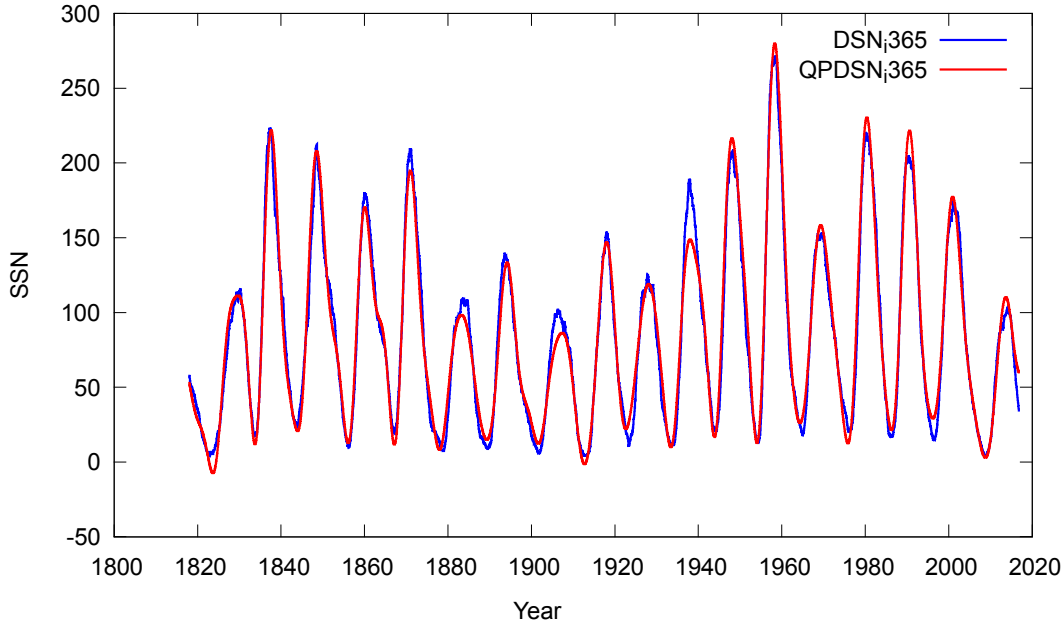


Figure 6.6 – DSN_i365 smoothed daily SSNs of 365 days ahead for the period from the 1st of January 1818 to 30th June 2015 (in blue), SSN from WDC-SILSO, Royal Observatory of Belgium, Brussels, and QPDSN_i365 is its reconstructed quasi-periodic approximate function (in red).

These figures might provide agreement between direct observed and QP variation which allows the use of these QP series for the reconstruction of long timescales. The long-term evolution of the reconstructed series are presented in Sec.6.5.1. The components of the frequency analysis of DSN_i365 and DSN_i400 are presented as the series of $\sum_{k=0}^n \alpha_k \cos(2\pi\nu_k t + \varphi_k)$, where $n = 28$ and 37 for DSN_i365 and DSN_i400 respectively. The frequency decomposition of QPDSN_i365 and QPDSN_i400 are presented in Tab.6.1 and 6.2. The maximum absolute and relative errors of QPDSN_i365 according to DSN_i365 are 0.000560 and $3.253349 - 10^{-5}$ re-

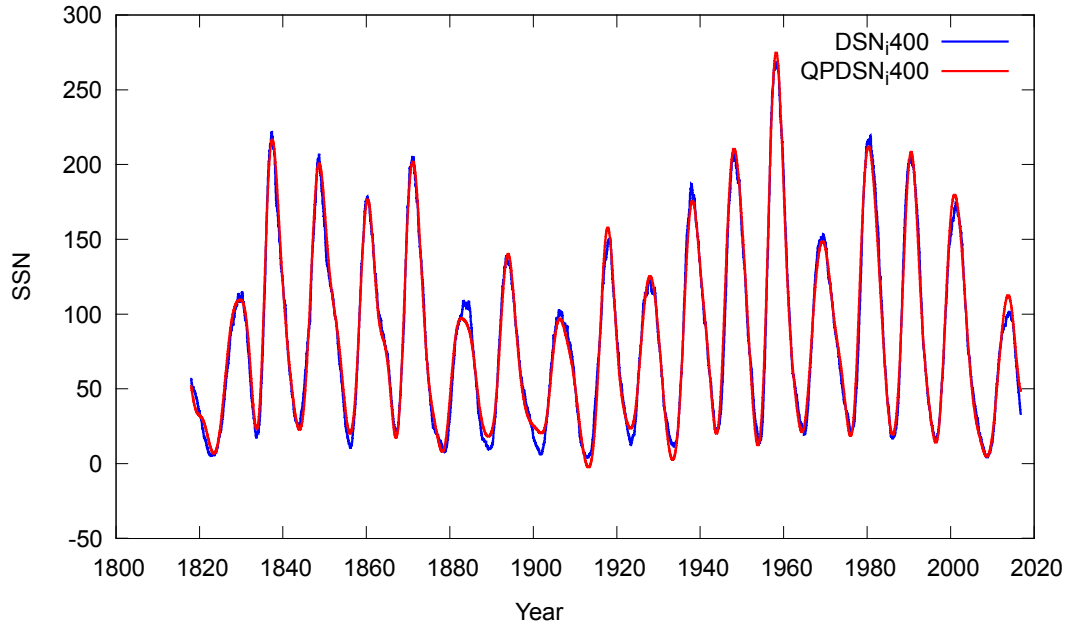


Figure 6.7 – DSNi400 is smoothed daily SSNs of 400 days ahead for the period from the 1st of January 1818 to 30th June 2015 (in blue), SSN from WDC-SILSO, Royal Observatory of Belgium, Brussels, and QPDSNi400 is its quasi periodic reconstructed function (in red).

spectively, with a 0.003253% percentage error margin. The frequencies in the two tables show similar values, which signify that small differences in the frequencies permit us to select more smoothed (less noisy) values to better predict the mid and long-term solar cycles. Also this similarity in the different smoothed series shows the accuracy of the used QP approximation. We note that some characteristic frequencies in solar cycles have appeared in the QP analysis. According to the identified cycles in Tab.6.1 and Tab.6.2, the periods of $\sim 4 - 8$ years are known as due to northern and southern hemispheres cycles (Zolotova et al., 2010). The tidal forces of the planets moving towards the Sun may be affected by the gravitational attraction of the planets. In this case it could explain why the orbiting periods of the inner planets may be also detectable in the solar activity periods. The periods are significant at the confidence average values of 8.5 – 10.5 year period which are associated with solar cycles. It has been shown that the solar cycle lengths are known to vary between 9 – 13 years (Hoyt & Schatten, 1998). The first dominant period of 10.89 years corresponds to the well known solar activity cycle of an 11 year period. The ~ 22 year period is the well known reversal magnetic, Hale cycle. The defined mean period of 29.84 – 37.87 years is also mentioned as is the average mean period of 31.1 years which is identified in sunspot number by spectral analysis (Clúa de Gonzalez et al., 1993). There is an assumption that 31 years is the solar origin of the 35 years Bruckner climatic periodicity (Raspopov et al., 2000). Finally, the periods of 84 and 108 years represent the Gleiberg cycle (Gleissberg, 1967a) and the identified period of 282 year known as Sues cycle (Schove, 1983d). These main recognized periods are used for the long-term timescale reconstruction of the proxy series and would confirm the reliability of the used QP approximation based on a frequency analysis method.

Table 6.1 – Frequency analysis of SILSO daily observed SSN data with one year smoothed series of S365 over 197 years (for more see Sec.6.3). The 29 terms of the quasi-periodic frequencies are presented. The mean value is 84.85. The columns show 1: The frequency number, 2: The frequency, 3: The period, 4: Modulus of the amplitude, 5: The phase.

k	$\nu_{\mathbf{k}}$ [rad/yr]	P [yr]	$\alpha_{\mathbf{k}}$	$\varphi_{\mathbf{k}}$ [°]
0	0.000000	inf	84.851	0.000
1	0.576883	10.891614	62.155	47.573
2	0.617123	10.181422	30.686	-158.410
3	0.057724	108.849092	27.318	-9.525
4	0.523230	12.008461	21.947	44.410
5	0.645748	9.730094	13.892	-119.545
6	0.786874	7.984992	13.120	-65.665
7	0.022288	281.902883	13.099	-23.278
8	0.340790	18.437144	11.122	-145.614
9	0.210584	29.836969	10.855	153.289
10	0.165909	37.871344	10.667	143.435
11	1.148589	5.470352	9.682	27.748
12	0.294001	21.371292	9.471	128.423
13	0.570881	11.006113	9.098	-143.576
14	0.698263	8.998314	8.508	-125.153
15	0.133448	47.083571	8.487	-120.514
16	0.739481	8.496754	7.871	-119.966
17	0.456895	13.751933	7.380	173.164
18	0.496337	12.659108	6.838	28.423
19	1.099349	5.715372	6.584	-130.914
20	1.072467	5.858627	6.369	-148.836
21	0.229498	27.377897	5.621	-28.423
22	0.343980	18.266132	5.527	22.203
23	1.203258	5.221809	5.147	8.142
24	0.081284	77.298962	3.991	29.890
25	1.308686	4.801142	3.890	164.560
26	0.877384	7.161269	3.705	-167.024
27	0.935822	6.714080	3.678	99.729
28	0.420026	14.959022	3.035	91.006

6.3. QUASI-PERIODIC SEARCH OF SHORT AND MID-TERM VARIATION OF SOLAR ACTIVITY INDICATORS

Table 6.2 – Frequency analysis of SILSO daily observed SSN data with 400 days smoothed series S400 over 197 years (for more see Sec.6.3). The 38 terms of the quasi-periodic frequencies are presented. The mean value is 84.84. The columns show 1: The frequency number, 2: The frequency, 3: The period, 4: Modulus of the amplitude, 5: The phase.

k	$\nu_{\mathbf{k}}$ [rad/yr]	P [yr]	$\alpha_{\mathbf{k}}$	$\varphi_{\mathbf{k}}$ [°]
0	0.000000	inf	84.842	0.000
1	0.576877	10.891729	61.569	48.237
2	0.617074	10.182226	30.967	-155.428
3	0.057726	108.845362	26.624	-12.461
4	0.523251	12.007965	18.756	35.409
5	0.645724	9.730444	13.699	-116.456
6	0.022297	281.798677	13.610	-21.357
7	0.787193	7.981757	12.659	-98.761
8	0.165901	37.873081	10.184	142.195
9	0.293368	21.417427	10.173	-163.937
10	0.698265	8.998287	9.692	-115.357
11	0.210578	29.837822	9.304	152.267
12	0.571241	10.999184	8.984	-178.301
13	0.132968	47.253354	8.346	-67.331
14	1.101884	5.702220	7.987	-47.950
15	0.455694	13.788153	7.913	-52.328
16	0.340751	18.439223	7.551	-127.204
17	0.739671	8.494563	6.739	-137.227
18	0.228548	27.491766	6.344	73.220
19	1.148929	5.468730	6.036	-14.607
20	0.493380	12.734970	5.916	-3.084
21	1.072655	5.857604	5.845	-166.346
22	1.203037	5.222771	5.424	24.326
23	0.076749	81.866821	4.748	161.490
24	0.531015	11.832401	4.640	-33.229
25	0.421150	14.919117	4.525	-28.866
26	0.666632	9.425272	4.147	153.475
27	0.878026	7.156037	4.047	121.032
28	1.307999	4.803664	3.798	-117.949
29	0.020271	309.956538	3.770	37.808
30	0.377356	16.650547	3.747	-152.856
31	0.708886	8.863468	3.695	65.898
32	0.935055	6.719586	3.500	-171.495
33	0.608069	10.333021	3.088	-121.617
34	1.236818	5.080122	2.965	-155.181
35	0.172150	36.498334	2.829	-68.275
36	1.546557	4.062692	2.805	-10.987
37	0.987011	6.365874	2.675	-120.297

Table 6.3 – Frequency analysis of SILSO yearly observed mean SSN over 316 years (for more see Sec.6.3). The 45 terms of the quasi-periodic frequencies are presented including the constant term. The mean value is 79.50. The columns show 1: The frequency number, 2: The frequency, 3: The period, 4: Modulus of the amplitude, 5: The phase.

k	$\nu_{\mathbf{k}}$ [rad/yr]	P [yr]	$\alpha_{\mathbf{k}}$	$\varphi_{\mathbf{k}}$ [°]
0	0.000000	inf	79.503	0.000
1	0.570882	11.006108	54.788	-4.927
2	0.629896	9.974958	30.344	-142.570
3	0.593993	10.577878	29.692	-73.611
4	0.062801	100.048976	29.609	142.546
5	0.533760	11.771548	24.717	-21.230
6	0.093406	67.267628	17.062	168.925
7	0.118421	53.057857	16.704	127.385
8	0.742953	8.457046	14.801	-130.280
9	0.482578	13.020045	13.218	170.302
10	0.771098	8.148357	13.056	-118.774
11	0.670792	9.366819	11.503	16.636
12	1.147676	5.474704	10.096	126.987
13	0.143001	43.937933	9.730	172.936
14	0.291435	21.559457	9.670	28.003
15	0.040271	156.021540	9.295	159.974
16	0.423511	14.835929	9.010	151.784
17	0.607382	10.344703	8.733	127.870
18	0.716976	8.763459	8.717	-13.473
19	0.224776	27.953157	8.296	58.724
20	0.018453	340.498012	7.404	80.696
21	0.837697	7.500542	7.271	-62.447
22	0.459324	13.679198	7.165	-10.186
23	0.578182	10.867142	6.476	154.564
24	0.369142	17.021034	6.279	6.418
25	0.499309	12.583768	6.139	-4.559
26	1.095178	5.737137	5.664	-39.539
27	1.197597	5.246492	5.557	-90.628
28	0.879946	7.140420	5.501	-101.827
29	1.222758	5.138533	5.359	-30.221
30	0.401953	15.631659	5.075	-161.511
31	1.063848	5.906093	4.919	69.391
32	1.302077	4.825508	4.588	159.136
33	1.458925	4.306724	4.506	-0.664
34	0.820016	7.662271	4.506	-89.321
35	0.254274	24.710335	4.364	-155.372
36	1.368325	4.591879	4.243	-77.976
37	0.782161	8.033106	3.842	61.019
38	0.536115	11.719843	3.707	42.534
39	1.728665	3.634703	3.616	168.925
40	1.036805	6.060141	3.503	28.327
41	0.927226	6.776325	3.154	-46.383
42	0.334086	18.807077	2.950	-112.615
43	1.158181	5.425048	2.388	-25.651
44	1.340260	4.688034	2.027	-161.727

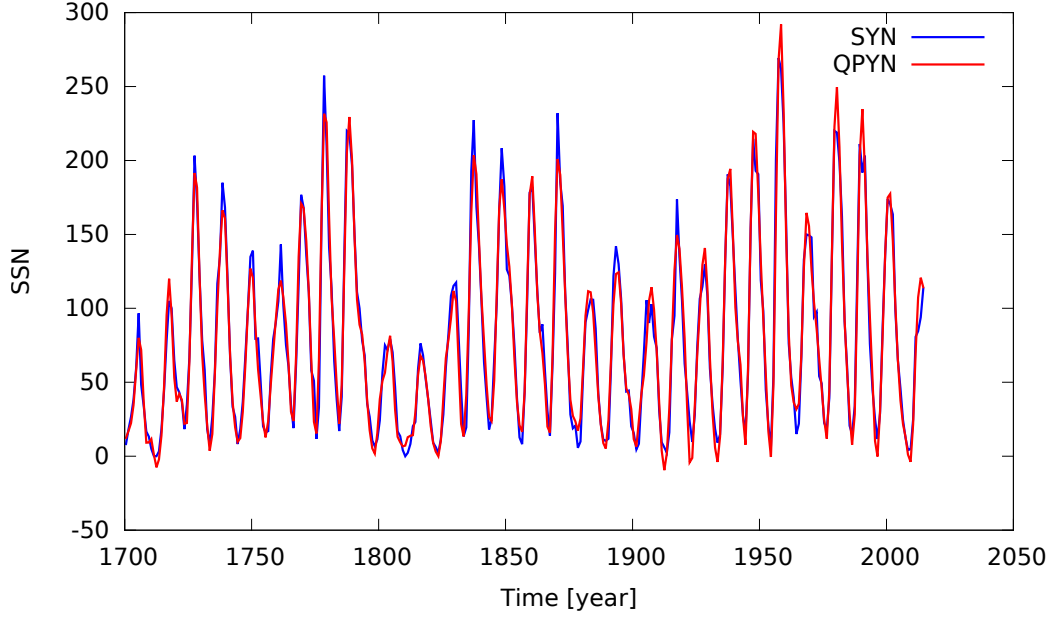


Figure 6.8 – YSN yearly observed SSN's series with its QPYN calculated quasi-periodic approximation for the period of 1700 to 2016.

In Fig.6.8 is displayed the yearly observed data with its QP approximation series. The yearly observed sunspot series between 1700 – 2016 years are determined with a total of 83 terms containing the main 45 and 38 additional periodicities. The frequency analysis is shown in Tab.6.3. It should be noted that apart from the well known periodicities (e.g. $\sim 11, \sim 22$ years etc.), the short periods i.e. from 5 – 9 years seem to be caused by the main lunar tidal cycle according to (Scafetta, 2014a), then the periodicity of 9.93 – 11.86 years represents solar cycle harmonics. The 50 – 60 and 90 – 100 year periods have been argued in (Ogurtsov et al., 2002, 2015) and is known as the Even-Odd effect cycle. While the 100 – 156 year periodicity is known from the ^{10}Be and ^{14}C cosmogenic records (Scafetta, 2014a) and the 150 – 280 years of period (Schöve, 1983d) is de Vries/Suess cycle, while the ~ 350 year unnamed cycle has been mentioned by Steinhilber et al. (2012b).

Due to their excellent coherence the QPDSN_{i365} and QPYN series were used for reconstruction of the solar activity proxies. It should be noted that the above assumptions were made to identify the determined periods, which requires verification. However, identification of the main dominated periods are important for our studies. The presented QP variations determined the frequencies of the observed data series. A detailed analysis of the above properties of the smoothed and QP approximations of direct observed SSN data can provide an accurately reconstructed series of solar activity evolution.

6.3.2 Periodicity in Group Sunspot Number Data

Solar activity reconstructions have been made, based on terrestrial cosmogenic isotope data for the interval covering millennium and multi-millennium timescales which differ from each other to some degree. Recently the sunspot group number (GSN) from various sources has been updated. Reconstruction of the group number is based on the backbone method (Svalgaard & Schatten, 2016) (herein, L15, yearly estimated GSN's, 1610.5 – 2015.5), and the new sunspot group number composite derived in (Usoskin et al., 2016c) (herein, U16, yearly GSN's, 1779.5 – 1995.5), a new revised collection of sunspot group numbers in (Vaquero et al., 2016) (herein, V16d daily and V16 yearly observed GSN's, 1610 – 2010), the sunspot group in (Cliver & Ling, 2016) (herein, C15, yearly GSN's, 1845.5 – 1976), the sunspot group number in (Hoyt & Schatten, 1998) (herein, H98d daily and H98 yearly estimated GSN, 1610 – 1995 years). Reliable reconstruction of activity data requires an accurate observed data series. For this purpose we show the variation of activity records together with the approximate values for verification of accuracy.

Interpretation of GSN's data. The daily estimated data of V16d during the period of 1610 – 2010 and H98d during the period of 1610 – 1995 are different as shown in Fig.6.9 until 1800. The observed GSN data before 1800 recorded more "– 1" for missing or "0" with no GSN uncertainty values, and after 1800 the data is more reliable with less missing values. The maximum value of the GSN's of V16d is 58, and for H98d is 26.41, while the variation

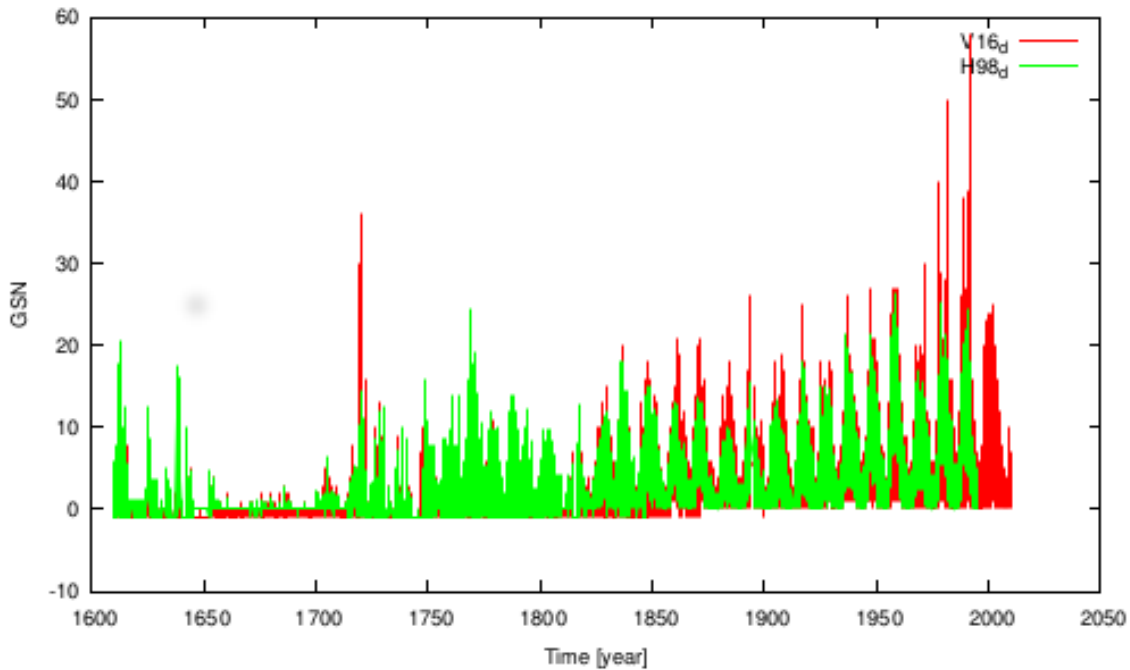


Figure 6.9 – Comparison of the daily estimated records of group sunspot numbers. H98 and V16 are (Hoyt & Schatten, 1998) and (Vaquero et al., 2016) data sets respectively.

of their amplitudes correspond to the maximum and minimum of the solar cycles. The daily data record contains many missing days and is quite different from each other that is why it is not convenient to fill the missing days with interpolation (see Figs. 6.10 and 6.11). Their interpolated comparison are shown in Fig.6.12. Finally, we used the mean yearly estimated GSN's data, as recently these data series has been updated and rerecorded by many authors.

6.3. QUASI-PERIODIC SEARCH OF SHORT AND MID-TERM VARIATION OF SOLAR ACTIVITY INDICATORS

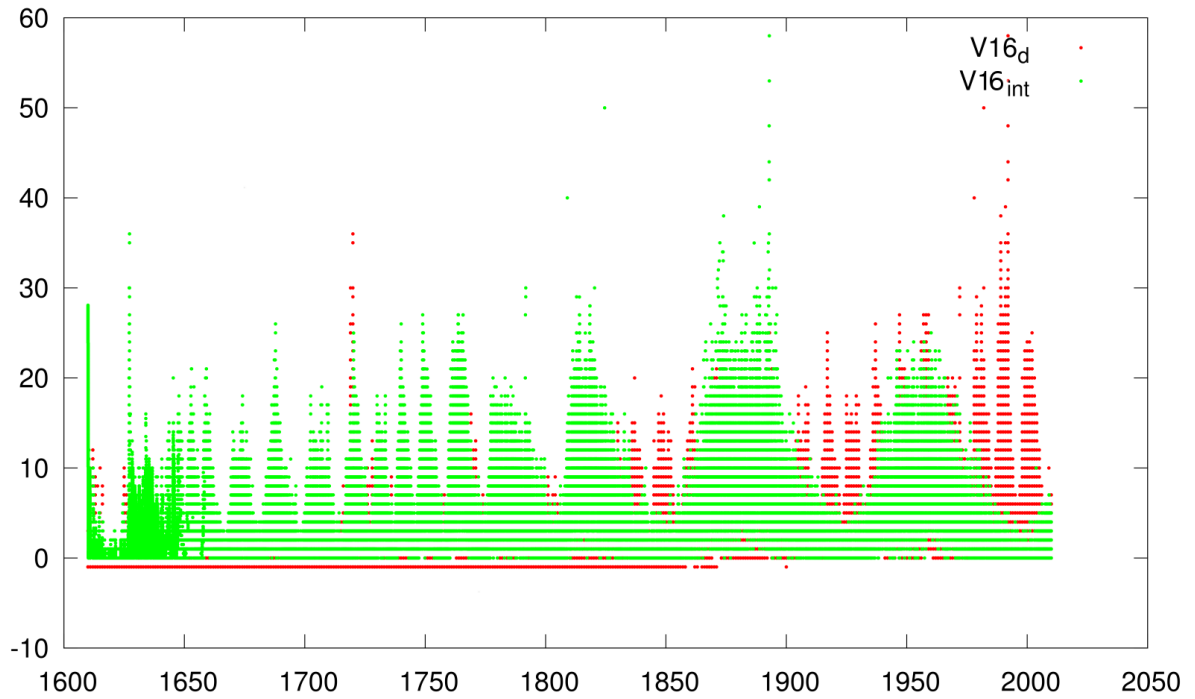


Figure 6.10 – Comparison of the daily estimated records of group sunspot number of V16_d from Vaquero et al. (2016) with its interpolation variation of V16_{int}.

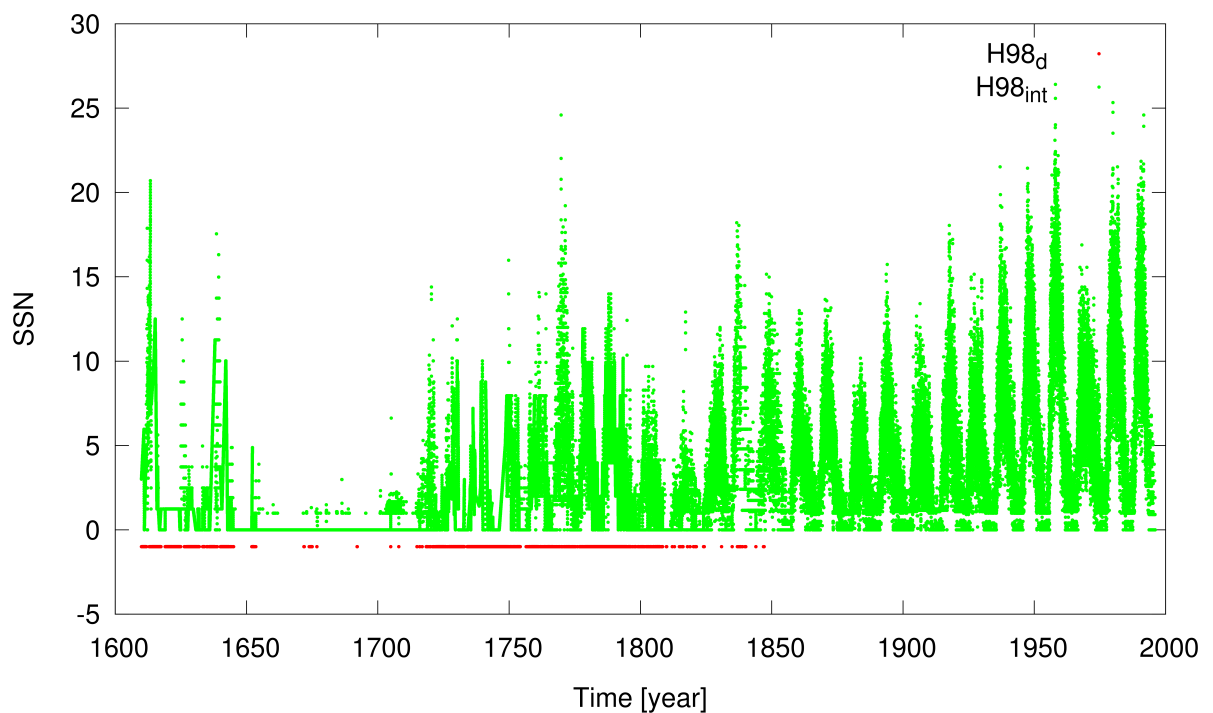


Figure 6.11 – Comparison of the daily estimated records of group sunspot number of H98_d from Hoyt & Schatten (1998) with its interpolation variation of H98_{int}.

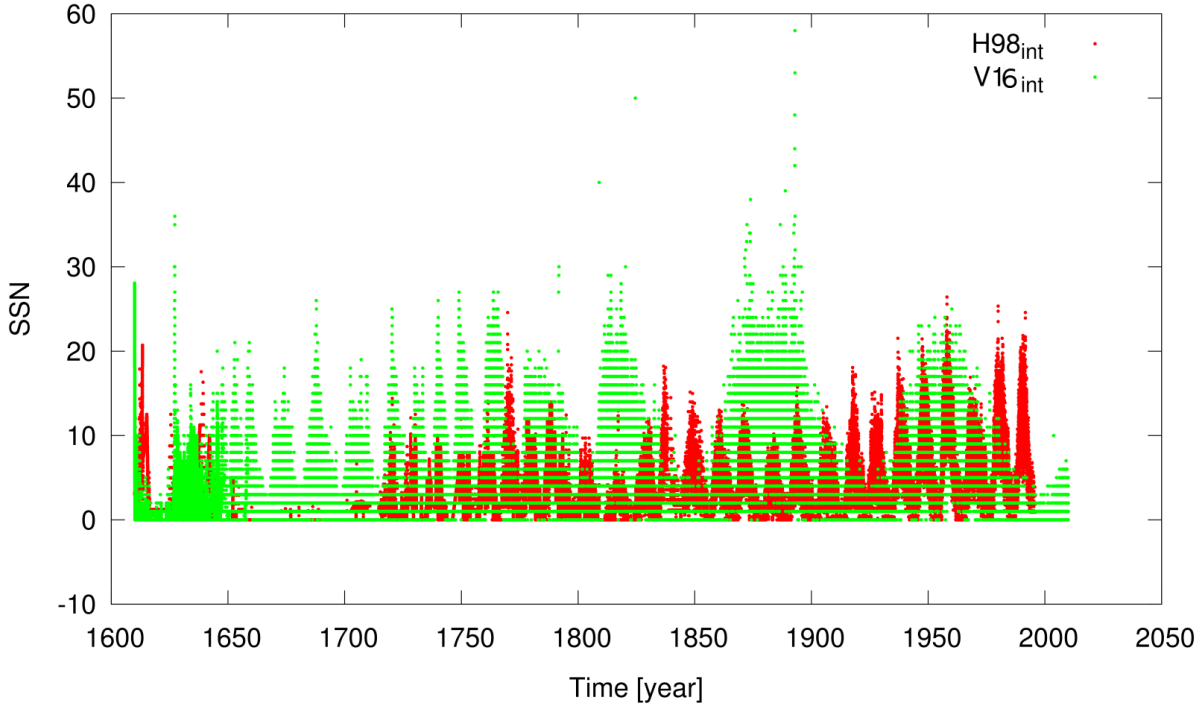


Figure 6.12 – Comparison of the interpolated daily records of group sunspot number of $H98_{int}$ from Hoyt & Schatten (1998) and $V16_{int}$ from Vaquero et al. (2016) with their interpolation variation.

Comparison of different GSN. The different estimated GSN data are plotted in Fig.6.13 for the purpose of choosing more accurate GSN's data. H98s and V16s are the yearly smoothed GSN's daily observed data, while the others (U16, L16, C16, H98) are in mean yearly estimated records. The updated observational sunspot number and group data are from different sources such as in (Clette et al., 2015; Usoskin et al., 2016c; Svalgaard & Schatten, 2016) and from the data center of WDC-SILSO.

In Fig.6.13, H98s and V16s show two little mini cones (peaks) during 1783 and 1792, while the known 4th solar cycle started in 1784 and finished in 1798, which is recognized in other records of GSN's (U16, L16, C16, H98). All of the GSNs records are well matched after 1800, but not before this time during periods of less sunspots (absence of sunspots). The Maunder (1645~1715) minimum in the L16 estimation presents the existence of quite high levels of sunspots and this is also supported by (Carrasco et al., 2015; Zolotova & Ponyavin, 2016; Neuhäuser & Neuhäuser, 2016) on the revision of ancient reports. The reports of Derham, Flamsteed, Hevelius, Picard, G.D. Cassini, and Fogel had mentioned the absence of sunspots with great significance. Usoskin et al. (2015) argued that the high level of solar activity during the Maunder minimum would have a low confidence level.

Smooth and QP approximation of GSN. The one year smoothed daily observed H98di data versus its QP approximation QPH98di is displayed in Fig.6.14 and its frequency components have 70 total terms with conjugations of 28 main, 41 additional and a constant term. In Tab.6.4 are presented the full frequency set of QPH98di as the series of $\sum_{k=0}^n \alpha_k \cos(2\pi\nu_k t + \varphi_k)$. Fig.6.14 shows that the QP approximation series QPH98di have close similarity on comparison with the original H98di data, which allows us to use the data in further research.

6.3. QUASI-PERIODIC SEARCH OF SHORT AND MID-TERM VARIATION OF SOLAR ACTIVITY INDICATORS

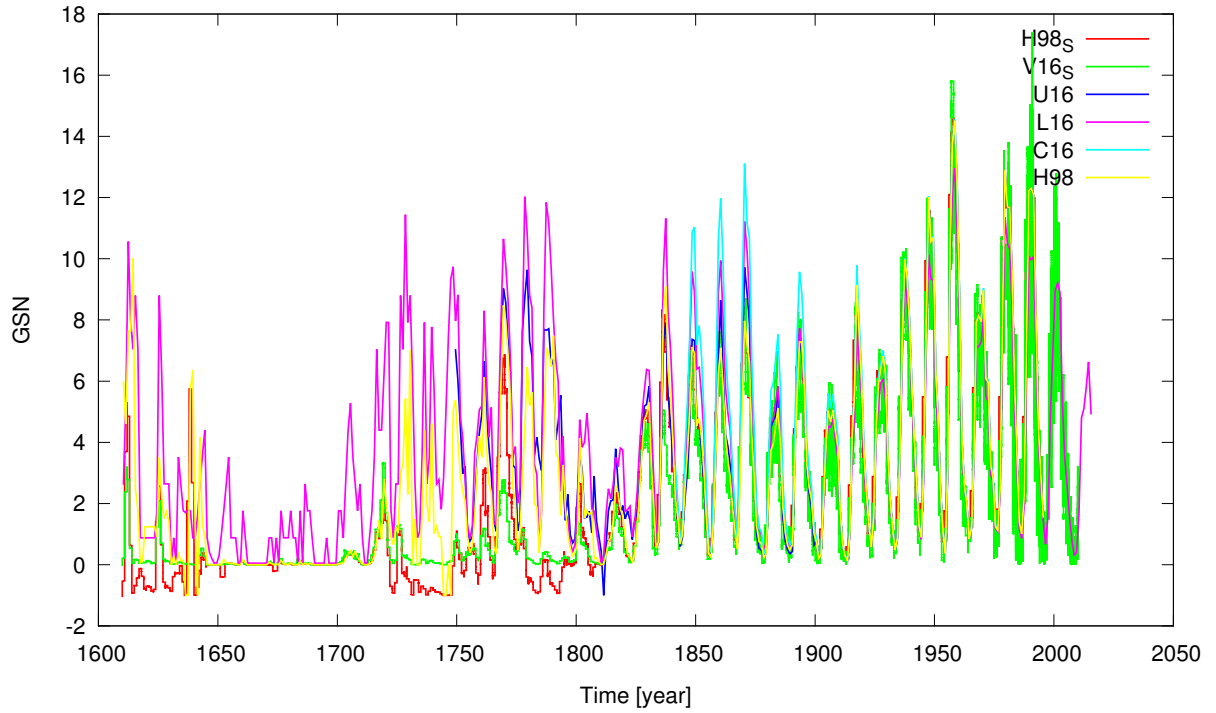


Figure 6.13 – Different estimated group sunspot numbers (GSN) variation. H98s and V16s are one year smoothed daily estimations of GSN, while U16, L16, C16 and H98 are yearly estimated GSN's.

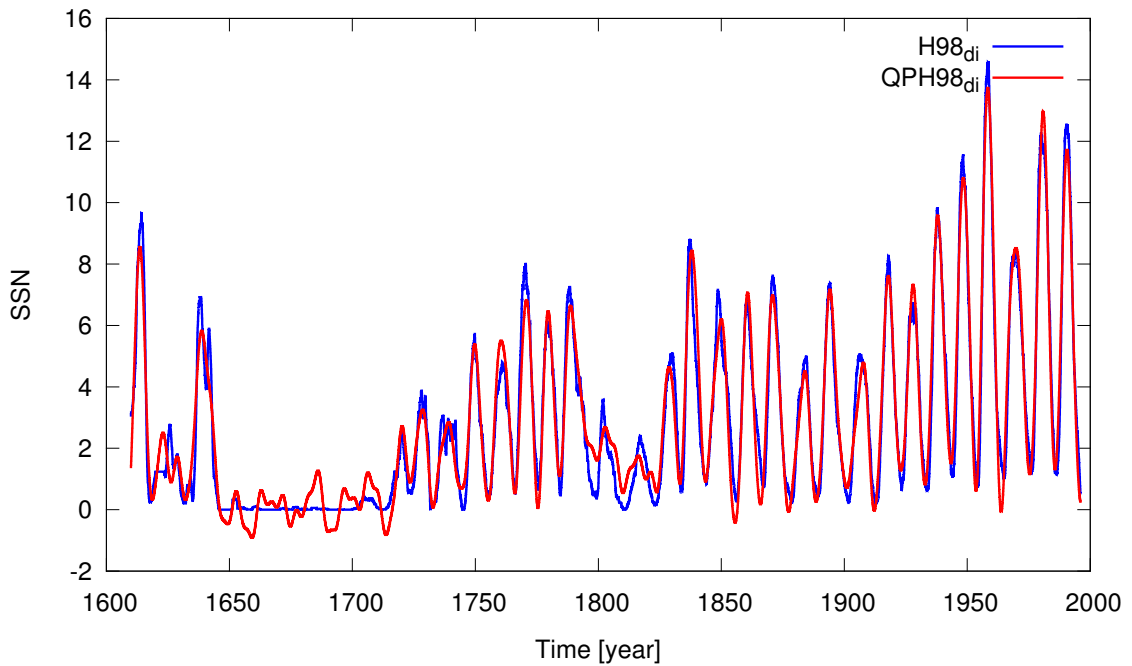


Figure 6.14 – H98di is an one year smoothed daily observed GSN's series with its QPH98di quasi-periodic approximation for the period of the 1610 to 1995.

Table 6.4 – Frequency components of one year smoothed daily observed GSN of H98di (Hoyt & Schatten, 1998). The 36 terms of the quasi-periodic frequencies have a mean value of 2.886. The columns show 1: The frequency number, 2: The frequency, 3: The period, 4: Modulus of the amplitude, 5: The phase.

k	ν_k [rad/yr]	P [yr]	α_k	φ_k [°]
0	0.000000	inf	2.886	0.000
1	0.011177	562.158595	2.615	178.112
2	0.567649	11.068791	1.602	-14.960
3	0.580257	10.828273	1.320	17.278
4	0.632373	9.935885	1.134	-56.019
5	0.032973	190.554376	1.118	-131.407
6	0.598443	10.499216	1.085	148.815
7	0.011303	555.904405	0.938	-16.378
8	0.536633	11.708529	0.788	4.316
9	0.053402	117.658620	0.631	67.162
10	0.075587	83.124706	0.577	-117.320
11	0.517755	12.135430	0.538	-84.853
12	0.292892	21.452262	0.490	-136.166
13	0.220454	28.501178	0.455	165.336
14	0.616179	10.197018	0.452	-85.430
15	0.568332	11.055488	0.451	-1.511
16	0.124671	50.398036	0.450	-169.417
17	0.770417	8.155560	0.418	-37.327
18	0.100711	62.388306	0.414	169.897
19	0.672942	9.336894	0.393	146.675
20	0.162743	38.607906	0.379	176.149
21	0.783194	8.022516	0.364	-27.294
22	0.746202	8.420220	0.353	-103.448
23	0.713724	8.803381	0.337	-41.240
24	0.470635	13.350454	0.320	27.703
25	0.199903	31.431246	0.282	-80.197
26	0.000000	inf	0.279	-0.289
27	0.249820	25.150874	0.272	-72.163
28	0.277368	22.652868	0.262	-134.686
29	0.453543	13.853559	0.244	-148.233
30	0.873408	7.193869	0.233	-114.262
31	0.419219	14.987822	0.232	-171.233
32	0.375557	16.730310	0.230	34.919
33	0.841795	7.464036	0.226	-137.536
34	1.301945	4.826001	0.202	-173.057
35	0.031801	197.575781	0.196	82.937

In Figs.6.15,6.16, 6.17 and 6.18 are shown a comparison of QP properties of observed group sunspot data yielding variation with their observed series. The frequency analysis of U16 GSN's data is defined (with conjugations) 10 main and 34 additional terms (see Tab.6.5). For C16 are defined (also with conjugations) 37 total terms with 10 main, 25 additional terms including the constant term (see Tab.6.6). For L16 are defined 6 main and 24 additional terms including the constant term (see Tab.6.7). Finally for the yearly observed record of H98 are defined 10 main, 90 additional terms with conjugations. The real part of the H98 GSN's series frequency components as function of $\sum_{k=0}^n \alpha_k \cos(2\pi\nu_k t + \varphi_k)$ are presented in Tab.6.8.

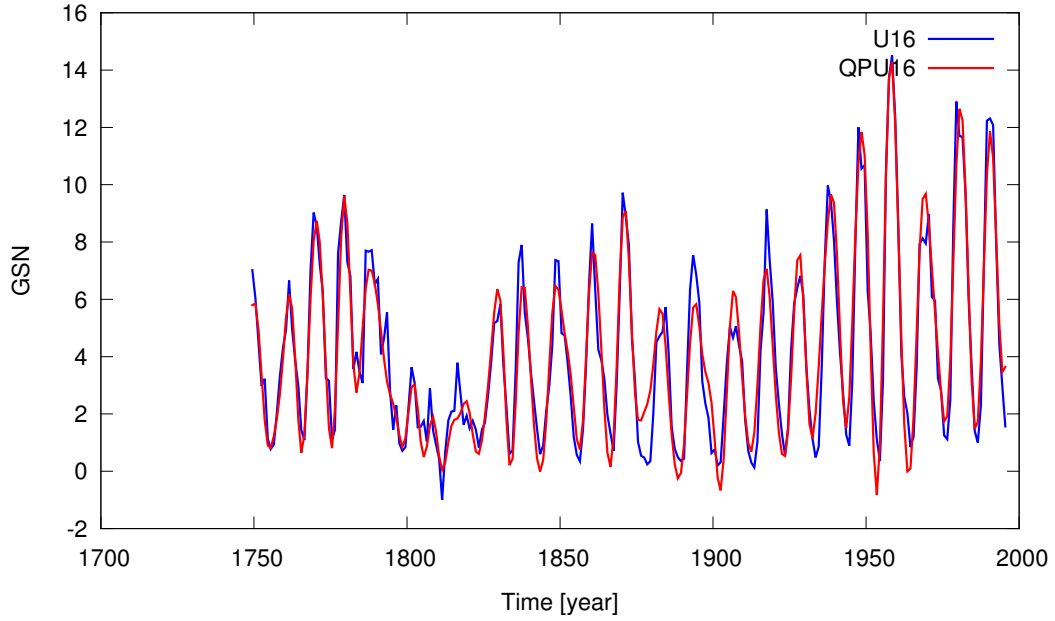


Figure 6.15 – U16 is a yearly observed GSN’s series with its QPU calculated quasi-periodic approximation for the period of the 1st of January 1750 to 30th June 2015.

Table 6.5 – Frequency analysis of the yearly mean estimated GSN of U16 (Usoskin et al., 2016c), representing the 23 terms of the quasi-periodic frequencies. The columns show 1: The frequency number, 2: The frequency, 3: The period, 4: Modulus of the amplitude, 5: The phase.

k	ν_k [rad/yr]	P [yr]	α_k	φ_k [°]
0	0.000000	inf	4.154	0.000
1	0.569807	11.026864	2.283	101.294
2	0.629943	9.974210	1.788	-158.225
3	0.594816	10.563249	1.333	-156.531
4	0.062368	100.744098	1.324	170.924
5	0.018090	347.335966	1.247	95.713
6	0.522669	12.021356	1.169	77.449
7	0.044540	141.066857	0.683	64.776
8	0.151407	41.498769	0.634	-2.234
9	0.744061	8.444451	0.634	111.609
10	0.775884	8.098098	0.624	83.395
11	0.088608	70.909744	0.588	-42.523
12	0.294922	21.304568	0.545	28.996
13	0.117712	53.377633	0.539	-128.011
14	0.835202	7.522952	0.524	-155.267
15	0.620524	10.125614	0.483	-108.321
16	1.097661	5.724157	0.447	39.431
17	0.670854	9.365954	0.416	22.358
18	0.490491	12.810002	0.383	25.977
19	0.405647	15.489288	0.368	-134.898
20	0.802737	7.827203	0.345	-21.725
21	0.511184	12.291436	0.296	24.652
22	0.895893	7.013320	0.285	54.399

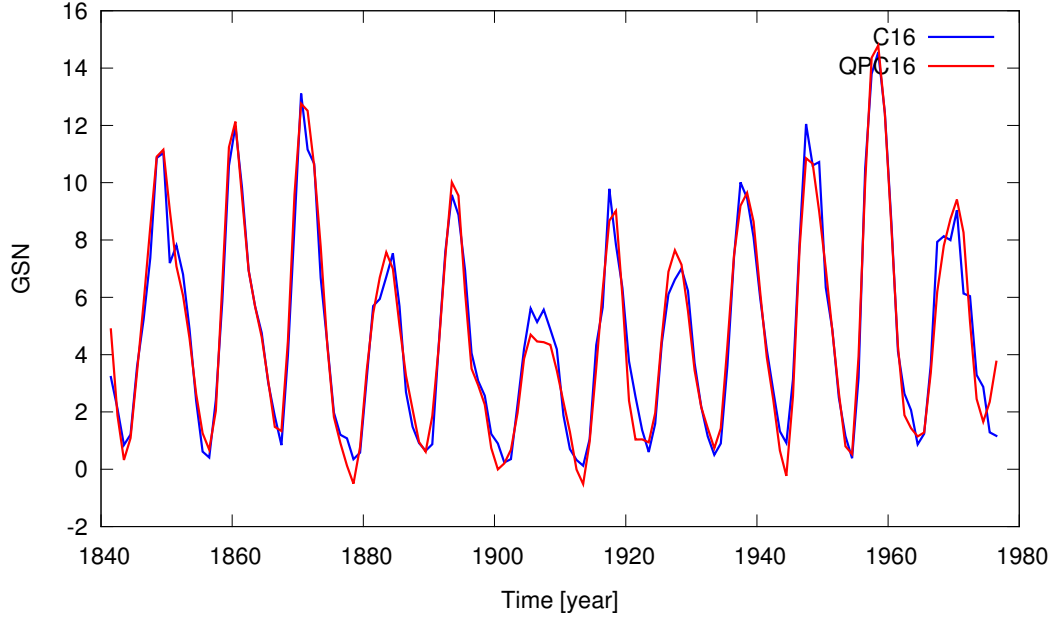


Figure 6.16 – C16 is the yearly observed GSN’s and its QPC16 calculated quasi-periodic approximation for the period of 1841 to 1976.

Table 6.6 – Frequency analysis of observed yearly GSN of C16 (Cliver & Ling, 2016). The 19 terms of the quasi-periodic frequencies have a mean value of 4.836. The columns show 1: The frequency number, 2: The frequency, 3: The period, 4: Modulus of the amplitude, 5: The phase.

k	$\nu_k[\text{rad/yr}]$	$P[\text{yr}]$	α_k	$\varphi_k[^\circ]$
0	0.000000	inf	4.836	0.000
1	0.574078	10.944821	3.742	-23.724
2	0.634799	9.897908	1.624	49.711
3	0.059878	104.932288	1.561	117.890
4	0.516716	12.159838	1.455	25.346
5	0.677114	9.279365	0.824	20.460
6	0.790221	7.951178	0.823	-67.450
7	0.283473	22.165007	0.806	-132.229
8	0.217144	28.935628	0.672	-167.726
9	1.083186	5.800652	0.640	159.363
10	1.287464	4.880279	0.500	-20.755
11	1.136424	5.528909	0.462	-130.908
12	0.362156	17.349403	0.445	52.600
13	0.957053	6.565139	0.388	-74.191
14	0.000000	inf	0.346	179.595
15	1.807104	3.476937	0.304	50.954
16	1.235415	5.085889	0.258	57.194
17	1.519792	4.134239	0.222	-19.652
18	0.425699	14.759700	0.175	-138.689

6.3. QUASI-PERIODIC SEARCH OF SHORT AND MID-TERM VARIATION OF SOLAR ACTIVITY INDICATORS

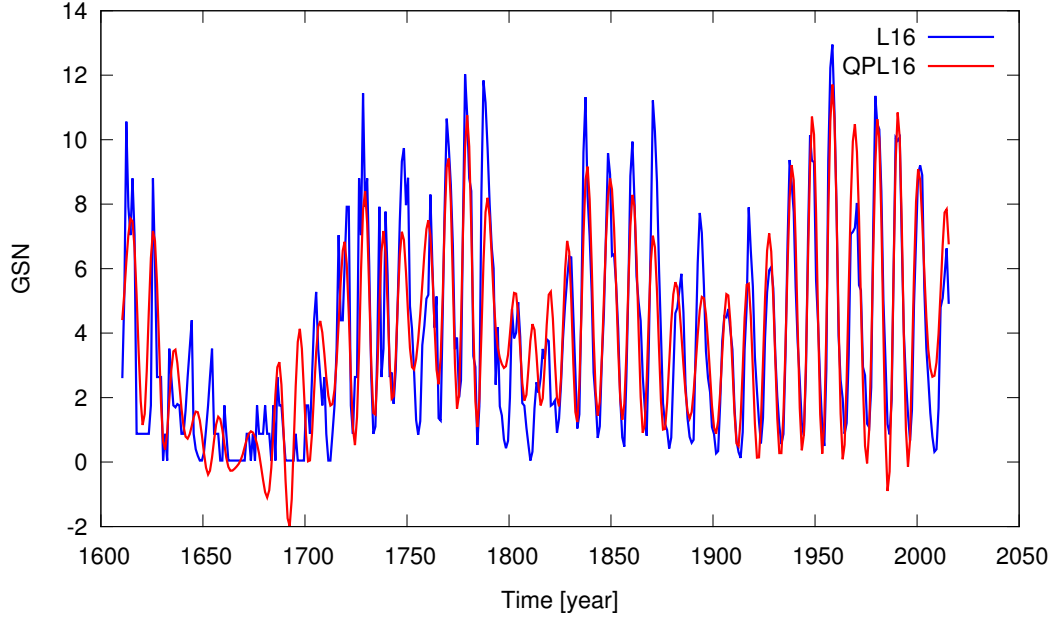


Figure 6.17 – L16 is yearly observed GSN’s and its QPL16 calculated quasi-periodic approximation for the period of 1610 to 2015.

Table 6.7 – Frequency analysis of observed yearly GSN of L16 (Svalgaard & Schatten, 2016). The 16 terms of the quasi-periodic frequencies have a mean value of 3.785. The columns show 1: The frequency number, 2: The frequency, 3: The period, 4: Modulus of the amplitude, 5: The phase.

k	ν_k [rad/yr]	P [yr]	α_k	φ_k [°]
0	0.000000	inf	3.785	0.000
1	0.568045	11.061072	1.632	-55.026
2	0.030522	205.860257	1.538	144.278
3	0.623226	10.081718	1.367	-149.367
4	0.599896	10.473800	1.248	3.608
5	0.016522	380.297208	1.098	34.234
6	0.051525	121.943732	1.008	-87.122
7	0.535607	11.730961	0.935	126.350
8	0.580806	10.818045	0.932	-44.665
9	0.745525	8.427868	0.743	-42.955
10	0.636242	9.875468	0.738	-105.659
11	0.771744	8.141545	0.737	166.259
12	0.421714	14.899158	0.588	-79.260
13	0.079988	78.551822	0.573	132.872
14	0.108853	57.721720	0.500	49.611
15	0.559731	11.225368	0.498	-168.964

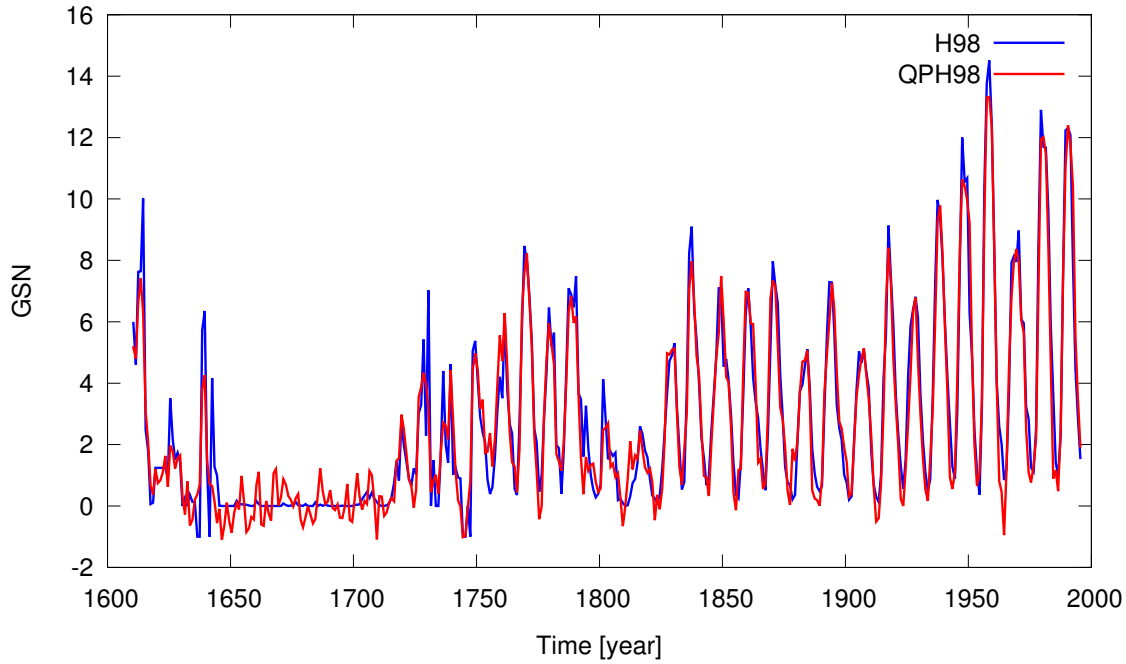


Figure 6.18 – H98 is the yearly observed GSN's and its QPH98 calculated quasi-periodic approximation for the period of 1610 to 1998.

Fig.6.19 shows the QP decompositions of the observed GSN, it can be compared to the GSN records as shown in Fig.6.13. These different QP approximations show good correlation. Finally, in the above figure are shown the well defined QP properties of the observed GSN records. These determine the mean characteristics for the reconstruction of mid and long-term evolution of solar activity. Discussed in the next section are defined the features of GSN's with the given timescales reconstructed (i.e. extrapolation) series.

6.3. QUASI-PERIODIC SEARCH OF SHORT AND MID-TERM VARIATION OF SOLAR ACTIVITY INDICATORS

Table 6.8 – Frequency analysis of observed yearly GSN of H98 (Hoyt & Schatten, 1998). The 51 terms of the quasi-periodic frequencies have a mean value of 2.799. The columns show 1: The frequency number, 2: The frequency, 3: The period, 4: Modulus of the amplitude, 5: The phase.

k	ν_k [rad/yr]	P [yr]	α_k	φ_k [°]
0	0.000000	inf	2.799	0.000
1	0.010926	11.888625	1.750	45.592
2	0.566633	11.088625	1.544	93.592
3	0.579153	10.848919	1.351	142.523
4	0.631126	9.955512	1.323	75.567
5	0.599227	10.485491	0.985	67.258
6	0.030463	206.259065	0.921	144.668
7	0.620428	10.127183	0.855	-148.991
8	0.054369	115.564866	0.839	-32.120
9	0.620428	10.507183	0.923	-133.991
10	0.536530	11.710777	0.718	17.362
11	0.077798	80.762617	0.656	21.699
12	0.110183	57.025118	0.572	-83.104
13	0.519220	12.101210	0.570	115.925
14	0.771147	8.147844	0.512	-117.749
15	0.744757	8.436553	0.495	43.881
16	0.670712	9.367927	0.459	21.158
17	0.624183	10.066250	0.436	9.116
18	0.568936	11.043743	0.406	-64.069
19	0.714146	8.798179	0.364	-77.706
20	0.165804	37.895366	0.362	-150.083
21	0.783421	8.020186	0.360	-50.564
22	0.220558	28.487654	0.350	148.042
23	1.938339	3.241531	0.340	132.474
24	0.396807	15.834367	0.331	85.756
25	0.197165	31.867629	0.291	-125.166
26	0.585935	10.723357	0.280	52.281
27	0.925938	6.785755	0.277	120.703
28	0.374570	16.774402	0.261	165.365
29	0.424267	14.809491	0.256	83.757
30	0.292446	21.484944	0.255	-80.351
31	1.994264	3.150629	0.253	-70.722
32	1.304632	4.816058	0.241	-106.159
33	0.059183	106.165390	0.234	75.290
34	1.202164	5.226561	0.233	121.832
35	1.493642	4.206621	0.227	114.642
36	1.739764	3.611516	0.222	24.942
37	0.473521	13.269088	0.218	87.062
38	0.245861	25.555883	0.205	18.651
39	2.858251	2.198262	0.204	-148.516
40	0.309464	20.303459	0.196	-57.786
41	1.085041	5.790734	0.195	-15.489
42	2.831929	2.218694	0.186	30.604
43	0.842188	7.460548	0.181	164.260
44	1.101528	5.704065	0.180	-22.162
45	0.492112	12.767806	0.179	-127.873
46	0.148393	42.341386	0.171	3.741
47	0.867679	7.241367	0.170	143.179
48	0.338213	18.577603	0.160	-123.342
49	0.306523	20.498234	0.156	163.254
50	2.808364	2.237312	0.064	150.067

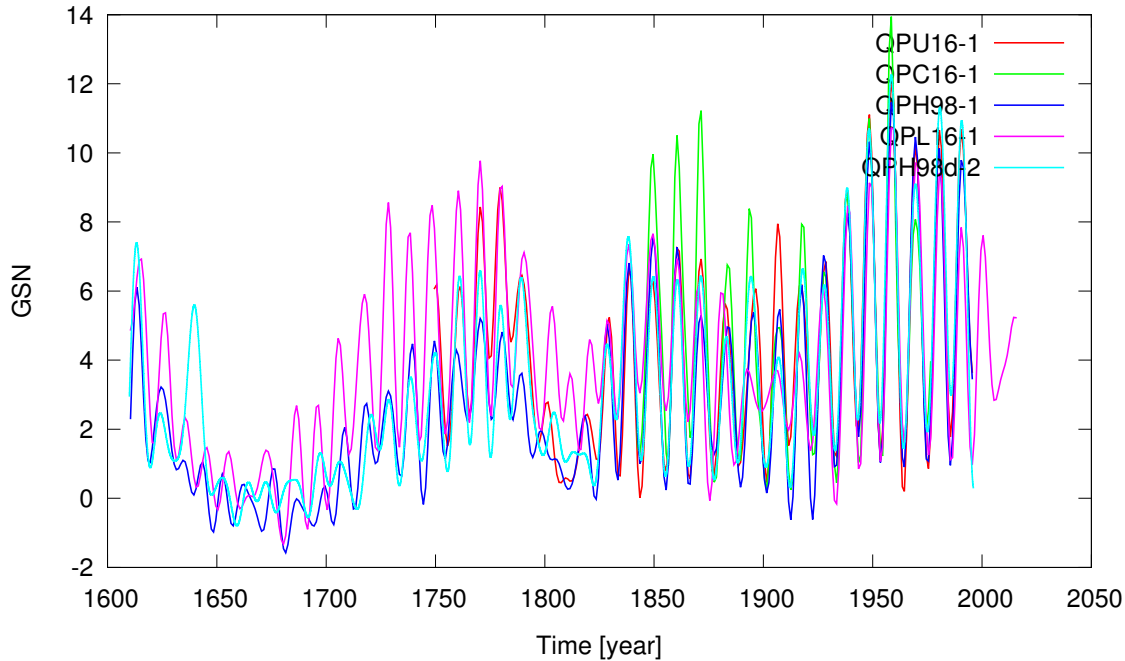


Figure 6.19 – Total set of the QP series of the different GSN data covering the interval of 1600 to 2016.

6.3.3 Verification of the QP variations of solar activity records

It is necessary to verify the determined QP approximations of the observed data by averaging in various ways the records and then computing their frequencies in order to search for a more reliable QP approximation series. For this purpose in Figs. 6.20-6.26 are plotted GSN's QP approximation functions with a smooth of between 1 to 5 years.

These various used averaged series allow us to find the closest QP function to the original data. These figures provide the reliability of the used smoothed values, which then can be used to study long timescale series. As shown in the above figures, for all of GSN's data records, the smoothed QP approximation between 1 and 2 years show excellent correlation when compared to the original data record. The new updated U16, C16, L16, standard H98 daily/yearly GSN's and new updated daily/annual SSN's data variations were shown for a synoptic review. The differently smoothed variations are displayed by providing an accurate correlation with their QP approximated values. Namely this QP approximation function will be used for the reconstruction of the short, mid and long-term behaviour of the solar cycles.

6.3. QUASI-PERIODIC SEARCH OF SHORT AND MID-TERM VARIATION OF SOLAR ACTIVITY INDICATORS

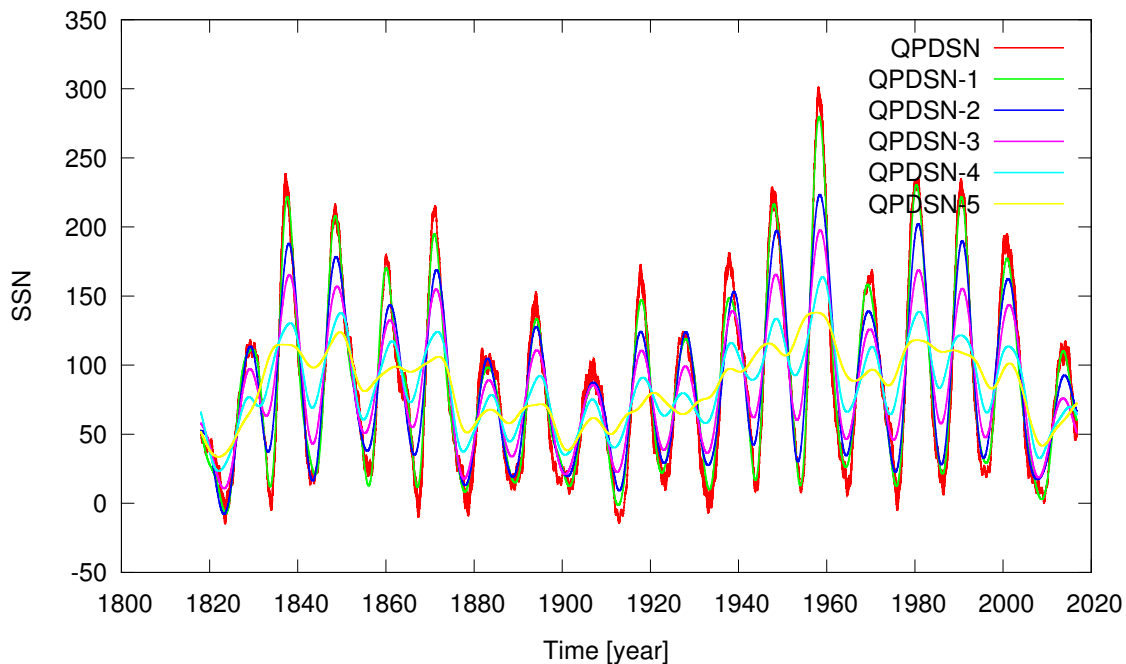


Figure 6.20 – 1 to 5 years averaged daily observed SSN variation QPDSN- i , ($i = 0, \dots, 5$) with its QP approximation from 1st of January from the 1818 to 30th September 2016, from the WDC-SILSO, Royal Observatory of Belgium records.

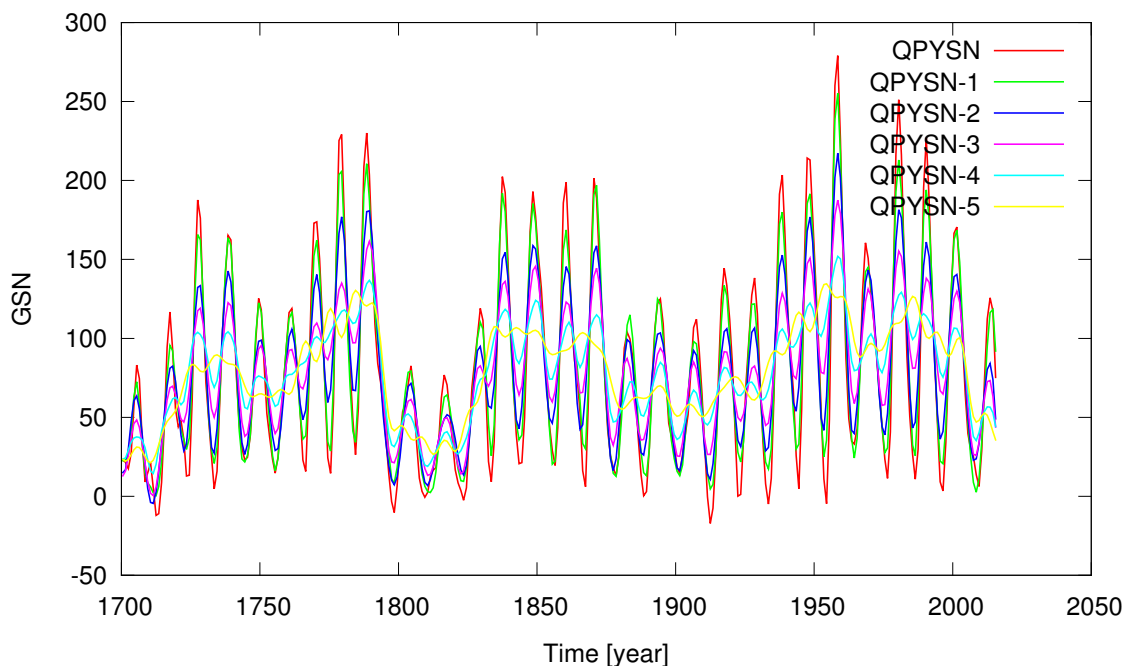


Figure 6.21 – 1 to 5 years averaged mean yearly observed GSN variation QPYSN- i , ($i = 0, \dots, 5$) with its QP approximation from 1700 to 2015, from the WDC-SILSO, Royal Observatory of Belgium records.

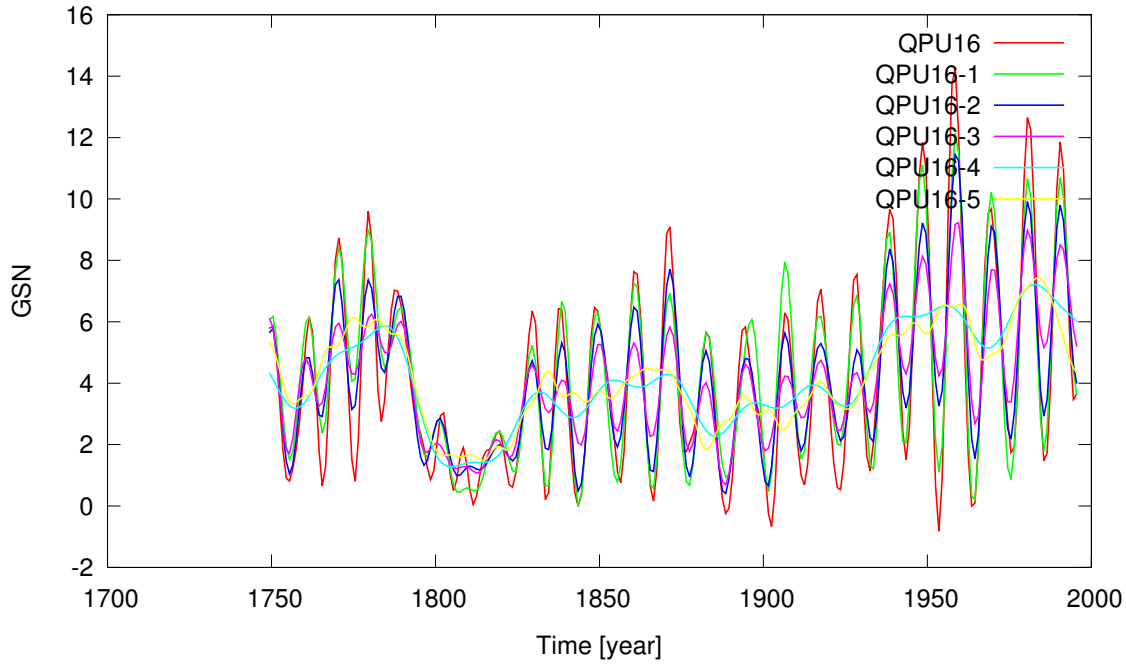


Figure 6.22 – 1 to 5 years averaged mean yearly observed GSN variation $QPU16-i$, ($i = 0, \dots, 5$) with its QP approximation from 1749 to 1995, (Usoskin et al., 2016c).

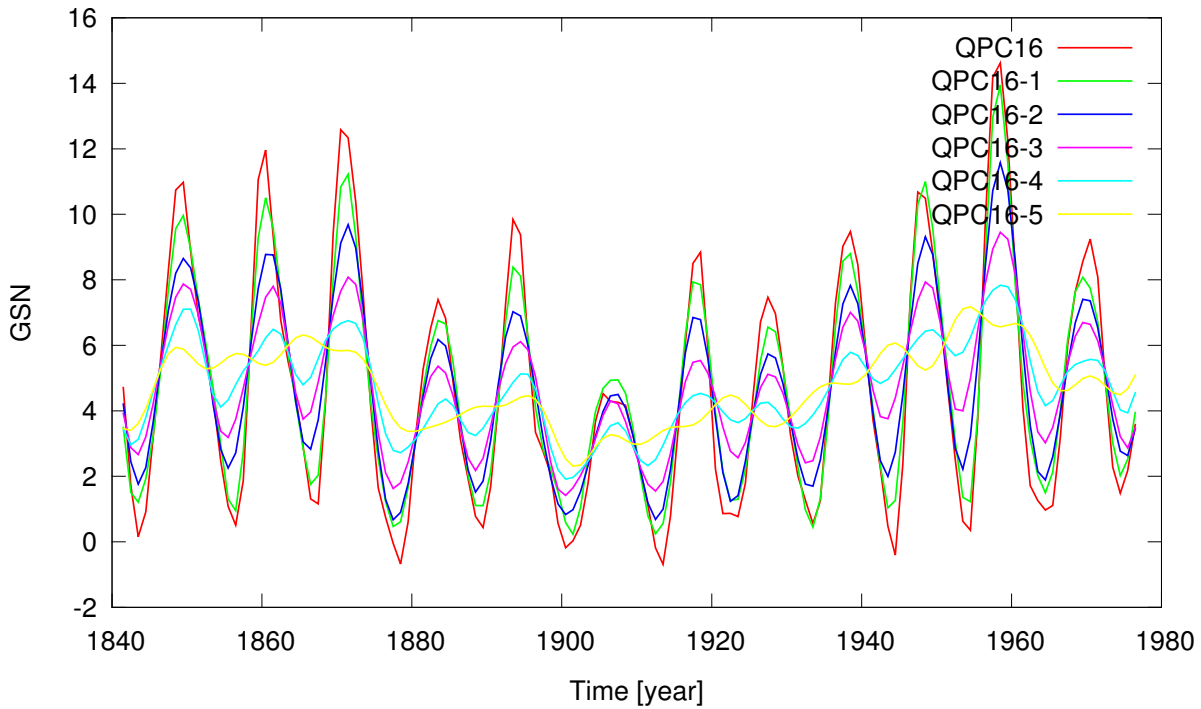


Figure 6.23 – 1 to 5 years averaged mean yearly observed GSN variation $QPC16-i$, ($i = 0, \dots, 5$) with its QP approximation from 1841 to 1976, (Cliver & Ling, 2016).

6.3. QUASI-PERIODIC SEARCH OF SHORT AND MID-TERM VARIATION OF SOLAR ACTIVITY INDICATORS

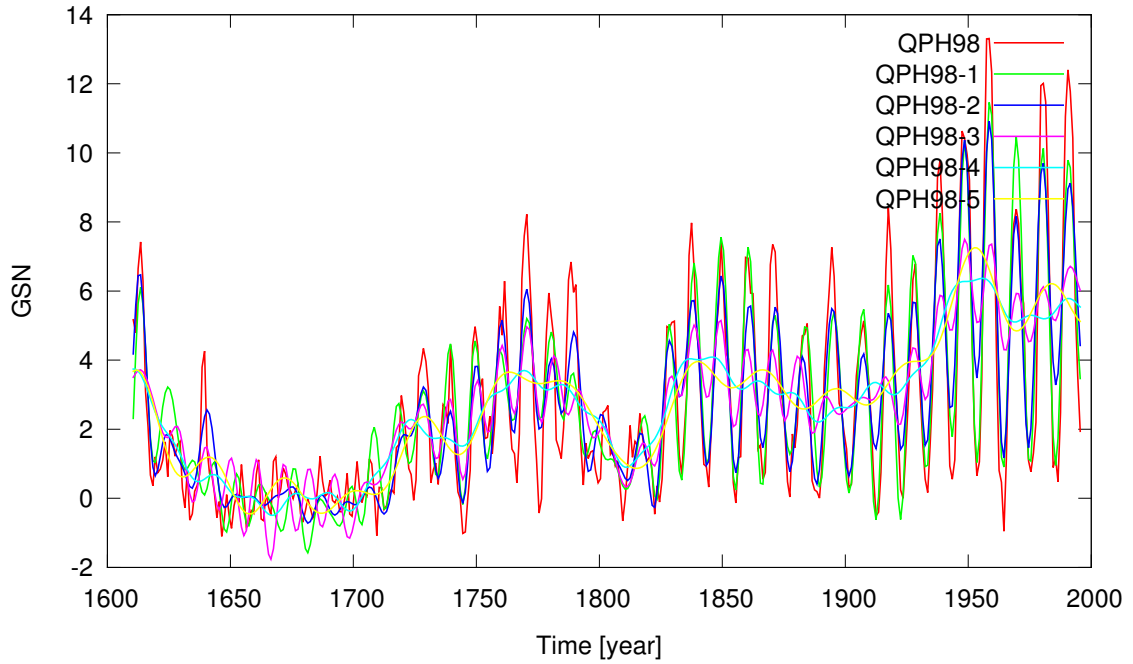


Figure 6.24 – 1 to 5 years averaged mean yearly observed GSN variation $QPH98-i$, ($i = 0, \dots, 5$) with its QP approximation $QPH98d$ over the time interval 1610 to 1995, (Hoyt & Schatten, 1998).

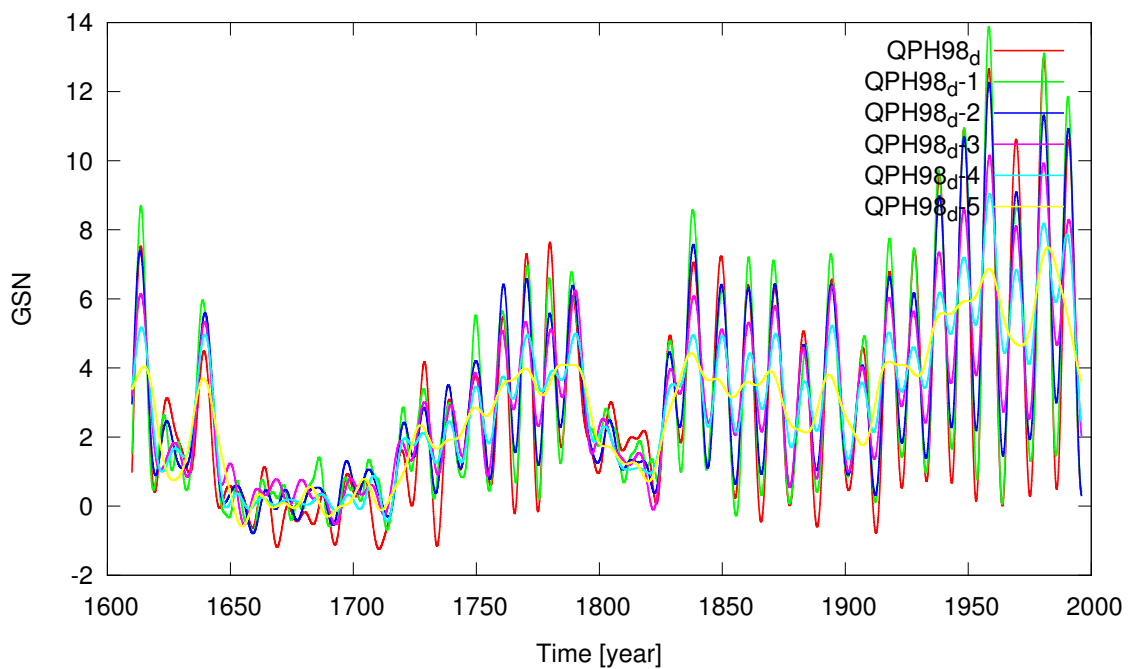


Figure 6.25 – 1 to 5 years averaged mean daily observed GSN variation $QPH98d-i$, ($i = 0, \dots, 5$) with its QP approximation 1st of January 1610 to 30th September 1995, (Hoyt & Schatten, 1998).

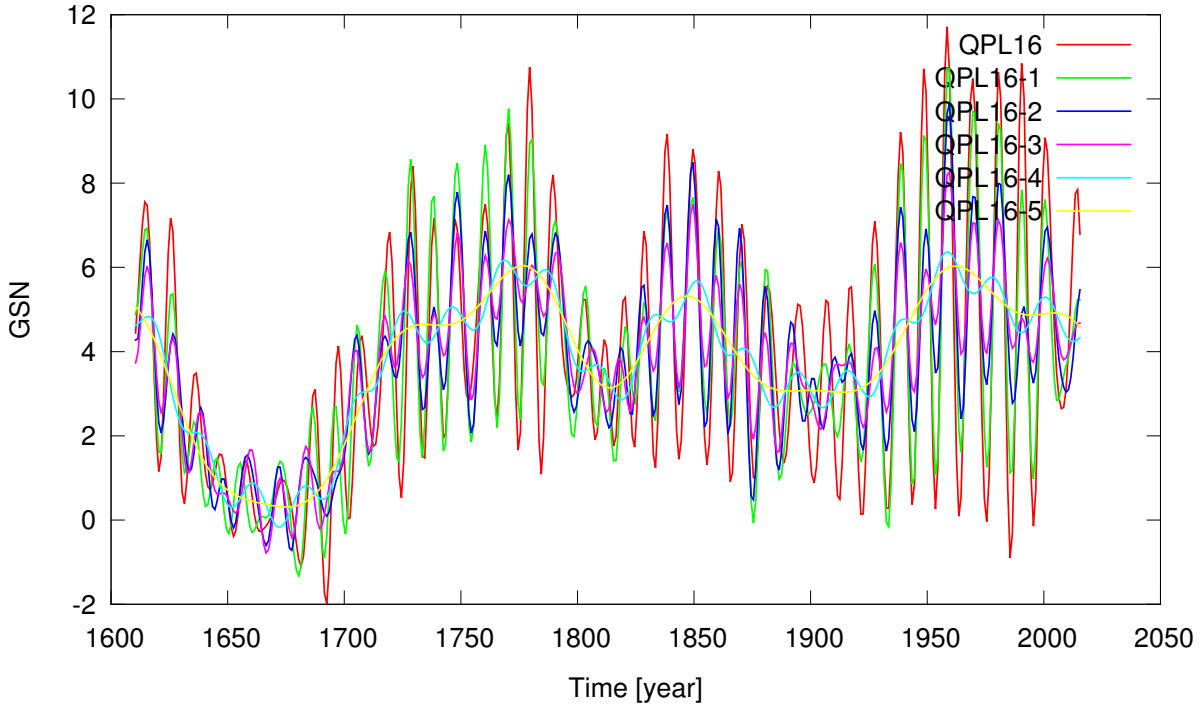


Figure 6.26 – 1 to 5 years averaged mean yearly observed GSN variation QPL16- i , ($i = 0, \dots, 5$) with its QP approximation from 1610 to 2015, (Svalgaard & Schatten, 2016).

6.4 Secular and millennial variation of solar activity proxies

The possibility of studying solar activity variation for long timescales is allowed by measuring proxies from paleo records, e.g. such as ^{14}C and ^{10}Be radio isotopes (for more see Sec.4.3). The main determined historical grand maxima and minima events have been distinguished from the variation of measured radio isotopes. From these radio proxies the GSN's series have been estimated, based on some physical parameters with the so-called force field model (for more see Secs.4.3.4 and 4.3.3). This has only one parameter, the modulation potential ϕ (it is reconstructed from direct measurements of the cosmic ray energy spectrum), for a given interstellar spectrum. This modulation potential parameter can be used to estimate the decadal GSN's series. In this section, the reconstructed GSN's series from the radio isotopes of ^{14}C and ^{10}Be were used for the purpose of verification via a reconstruction of the SSN and GSN series. The measured ^{14}C and ^{10}Be radio isotopes have discrepancies, while the variation of radio isotopes shows the dominance of solar modulation of cosmogenic nuclides production variations during the last millennium (Usoskin et al., 2003).

6.4.1 Periodicity in the isotope proxies of carbon ^{14}C

The cosmogenic proxies are used mostly to study the long-term evolution of solar variability. In Fig.6.27 are illustrated the IntCal98 and IntCal13 northern hemisphere atmospheric radiocarbon calibration curves for ^{14}C (Reimer, 2013).

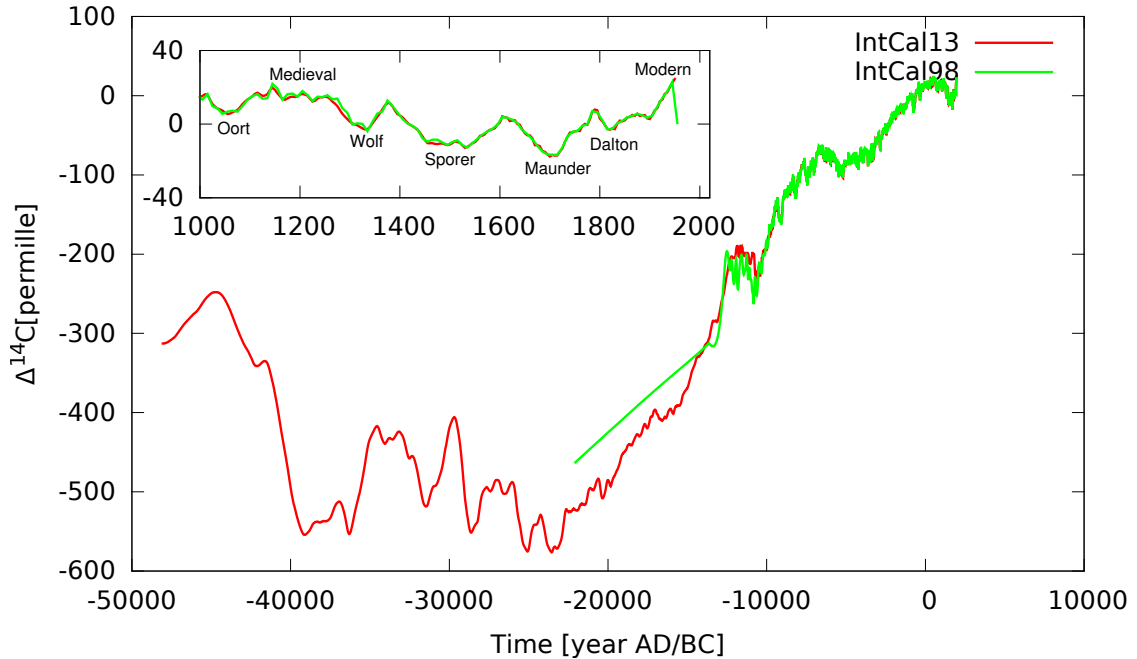


Figure 6.27 – Reconstruction of IntCal13 and IntCal98 northern hemisphere atmospheric radiocarbon calibration curves for ^{14}C . Inserted is enlarged graph for demonstration of well known historical events.

The variation of IntCal98 and IntCal13 are shown in Fig.6.28, for the interval of 1500B.C. to 2000A.D. The variation of ^{14}C well represents the grand maxima and minima events which have been recorded from historical and observational indicators.

6.4.2 Periodicity of the solar activity indicators in beryllium ^{10}Be

Decadal sunspot numbers reconstructed from cosmogenic ^{10}Be data in polar ice from Greenland and Antarctic data cover the period between the years 855 and 1975 (Usoskin et al., 2003) (herein, U03). Shown in Fig.6.29 is a plot of the reconstruction of average GSN's activity levels based on the method of used physical models for processes connecting ^{10}Be concentration to the period, given in (Usoskin et al., 2003), with its QP representation. The use of frequency analysis determined with the conjugation gave 10 main and 11 complementary terms with the mean of 28 including the constant term. The real part of the components is shown in Tab.6.9. The quasi-periodic variation of reconstruction of GSN's series shows periods of high and low solar activity events throughout the past multi secular timescales reliably. This treatment nearly triples the time interval for which such a statement could be made previously. The agreement of QP properties allows the reconstruction of multi millennial variation of solar activities.

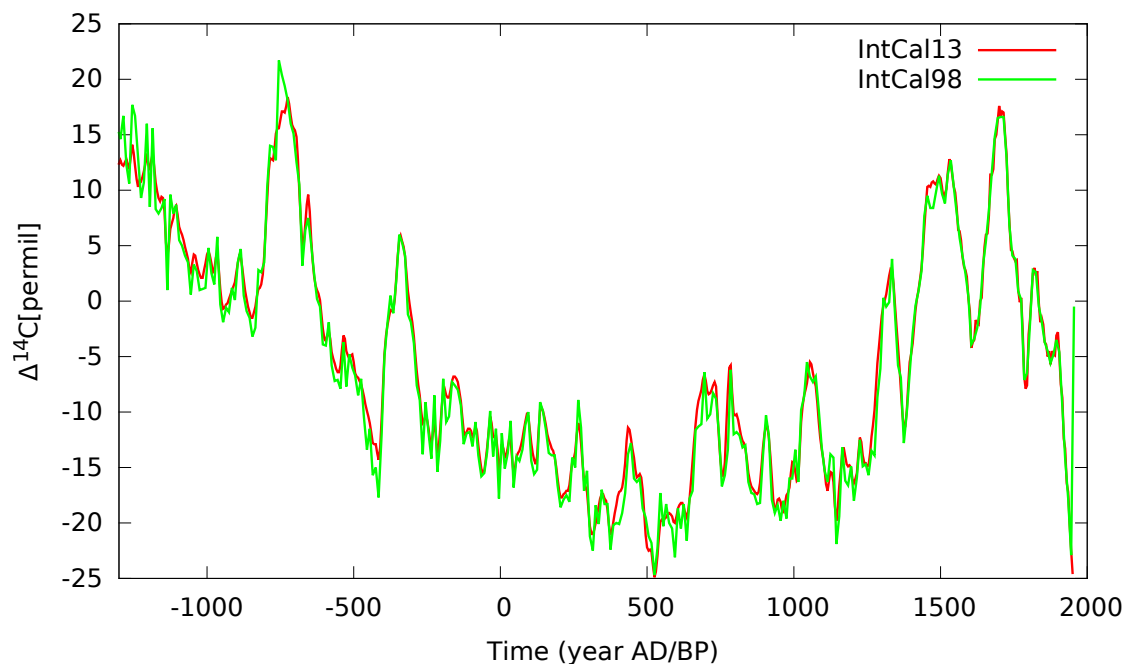


Figure 6.28 – Reconstruction of IntCal13 and IntCal98 northern hemisphere atmospheric radiocarbon calibration curves for ^{14}C , over the interval of 1500 B.C. to 2000 A.D. (Reimer, 2013)

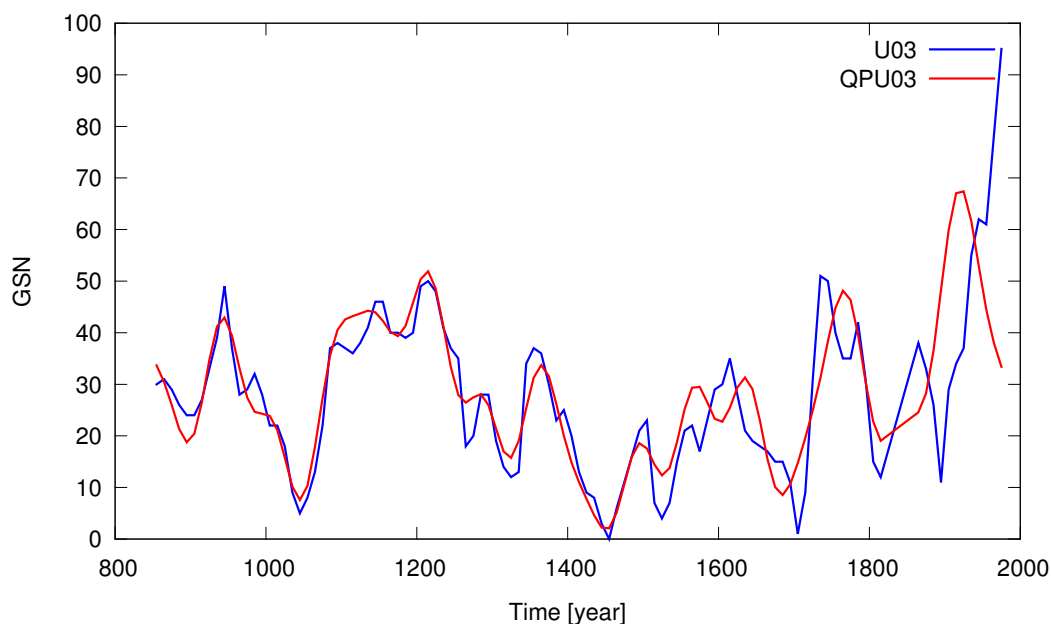


Figure 6.29 – U03 is the reconstruction of GSN's based on ^{10}Be (Usoskin et al., 2003) with its QPU03 calculated quasi-periodic approximation.

Table 6.9 – Frequency analysis of the decadal mean estimated GSN from Usoskin et al. (2003) (for more see Sec.4.3.3), representing the 12 terms of the quasi-periodic frequencies with a mean value of 28.03. The columns show 1: The frequency number, 2: The frequency, 3: The period, 4: Modulus of the amplitude, 5: The phase.

k	$\nu_{\mathbf{k}}$ [rad/yr]	P [yr]	$\alpha_{\mathbf{k}}$	$\varphi_{\mathbf{k}}$ [°]
0	0.000000	inf	28.028	0.000
1	0.008187	767.492190	11.125	-168.156
2	0.017996	349.135150	8.681	-154.158
3	0.032309	194.472036	8.484	25.852
4	0.046458	135.244756	7.263	-36.329
5	0.033974	184.938552	5.598	132.459
6	0.015816	397.278513	4.243	-96.219
7	0.090516	69.414987	3.804	154.152
8	0.023713	264.967100	3.785	-94.711
9	0.069089	90.942758	3.634	-77.324
10	0.000000	inf	3.565	178.386
11	0.039306	159.851255	3.205	-12.772

6.4.3 Periodicity of the estimated solar activity indicators in carbon ^{14}C

The reconstructions of sunspot series from radio isotopes are required for identification of the cause of its variation. The radio isotopes has possible links with planetary harmonics, a possible solar influence on climate and for testing models of the solar dynamo etc. In our research for a study of long timescale variation of solar activity the reconstructed decadal sunspots number series was used covering the past 11,400 years. It is based on dendrochronologically dated ^{14}C radiocarbon concentrations, which combine physics-based models (Solanki et al., 2004b), covering the interval 11,450B.C.-1955A.D., (herein, S04). The variation of radioisotope reconstruction sources depends on location, used models and methods of reconstruction. Fig. 6.30 presents the reconstruction of SSN's proxy in (Solanki et al., 2004b) based on ^{14}C , and its QP variation based on outlined frequency analysis determining 24 main and 66 supplementary terms including their conjugations with a mean value of 28.69. The real part of frequency components are shown in Tab.6.10.

The physical reconstruction of solar activity over the past three millennia is based on the carbon cycle, ^{14}C production and archeomagnetic field models (Usoskin et al., 2014), covering the interval 1150B.C.-1950A.D.,(herein, U14). Fig.6.31 shows the reconstruction of SSN's series based on the carbon cycle of ^{14}C production (Usoskin et al., 2014) yielding its QP representation with 2 main and 8 supplementary terms including their conjugations, with a mean value of 39.16. The U14 real part frequency components is presented in Tab.6.11.

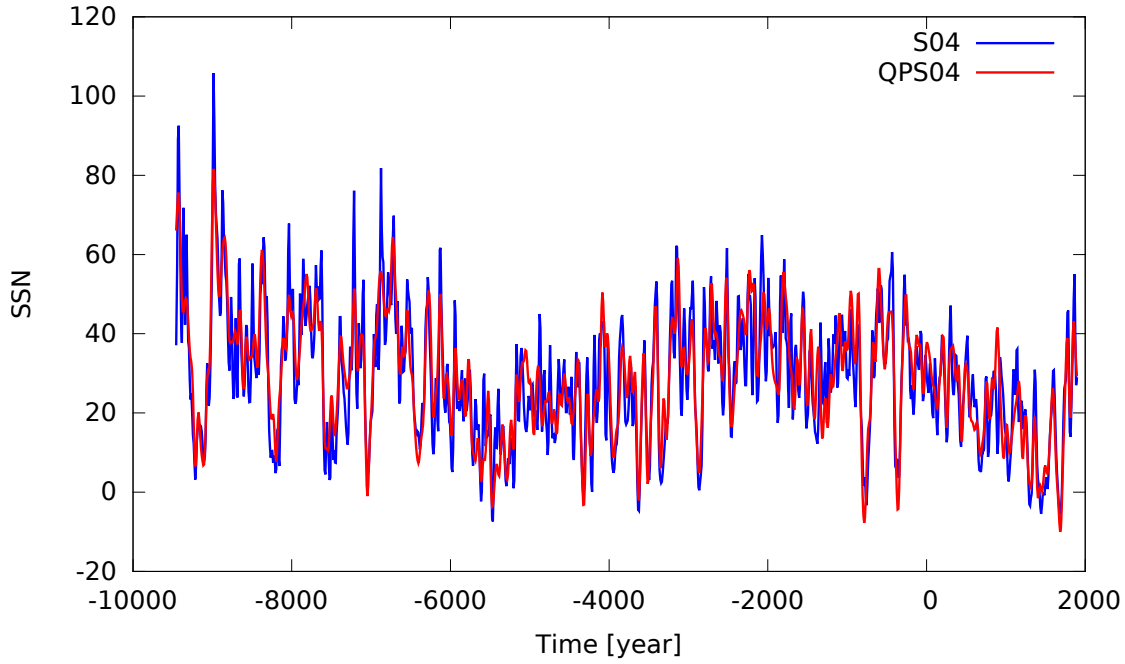


Figure 6.30 – Reconstruction of SSN's based on the ^{14}C radiocarbon measurement S04 of Solanki et al. (2004b) with its QPS04 calculated quasi-periodic approximation.

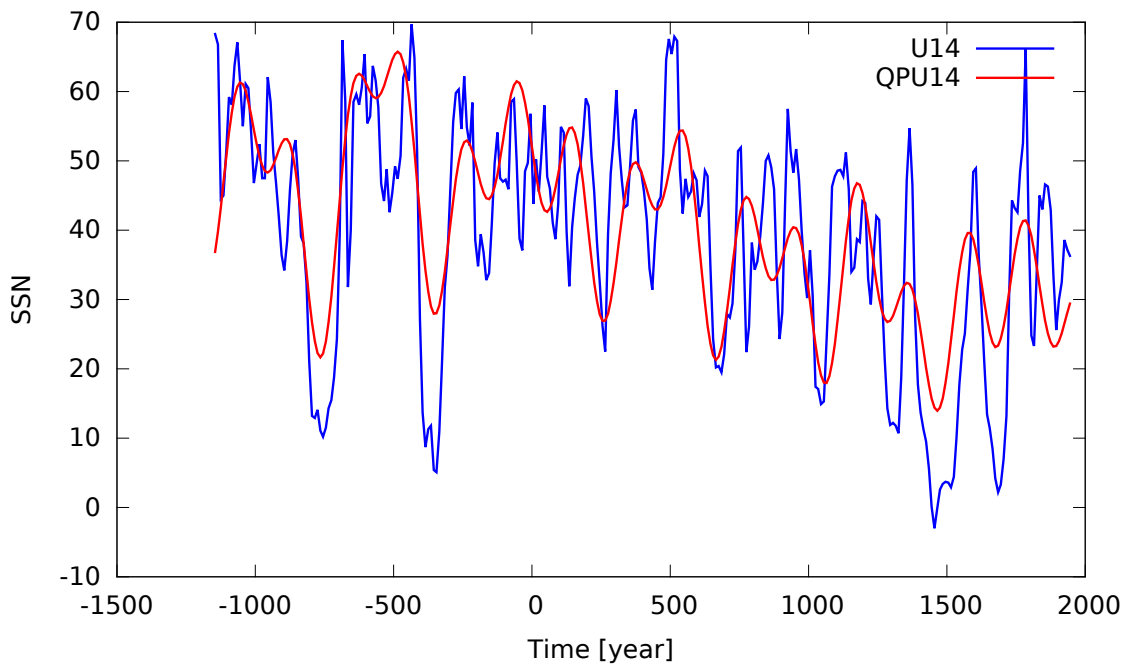


Figure 6.31 – U14 is the reconstruction of SSN's based on the ^{14}C carbon concentration in tree ring measurements (Usoskin et al., 2014) with its QPU14 calculated quasi-periodic approximation.

Table 6.10 – Frequency analysis of the yearly mean GSN from Solanki et al. (2004b) over 11,356 years (for more see Sec.4.3.4). The 46 terms of the quasi-periodic frequencies have a mean value of 28.70. The columns show 1: The frequency number, 2: The frequency, 3: The period, 4: Modulus of the amplitude, 5: The phase.

k	$\nu_{\mathbf{k}}$ [rad/yr]	P [yr]	$\alpha_{\mathbf{k}}$	$\varphi_{\mathbf{k}}$ [°]
0	0.000000	inf	28.697	0.000
1	0.000962	6528.187976	10.148	100.599
2	0.006494	967.495569	4.976	25.315
3	0.012086	519.877425	4.862	27.224
4	0.002787	2254.354187	4.720	-5.218
5	0.017850	352.008449	4.092	-123.511
6	0.014188	442.864764	3.997	69.128
7	0.027989	224.487562	3.943	8.991
8	0.011139	564.058857	3.778	-62.847
9	0.030165	208.296442	3.167	113.800
10	0.011634	540.062569	3.139	161.183
11	0.006955	903.421994	3.136	-128.011
12	0.041769	150.426001	2.832	-102.878
13	0.051017	123.157784	2.712	-63.348
14	0.033306	188.652348	2.563	172.012
15	0.015039	417.779010	2.544	126.287
16	0.021937	286.425136	2.541	31.723
17	0.032036	196.131260	2.520	77.493
18	0.071709	87.620468	2.485	-91.655
19	0.020226	310.654800	2.377	6.732
20	0.008982	699.547522	2.348	-171.256
21	0.060252	104.281434	2.328	17.294
22	0.015893	395.331464	2.323	-156.141
23	0.039782	157.939451	2.322	-81.706
24	0.019086	329.198029	2.279	-179.071
25	0.046197	136.008556	2.232	95.885
26	0.026685	235.457172	2.129	-151.954
27	0.002025	3103.362312	2.118	11.617
28	0.004313	1456.922112	2.117	149.232
29	0.020933	300.152422	2.117	-73.009
30	0.027323	229.960918	2.061	-3.547
31	0.042539	147.704278	2.024	-0.295
32	0.012820	490.122705	1.988	90.821
33	0.043976	142.877586	1.987	-67.856
34	0.064440	97.503794	1.985	-30.543
35	0.000668	9399.682585	1.974	-107.618
36	0.036748	170.978634	1.959	-98.253
37	0.048220	130.303566	1.953	156.847
38	0.071027	88.462004	1.821	154.649
39	0.024535	256.090245	1.765	-81.736
40	0.074202	84.676298	1.723	54.369
41	0.104862	59.918648	1.699	87.483
42	0.053473	117.501360	1.657	122.043
43	0.092206	68.143082	1.581	-37.460
44	0.038136	164.757782	1.576	-118.075
45	0.003590	1750.364710	1.405	-121.387

Table 6.11 – Frequency analysis of the decadal GSN estimated from radio isotopes over 3090 years (Usoskin et al., 2014) (for more see Sec.4.3.4). The 6 terms of the quasi-periodic frequencies have a mean value of 39.16. The columns show 1: The frequency number, 2: The frequency, 3: The period, 4: Modulus of the amplitude, 5: The phase.

k	ν_k [rad/yr]	P [yr]	α_k	φ_k [$^\circ$]
0	0.000000	inf	39.160	0.000
1	0.001542	4075.601196	10.559	35.511
2	0.030926	203.170044	8.685	89.411
3	0.013359	470.344978	6.832	65.346
4	0.011507	546.019272	6.330	-16.315
5	0.017740	354.182779	5.847	-144.391

6.4.4 Comparison of the physical based reconstruction of the solar activity proxies

The reliability of the reconstructed mean GSN variation over millennia are provided only by comparing the measured radio carbon nuclides. The comparison of reconstructed decadal sunspot numbers (U03, S04, U14) revealed from radioisotopes of ^{14}C , ^{10}Be and with IntCal13 radiocarbon curve of ^{14}C are shown in Fig.6.32. The variation of the reconstructed series

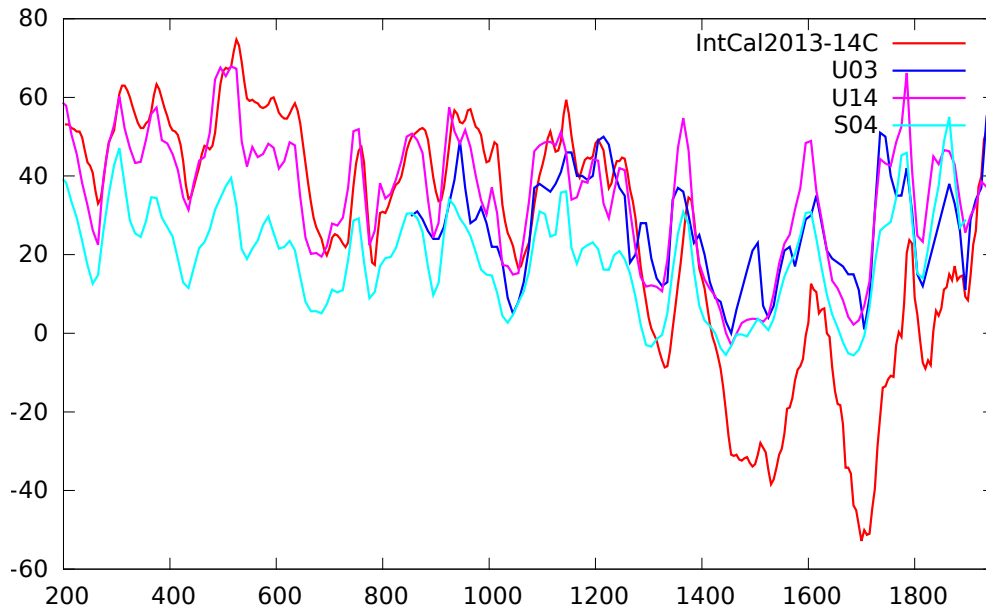


Figure 6.32 – Comparison of the measured radio carbon isotope IntCal2013- ^{14}C with U03, U14 and S04. The physical model is based on the reconstruction of the decadal GSN, covering the period from 200 to 2000.

covering the interval from 200A.D. to 1800A.D. shows a good correlation. This is expected as the reconstruction of the GSN series is based on the measurement of radio isotopes. The comparison between the observed GSN and the ^{14}C based physical reconstructions (Figs.6.30 and 6.31) have good correlation between the actual and reconstructed GSN with a correlation coefficient of $r = 0.93$. The RMS deviation between the two series is six for the period of 1610 – 1900. The good correlation between GSN's reconstructions based on ^{14}C and ^{10}Be provide $r = 0.78$ m RMS= 10 for 1700 – 1985 (Usoskin, 2013). This series follows the real GSN series, depicting the same main features, such as the Maunder (1645–1715) minimum, the tiny Dalton (~ 1795 –1830) minimum and Gleissberg (or) Gleissberg–Gnevishev (1898–1923) and a slight decrease of activity around Modern minimum from the year 1900. Three quasi-cyclic waves of increasing and decreasing amplitude of the 11 year sunspot Schwabe–Wolf's cycles are clearly visible with a mean duration of 80 – 100 years. Agreement provides reliability of the physics-based reconstruction of the GSN. Fig.6.33 shows the daily observed DSN_{obs} records with a smooth of 700 days compared with its extrapolation series DSN_{ext} . This is based on the frequency analysis described in Sec.6.2 and using the QP approximation as series of $\sum_{k=0}^n \alpha_k \cos(2\pi\nu_k t + \varphi_k)$ shown in Tab.6.12 presenting the 5 main and constant terms. The DSN_{ext} covers the interval of 1000 – 2100, with a daily step, while DSN_{obs} covers the interval from 1850 – 2016.

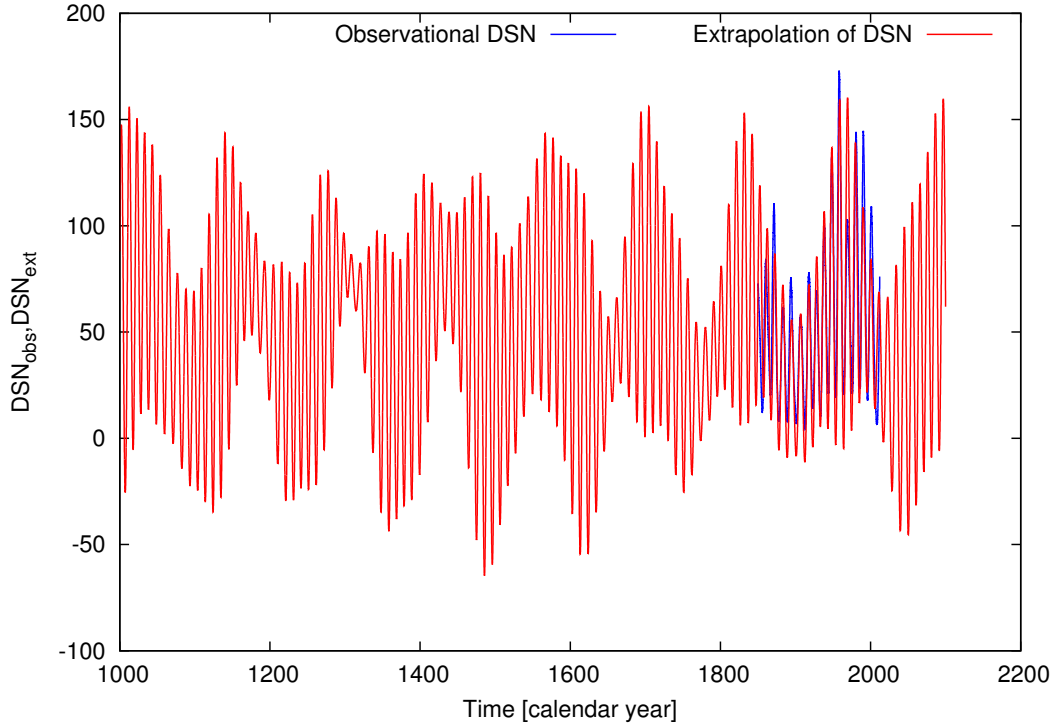


Figure 6.33 – Comparison of daily observed sunspots data DSN_{obs} from WDC-SILSO (Clette et al., 2015) with its extrapolation of DSN_{ext} based on its quasi-periodic approximation, covering interval of 1000 – 2100.

Table 6.12 – Frequency analysis of observed daily DSN of WDC-SILSO. The 6 terms of the quasi-periodic frequencies with constant term. The columns show 1: The frequency number, 2: The frequency, 3: The period, 4: Modulus of the amplitude, 5: The phase.

\mathbf{k}	$\nu_{\mathbf{k}}[\text{rad/day}]$	$\mathbf{P}[\text{day}]$	$\alpha_{\mathbf{k}}$	$\varphi_{\mathbf{k}}[^\circ/\text{day}]$
0	0.000000	inf	51.072	0.560
1	0.001616	3887.191608	50.197	-98.188
2	0.000129	48894.008119	28.244	44.006
3	0.001763	3563.261146	23.227	-59.420
4	0.001369	4590.979297	11.783	151.670
5	0.001586	3960.523444	10.750	73.227

The reconstruction of the DSN is based on the QP properties of the daily observed data from WDC-SILSO, Royal Observatory of Belgium, Brussels. In the Fig. 6.33 the excellent match between observed records with its extrapolation series is notable. In the next section these proxies are used for verification of our reconstructed solar activity series.

6.5 Reconstruction of the long-term evolution of solar activity

The available mid and long-term reconstructed solar activity proxies are based on the physical models and on the paleo records (see for more, Sec.4.3.4 and 4.3.3). Also the various observed SSN/GSN data are used here to study the purely mathematically extrapolated solar activity series using frequency analysis which is described in Sec.6.2. The various observed DSN and GSN data records of QP decompositions demonstrated in the above Sec.6.3 can be used for reconstruction of solar activity evolution. It should be noted that we used four types of solar activity indicators such as: daily DSN and yearly YSN observed records, daily and yearly estimated GSN records, physical-based (i.e. on radionuclides) estimation of GSN series, and finally radio nuclides proxies. Using the QP approximations of these listed series (see Sec.4), the mid and long-term variation of solar activity are studied in this section.

6.5.1 Mid and long-term reconstruction of the direct observed solar activity variation

Generally several prediction methods are used to forecast solar cycles (see for more, Sec.3.6). For example, precursor techniques are based on parameters (value of some measure from earlier in the solar cycle) of solar activity at a specified time to predict the amplitude of the following solar cycle. This method was used in several works (Echer et al., 2004; Rigozo et al., 2010). In our research we used several sources of solar activity indicators which were discussed in Sec.4. The extrapolation methods used the time series of sunspot numbers but they generally rely on more than one previous point to identify trends that can be used to extrapolate the data into the future. Many models can be used to find the main feature of the observed sunspot series, e.g., a modulated carrier frequency or a multi-harmonic representation, then extrapolated forward or backwards in time. Indeed, numerous attempts of this kind have been made recently (Echer et al., 2004; Nagovitsyn, 1997; De Meyer, 1998; Rigozo et al., 2001). The above approach is not a reconstruction based on measured or observed quantities, but a prediction based on extrapolation. Methods of extrapolation are often used for short and mid-term predictions, but they can also be used for long-term reconstructions of solar activity. In general, the sunspot time series is assumed to be stationary, i.e. a limited time series contains, the main information on its past and future. For grand solar minima and maxima the reconstruction models based e.g. on a modulated carrier frequency or a multi-harmonic representation cannot include periods exceeding the time span of observations on which the extrapolation is based. Extrapolated long timescale reconstruction prediction becomes increasingly unreliable with growing extrapolation time and its accuracy is hard to estimate.

Millennial reconstructions of daily and yearly observed SSN records. The reconstruction of the daily DSN and yearly YSN observed records are based on its QP decomposes which were calculated and presented in Fig.6.6 and Fig.6.8, in Tab.6.1 and Tab.6.3 for DSN and YSN respectively.

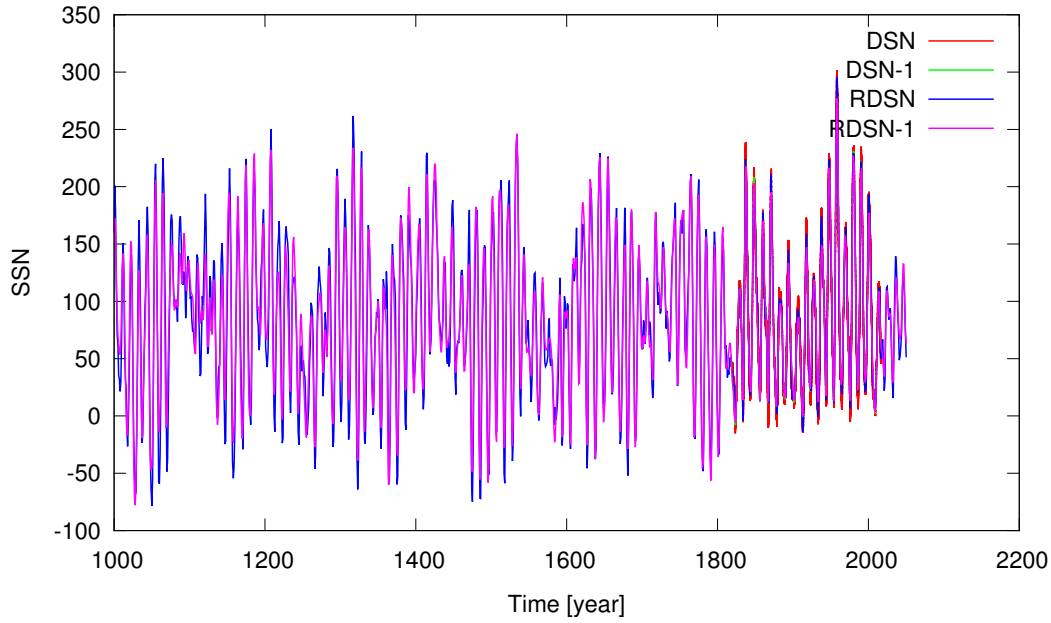


Figure 6.34 – The direct observed DSN and DSN-1 one year smoothed solar activity variation with its RDSN and RDSN-1 reconstruction respectively, covering the interval of 1000 – 2050 over one solar cyclic step.

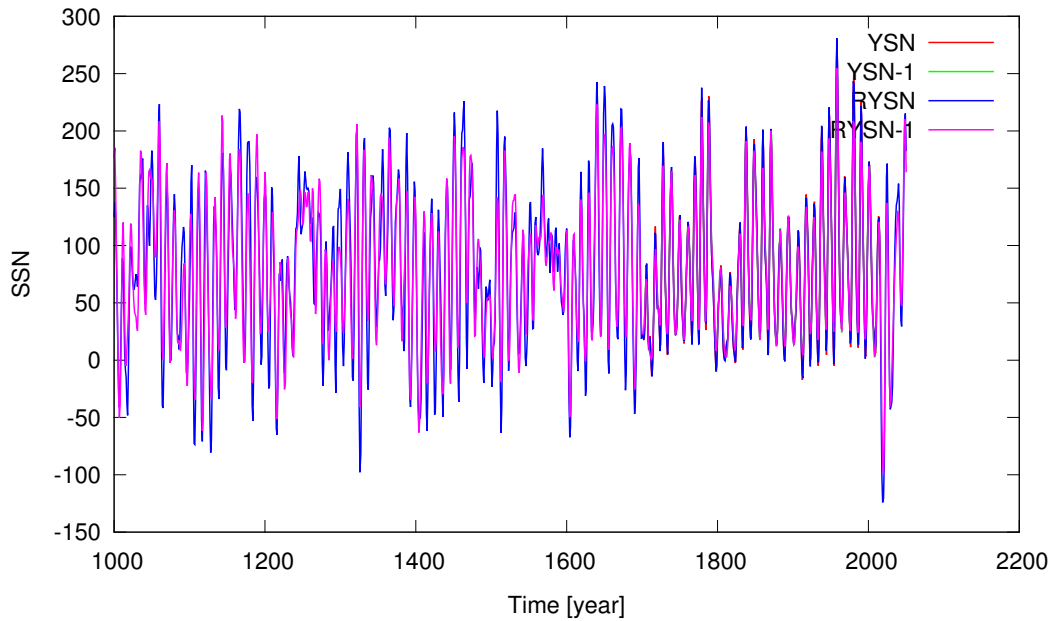


Figure 6.35 – The direct observed YSN and YSN-1 one year smoothed solar activity variation with its RYSN and RYSN-1 reconstruction respectively, covering the interval of 1000 – 2050 over one solar cyclic step.

These QP properties of the observed records were calculated by frequency analysis (see for more, Sec.6.2). As we see in the previous section QP approximations of DSN-1 and YSN-1 have a similar variability comparing to the original data. Thus we are interested in studying

the one year smoothed series of DSN and YSN. Reconstruction of the millennial evolution of solar activity variation for DSN and YSN is shown in Figs.6.34 and 6.35. Extrapolation was used to extend the sunspot series between 1000A.D. to 2050A.D. In Fig.6.34 and Fig.6.8 are shown daily DSN and yearly YSN observed SSN records, where DSN-1 and YSN-1 are one year averaged DSN and YSN records. RDSN, RDSN-1, RYSN and RYSN-1 are their reconstructions based on QPDSN and QPYN QP approximations respectively (see Sec. 6.3.1). To millennial reconstructions of observed DSN and YSN data in previous sections it was attempted to estimate and then to select the most accurate series which are presented in Figs.6.20 and 6.21. Thus, from Figs.6.20 and 6.21 the closest to the original series have QP functions with a smooth of one year. For the different QP decompositions the accurate series remained with an average of one year. These smoothed DSN and YSN series were then extrapolated using the QP series of this observed data representing the decadal (10 year) reconstructed variations to predict previous and further solar cycle forecasts. These one year smoothed and standard reconstructions of the SSN data are necessary to control the accuracy of the reconstructed series from original records. Using the different smoothed series and their extrapolations, it can be determined when the reconstruction series becomes non convergent in comparison with the original data. The extrapolation of the RDSN, RDSN-1, RYSN and RYSN-1 shows very close coherence which allows us to reconstruct the DSN and YSN data over a multi-millennium time span.

Multi-millennial reconstructions of daily and yearly observed SSN records. The multi-millennial reconstruction of the daily DSN and yearly YSN observed records are presented here. The spectral decomposition of the SSN reconstruction throughout the Holocene in decadal variation are depicted in Figs.6.36 and 6.37. The QP functions of DSN and YSN data were chosen as its one year smoothed and without averaged variations that have convergences with observed data.

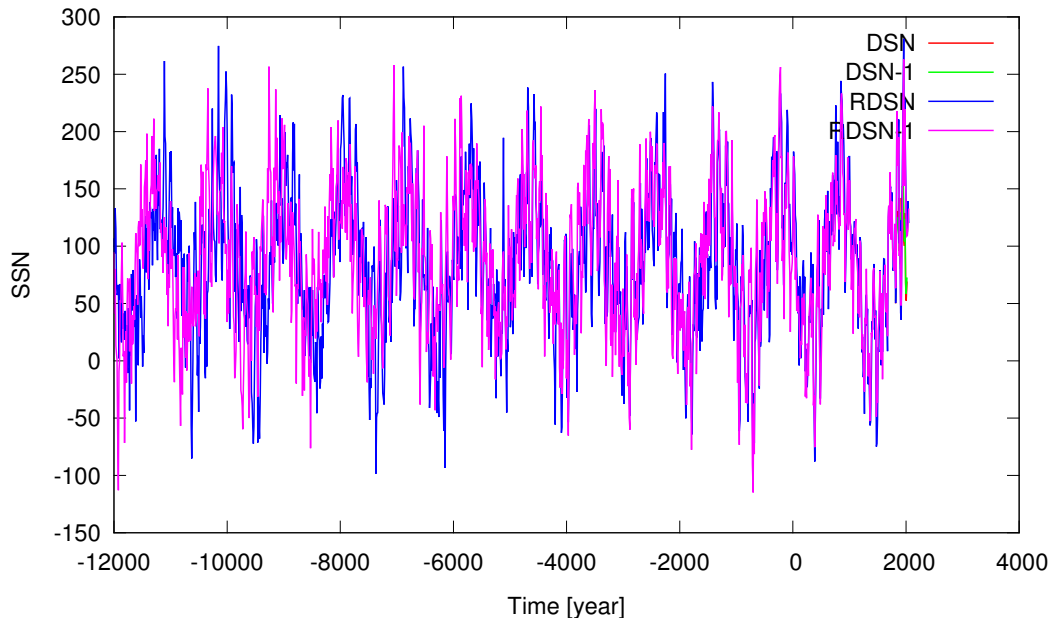


Figure 6.36 – The direct observed DSN and DSN-1 one year smoothed solar activity variation with its RDSN and RDSN-1 multi-millennial reconstruction respectively, covering the interval of 12,000B.C. to 2050A.D. over one solar cyclic step.

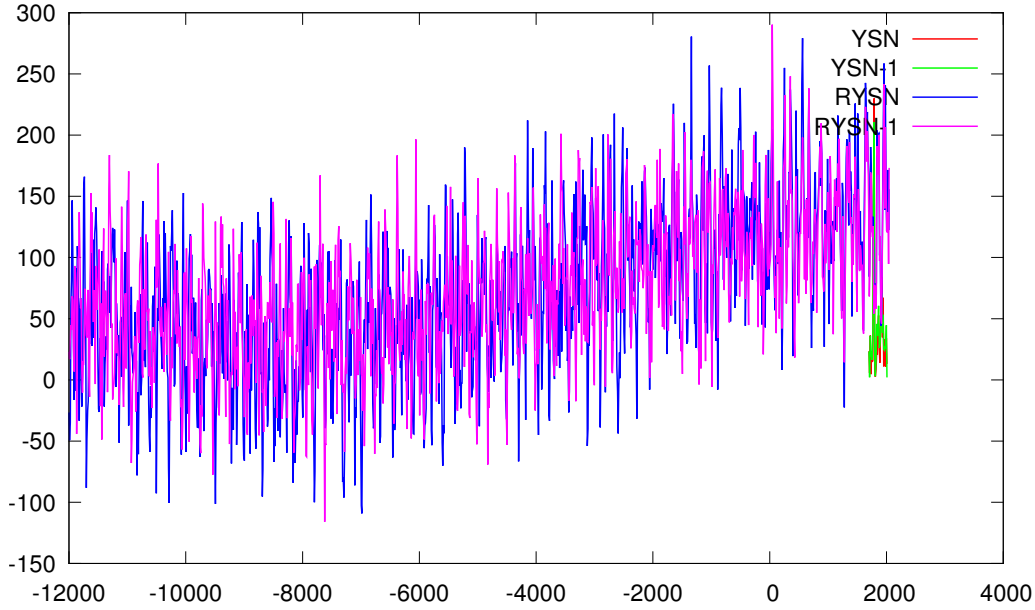


Figure 6.37 – The direct observed YSN and YSN-1 one year smoothed solar activity variation with its RYSN and RYSN-1 multi-millennial reconstruction respectively, covering the interval of 12,000B.C. to 2050A.D. over one solar cyclic step.

The figures have negative SSN values in the reconstructed series that were obtained by cosine function calculation ($\sum_{k=2}^n S + A_k \cos(\nu_k t + \varphi_k)$, where $S = t_0 + A_1$ is the constant term, ν_k is the frequency, φ_k is the phase, A_k is the amplitude) and were arbitrarily set to zero because they do not have physical significance. The decadal reconstruction of the DSN, YSN and its one year smoothed DSN-1, YSN-1 series has a convergent variation. The correspondence is reasonable, especially in terms of sunspot cycle maximum amplitudes. We may assume that a reconstruction seems to adequately describe solar cycle behaviour, including long-term periods, and is able to fit adequately with the solar maximum values.

Millennial reconstruction of yearly estimated GSN records. Presented here is a similar reconstruction of the estimated GSN data based on GSN frequency analysis. The QP approximation of the GSN studied in Sec.6.3.2, for different GSN data such as L16, U16, H98d, C16 and H98.

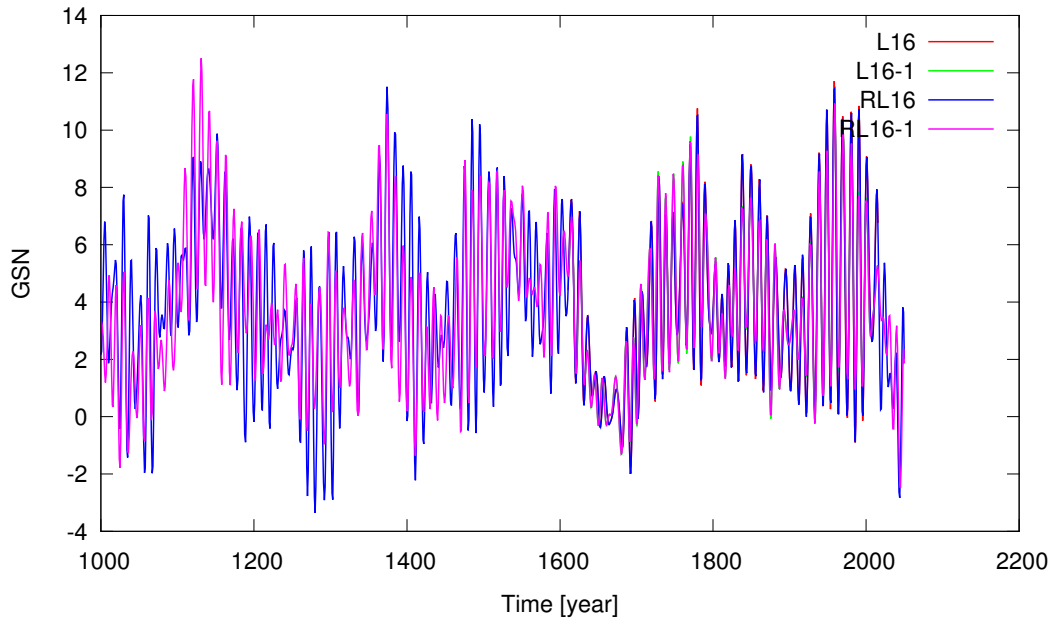


Figure 6.38 – The direct observed L16 and L16-1 one year smoothed solar activity variation with its RL16 and RL16-1 reconstruction respectively, covering the interval of 1000 – 2050 over one solar cyclic step.

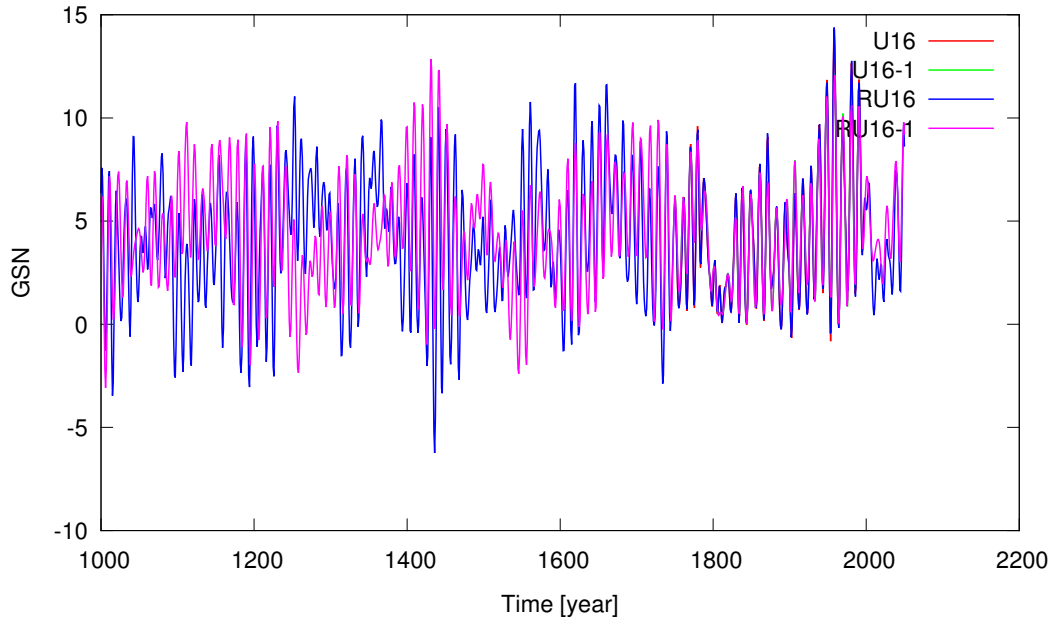


Figure 6.39 – The direct observed U16 and U16-1 one year smoothed solar activity variation with its RU16 and RU16-1 reconstruction respectively, covering the interval of 1000 – 2050 over one solar cyclic step.

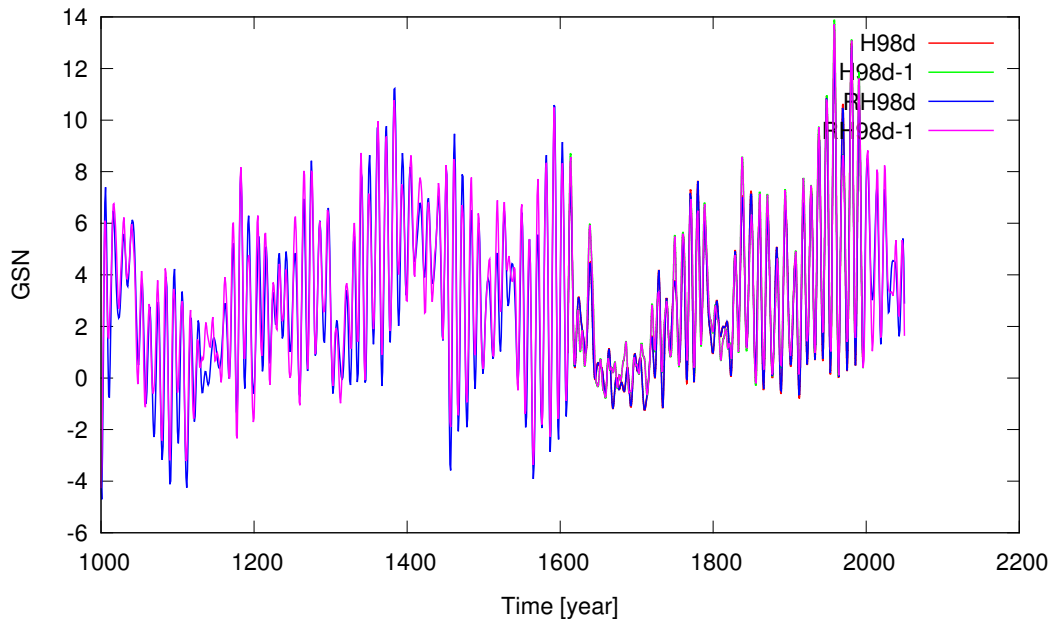


Figure 6.40 – The direct observed H98d and H98d-1 one year smoothed solar activity variation with its R98d and R98d-1 reconstruction respectively, covering the interval of 1000 – 2050 over one solar cyclic step.

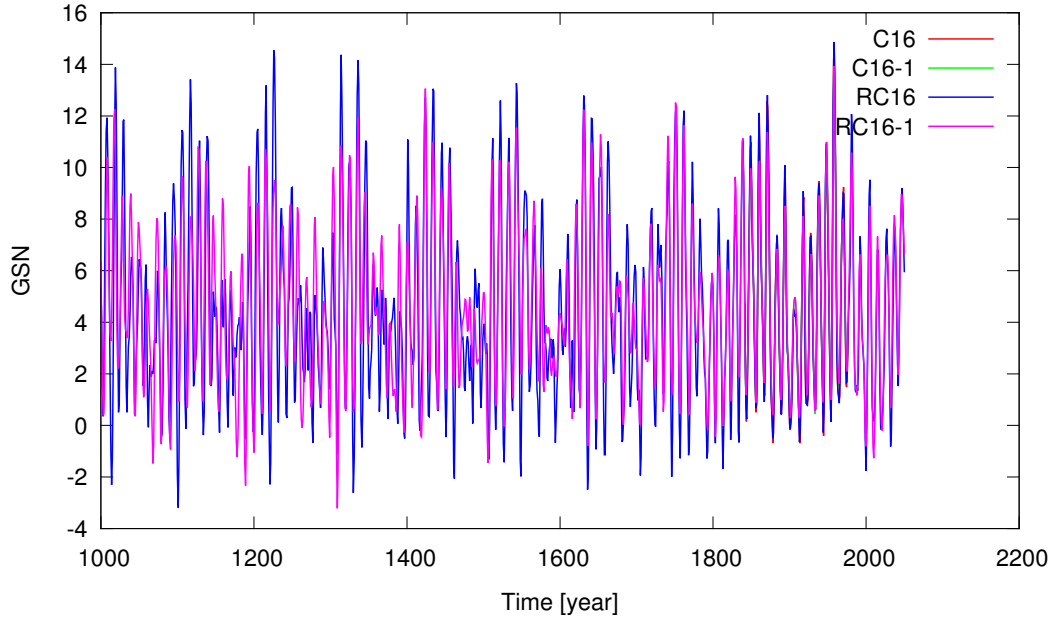


Figure 6.41 – The direct observed C16 and C16-1 one year smoothed solar activity variation with its RC16 and RC16-1 reconstruction respectively, covering the interval of 1000 – 2050 over one solar cyclic step.

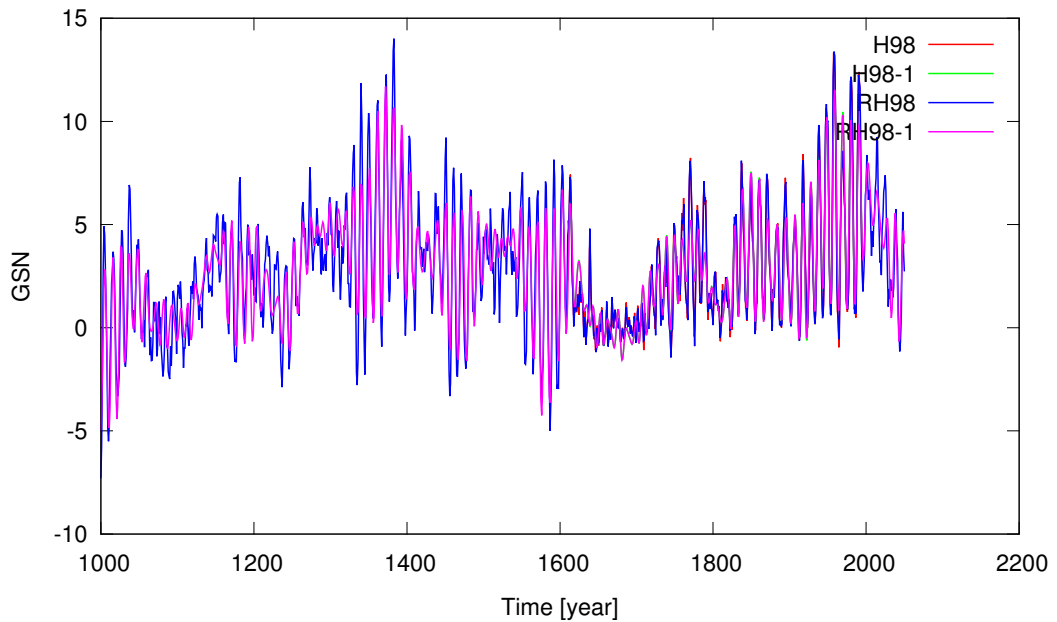


Figure 6.42 – The direct observed H98 and H98-1 one year smoothed solar activity variation with its RH98 and RH98-1 reconstruction respectively, covering the interval of 1000 – 2050 over one solar cyclic step.

Extrapolation of the GSM data is based on frequency analysis. The calculated QP decompositions for L16 are shown in Tab.6.7, for U16 in Tab.6.5, for H98d in Tab.6.4, for H98 in Tab.6.8 and for C16 in Tab.6.6. Also their millennial reconstructions were calculated and

are shown in Figs.6.38-6.42. Extrapolation was used to extend the group of sunspot series between 1000A.D.to 2050A.D with decadal steps. For the purpose of reconstruction of the reliable GSN data (in previous Sec.6.3.3) it was attempted to estimate the QP approximation of the GSN data and then to select the most accurate series. In order to discuss spectral features of observed records of solar activity Figs.6.22-6.26 show the different smoothed QP variations of GSN. These QP approximations of 1 – 5 years smoothed series show that the QP functions of one year smoothed GSN series represent the initial estimated GSN data accurately. Thus, for the different QP decompositions the standard and averaged over one year were chosen to calculate the millennial variation of GSN. Using the QP series of the observed data (GSN one year smoothed, or without smoothed original data) was extrapolated a decadal (10 year) reconstruction series to predict previous and further solar cycle forecasts.

Multi-millennial reconstructions of daily and yearly observed GSN data. The spectral decomposition of the GSN reconstruction throughout the Holocene presenting a decadal variation are depicted in Figs.6.43-6.47.

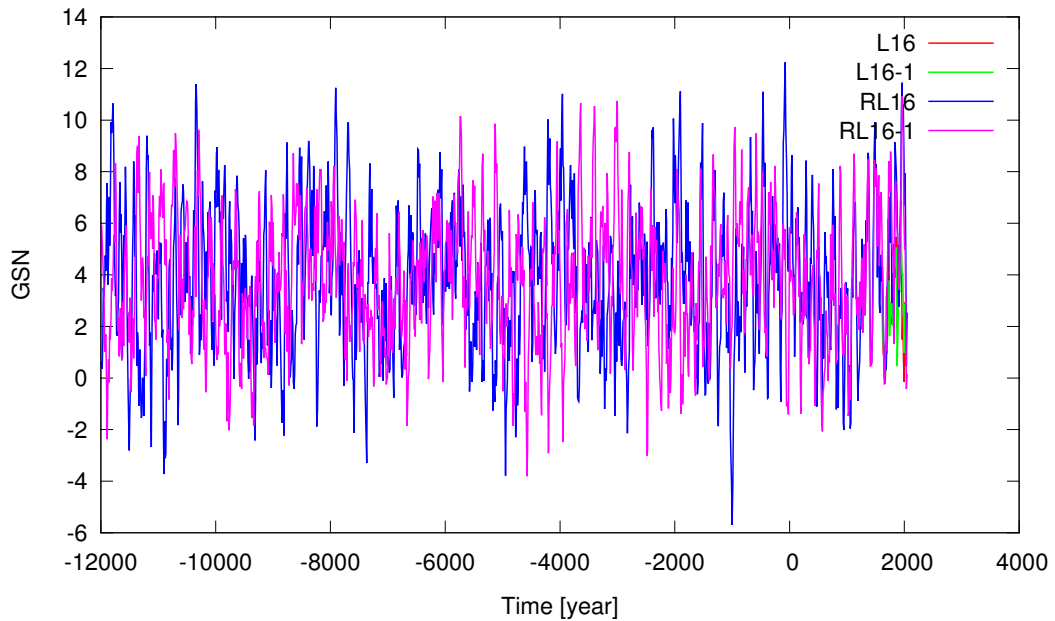


Figure 6.43 – The direct observed L16 and L16-1 one year smoothed solar activity variation with its RL16 and RL16-1 reconstruction respectively, covering the interval of 12,000B.C. to 2050A.D. over one solar cyclic step.

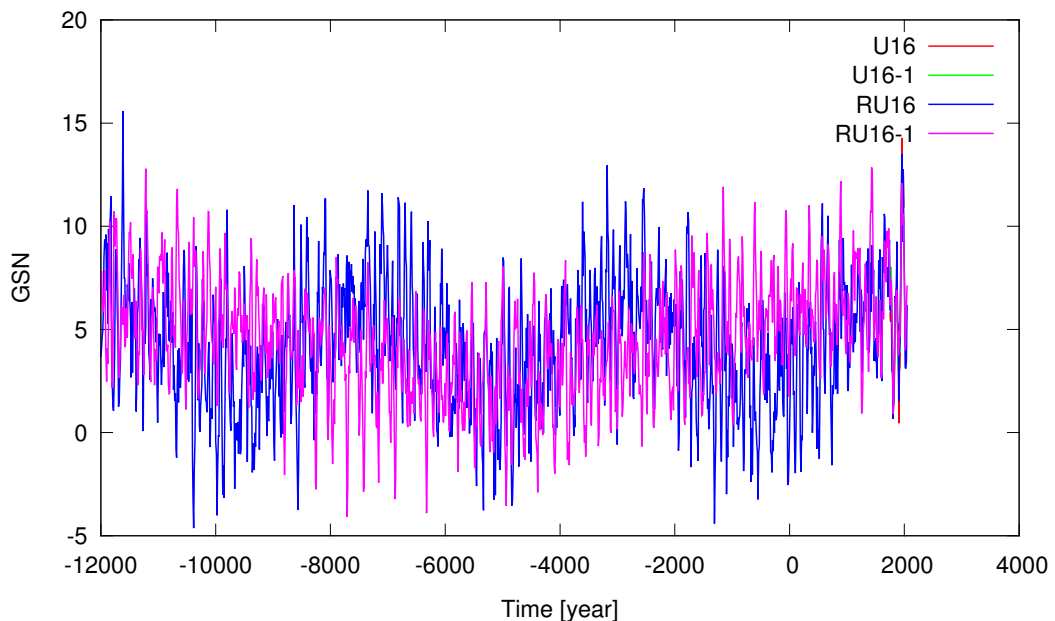


Figure 6.44 – The direct observed U16 and U16-1 one year smoothed solar activity variation with its RU16 and RU16-1 reconstruction respectively, covering the interval of 12,000B.C. to 2050A.D. over one solar cyclic step.

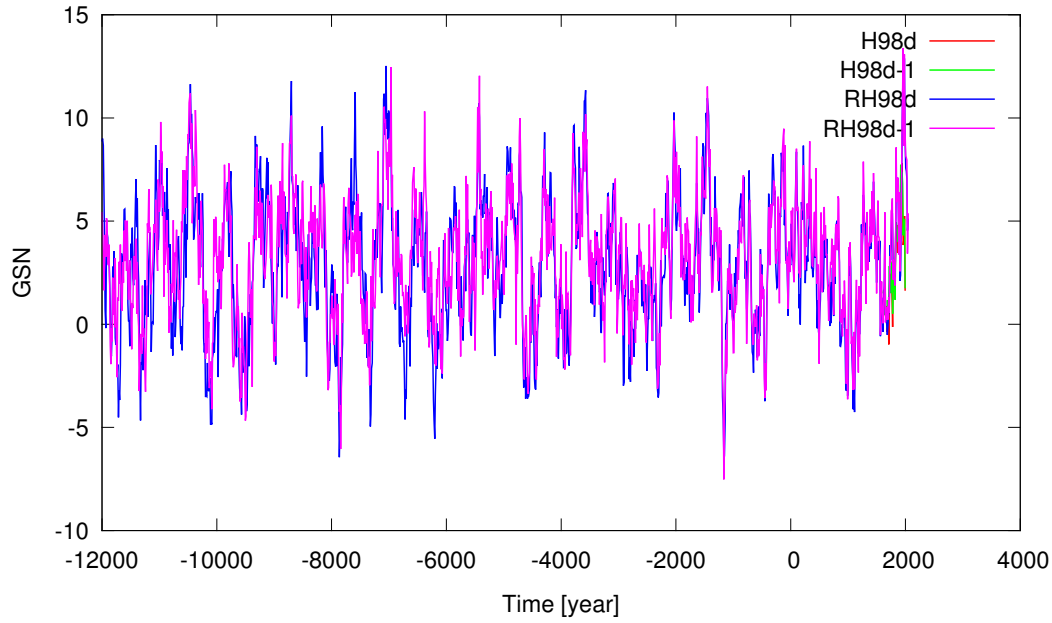


Figure 6.45 – The direct observed H98d and H98d-1 one year smoothed solar activity variation with its RH98d and RH98d-1 reconstruction respectively, covering the interval of 12,000B.C. to 2050A.D. over one solar cyclic step.

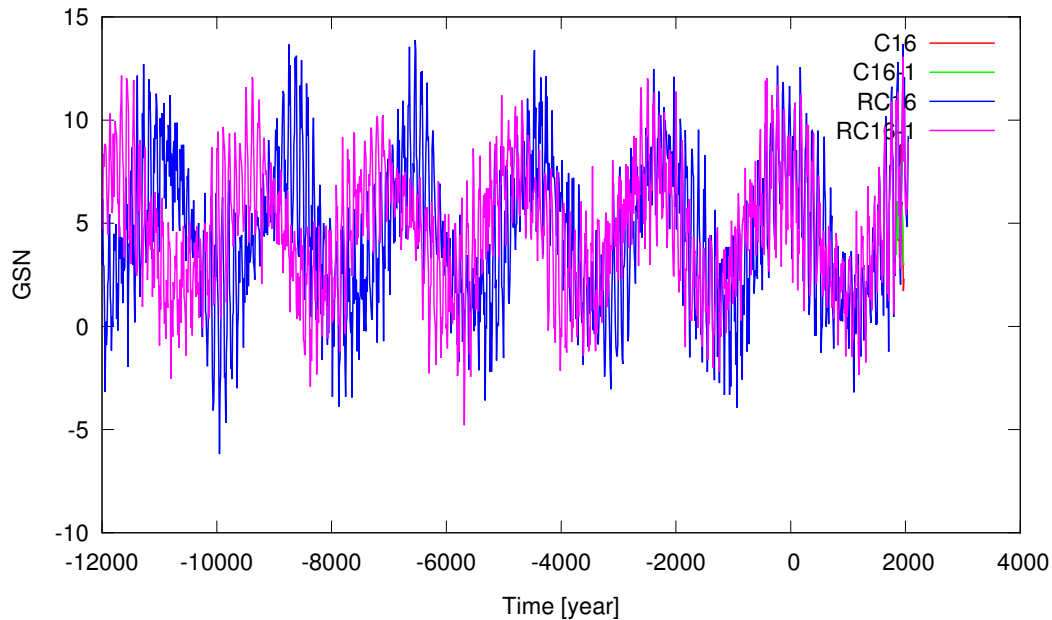


Figure 6.46 – The direct observed C16 and C16-1 one year smoothed solar activity variation with its RC16 and RC16-1 reconstruction respectively, covering the interval of 12,000B.C. to 2050A.D. over one solar cyclic step.

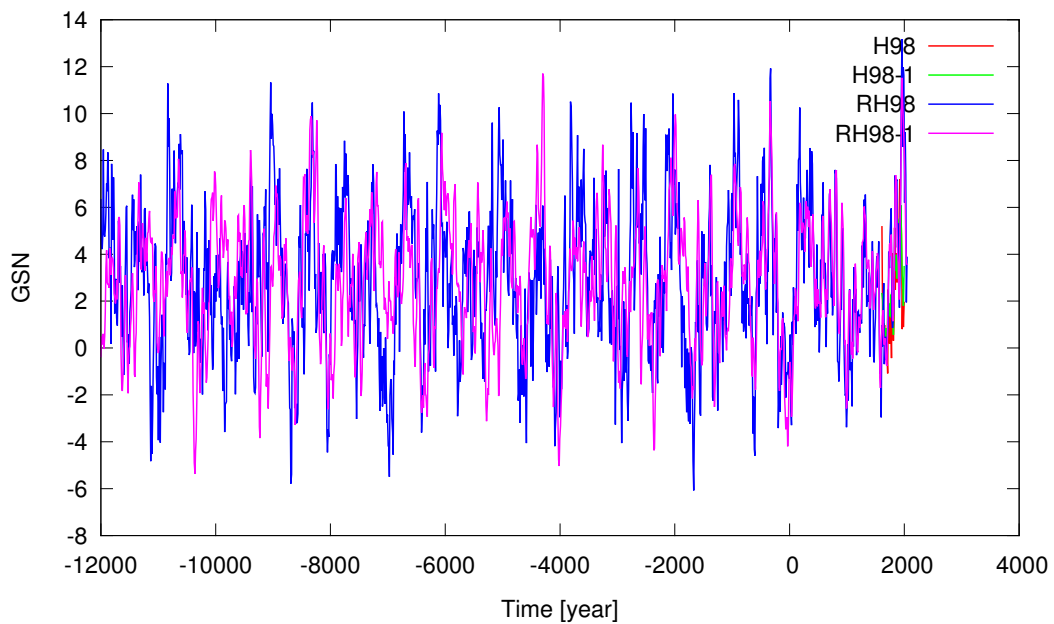


Figure 6.47 – The direct observed H98 and H98-1 one year smoothed solar activity variation with its RH98 and RH98-1 reconstruction respectively, covering the interval of 12,000B.C. to 2050A.D. over one solar cyclic step.

Comparisons of the different reconstructed SSN and GSN records. The above presented results provide long variations based on the QP properties. This allows for a quantitative estimate of the average decadal variation of millennial timescales.

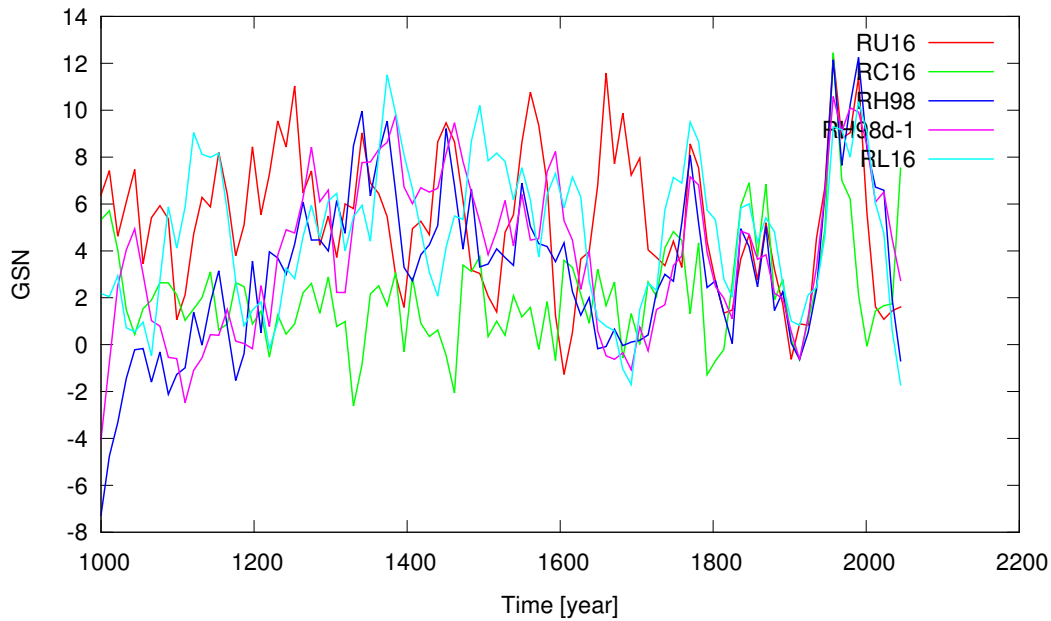


Figure 6.48 – Comparison of the different decadal reconstructed GSN series covering the interval between 1000 to 2050.

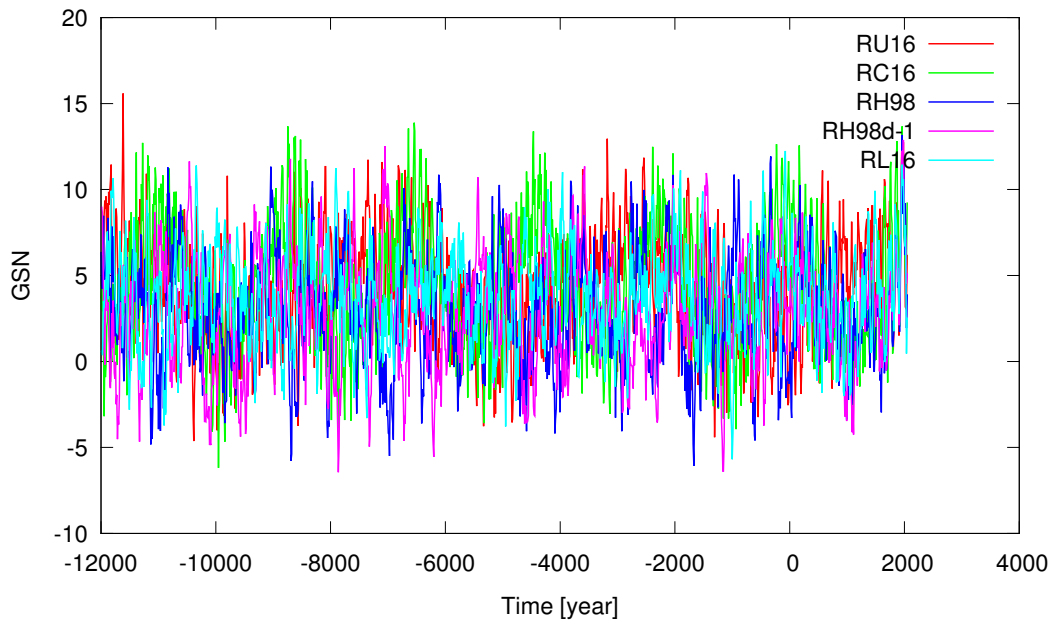


Figure 6.49 – The multi-millennial reconstruction of the decadal GSN based on the QP model covering the interval between 12,000B.C. to 2050A.D.

A comparison with other occasional direct measurements of solar activity data confirms the reliability of the present reconstruction shown in Fig.6.48 for time span of 1000 – 2050. These

different reconstructions of GSN's data present similar variations identifying the known solar activity events and are discussed in next section. Multi-millennial timescale reconstructions of GSN are based on the QP model and are depicted in Fig.6.49 for the time span of 12,000B.C. to 2050A.D. These results show very chaotic variation which is complicated due to assumptions on the extrapolation of GSN. For this purpose the multi-millennial reconstruction of the GSN series is shown in detail by enlarging each cycle.

These results can be applied in studies of long-term solar terrestrial relations and the global evolution of solar activity. In the next section it was attempted to verify these calculated reconstruction series of the GSN by comparing with estimated GSN based on the physical model and identifying the historically known solar events as grand solar maxima and minima.

6.5.2 Verification of the reconstructed series

It is important to verify the variations of solar activity reconstruction, although full verification is quite impossible. In some periods the variation of initial solar activity indicators disagrees even with each other. We see in a previous Sec.6.3.2 (see Fig.6.13), the L16, U16, C16, H98 and V16 series show some disagreements which might be due to systematic effects. An independent method is needed to verify the results in order to provide a reliable quantitative estimate of the variation and the level of solar activity in the past, prior to the era of direct observations. The most used direct verification of solar activity reconstructed series is a comparison between actual SSN records and physical based reconstructions covered on a millennium timescales. These physical-based GSN reconstructions allow the testing of reconstruction of regression-based models, provided there is a long set of independent direct data. Additionally, this included all the available data to increase the number of statistics of the regression and the possibility of testing the model. The verification of the reconstructed series (see Figs.6.36-6.47) for the period of the observed interval is convenient for testing purposes as it includes the whole range of solar activity variation levels from the almost spotless Maunder minimum (MM) to the modern period of a very active Sun.

Verification of GSN reconstruction via physical-based proxies. Fig.6.50 depicts the decadal observed GSN data variations for the last four centuries, but it should be noted that the estimated data of different GSN do not present perfect correlations between each other. The data of U16 for example has a high level of activity during the period of 1930 – 1975. Non coherence of observed/estimated GSN's occur so that it is difficult to verify variation of their reconstructions.

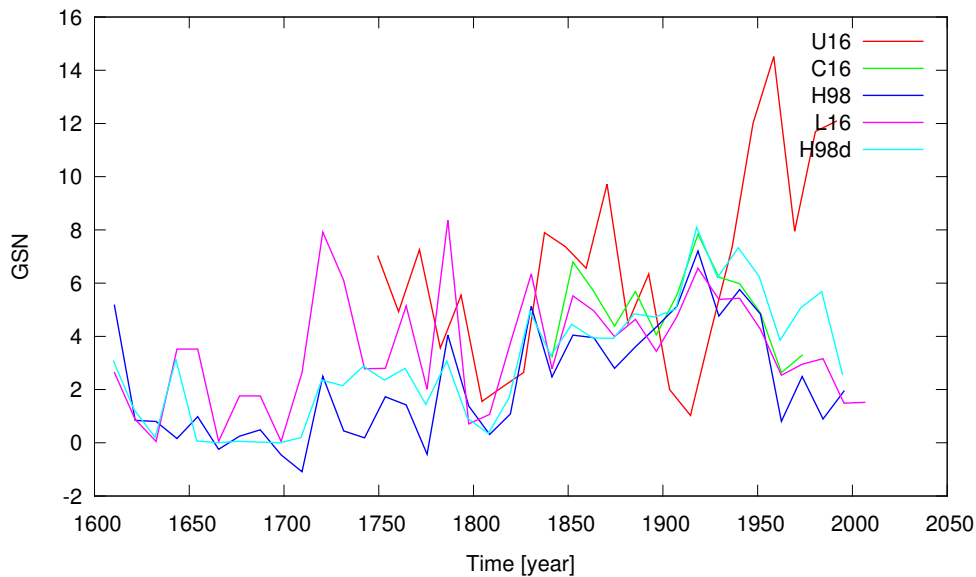


Figure 6.50 – Comparison of estimated decadal GSN's based on the observed records (U16, C16, H98, H98d and L16).

In Fig.6.51 is depicted a comparison of the QP approximation based reconstructions of U16, C16, H98, H98-1 (one year smoothed daily observed H98d), L16 (see Sec.6.3.2) and physical model (radio nuclides) based reconstruction of U03, U14 and S04 (see Sec.6.4). The reconstruction series of observed GSN data presents the decadal variation as the physical-based reconstructions of GSN which are given in decadal steps.

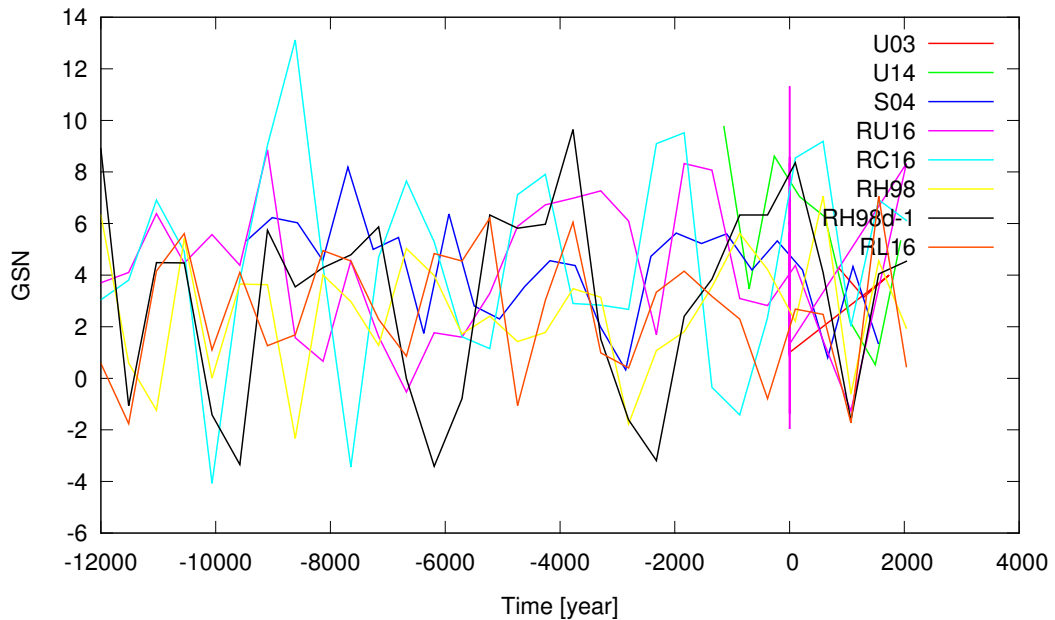


Figure 6.51 – Comparison of the physical based model reconstruction of the GSN (U03, U14 and S04-for the quantitative view was divided by a factor 5) and with reconstruction of the estimated GSN's based on the observed records (RU16, RC16, RH98, RH98d and RL16), the series are averaged over one magnetic cycle.

The comparison between isotopes is an indirect test of solar activity reconstruction. The extrapolation of the SSN data for the last millennium, yields very similar results when compared to the isotopic based reconstruction data series, which have some differences in small details. It was argued that with a longer comparison over the entire Holocene timescale, the variation of the solar activity reconstruction from the radio nuclides throughout centennial timescales is similar but with discrepancies in long-term trends (Vonmoos et al., 2006). Fig.6.51 shows a different variation of the reconstructed series but it is difficult to confirm the accuracy of the extrapolations of GSN's records. Thus, we need additional verification of these reconstructions. The QP features based on the reconstruction of long-term solar activity dynamics present global peaks around an 80 year period which corresponds to the Gleissberg periodicity. The period of about 210 years is known as the de Vries/Suess cycle, which is prominent in QP properties as is the period around 350 years identified after 6000 B.C. (Steinhilber et al., 2012). The 2000 – 2400 year Hallstatt cycle manifests itself as a modulation of long-term solar activity (Vitinskij et al., 1986), leading a clustering of grand minima (Usoskin et al., 2007).

Verification of SSN reconstructions determined by known solar events. Another verification of the reconstructed GSN's data is to identify known solar events which are recorded from history. Comparison of the decadal reconstructed variation of yearly smoothed daily observed SSN data and radio isotope based reconstruction of the GSN data is displayed in Fig.6.52 for the interval between 200 and 2050. The reconstruction of DRDSN series the identifies main known historical events and is correlated with the physical-based reconstruction of GSN as U14 and S04 series. There are also some peaks inversely correlated and

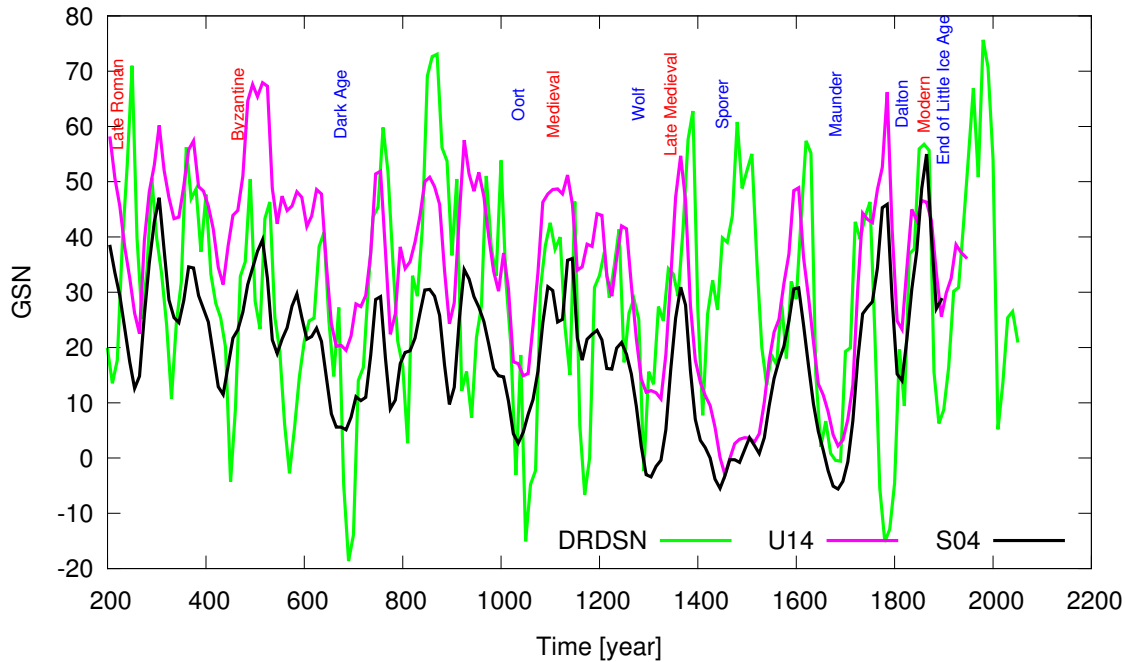


Figure 6.52 – Comparison of the yearly smoothed daily observed reconstruction of DRDSN (divided by factor of 10 for the purpose of a quantitative view) vs the radio nuclide based decadal reconstruction of U14 and S04, covering the interval of 200 – 2050 over one solar cyclic step.

delayed e.g. the interval of 1399 – 1524 years which overlaps with Sporer minimum during the period 1416 – 1534. Comparison of the decadal reconstructed variation of the yearly observed YSN data and the radio isotope based reconstruction of the GSN data displayed in Fig.6.53 for the interval of 200 to 2050. The reconstruction of the DRYSN series identifies the main known historical events and is perfectly correlated with the physical-based reconstruction of the GSN. It should be noted that the reconstructions of the DRYSN and DRDSN are based on the observed data records which is independent to the U14 or S04 isotopes based reconstructed proxies. Thus, good correlation of two independent series prove reliability for the used QP properties and then its long-term variations. In Fig.6.54 is presented the decadal reconstruction of the recorded L16 solar GSN data (DRL16) and the isotopes based reconstruction of GSN (U14 and S04 series). In Fig.6.54 the variation of two series show the same correlation, except with some inverted minima such as the Oort ($\sim 1010 - 1050$) period.

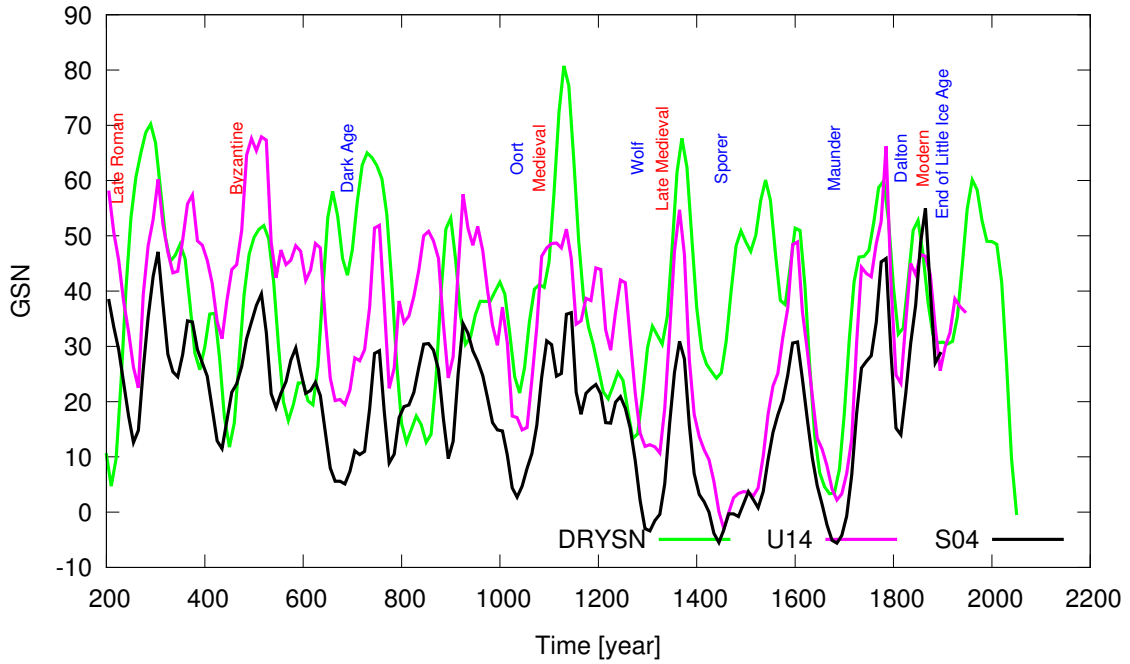


Figure 6.53 – Comparison of the yearly observed reconstruction of DRYSN (multiplied by factor of 10 for the purpose for a quantitative view) vs the radio nuclide based decadal reconstruction of U14 and S04, covering the interval between 200 – 2050 over one solar cyclic step.

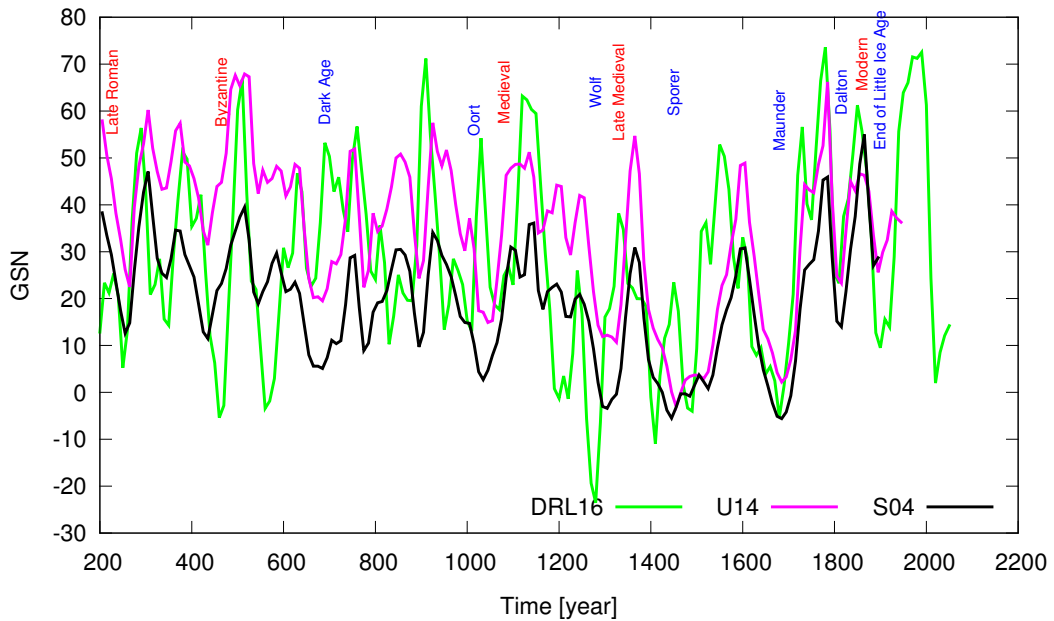


Figure 6.54 – Comparison of the yearly observed reconstruction of DRL16 (multiplied by factor of 7 for the purpose of a quantitative view) vs the radio nuclide based decadal reconstruction of U14 and S04, covering the interval between 200 – 2050 over one solar cyclic step.

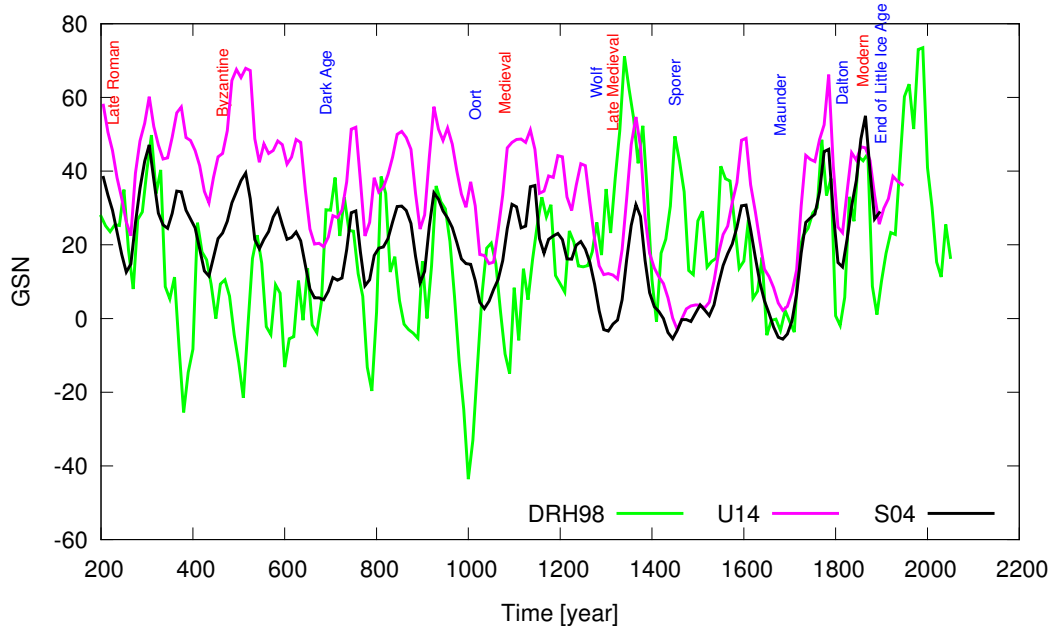


Figure 6.55 – Comparison of the yearly observed reconstruction of DRH98 (multiplied by factor of 6 for the purpose of a quantitative view) vs the radio nuclide based decadal reconstruction of U14 and S04, covering the interval between 200 – 2050 over one solar cyclic step.

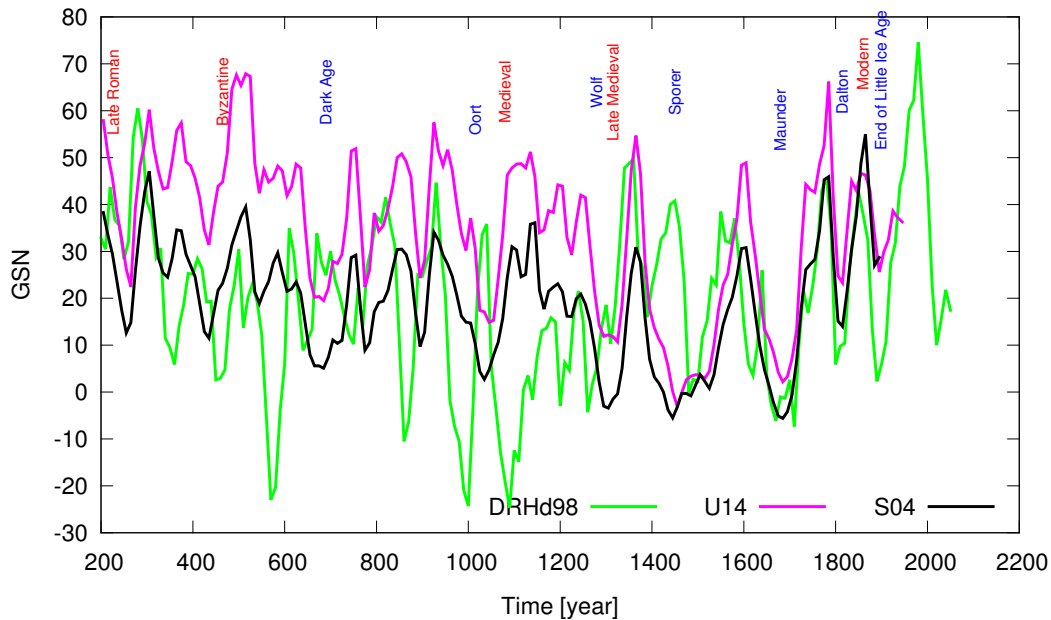


Figure 6.56 – Comparison of the yearly observed reconstruction DRHd98 (multiplied by factor of 6 for the purpose of a quantitative view) vs the radio nuclide based decadal reconstruction of U14 and S04, covering the interval between 200 – 2050 over one solar cyclic step.

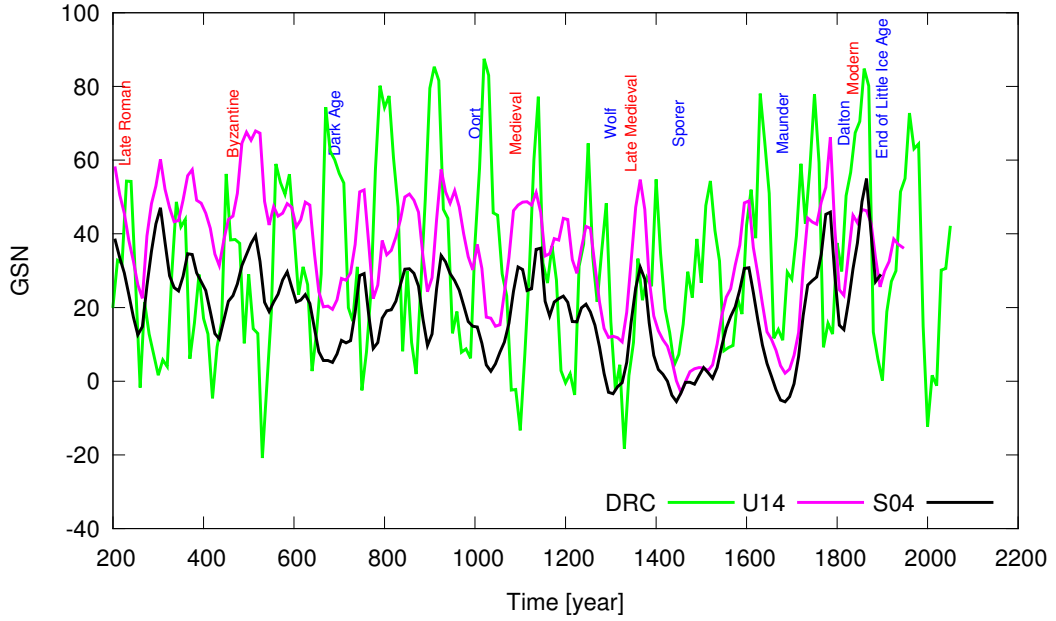


Figure 6.57 – Comparison of the yearly observed reconstruction DRC (multiplied by factor of 7 for the purpose of a quantitative view) vs the radio nuclide based decadal reconstruction of U14 and S04, covering the interval between 200 – 2050 over one solar cyclic step.

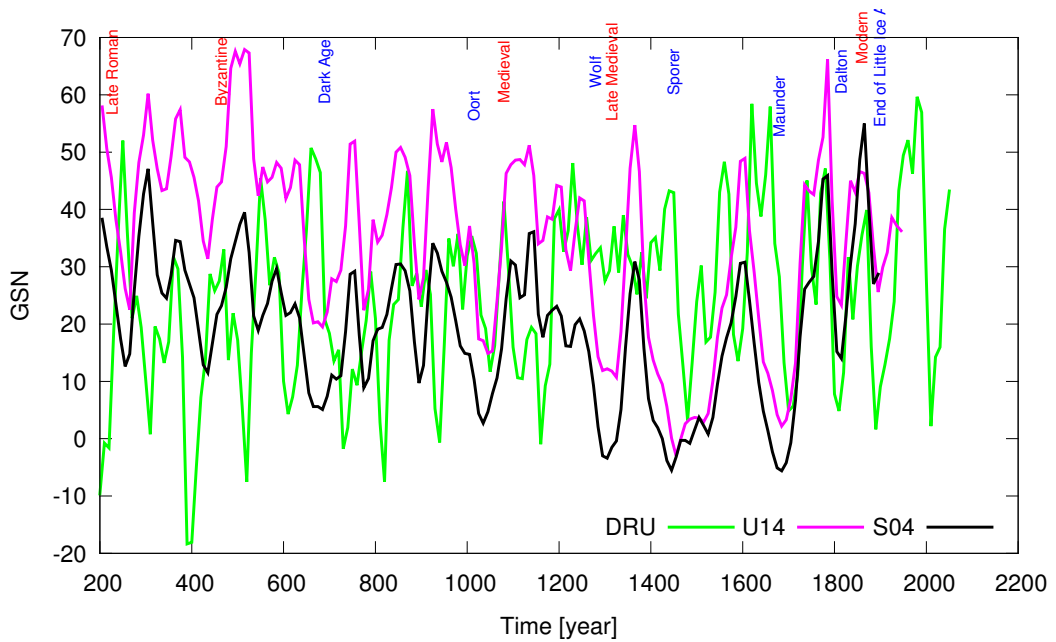


Figure 6.58 – Comparison of the yearly observed reconstruction DRU (multiplied by factor of 6 for the purpose of a quantitative view) vs the radio nuclide based decadal reconstruction of U14 and S04, covering the interval between 200 – 2050 over one solar cyclic step.

The Figs6.55-6.58 show a pattern between the decadal GSN reconstruction (DRH98, DRHd98, DRC and DRU) based on the QP approximations of the observed GSN and the independent radio nuclide based GSN reconstruction (U14 and S04). In each maxima and minima amplitudes the historically known recorded events are marked vertically in the figures. The correlations of the reconstructed GSN are remarkable, although some known minima and maxima are inverted or delayed. Some historically known grand maxima and minima events periods are not completely determined and the duration (start and end timings) of these events have been recorded differently on the various records.

Additionally, Figs.6.59 and 6.60 show the comparison of the long-term reconstruction proxies.

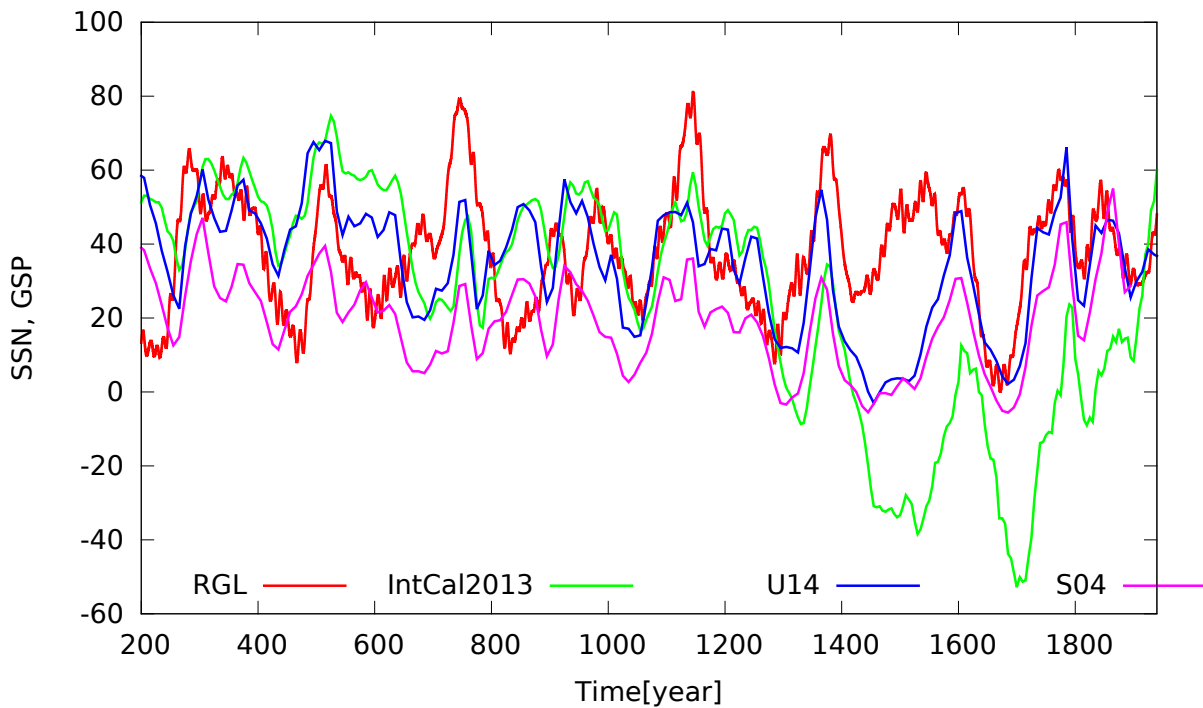


Figure 6.59 – Comparison of the yearly observed decadal reconstruction of RGL one year smoothed for quantitative view vs the radio nuclide based decadal reconstruction of U14, S04 and the radiocarbon calibration curve of IntCal2013 (multiplied by a factor of 3), covering the interval between 200 – 2050 over one solar cyclic step.

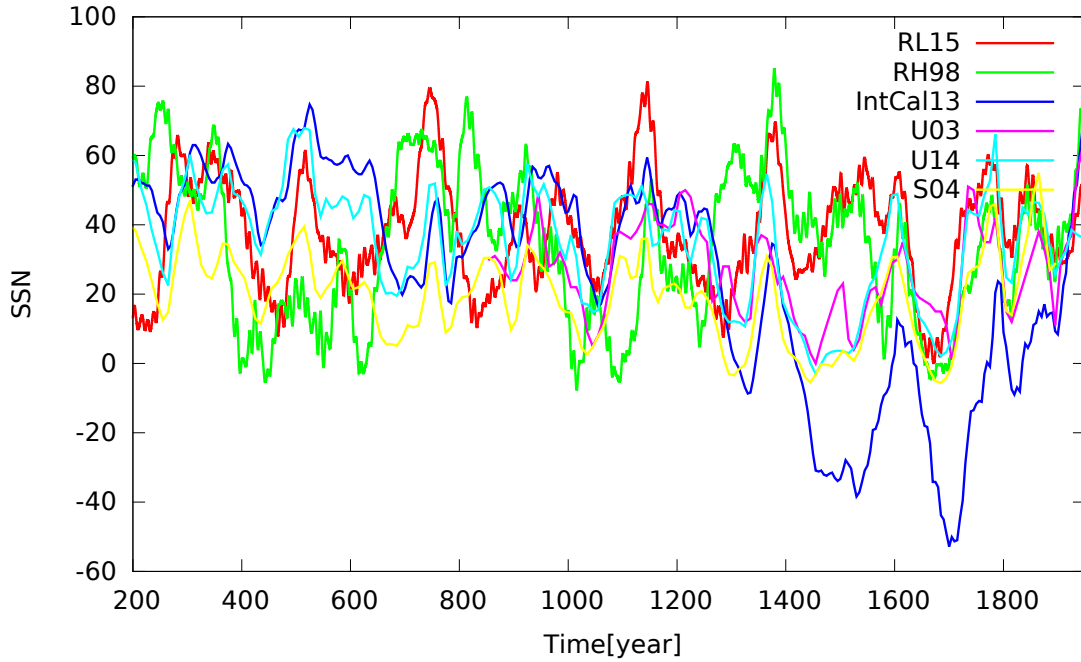


Figure 6.60 – Comparison of the yearly observed decadal reconstruction of RL15, RH98 (one year smoothed for quantitative view) vs the radio nuclide based decadal reconstruction of U14, U03, S04 and the radiocarbon calibration curve of IntCal2013 (multiplied by a factor of 3), covering the interval between 200 – 2000 over one solar cyclic step.

The reconstructed decadal GSN using the QP approximation with one year smoothed variation are noted as RL15 and RH98. IntCal13 is a northern hemisphere atmospheric radiocarbon calibration curve from ^{14}C (Reimer, 2013). The reconstructed GSN records are from radio nuclides noted as U03, U14 and S04. It is notable that the main maxima and minima peaks are well represented.

Verification of multi-millennial reconstructions of DSN and YSN series. As were shown in previous results the reconstruction of SSN series between 200–2050 demonstrated reliable results presenting the well known solar events. Thus, we can estimate the reconstructions of SSN data for longer time spans i.e. for multi-millennial timescales. The multi-millennial reconstruction of daily observed DSN shown in Figs.6.61-6.62 and for yearly observed YSN shown in Figs.6.63-6.64.

The DRDSN is a daily observed decadal one year smoothed reconstruction, while DRYSN is a yearly observed decadal reconstruction. The U14 and S04 proxies are physical-based reconstruction of GSN. Figs.6.62 and 6.64 show the comparison between reconstructed DSN, YSN and S04, as the data of S04 is given for interval of 1145B.C.-1955A.D., while for U14 is 1150B.C.-1950A.D.(for more see Sec.6.4.3).

It should be noted that DRDSN and DRYSN reconstructions are based on the observed SSN data while U14 and S04 are based on the radio isotopes proxies. This means that the two series are independent and measured from different solar activity indicators. The results of DSN and YSN reconstructions from Figs.6.61 and 6.63 for the interval of 1200B.C. to 200A.D. demonstrate the excellent coherence presenting well matched peaks of maxima and minima. Although, comparisons shown in Figs.6.62 and 6.64 present some variation of inverse amplitudes between DRDSN/DRYSN and S04 reconstruction series.

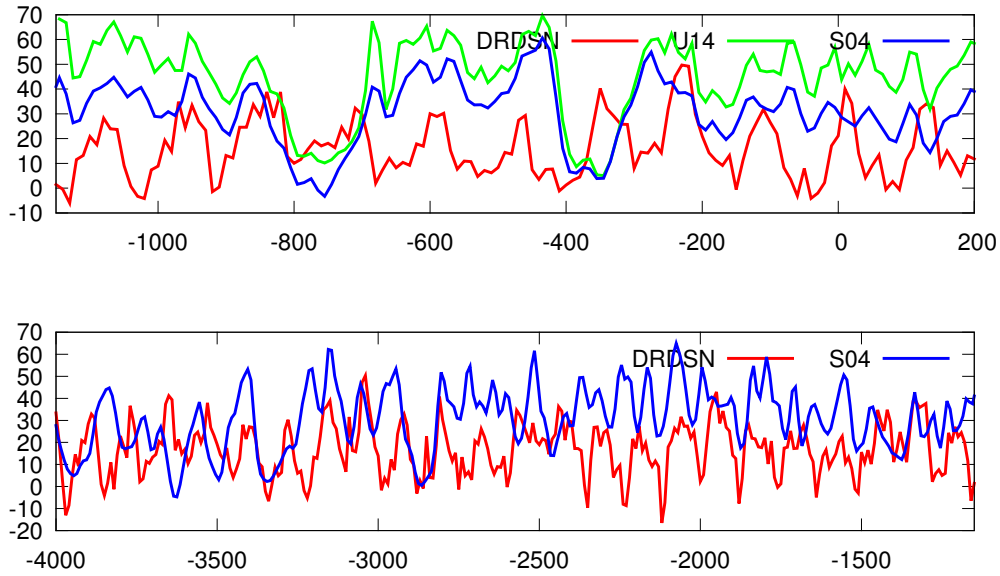


Figure 6.61 – Comparison of the daily observed one year smoothed decadal reconstruction of DRDSN (divided by a factor of 5) vs the radio nuclide based decadal reconstruction of U14 and S04, covering the interval from 4000B.C. to 200A.D. over one solar cyclic step.

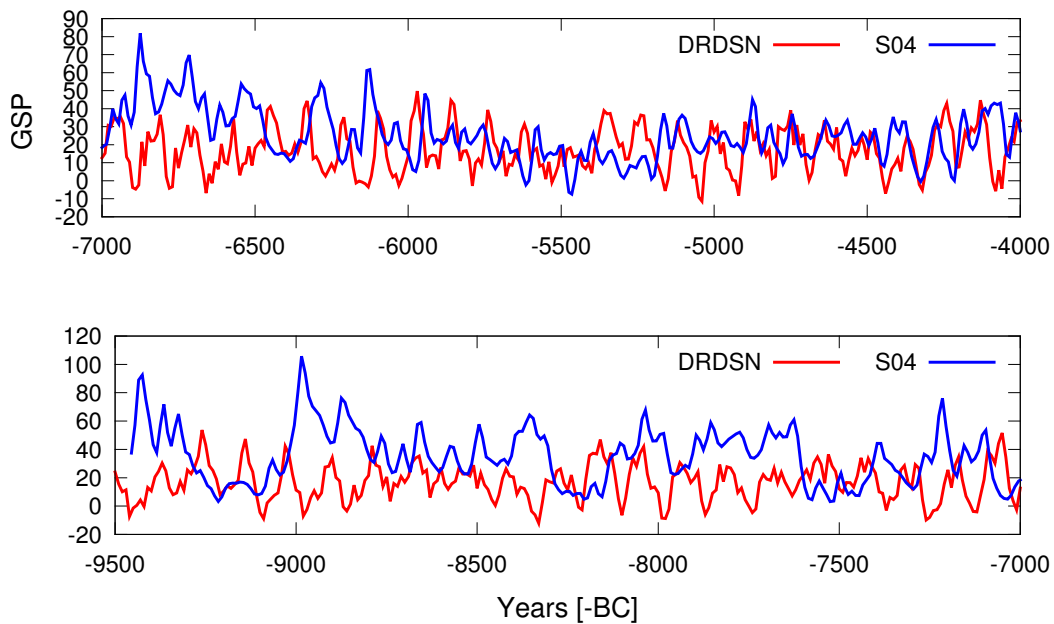


Figure 6.62 – Comparison of the daily observed one year smoothed decadal reconstruction of DRDSN (divided by a factor of 8) vs the radio nuclide based decadal reconstruction of S04, covering the interval from 9500B.C. to 4000B.C. over one solar cyclic step.

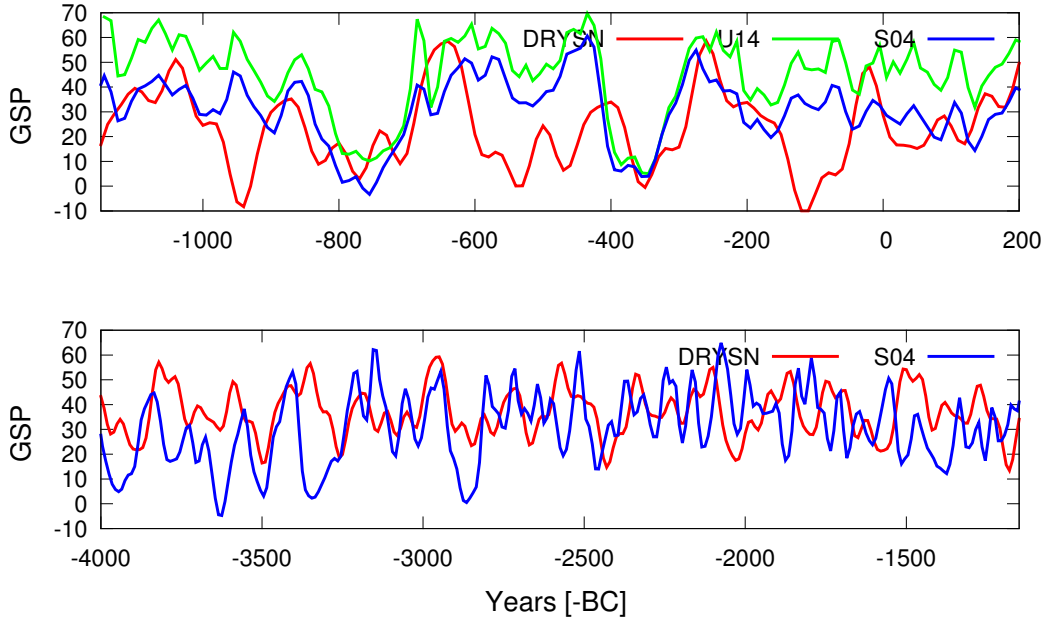


Figure 6.63 – Comparison of the yearly observed decadal reconstruction of DRYSN (multiplied by a factor of 10) vs the radio nuclide based decadal reconstruction of U14 and S04, covering the interval from 4000B.C. to 200A.D. over one solar cyclic step.

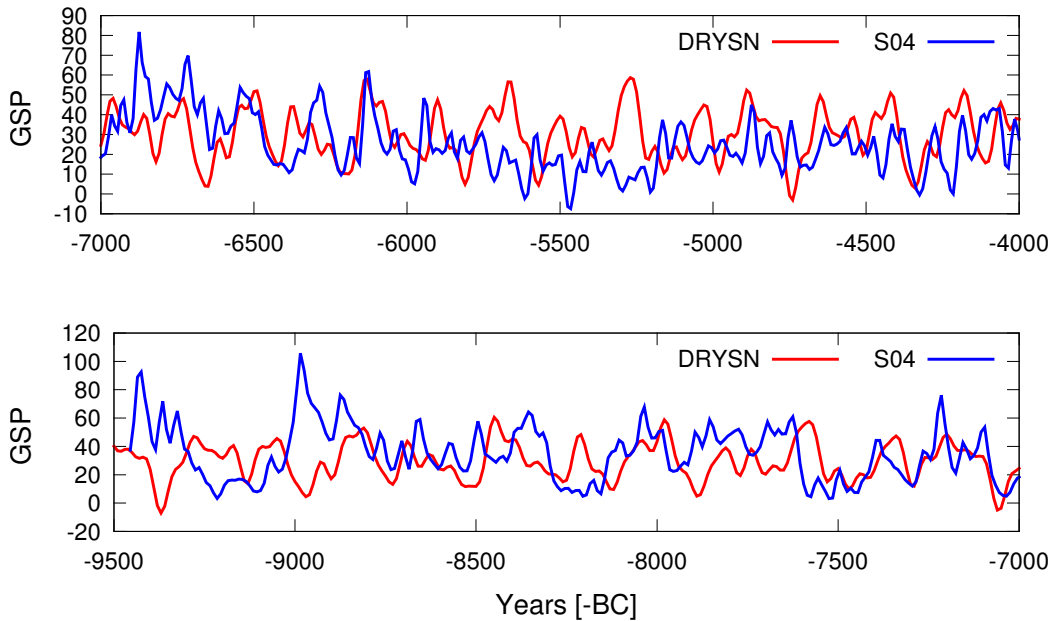


Figure 6.64 – Comparison of the yearly observed decadal reconstruction of DRYSN (multiplied by a factor of 10) vs the radio nuclide based decadal reconstruction of S04, covering the interval from 9500B.C. to 4000B.C. over one solar cyclic step.

Verification of multi-millennial reconstructions of GSN series. In exactly same way as calculated for DSN and YSN, in Figs.6.65-6.73 are shown the decadal reconstruction of the GSN records as L16, U16, H98d, H98, C16 respectively (see Sec.6.3.2) covering the interval of 4000B.C. to 200A.D.

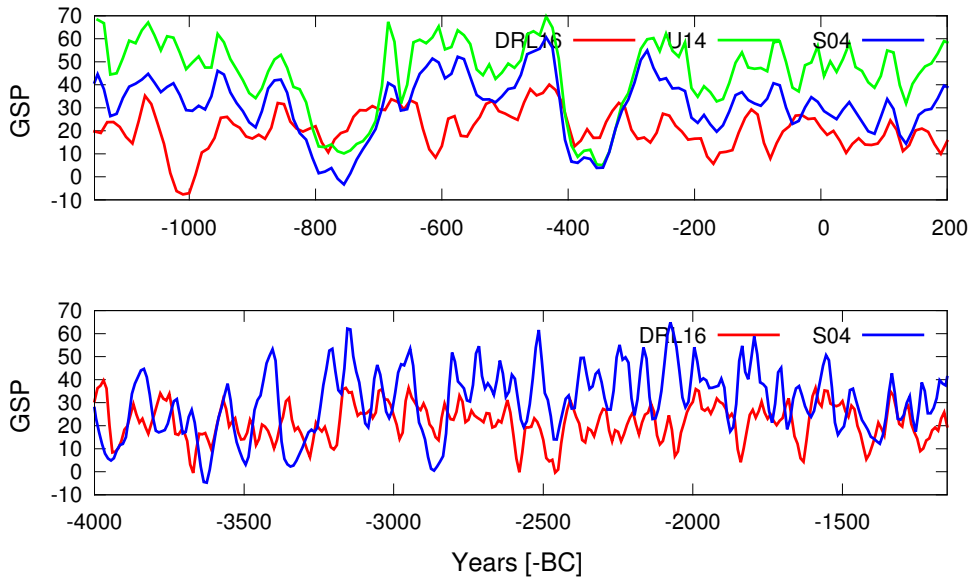


Figure 6.65 – Comparison of the yearly estimated decadal reconstruction of DRL16 (multiplied by a factor of 3) vs the radio nuclide based decadal reconstruction of U14 and S04, covering the interval from 4000B.C. to 200A.D. over one solar cyclic step.

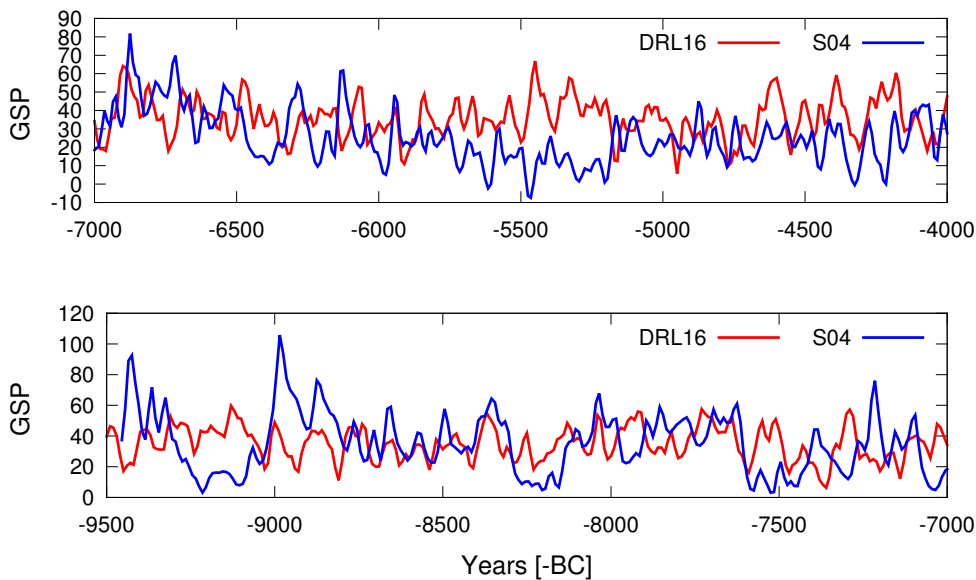


Figure 6.66 – Comparison of the yearly estimated decadal reconstruction of DRL16 (multiplied by a factor of 3) vs the radio nuclide based decadal reconstruction of S04, covering the interval from 9500B.C. to 4000B.C. over one solar cyclic step.

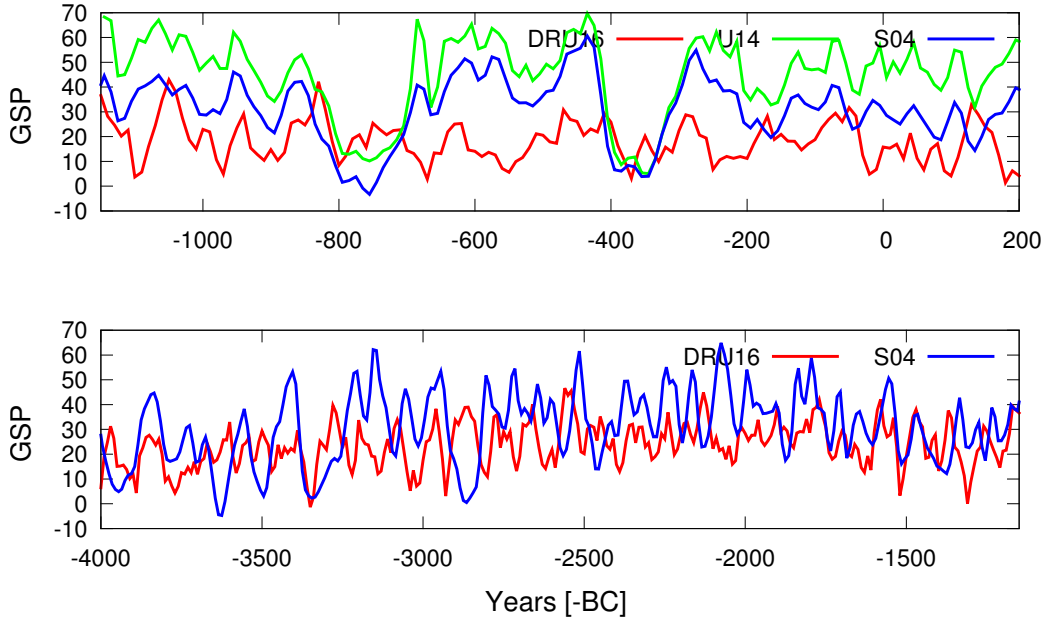


Figure 6.67 – Comparison of the yearly estimated decadal reconstruction of DRU16 (multiplied by a factor of 3) vs the radio nuclide based decadal reconstruction of U14 and S04, covering the interval from 4000B.C. to 200A.D. over one solar cyclic step.

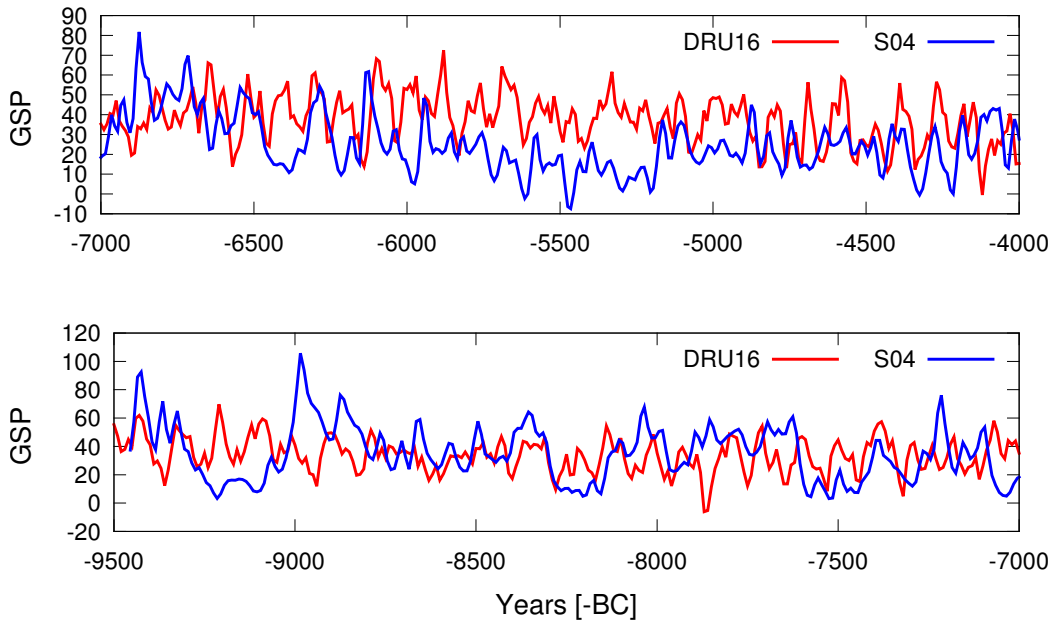


Figure 6.68 – Comparison of the yearly estimated decadal reconstruction of DRU16 (multiplied by a factor of 3) vs the radio nuclide based decadal reconstruction of S04, covering the interval from 9500B.C. to 4000B.C. over one solar cyclic step.

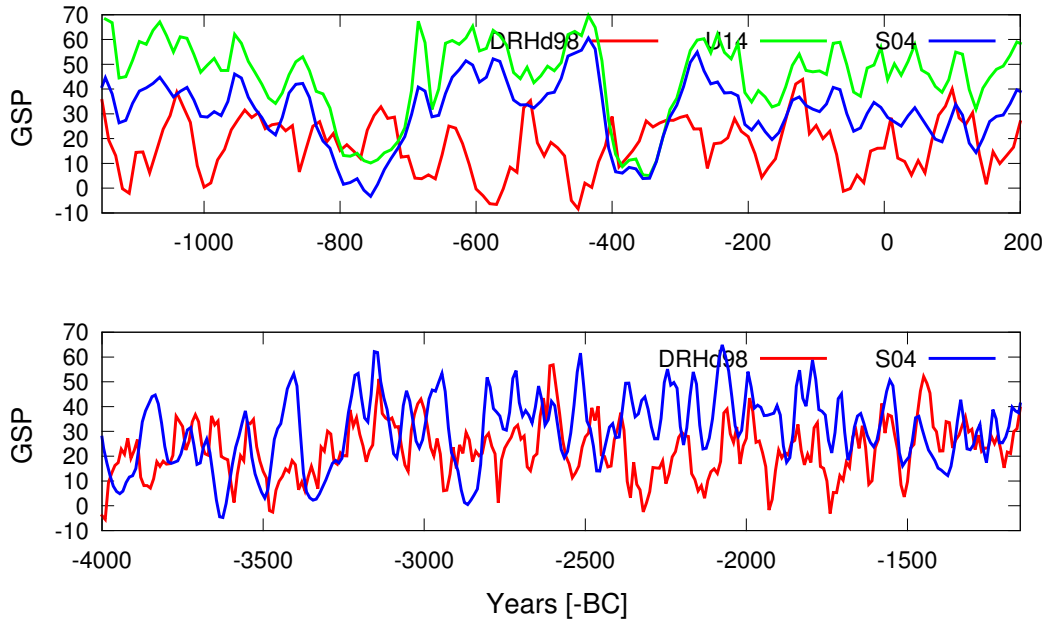


Figure 6.69 – Comparison of the daily estimated decadal one year smoothed reconstruction of DRHd98 (multiplied by a factor of 3) vs to the radio nuclides based decadal reconstruction of U14 and S04, covering the interval from 4000B.C. to 200A.D. over one solar cyclic step.

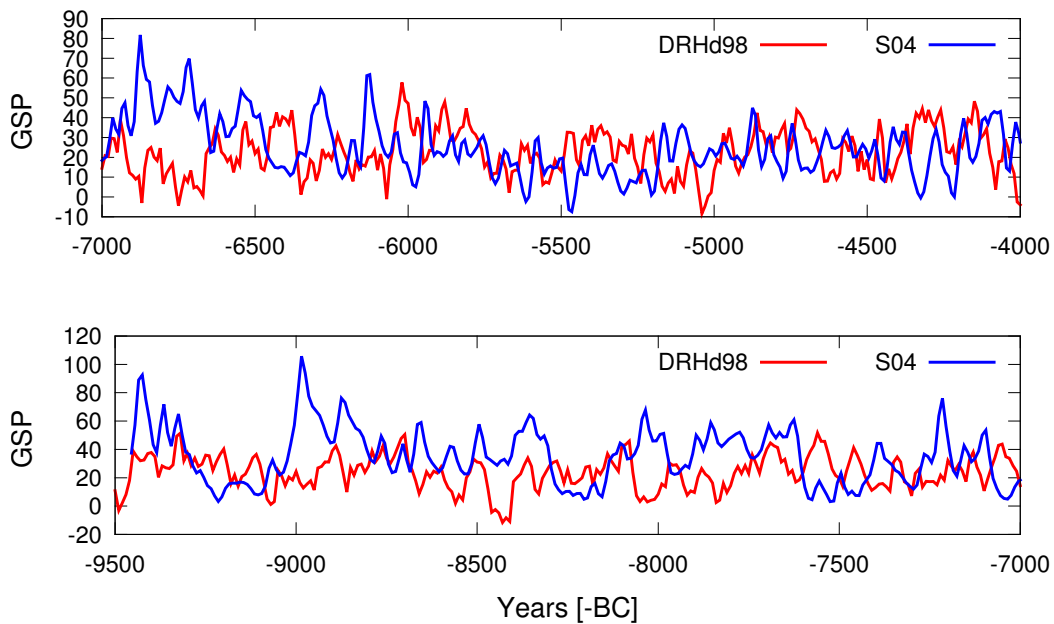


Figure 6.70 – Comparison of the yearly estimated decadal reconstruction of DRHd98 (multiplied by a factor of 3) vs to the radio nuclides based decadal reconstruction of S04, covering the interval from 9500B.C. to 4000B.C. over one solar cyclic step.

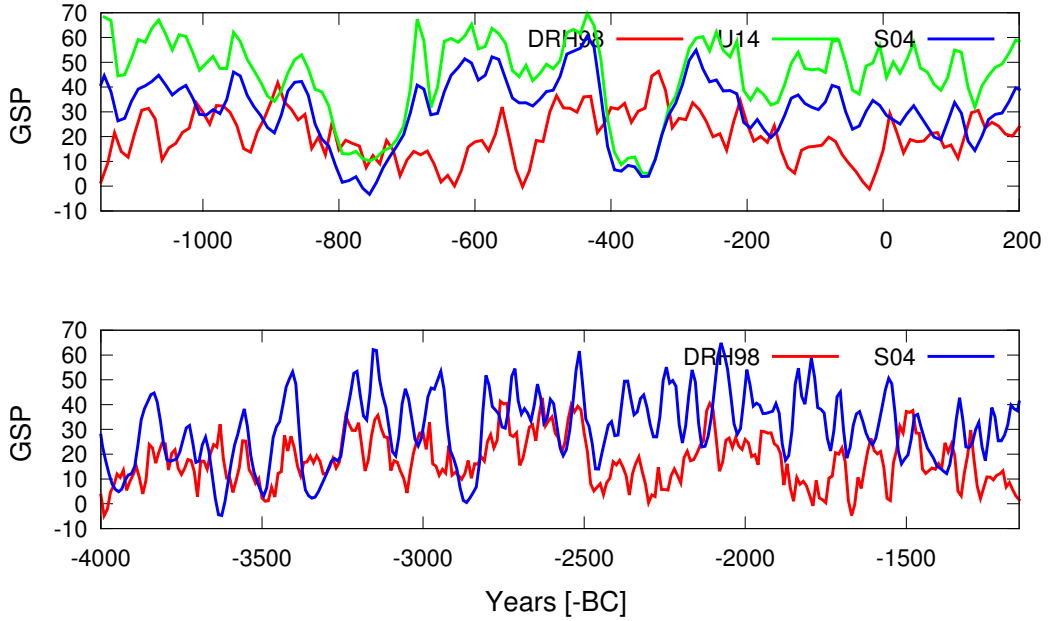


Figure 6.71 – Comparison of the yearly estimated decadal reconstruction of DRH98 (multiplied by a factor of 3) vs the radio nuclide based decadal reconstruction of U14 and S04, covering the interval from 4000B.C. to 200A.D. over one solar cyclic step.

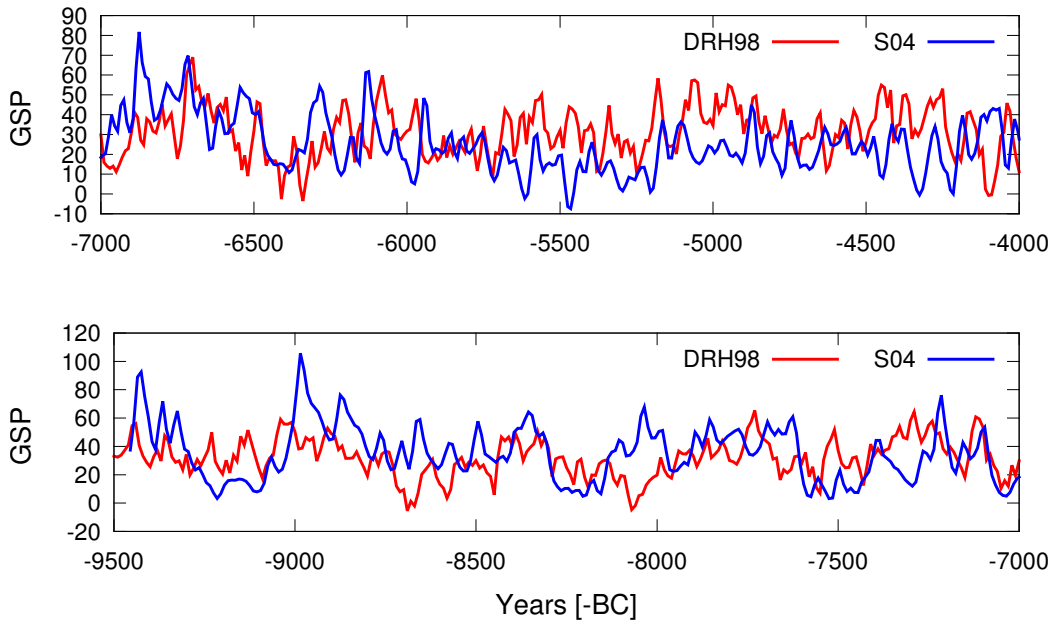


Figure 6.72 – Comparison of the yearly estimated decadal reconstruction of DRH98 (multiplied by a factor of 3) vs the radio nuclide based decadal reconstruction of S04, covering the interval from 9500B.C. to 4000B.C. over one solar cyclic step.

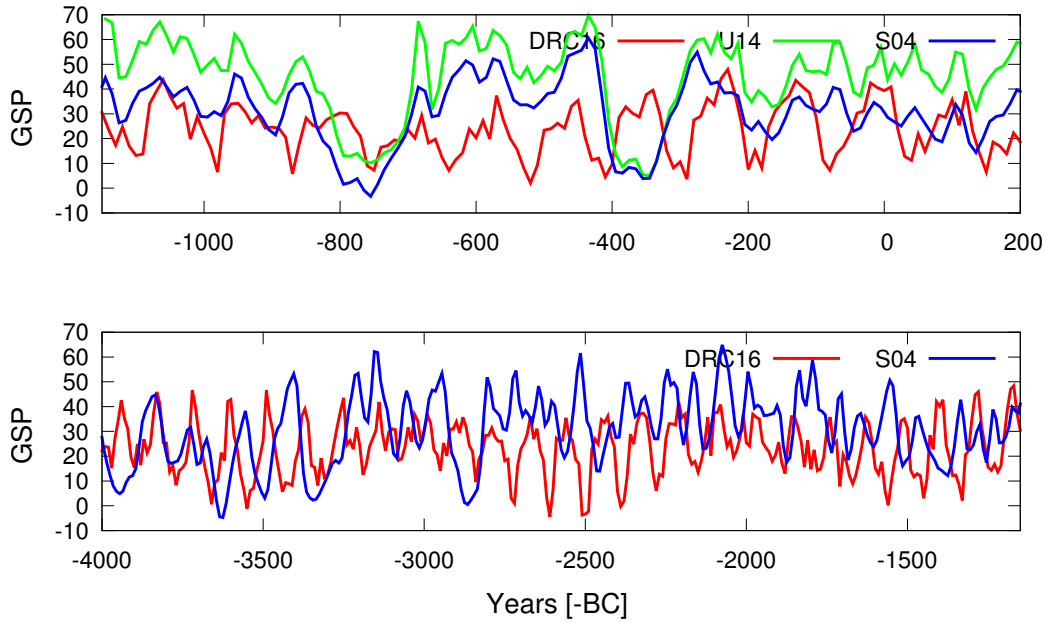


Figure 6.73 – Comparison of the yearly estimated decadal reconstruction of DRC16 (multiplied by a factor of 3) vs the radio nuclide based decadal reconstruction of U14 and S04, covering the interval from 4000B.C. to 200A.D. over one solar cyclic step.

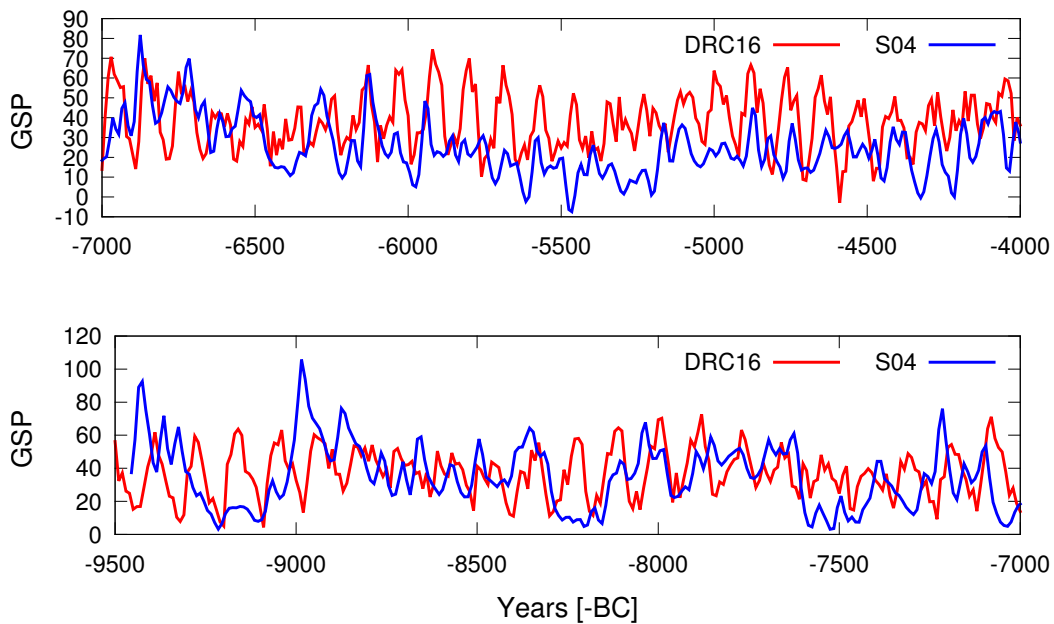


Figure 6.74 – Comparison of the yearly estimated decadal reconstruction of DRC16 (multiplied by a factor of 3) vs the radio nuclide based decadal reconstruction of S04, covering the interval from 9500B.C. to 4000B.C. over one solar cyclic step.

The reconstruction of the GSN records based on their QP approximation as calculated in Sec.6.3.2 and shown with full frequency sets. The reconstructions of DRL16, DRU16, DRHd98, DRH98 and DRC16 series show the similar variation with the physical-based U14 and S04 proxies. For interval of 9500B.C. to 4000B.C. the reconstructions of QP based GSN series (DRL16, DRU16, DRHd98, DRH98, DRC16) are also compared with S04 proxies as shown in Figs. 6.66-6.74. These results show also inverted peaks of amplitudes although the periods present the similar decadal variations.

The above presented decadal multi-millennial reconstructions of the SSN and GSN series have some correlation with the estimated U14 and S04 proxies prior to 4000B.C., which reveals the reliability of the used QP decompositions. The identified grand minima and maxima events coincidentally follow the estimated U14 and S04 series, according to the millennial evolution of the solar activity reconstruction. Identified grand maxima and minima have the periodicity of long-term cyclic variability. Considering that the QP based decadal extrapolation (DRL16, DRU16, DRHd98, DRH98 and DRC16) of GSN observed data and the physical-based GSN proxies (U14 and S04) are independently reconstructed, these series show excellent correlation of periods. However, it is defined by stochastic and chaotic processes (based on a purely mathematical method without taking into account of physics of the Sun) which also needs deeper investigation by taking into account the internal physical processes of the Sun.

The presented results and estimations draw the following conclusions: The observed SSN and GSN series are based on cosmogenic isotopes and proxies of radio nuclides were analysed by means of modern frequency analysis.

It is evident that we need reliable information on the behaviour of different parameters of solar activity over long timescales. The global magnetic field of the Sun, measurements of galactic cosmic ray intensity and fluxes of solar radiation in different spectral ranges provide reliable information only for the last few decades from direct observations. Longer time interval records of solar activity are substantially less reliable but can be obtained only from solar proxies as historical records and cosmogenic isotopes. Another approach is to reconstruct solar activity proxies to study the long secular solar variability.

The QP based long-term reconstruction variation of solar activity are distinguished at least during the last millennium the cycles of Gleissberg and Suess (see for example Tab.6.1 and Tab.6.2). The Gleissberg cycle shows a wide frequency band with a double structure consisting of 50 – 80 years and 90 – 140 years periodicities while the Suess cycle shows a variation with a period of 150 – 280 years. The centennial cycle revealed by Gleissberg (Gleissberg, 1944) is considered to have a variation with period of 80 – 90 years. The variation of solar activity with a period of about 160 – 270 years (Schove, 1983d) known as Suess cycle was found from variation in tree-ring radiocarbon records. QP distinguished the frequencies as 55, 160, 80 – 130, 58 and 65 years, which was suggested by Schove (1983a) as periodicities of solar cycles.

The centennial solar variability also have spectral power in a wider frequency band than Gleissberg cycle, such as 57 – 80. The amplitude variations with periods of 88, 59, 78.5 and 94.5 years are according to Cole (1973) due to an amplitude modulation of the solar cycles by a period of 11.9 ± 0.3 years, while a 10.45 year period is the basic phase variation of 190 years. Wittmann (1978) showed that the yearly averaged spectrum of SSN clearly reveals a dependence of 92 and 55 years of periodicities. These periodicities also were identified in the results using frequency analysis. The ~ 89 , ~ 148 and ~ 126 year periodicities were found by Stuiver & Quay (1980) using carbon proxies. Chistyakov (1983) identified two kinds of

centennial solar variability ~ 115 and ~ 95 cycles. The centennial solar cycle is not constant and most likely changes from about 65 to more than 130 years with dominating modes of 70 – 80 and 100 – 120 years. These solar centennial variability over a long-term scale was investigated by Nagovitsyn (1997) using historic data.

In next section these QP based reconstructions of SSN and GSN series are used to search for correlations of the deformation of the solar surface.

Chapter 7

Approaches of the dynamical model of planetary influences

a strong climatic change caused by a weak forcing of planetary orbits ...

Milankovitch's theory concept

7.1 Physical model of planetary influence

In this section we studied the deformation coefficients of the surface of the Sun exerted by planetary tidal forces. Current models of solar activity suggest that the origin and modulation of the solar activity are related with the Sun's dynamo, although its causes are still unclear. Thus, research is being undertaken based on an external effect. Mostly these approaches are based on some of the physical dynamical characteristics of planetary theory. Examples include its tidal effect on the Sun's surface, its orbital angular momentum relative to Sun, acceleration of the planets and its derivatives etc. These various planetary phenomena seem to be related with the sunspot cycle and may imply some resonance (Scafetta, 2010b). These approaches still require verification to explain modulation and to therefore be a cause of phenomenal solar events. While energy considerations clearly show that planets cannot be the direct cause of solar activity, it remains an open question: can planets perturb the operation of the solar dynamo with small effects?

In this section we present a simple dynamical approach based on the tidal theory and an analysis of planetary harmonics without taking into account any physical processes of the solar or planetary interior. We compute the deformation of the Sun from the positions of the generative bodies to estimate the gravity field coefficients. A similar investigation was presented by Scafetta (2009, 2010b, 2014) as a prediction of the solar dynamo based upon analysis of observational data. The research is based on use of physical dynamo models in attempts to forecast the solar activity. Recently, more attention has been taken to link solar cycles with planetary harmonics, i.e. a planetary dynamical approach of Abreu et al. (2012). In our research we present formalism designed to model a tidal perturbation of each of the planets which effects the Sun's surface. Namely to investigate the relationship of the sunspot cycle and planetary tidal forces. Our approach is based on a purely dynamical model of planetary motions and the Sun is considered as an elastic three axis body with constant spin rate. Here we present 2nd degree potential coefficients of the Sun which are varying due to

tidal forces of the planets. The shape of the Sun is described by its gravity field coefficients. We are only interested in the dynamical effects between the planets and the Sun. The model does not take into account any internal physical processes of the Sun. The solar pole vector K is fixed and the speed of rotation around this vector K is constant. Thus the Sun is not deformed by its rotation around its spin-axis which is constant. In this model the Sun is deformed only by the differential gravitational field of the planets which are considered as point masses. Our dynamical model is developed for describing the tidal effect exerted by planetary motion on the deformation of the non-spherical Sun's surface. The results are compared to the corresponding variation of solar activity records. The present work mainly used the annual, averaged relative SSN and GSN during the period of 1610 – 2016 to study the long-term variations, to identify some meaningful insights for the past and coming solar activity cycles.

7.1.1 Interaction between non-spherical and material bodies

Here are the expressions that allow the calculation of interactions between material bodies of not negligible dimensions in front of the separation distance. This approximation is often sufficient to describe the interactions in the Solar System. The object here is a development of potential at any point between an extended body without particular symmetry and another material body, which will be called perturbative. The purpose here is to provide a consistent basis of two different reference frames from \mathcal{R}_0 fixed reference frame to \mathcal{R}_E mobile reference frame where the position vector and velocity of the material perturbative bodies expressed, which will be based on that proposed by Lambeck (1980). The reference $\mathcal{R}_E = (O_E, \mathbf{I}, \mathbf{J}, \mathbf{K})$ of the non-spherical body whose origin O_E coincides with the center of mass. As the extended body usually has a rotation, \mathcal{R}_E is in motion with respect to the inertial reference frame \mathcal{R}_0 where the integration is performed. The passage from one reference frame to the other is treated in Sec.7.4.2.

7.1.2 Expression of the potential

Let a perturbative punctual body, of mass m , be located at P on the outside of the extended body with coordinates $\mathbf{r} = (x, y, z)$ in the reference frame \mathcal{R}_E . Let δm , an element of mass of the extended body, from coordinates $\boldsymbol{\rho} = (x', y', z')$ in \mathcal{R}_E , as shown in Fig.7.1. The gravitational potential δU at P due to δm , G is the gravitational constant, is then:

$$\delta U(\mathbf{r}) = -\frac{G}{\Delta} \delta m. \quad (7.1)$$

In this expression

$$\Delta^{-1} = \|\mathbf{r} - \boldsymbol{\rho}\|^{-1} = (r^2 + \rho^2 - 2r\rho \cos \psi)^{-1/2} \quad (7.2)$$

$$= \frac{1}{r} \left(1 + \left(\frac{\rho}{r} \right)^2 - 2 \frac{\rho}{r} \cos \psi \right)^{-1/2}. \quad (7.3)$$

By introducing Legendre polynomials $P_n(\cos \psi)$ (Lambeck, 1988) we have:

$$\delta U = -\frac{G}{r} \sum_{n=0}^{+\infty} \left(\frac{\rho}{r} \right)^n P_{n0}(\cos \psi) dm. \quad (7.4)$$

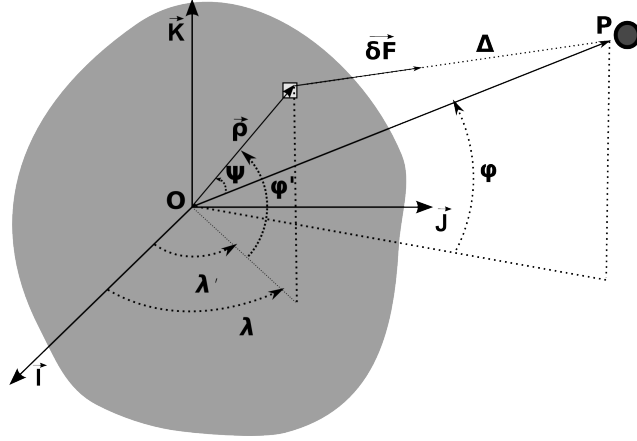


Figure 7.1 – Scheme and notations for correlations between a solid body and a punctual mass.

Knowing that an angle between the radius vector of P (\mathbf{r}) and δm ($\boldsymbol{\rho}$) is $\cos \psi = \frac{\mathbf{r}\boldsymbol{\rho}}{\|\mathbf{r}\|\|\boldsymbol{\rho}\|}$, it can be expressed as:

$$\cos \psi = \frac{\mathbf{r}\boldsymbol{\rho}}{\|\mathbf{r}\|\|\boldsymbol{\rho}\|} = \sin \varphi \sin \varphi' + \cos \varphi \cos \varphi' \cos (\lambda - \lambda'), \quad (7.5)$$

at the spherical coordinates of δm (ρ, φ', λ') and P (r, φ, λ) which is given in App.A.

We can express the potential of the extended body given by (Lambeck, 1988). The development in spherical harmonics of the potential at a point P due to an extended body with spherical (r, φ, λ) coordinates is given:

$$U(r, \varphi, \lambda) = -\frac{GM}{r} \sum_{n=0}^{+\infty} \sum_{m=0}^n \left(\frac{R}{r}\right)^n P_{nm}(\sin \varphi) (C_{nm} \cos m\lambda + S_{nm} \sin m\lambda).$$

C_{nm} and S_{nm} are called Stokes coefficients (see App.Eq.A.4) of a body that is dependent on the internal distribution of masses as a geometry and a density. It is also dependent on the reference frame in which it is expressed. The flattening J_2 of body is equal to $-C_{20}$. More generally, for all $n \geq 2$, $J_n = -C_{n0}$.

7.1.3 The relation between 2^{nd} degree coefficients and coefficients of the inertia matrix

We can also express the five potential coefficients of an extended body in six coefficients of its matrix of inertia (see for more App.A):

$$\begin{aligned} MR^2 C_{20} &= \frac{1}{2} (I_{11} + I_{22}) - I_{33}, \\ MR^2 C_{21} &= -I_{13}, & MR^2 S_{21} &= -I_{23}, \\ MR^2 C_{22} &= \frac{1}{4} (I_{22} - I_{11}), & MR^2 S_{22} &= -\frac{I_{21}}{2}. \end{aligned} \quad (7.6)$$

In above the potential coefficients of an extended body are expressed in the second degree of eccentricity (see for more App.A).

To express the inertia matrix of the extended body, let \mathcal{I} be the matrix of inertia of the extended body expressed in the reference frame \mathcal{R}_E . The coefficients of potential expressed in Eq.7.6 can be written in the second degree as:

$$\mathcal{I} = \begin{pmatrix} I_{33} & 0 & 0 \\ 0 & I_{33} & 0 \\ 0 & 0 & I_{33} \end{pmatrix} + MR^2 \begin{pmatrix} C_{20} - 2C_{22} & -2S_{22} & -C_{21} \\ -2S_{22} & C_{20} + 2C_{22} & -S_{21} \\ -C_{21} & -2S_{21} & 0 \end{pmatrix}, \quad (7.7)$$

which estimates the matrix of inertia of the extended body. The potential coefficients given in the 2^{nd} degree ($C_{20}, C_{21}, C_{22}, S_{21}$ and S_{22}), however are not sufficient to determine the inertia matrix \mathcal{I} . This is because these 5 potential coefficients of second degree for 6 coefficients in the inertia matrix (3×3 symmetric). Thus the moment of inertia I_{33} along the axis \mathbf{K} remains unknown. The matrix of inertia of any body is symmetrical as there is an orthogonal basis $\mathcal{B}' = (\mathbf{I}', \mathbf{J}', \mathbf{K}')$ wherein \mathcal{I} is diagonal. In this reference frame, the coefficients of the potential C_{21}, S_{21} and S_{22} are zero.

7.2 Deformation of extended body due to tidal effect

In an extended body, the forces which are acting on the elements of mass that compose this body can vary in intensity and direction. These variations generate internal pressures, which may deform the body if it is not perfectly rigid. In Sec. 7.1.1 we have seen that the coefficients of the potential of an extended body depend on its distribution of masses. If a body is deformed, the coefficients of the potential, and coefficients of the inertia matrix vary in time. The purpose of this part is to express the variations of the coefficients of the potential induced by the effects of solid tides.

7.2.1 Solid tides

Generally, a solid tide shows the presence of a tidal effect when the bodies are subjected to gravitational forces generated by an external body. This force, applied at two distinct points can differ in intensity and in direction at the same time. The calculation of the tidal deformation of a body is based on the tidal potential theory initiated by Darwin (1879), who supposed that deformation of the surface of bodies could be derived from the Newtonian creep law. According to tidal theory we compute instantaneous deformation of the extended body (which is in our case the Sun) directly from the positions of generative bodies for the gravity field coefficients. In our model the complex inertial structures of the Sun are not taken into account. The deformation of an extended body due to the presence of another massive body (called the generator, as shown in Fig.7.2) has an effect on the solid tide. Our reference frame is linked to a deformable body \mathcal{R}_E . In this reference frame, the generator body (supposed punctual) has spherical coordinates $(r_g, \varphi_g, \lambda_g)$. Let P be a point on the deformable body with coordinates of (r, φ, λ) as shown in Fig.7.2. We can develop the potential P due to the presence of the generated body tides:

$$V(r, \varphi, \lambda) = -\frac{GM_g}{r_g} \sum_{n=0}^{+\infty} \left(\frac{r}{r_g}\right)^n P_{0n}(\cos \psi) = -\frac{GM_g}{r_g} \sum_{n=0}^{+\infty} \sum_{m=0}^n \left(\frac{r}{r_g}\right)^n (2 - \delta_{0,m}) \frac{(n-m)!}{(n+m)!} P_{nm}(\sin \varphi) \times P_{nm}(\sin \varphi_g) (\cos m(\lambda - \lambda_g)),$$

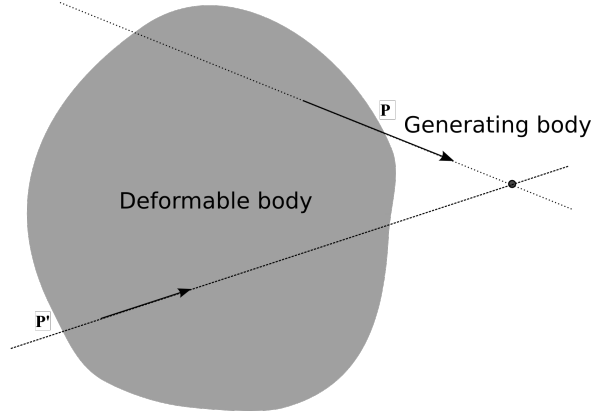


Figure 7.2 – Illustration of the effects of solid tides. The Newton force exerted at P by the generative body is different in direction and in intensity of that in P' . This difference induces internal pressures, which can deform the extended body if it is not rigid.

where M_g and r_g are respectively mass and radius vectors of a generative body, which in our case are the planets.

7.2.2 Harmonic degrees $n \geq 2$

Assuming that a body is elastic and does not dissipate, each harmonic of the variation potential at the surface ($r = R$) of the body is proportional to the same harmonic of the perturbation potential in Eq.7.8, following (Love, 1927) we assume :

$$\begin{aligned} \Delta U(R, \varphi, \lambda) &= k_n V_n & (7.8) \\ &= - \frac{GM_g}{r_g} \sum_{n=2}^{+\infty} \sum_{m=0}^n k_n \left(\frac{R}{r_g}\right)^n (2 - \delta_{0,m}) \frac{(n-m)!}{(n+m)!} \times \\ &\quad P_{nm}(\sin \varphi) P_{nm}(\sin \varphi_g) (\cos m(\lambda - \lambda_g)), \end{aligned}$$

where k_n is the Love number of potential. The variation of the potential $\Delta U(r, \varphi, \lambda)$ is defined for $r \in A =]R, +\infty[$ and is continuous on this set A, its Laplacian is zero at A. Its value on the sphere of radius R is given by Eq.7.8 expression $\Delta U(R, \varphi, \lambda)$. We can then solve the problem of Dirichlet for its value of any point:

$$\begin{aligned} \Delta U(r, \varphi, \lambda) &= - \frac{GM_g}{r_g} \sum_{n=2}^{+\infty} \sum_{m=0}^n k_n \left(\frac{R}{r_g}\right)^n \left(\frac{R}{r}\right)^{n+1} (2 - \delta_{0,m}) \frac{(n-m)!}{(n+m)!} \times \\ &\quad P_{nm}(\sin \varphi) P_{nm}(\sin \varphi_g) (\cos m(\lambda - \lambda_g)) \\ &= - \frac{GM}{r} \sum_{n=2}^{+\infty} \left(\frac{R}{r}\right)^n \sum_{m=0}^n k_n \frac{M_g}{M} \left(\frac{R}{r_g}\right)^{n+1} (2 - \delta_{0,m}) \frac{(n-m)!}{(n+m)!} \times \\ &\quad P_{nm}(\sin \varphi) P_{nm}(\sin \varphi_g) (\cos m\lambda_g \cos m\lambda + \sin m\lambda_g \sin m\lambda). \end{aligned}$$

By analogy with Eq.7.6 if the body is elastic, one can define the variation of the potential coefficients as follows:

$$\begin{cases} \Delta C_{nm} = (2 - \delta_{m,0})k_n \frac{M_g}{M} \left(\frac{R}{r_g}\right)^{n+1} \frac{(n-m)!}{(n+m)!} P_{nm}(\sin \varphi_g) \cos m\lambda_g, \\ \Delta S_{nm} = (2 - \delta_{m,0})k_n \frac{M_g}{M} \left(\frac{R}{r_g}\right)^{n+1} \frac{(n-m)!}{(n+m)!} P_{nm}(\sin \varphi_g) \sin m\lambda_g. \end{cases} \quad (7.9)$$

Thus, the expression of the variation of potential as a function of the variation of potential coefficients is given as:

$$\Delta U = -\frac{GM}{r} \sum_{n=2}^{+\infty} \left(\frac{R}{r}\right)^n \sum_{m=0}^n P_{nm}(\sin \varphi) (\Delta C_{nm} \cos m\lambda + \Delta S_{nm} \sin m\lambda).$$

In the case of an inelastic body, the Love (k_n) numbers depend on the order of the harmonic which is expressed in variations of the potential coefficients:

$$\begin{cases} \Delta C_{nm} = (2 - \delta_{m,0})k_{nm} \frac{M_g}{M} \left(\frac{R}{r_g}\right)^{n+1} \frac{(n-m)!}{(n+m)!} P_{nm}(\sin \varphi_g) \cos m\lambda_g, \\ \Delta S_{nm} = (2 - \delta_{m,0})k_{nm} \frac{M_g}{M} \left(\frac{R}{r_g}\right)^{n+1} \frac{(n-m)!}{(n+m)!} P_{nm}(\sin \varphi_g) \sin m\lambda_g. \end{cases} \quad (7.10)$$

Eq.7.10 describes the coefficients of deformations of the extended body due to the motions of the external bodies around the extended body, (see Lambeck, 1988). We have:

$$\Delta U(r, \varphi, \lambda) = -\frac{GM}{r} \sum_{n=2}^{+\infty} \left(\frac{R}{r}\right)^n \sum_{m=0}^n P_{nm}(\sin \varphi) (\Delta C_{nm} \cos m\lambda + \Delta S_{nm} \sin m\lambda).$$

From Eq.7.8 showing the potential deformation of body's surface, ΔU has the same harmonic of the perturbation potential of V_n . This means that periods of each deformation coefficients depend on the integer parameter of m , which shows the frequencies multiplied to the longitudes of planets as expressed by $\sin m\lambda_g$ and $\cos m\lambda_g$ in Eq.7.10.

7.2.3 2^{nd} degree deformation coefficients

The evolution of the deformation of the Sun is given by the expressions of the variation coefficients of 2^{nd} order. These potential coefficients then are integrated numerically together with the positions of planets. By limiting the potential coefficients to the 2^{nd} degree in Eq.7.10, the following expressions, in cartesian coordinates where (r_x, r_y, r_z) are coordinates of the tidal raising body in the extended body's reference frame:

$$\begin{aligned} \Delta C_{20} &= \frac{m_g}{M} \left(\frac{R}{r_g}\right)^3 \frac{k_{20}}{2} \frac{2r_z^2 - r_x^2 - r_y^2}{r_g^2}, \\ \Delta C_{22} &= \frac{m_g}{M} \left(\frac{R}{r_g}\right)^3 \frac{k_{22}}{4} \frac{r_x^2 - r_y^2}{r_g^2}, & \Delta C_{21} &= \frac{m_g}{M} \left(\frac{R}{r_g}\right)^3 k_{21} \frac{r_z r_x}{r_g^2}, \\ \Delta S_{22} &= \frac{m_g}{M} \left(\frac{R}{r_g}\right)^3 \frac{k_{22}}{2} \frac{r_x r_y}{r_g^2}, & \Delta S_{21} &= \frac{m_g}{M} \left(\frac{R}{r_g}\right)^3 k_{21} \frac{r_z r_y}{r_g^2}, \end{aligned} \quad (7.11)$$

where M and R are the mass and radii of the extended body (in our case the Sun), while m_g and r_g are the mass and radius vector of the generating body (herein the planets), k_{nm} is the Love number corresponding to each deformation coefficient.

7.2.4 Tidal effect

Let's call $I(t)$ the matrix of inertia of the extended body when it undergoes deformation due to the effects of tides and it's spin can be expressed as in Eq.7.7. At every moment, we can decompose the matrix $I(t)$ in the sum of 3 matrices by $I(t) = I_0 + I_t(t) + I_s(t)$. I_0 is the matrix of non-deformed body and thus independent of the time, $I_t(t)$ is part due to the effects of solid tides and $I_s(t)$ is due to the spin. Here we consider only one Love number k which is independent of the order of the harmonic. We will also neglect the part of $I_s(t)$. The following expressions is then obtained for $I_t(t)$:

$$I_t(t) = m_g \left(\frac{R}{r_g} \right)^5 k \begin{pmatrix} \frac{1}{3} (-2r_x^2 + r_y^2 + r_z^2) & -r_x r_y & -r_x r_z \\ -r_x r_y & \frac{1}{3} (r_x^2 - 2r_y^2 + r_z^2) & -r_y r_z \\ -r_x r_z & -r_y r_z & \frac{1}{3} (r_x^2 + r_y^2 - 2r_z^2) \end{pmatrix} \quad (7.12)$$

Eq.7.12 estimates the deformation of the inertia matrix. In the next section we calculate the tidal effect of the planets on the Sun. Finally, we search for any possible correlation of this deformation with the solar activity data.

7.3 Estimation of the planetary effects

The Sun is not rigid and can be deformed under the action of a perturbing potential, thus the gravity field coefficients ΔC_{20} , ΔC_{21} , ΔC_{22} , ΔS_{21} and ΔS_{22} are not constant and are variable according to deformation law. In this section we express the analytical expression of the deformation potential coefficients, and the numerical estimation of the secular part of these deformation coefficients (DC).

7.3.1 Analytical expression of the deformation coefficients

An analytical representation of the 2nd degree deformation potential coefficients are presented here (for more detail see App.D). The coordinates of the generated body in the orbital elements can be written as:

$$\begin{cases} x = r (\cos u \cos \Omega - \sin u \sin \Omega \cos i) \\ y = r (\cos u \sin \Omega + \sin u \cos \Omega \cos i) \\ z = r \sin u \sin i, \end{cases} \quad (7.13)$$

with $u = \omega + v$. Considering the following known series, up to the 5th degree in eccentricity:

$$\begin{aligned}
 \left(\frac{a}{r}\right)^3 \epsilon^{i2v} &= \sum_{k=-5}^{+5} X_k^{-3,2} \epsilon^{ikM} \\
 \left(\frac{a}{r}\right)^3 \sin 2u &= \sum_{k=1}^{+5} S_k^{-3,2} \sin(kM + 2\omega) \\
 \left(\frac{a}{r}\right)^3 &= \sum_{k=0}^{+5} C_k^{-3,2} \cos(kM) \\
 \left(\frac{a}{r}\right)^3 \cos 2u &= \sum_{k=0}^{+5} C_k^{-3,2} \cos(kM + 2\omega).
 \end{aligned} \tag{7.14}$$

where the Stock coefficients $C_k^{m,n}$ can be expressed in terms of usual Hansen coefficients $X_k^{m,n}$, as:

$$\begin{aligned}
 C_0^{-3,2} &= X_0^{-3,2} \\
 C_k^{-3,2} &= X_k^{-3,2} + X_{-k}^{-3,2} \\
 S_k^{-3,2} &= X_k^{-3,2} - X_{-k}^{-3,2} \\
 k &= 1, 2..5.
 \end{aligned}$$

From Eq.7.13 the components of the tidal raising body in orbital elements are expressed as:

$$\begin{aligned}
 (xz) &= r (\cos u \cos \Omega - \sin u \sin \Omega \cos i) \cdot r \sin u \sin i \\
 &= \frac{r^2}{2} \left(\sin 2u \cos \Omega \sin i - \sin 2i \sin \Omega \left(\frac{1 - \cos 2u}{2} \right) \right) \\
 (x^2 - y^2) &= (r \cos u \cos \Omega - r \sin u \sin \Omega \cos i)^2 \\
 &\quad - (r \cos u \sin \Omega + r \sin u \cos \Omega \cos i)^2 \\
 &= r^2 \left(\frac{\cos 2\Omega}{2} (\cos 2u (1 + \cos^2 i) + 1 - \cos^2 i) \right. \\
 &\quad \left. - \sin 2\Omega \sin 2u \cos i \right) \\
 (xy) &= (r \cos u \cos \Omega - r \sin u \sin \Omega \cos i) \\
 &\quad \cdot (r \cos u \sin \Omega + r \sin u \cos \Omega \cos i) \\
 &= \frac{r^2}{2} \left(\frac{1}{2} \sin 2\Omega (\cos 2u (1 + \cos^2 i) + 1 - \cos^2 i) \right. \\
 &\quad \left. + \sin 2u \cos i \cos 2\Omega \right) \\
 (zy) &= r^2 \sin i \sin u (\sin \Omega \cos u + \cos \Omega \cos i \sin u) \\
 &= \frac{r^2}{2} \left(\sin 2u \sin \Omega \sin i + \sin 2i \cos \Omega \left(\frac{1 - \cos 2u}{2} \right) \right).
 \end{aligned} \tag{7.15}$$

The values for each coefficient in Eq.7.11 and 7.10 can be obtained using Eq.7.15 by developing series with an infinite degree of eccentricity by the following expressions:

$$\begin{aligned}
 \Delta C_{20} &= P \frac{k_{20}}{2} \left(\frac{3 \sin^2 i}{2} (\Phi^{-3,0} - \Phi^{-3,2}) - \Phi^{-3,0} \right) \\
 \Delta C_{21} &= P \frac{k_{21}}{2} \left(\Psi^{-3,2} \cos \Omega \sin i - \frac{1}{2} \sin 2i \sin \Omega (\Phi^{-3,0} - \Phi^{-3,2}) \right) \\
 \Delta C_{22} &= P \frac{k_{22}}{4} \left(\frac{\cos 2\Omega}{2} (\Phi^{-3,2} (1 + \cos^2 i) + \Phi^{-3,0} \sin^2 i) \right. \\
 &\quad \left. - \Psi^{-3,2} \sin 2\Omega \cos i \right) \\
 \Delta S_{21} &= P \frac{k_{21}}{2} \left(\Psi^{-3,2} \sin \Omega \sin i + \frac{1}{2} \sin 2i \cos \Omega (\Phi^{-3,0} - \Phi^{-3,2}) \right) \\
 \Delta S_{22} &= P \frac{k_{22}}{4} \left(\frac{\sin 2\Omega}{2} (\Phi^{-3,2} (1 + \cos^2 i) - \Phi^{-3,0} \sin^2 i) \right. \\
 &\quad \left. - \Psi^{-3,2} \cos 2\Omega \cos i \right),
 \end{aligned} \tag{7.16}$$

where

$$\begin{aligned}
 \Phi^{-3,0} &= \sum_{k=0}^{\infty} C_k^{-3,0} \cos(kM), & \Phi^{-3,2} &= \sum_{k=0}^{\infty} C_k^{-3,2} \cos(kM + 2\omega) \\
 \Psi^{-3,2} &= \sum_{k=1}^{\infty} S_k^{-3,2} \sin(kM + 2\omega), & P &= -\frac{m_p}{M_{\odot}} \left(\frac{R}{a} \right)^3,
 \end{aligned}$$

are the Hansen's coefficients which depend only on the eccentricity of orbit e , M_{\odot} and m_p are the masses of the planets and R is the radius of the Sun. The variables a, i, Ω, ω are the elliptical elements of the planetary orbits. The angles elements are i - inclination, Ω -longitude of the node, ω -argument of the perihelia are expressed on the reference frame linked with the Sun.

Analytical and numerical estimated deformation coefficients of Earth.

The potential coefficients are estimated both analytically and numerically, using the expressions in Eq.7.11 and Eq.7.16 respectively. A plot of the numerical CD_{num} and analytical CD_{anal} calculation of the Sun's deformation coefficients ΔC_{20} due to Earth perturbation using Eq.7.16 is shown in Fig.7.3. The analytical expression of the deformation coefficient CD_{anal} of ΔC_{20} are developed in power of the eccentricities up to 5th order. The $-C_{20} = J_2$ zonal coefficient for the Sun is calculated as it is the more significant coefficient when compared with the other deformation coefficients. As shown in Fig.7.3 the difference between the numerical and analytical calculation after the 5th order of the development of eccentricity stationally becomes less significant.

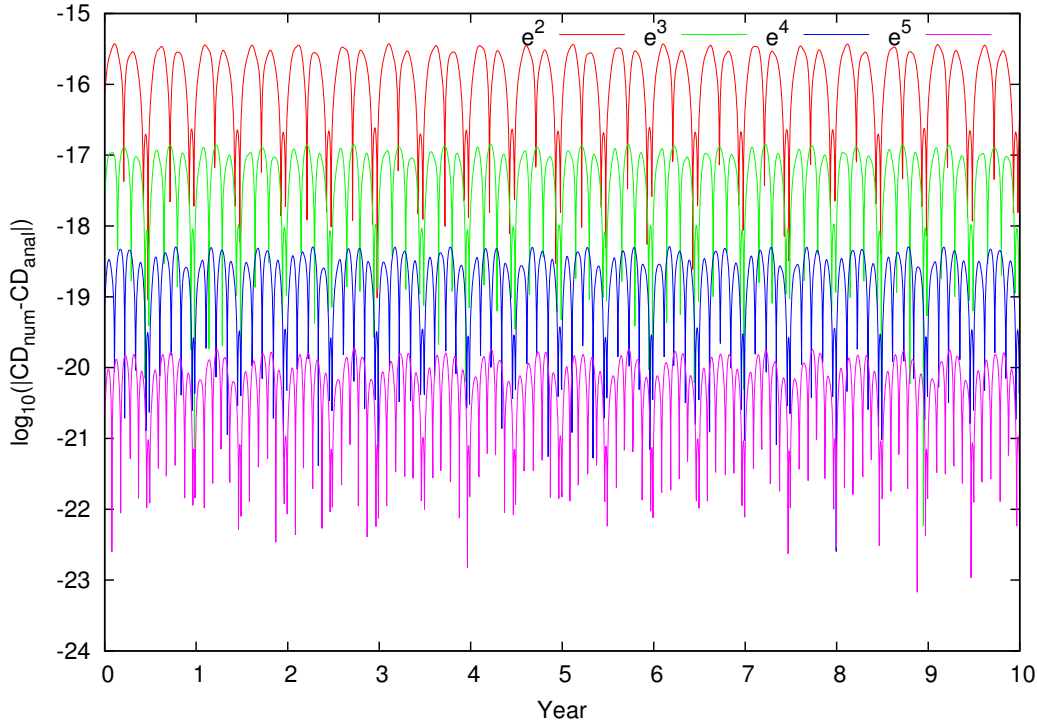


Figure 7.3 – Numerical CD_{num} and analytical CD_{anal} (until the 5th order of eccentricity) computed deformation coefficients exerted by Earth's influence over a period of 10 years.

This shows that development of the analytical expressions of the deformation coefficient in power of eccentricity provides a good estimation where the difference between numerical CD_{num} and analytical CD_{anal} deformation coefficients are only $10^{-15} - 10^{-23}$.

7.3.2 Secular part of the deformation coefficients

Here we compute the variations of the secular part of the deformation coefficients, depending on argument of the perihelion's, as this element of the orbit has a secular variation. This secular part will dominate in the long-term deformations of the Sun. The values of the secular part of the deformations present a time scale of about 300 years. It is important to study the secular variation of the deformation coefficients to understand the long-term variation. The secular part of the deformation coefficients $\Phi^{-3,2}$ and $\Psi^{-3,2}$ from Eq.7.16 are expressed by averaging the mean anomaly as:

$$C(\omega) = \sum_{k=0}^5 C_k^{-3,2}(e) \begin{pmatrix} \cos(2\omega) \\ \sin(2\omega) \end{pmatrix}, \quad S(\omega) = \sum_{k=0}^5 S_k^{-3,2}(e) \begin{pmatrix} \cos(2\omega) \\ \sin(2\omega) \end{pmatrix} \quad (7.17)$$

In Fig.7.4 is shown the variation of the deformation coefficients $\Phi^{-3,2}$ and $\Psi^{-3,2}$ as given in Eq.7.17 expanded up to the fifth power of Jupiter's eccentricity. The Hansen coefficient consists of a secular part and a scalar dependent. Linear regression of the secular part assists in modelling the relationship between the scalar dependent to the given explanatory time interval. In Fig.7.5 is shown the linear regression Rg function of the secular part of the deformation coefficients of Jupiter as $\text{Rg}(C_k^{-3,0}, t)$, $\text{Rg}(C_k^{-3,2} \cos(2\omega), t)$, $\text{Rg}(S_k^{-3,2} \cos(2\omega), t)$, $\text{Rg}(C_k^{-3,2} \sin(2\omega), t)$, and $\text{Rg}(S_k^{-3,2} \sin(2\omega), t)$ for the t interval of 162 years. The multi regression of the secular part of the deformation coefficients for Jupiter's eccentricity are shown in Fig.7.6 for the purpose of studying its long-term variation.

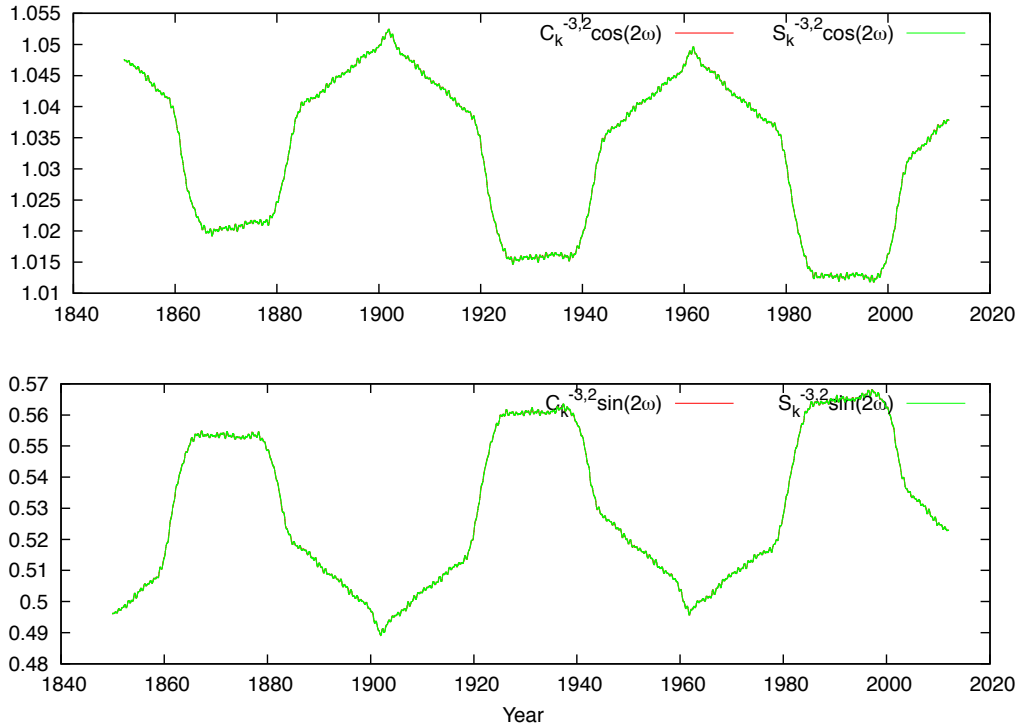


Figure 7.4 – Estimation of secular part of the deformation coefficients, for the eccentricity of Jupiter. The length of time scale is 162 years.

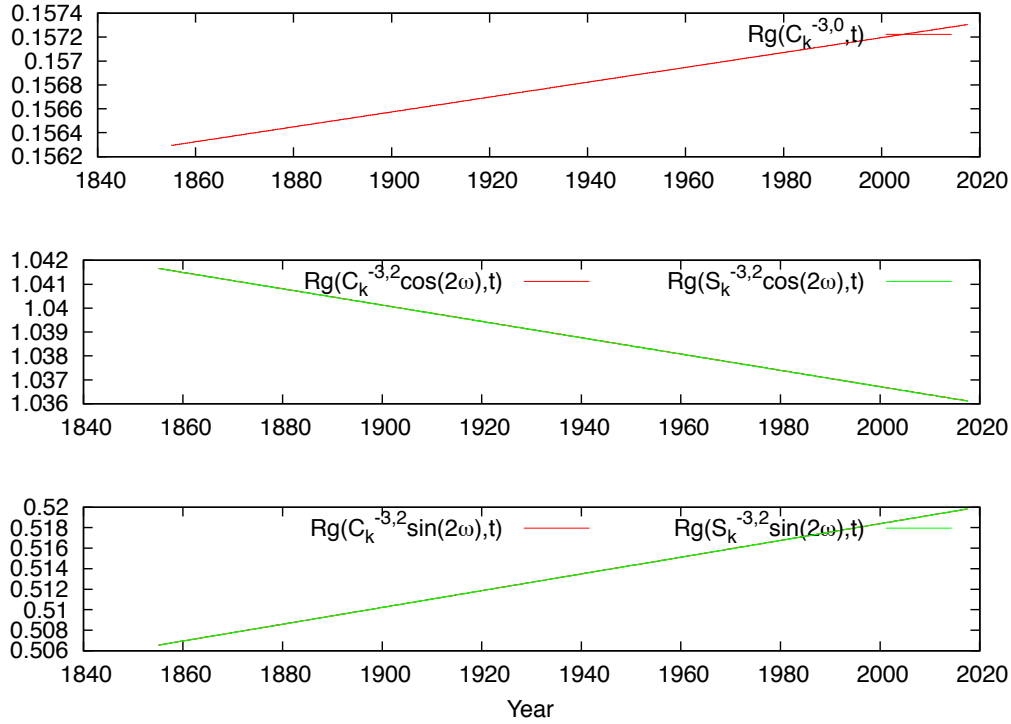


Figure 7.5 – Linear regression of the secular part of the deformation coefficients for the eccentricity of Jupiter, covering the interval of 162 years.

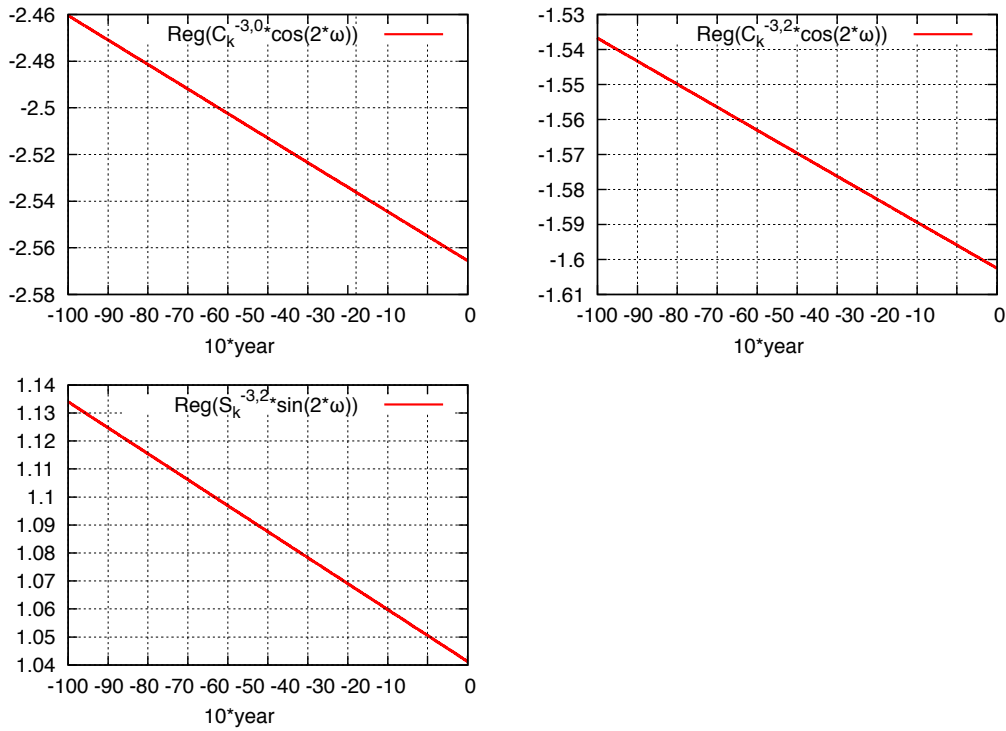


Figure 7.6 – Regression of the secular part of the deformation coefficients for the eccentricity of Jupiter, covering the interval of 1000 years.

These displayed secular parts of the deformation coefficient variations provide identification in the variation of the total potential coefficients ΔC_{20} , ΔC_{21} , ΔC_{22} , ΔS_{21} and ΔS_{22} of the Sun due to the planets tides. The analytic development of Hansen coefficients $C_k^{-3,0}$, $C_k^{-3,2}$ and $S_k^{-3,2}$ expressed in power series of the eccentricity up to 5th order (see App.D):

$$C(e)^{-3,0} = \sum_{k=0}^5 C_k(e)^{-3,0}, \quad C(e)^{-3,2} = \sum_{k=0}^5 C_k^{-3,2}(e), \quad S(e)^{-3,2} = \sum_{k=0}^5 S_k^{-3,2}(e). \quad (7.18)$$

In Fig.7.7 is presented an estimation for each part of the analytical expression of Hansen's coefficients for Jupiter's eccentricity. It should be noted that in all calculations t_0 corresponds to JD (1st of January 2000). The secular parts of the deformation coefficients are shown

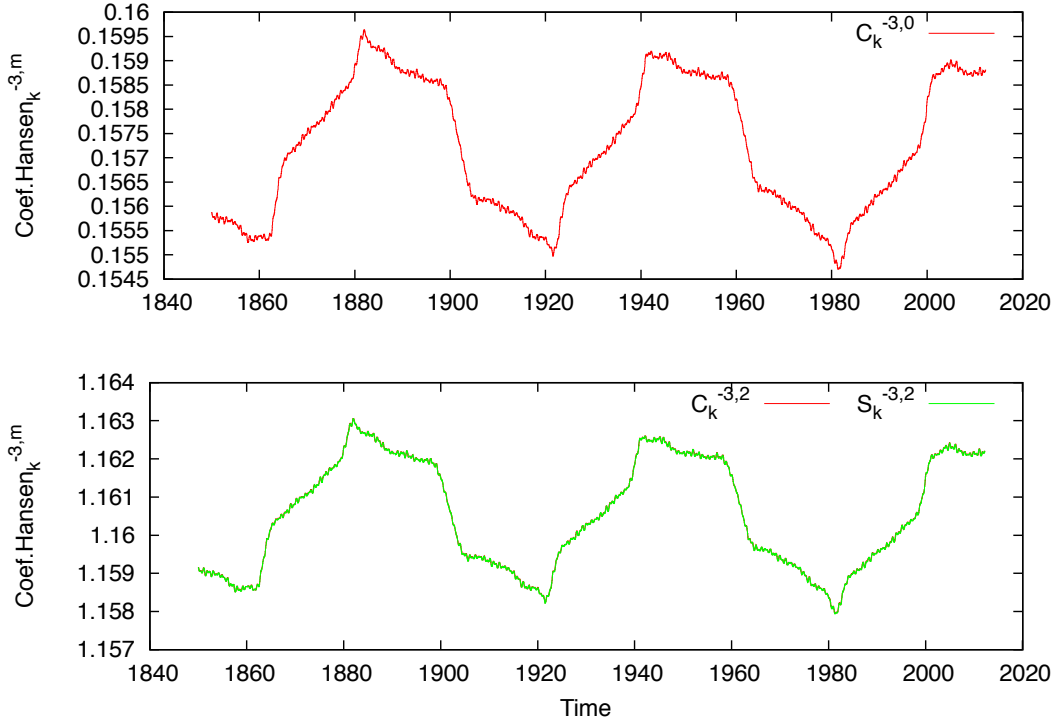


Figure 7.7 – Estimation of the Hansen's coefficients with eccentricity of Jupiter. The time scale is 162 years.

in Fig.7.4 and Fig.7.5 represents the secular evolution of these coefficients with periodicities of about 60 years. The above presented secular and millennial variations of the deformation coefficients will dominate over the estimated variation of the full ΔC_{20} , ΔC_{21} , ΔC_{22} , ΔS_{21} , ΔS_{22} deformation coefficients which contain both secular and periodic parts. This secular behavior of the potential coefficients are important to understand the long-term evolution of deformation in the Sun's surface induced by planetary tides.

7.4 Data

We use observation data of sunspots from SILSO (Sunspot Index and Long-term Solar Observations) (Frédéric et al., 2015), the planetary ephemerides INPOP (Integration Numerique Planetaire de l’Observatoire de Paris) (Fienga et al., 2015) and the long-term orbital solution La2004 (Laskar, 1994; Laskar et al., 2011) where the orbital model includes all eight planets of the Solar System and Pluto to calculate the tide perturbation of each of the planets.

7.4.1 The solar activity indices, its direct and indirect proxies

There are various methods for quantifying solar activity. Classical methods include the SSN and GSN, which are considered significant indicators of solar activity. The data set for SSN can be downloaded from the SILSO in the website: <http://sidc.be/silso> (for more see Sec.4). The given SSN are made from 60,385 points without fragments for the period of 1850 – 2016 years. Although there are missing data between the years of 1600 to 1850. Daily, monthly and yearly observed data of the SSN are shown in Fig.7.8.

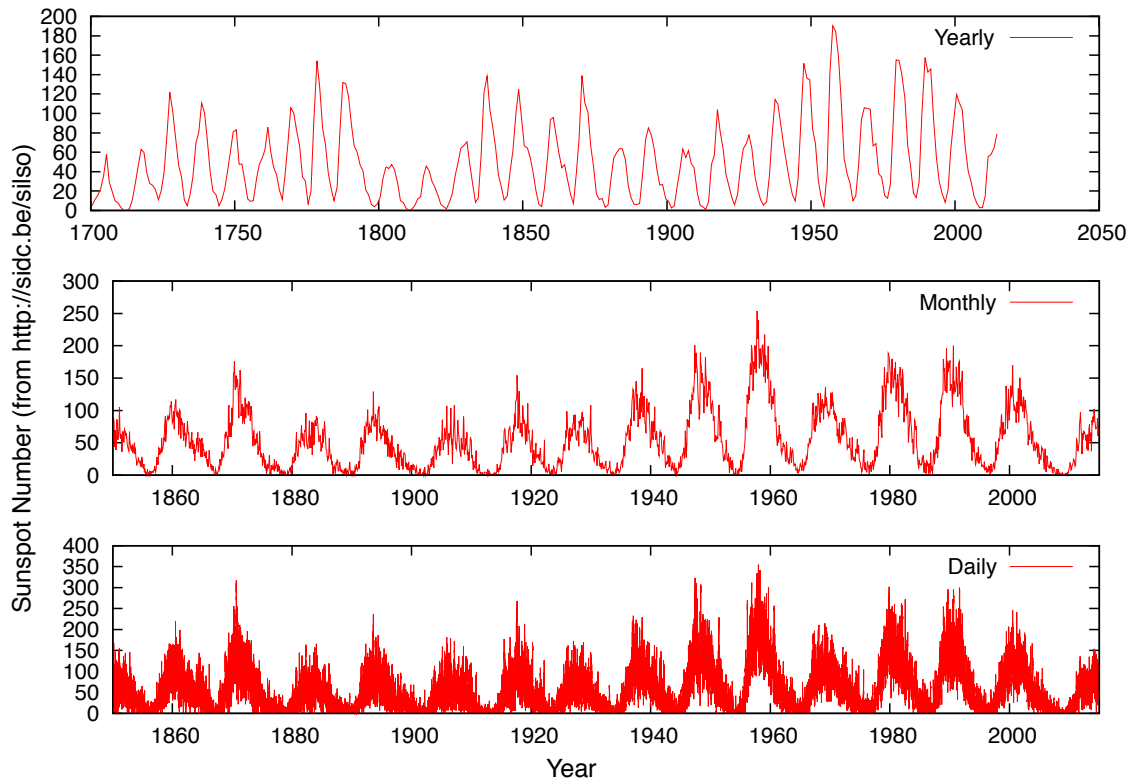


Figure 7.8 – The daily, monthly and yearly sunspot numbers records sampled from 01.01.1850 to 30.04.2015 from **SILSO**.

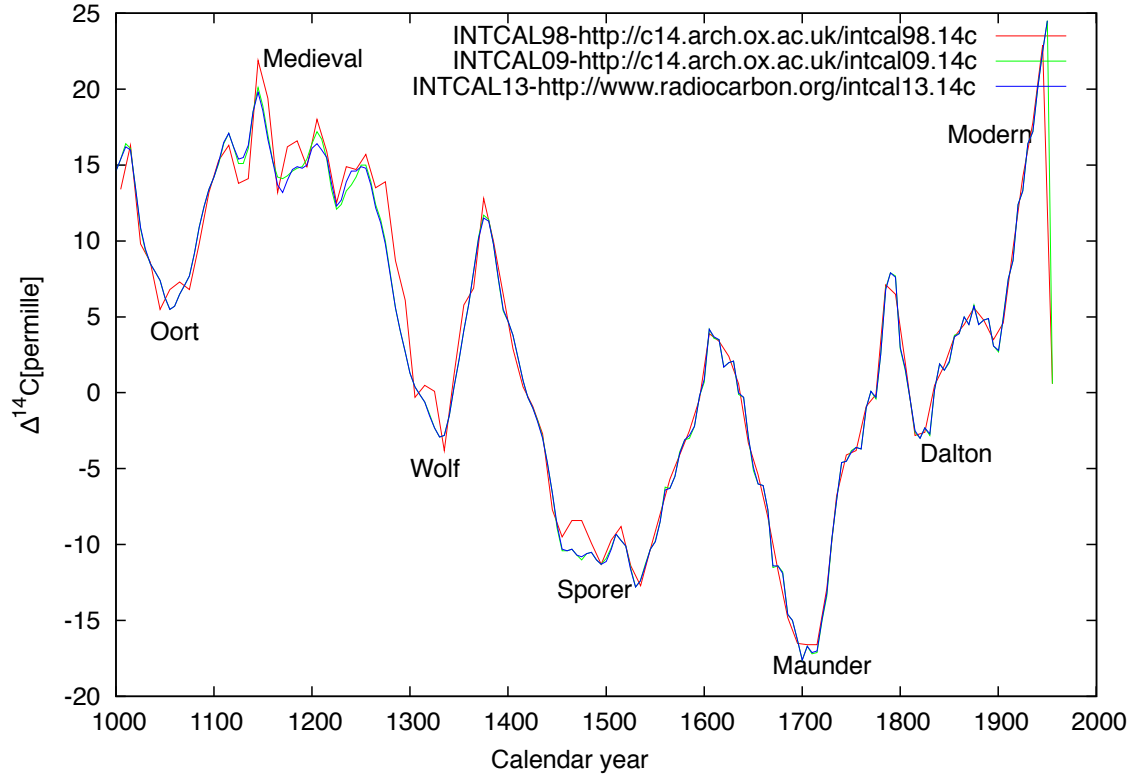


Figure 7.9 – Properties of solar activity reconstructed from global tree ring and cosmogenic radionuclides data. Comparison of the radionuclides IntCal98, IntCal09 and IntCal13. The grand solar maxima, Medieval and Modern are labelled. The grand solar minima, Oort, Wolf, Sporer, Maunder and Dalton are marked.

The study related with planetary theory investigates a possible contribution of solar energetic particle events to the production of cosmogenic ^{10}Be and ^{14}C in the atmosphere. The solar particle effects is negligible in the ^{14}C proxy, but extreme effects may be detectable in high-resolution ^{14}C data (Usoskin et al., 2005). The cosmogenic isotopes proxies were analyzed by mean statistical methods, for long-period cycles of the Sun's activity reconstruction in direct solar proxies (Ogurtsov, 2012). The Gleissberg 88-year solar cycle is presented over the last $\sim 12,000$ years. The basic reconstructed radio isotopes are from IntCal98, IntCal09 and IntCal13, they are plotted in Fig.7.9 with sources indicated.

7.4.2 INPOP and La2004

To compute the possible implication of the tidal effects of planets on the Sun, we use two sources of data, one of them is the planetary ephemerides from INPOP/CALCEPH of IMCCE (www.imcce.fr/inpop/calceph) (Fienga et al., 2015). The coordinates are in the ICRF reference frame from J2000 with a daily step, velocity and constant values of eight planets, including Pluto and the Moon from -1000 to $+1000$ years around J2000, i.e. from 1000AD to 3000AD. This is used to investigate the influence of tidal forces on the deformation of the surface of the Sun. We also use the solution in heliocentric coordinates for the eight planets, also Pluto and the Moon, which were obtained from La2004 (Laskar, 1994; Laskar et al., 2011). The data is given in a "nearly ecliptic" reference frame with length of one 250

Myr from J2000 with steps of 1000 years. The data of La2004 is used to analyze the long-term evolution of the gravitational field coefficients of the Sun variations.

7.4.2.1 The transformation of ICRF (INPOP) to J2000 mean equator

All the expressed potential coefficients in Eq.7.16 are given in the reference frame of the solar equator. The positions/velocities of the planets in INPOP are given in the ICRF (International Celestial Reference Frame). For this purpose, \mathbf{r}_{ICRF} in ICRF and \mathbf{r}_{J2000} in the mean equator J2000 reference frame do not coincide and a transformation is needed. Thus, the application of a transformation matrix is required for passage from one to another. The expression of the matrix may be written as follows:

$$\mathbf{r}_{J2000} = \begin{pmatrix} 1 & 0 & 0 \\ 0 & \sin \delta_0 & \cos \delta_0 \\ 0 & -\cos \delta_0 & \sin \delta_0 \end{pmatrix} \begin{pmatrix} -\sin \alpha_0 & \cos \alpha_0 & 0 \\ -\cos \alpha_0 & -\sin \alpha_0 & 0 \\ 0 & 0 & 1 \end{pmatrix} \mathbf{r}_{ICRF}, \quad (7.19)$$

where α_0 and δ_0 are coordinates of solar pole at J2000 mean equator, i.e. the right ascensions and declination of the pole respectively, with values expressed in degrees in INPOP13c:

$$\alpha_0 = 286.13^\circ, \quad \delta_0 = 63.87^\circ. \quad (7.20)$$

7.4.2.2 The passage of "nearly ecliptic" (La2004) to J2000 mean equator

All of the equations of potential coefficients in Sec 7.2.3 are expressed in a reference frame which is related to the extended body (Sun). Before passage to the equator reference frame of the Sun, it is necessary to transform the coordinates of the planets from the nearly ecliptic to the solar equator. The positions/velocities of the planets in La2004 are given in nearly ecliptic $\widetilde{\mathbf{r}}_{EcJ2000}$ reference frame. The transformation from the nearly ecliptic $\widetilde{\mathbf{r}}_{EcJ2000}$ reference frame to the $\mathbf{r}_{EcJ2000}$ ecliptic reference frame of the Sun and then to the equator of the Sun $\mathbf{r}_{Eq\odot}$. Thus the expression of the matrix is constructed as follows:

$$\begin{pmatrix} \mathbf{r} \\ \dot{\mathbf{r}} \end{pmatrix}_{EcJ2000} = \mathcal{R}_1(\varepsilon) \mathcal{R}_3(\phi) \begin{pmatrix} \mathbf{r} \\ \dot{\mathbf{r}} \end{pmatrix}_{\widetilde{EcJ2000}}, \quad (7.21)$$

$$\begin{pmatrix} \mathbf{r} \\ \dot{\mathbf{r}} \end{pmatrix}_{Eq\odot} = \mathcal{R}_1(\delta_0) \mathcal{R}_3(\alpha_0) \begin{pmatrix} \mathbf{r} \\ \dot{\mathbf{r}} \end{pmatrix}_{EcJ2000}. \quad (7.22)$$

where the matrices of rotations around x axis $\mathcal{R}_1(\phi)$ and z axis $\mathcal{R}_3(\phi)$ are given in App.D.3. At the rotation angles the mean obliquity and precession constants (cf. J.Chapront et al.) are:

$$\varepsilon_{J2000} = 23.439^\circ, \quad \phi_{J2000} = -3.0064E - 05^\circ.$$

Applying in the above transformation matrices, we can transform the ephemerides of the planets to the corresponding solar equator reference frame. The coordinates and the velocities of each planet depend on the Sun's reference frame. As noted the equations of potential coefficients in Eq.7.16 are expressed at the Solar equator.

7.5 Semi-analytical and numerical estimation of the deformation coefficients

The secular behaviour of solar cycles has been presented by many authors (etc. Gleisberg, 1967a; Nagovitsyn, 1997; Frick et al., 1997b; Le & Wang, 2003; Hiremath, 2008b). The grand minima such as Sporer, Maunder and Dalton minimum etc. causes debate among solar specialists as to whether such grand minima are chaotic or regular trends. Herein we are interested in the long-term evolution of solar activity and its possible variations are affected by the planetary tidal effects.

7.5.1 Variation of the potential coefficients of the Sun due to the tidal effect of planets

7.5.1.1 Maximum values of the tide effect

The maximum values of the potential coefficients ΔC_{20} , ΔC_{21} , ΔC_{22} , ΔS_{21} and ΔS_{22} of all planets according to Eq. 7.16 are plotted in Fig.7.10.

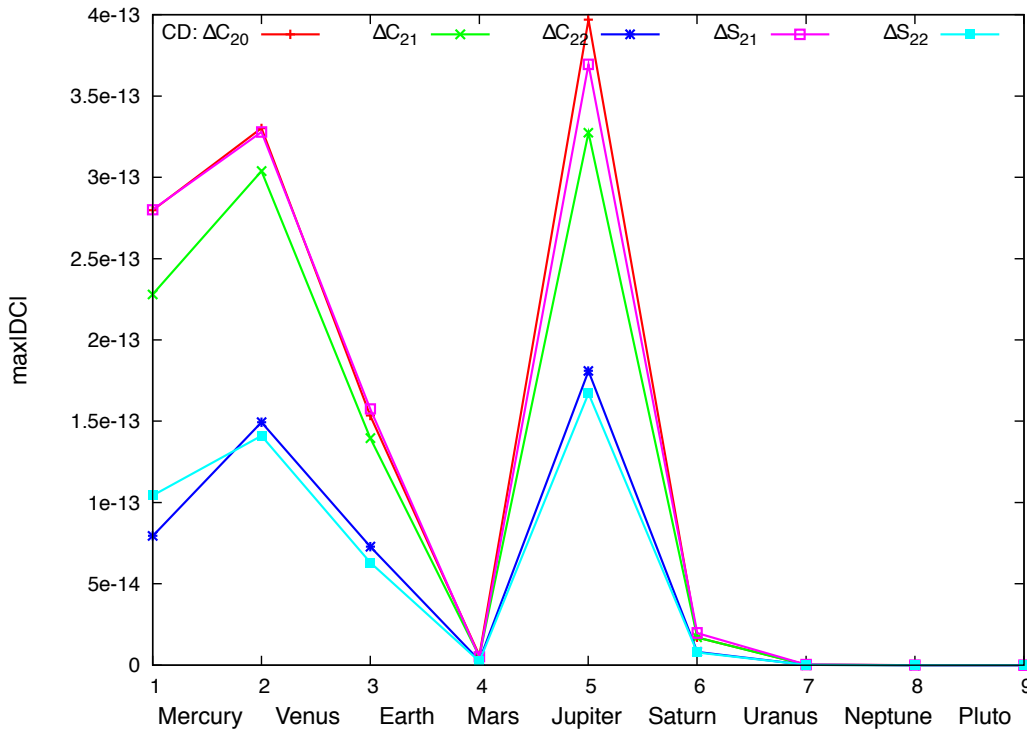


Figure 7.10 – The maximum absolute values of the deformation coefficients (ΔC_{20} , ΔC_{21} , ΔC_{22} , ΔS_{21} and ΔS_{22}) for each planet.

Fig.7.10 shows the maximum values occurring for Jupiter, then follows less dominant planets such as Venus, Mercury, Earth, Saturn, Mars, Uranus, Neptune and Pluto. The reducing order of dominance of the planets shows good correlation with the results of other researchers (e.g. (Scafetta, 2012)). It should be noted that as expected the more significant deformation coefficients are ΔC_{20} and ΔS_{21} , then ΔC_{21} , and finally are ΔC_{22} and ΔS_{22} .

7.5.1.2 Variation of the evolution of the Sun's deformations coefficients

Here we calculated the numerical and semi-analytical computation of the potential deformation coefficients of the extended body i.e. the Sun due to perturbation of the planets (i.e. Mercury, Venus, the Earth, the Moon, Mars, Jupiter, Saturn, Uranus and Pluto).

Short-term evolution of the potential coefficients. Before studying the long-term variation of the gravity coefficients, we need to compute their short-term variation. The numerical potential coefficients of the Sun have been calculated according to Eq.7.11, while the semi-analytical deformation coefficients have been calculated according to Eq.7.16. The heliocentric coordinates of the planets at ICRF in INPOP are used with a daily step and the ecliptic elements in La2004 with a 1000 year step. Figures Fig.7.11 to Fig.7.15 correspond respectively to gravity field coefficients of ΔC_{20} , ΔC_{21} , ΔC_{22} , ΔS_{21} and ΔS_{22} . The deformation coefficients show the numerical and analytical logarithmic absolute value comparisons for a one year period corresponding to each planets marked on the top right of each figure. Also, the numerical and semi-analytical variations correspond to respectively Eq.7.11 and Eq.7.16 for the potential coefficients of ΔC_{20} , ΔC_{21} , ΔC_{22} , ΔS_{21} and ΔS_{22} . The results of the two calculations present quite similar variations, which show the correct calculations of the analytical results. It should be noted that in the analytical calculation the developments of the eccentricity is taken up to 5th order.

7.5. SEMI-ANALYTICAL AND NUMERICAL ESTIMATION OF THE DEFORMATION COEFFICIENTS

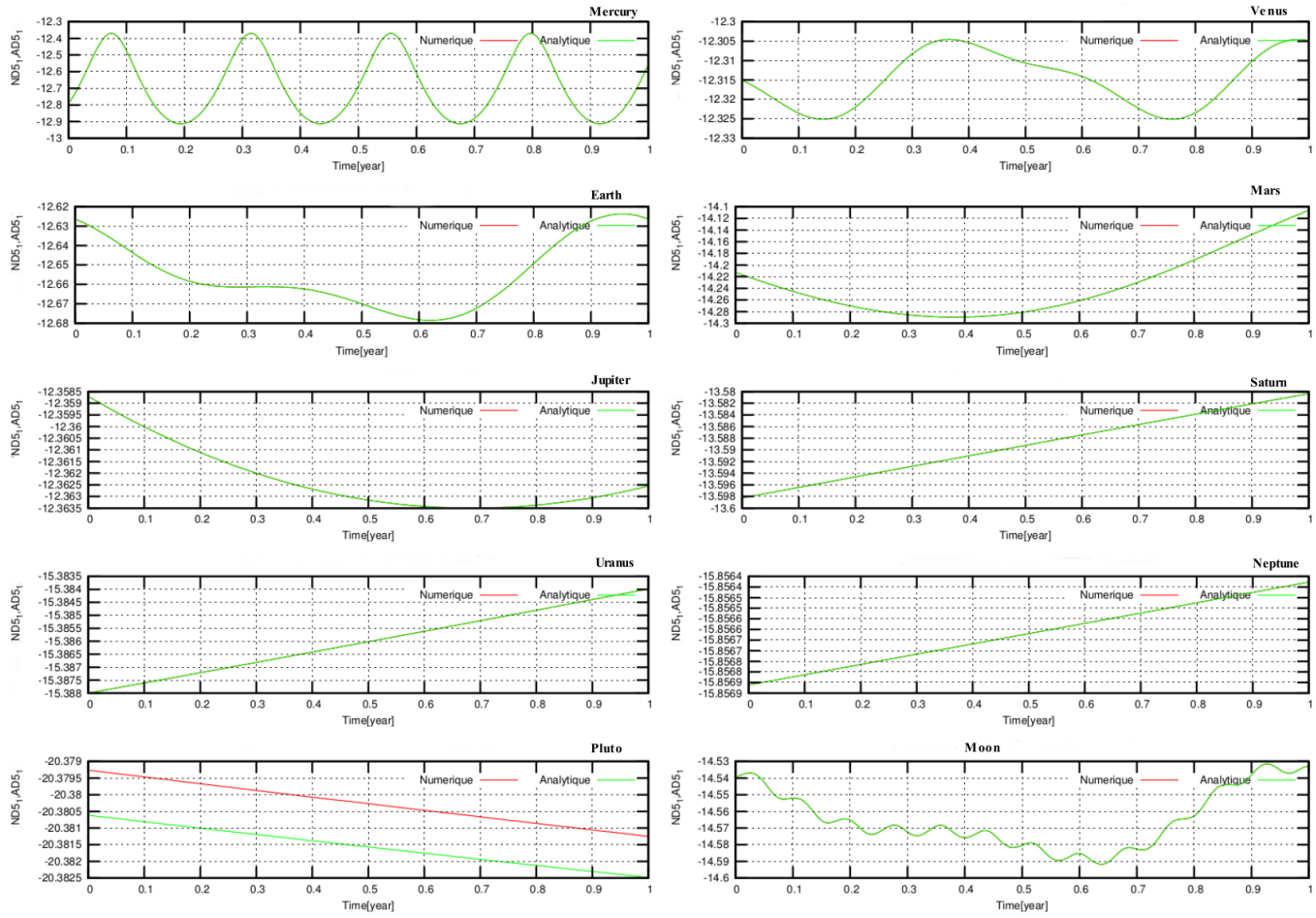


Figure 7.11 – Comparison of the numerical (Eq.7.16) and analytical (Eq.7.11 with eccentricity of order ϵ^5) evolution of the tidal deformation coefficients of $\log_{10}(\Delta C_{20})$ over one year. The ΔC_{20} calculated for each planet as noted on the top right.

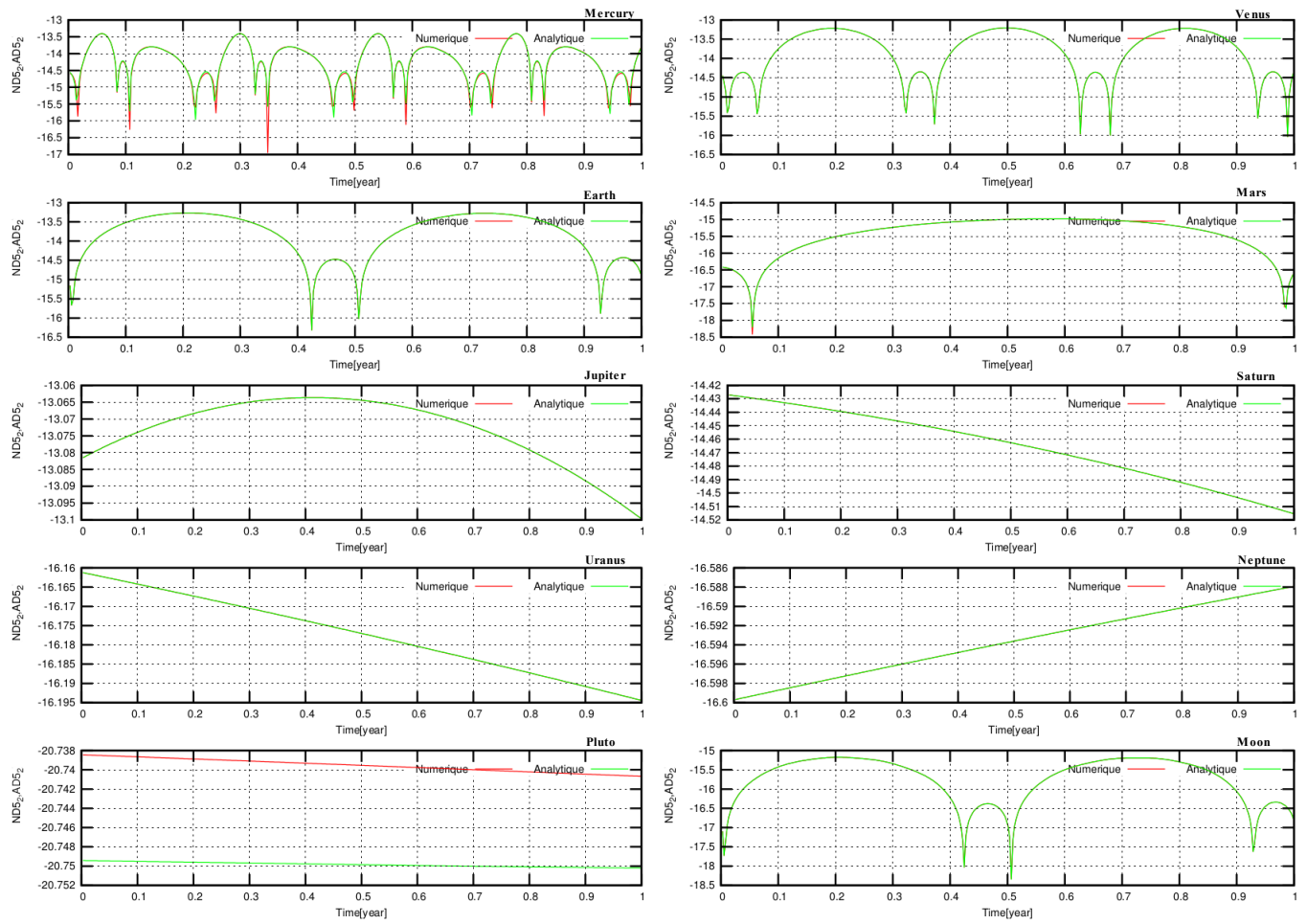


Figure 7.12 – Comparison of the numerical (Eq.7.16) and analytical (Eq.7.11 with eccentricity of order ϵ^5) evolution of the tidal deformation coefficients of $\log_{10}(\Delta C_{21})$ over one year. The ΔC_{21} calculated for each planet as noted on the top right.

7.5. SEMI-ANALYTICAL AND NUMERICAL ESTIMATION OF THE DEFORMATION COEFFICIENTS

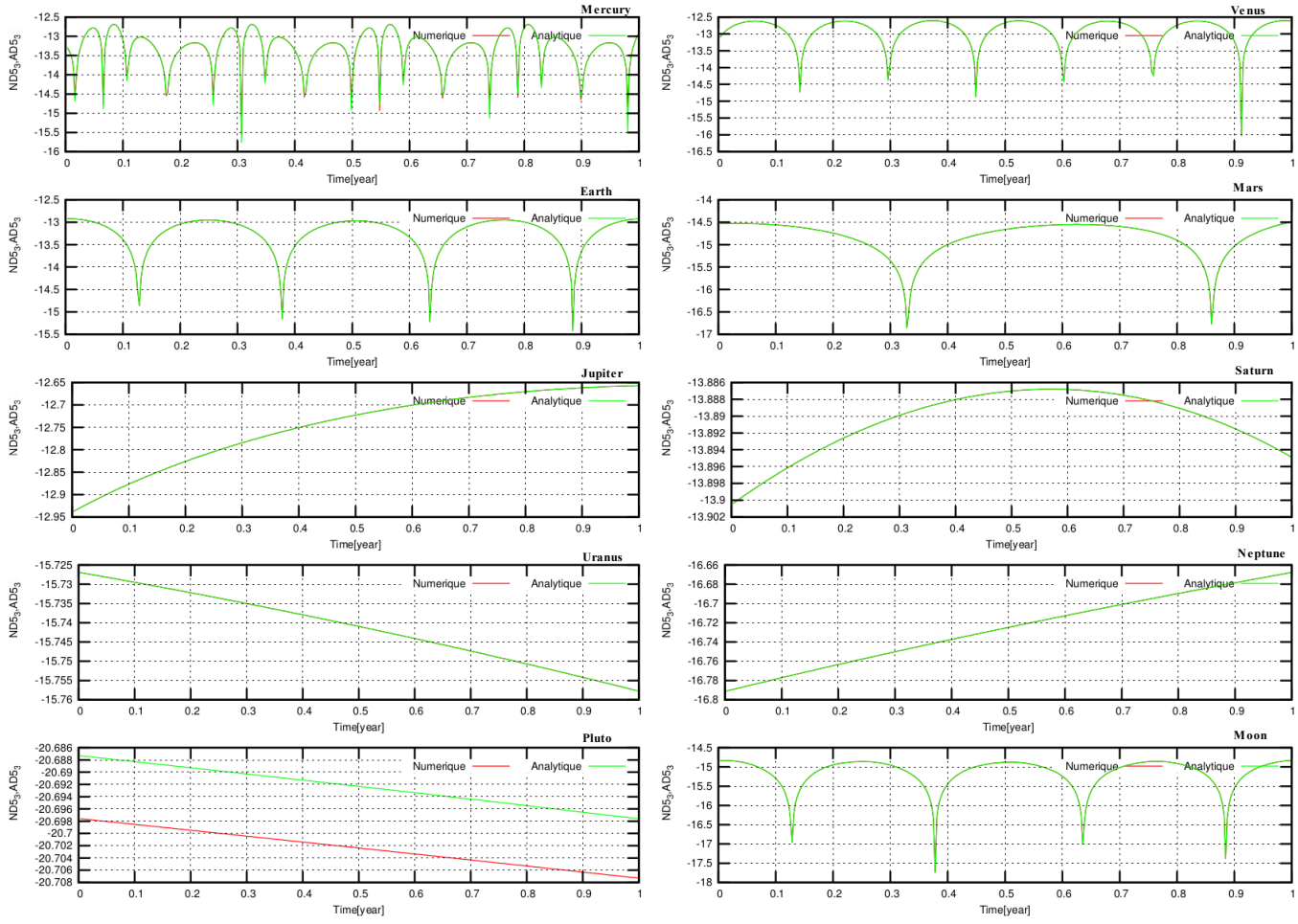


Figure 7.13 – Comparison of the numerical (Eq.7.16) and analytical (Eq.7.11 with eccentricity of order ϵ^5) evolution of the tidal deformation coefficients of $\log_{10}(\Delta C_{22})$ over one year. The ΔC_{22} calculated for each planet as noted on the top right.

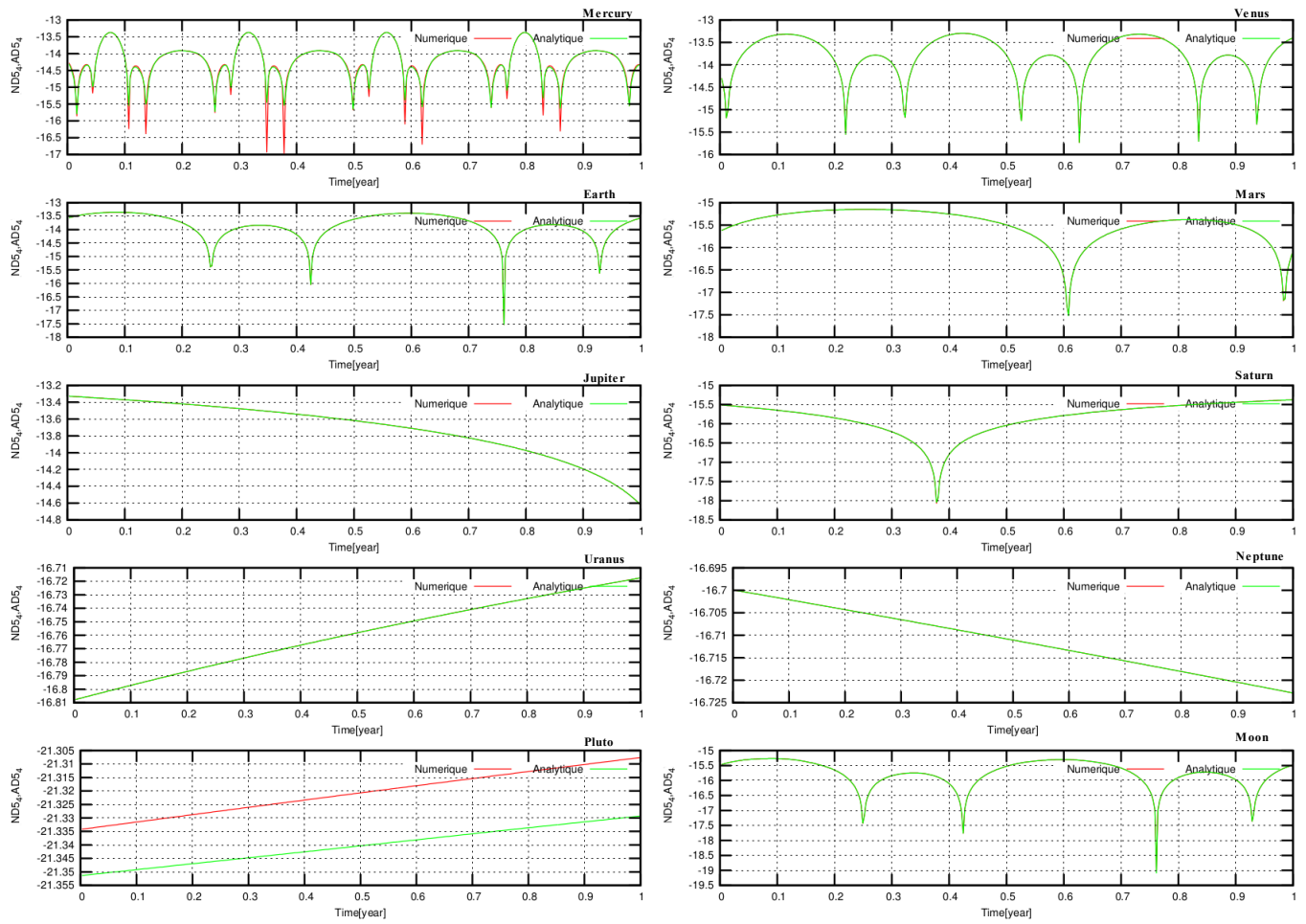


Figure 7.14 – Comparison of the numerical (Eq.7.16) and analytical (Eq.7.11 with eccentricity of order ϵ^5) evolution of the tidal deformation coefficients of $\log_{10}(\Delta S_{21})$ over one year. The ΔS_{21} calculated for each planet as noted on the top right.

7.5. SEMI-ANALYTICAL AND NUMERICAL ESTIMATION OF THE DEFORMATION COEFFICIENTS

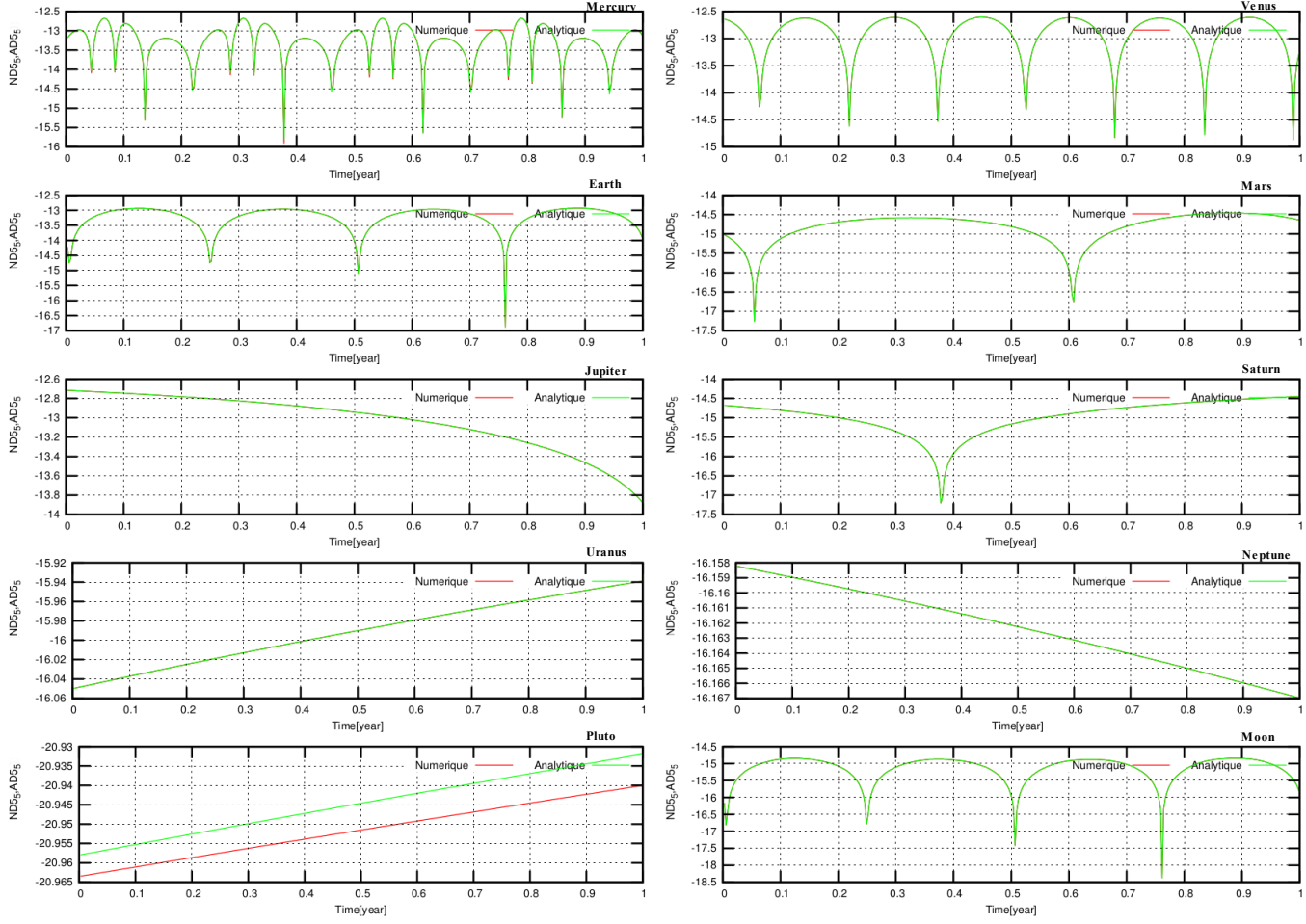


Figure 7.15 – Comparison of the numerical (Eq.7.16) and analytical (Eq.7.11 with eccentricity of order ϵ^5) evolution of the tidal deformation coefficients of $\log_{10}(\Delta S_{22})$ over one year. The ΔS_{22} calculated for each planet as noted on the top right.

From the above presented figures the most significant deformation coefficient is identified as ΔC_{20} of Jupiter at about $10^{-12.3}$. For all the potential coefficients was used the same Love number. This also corresponds to the result shown in Fig.7.10 and it permits us to compute the gravity field coefficients of the Sun over longer timescales.

Long-term evolution of the potential coefficients. According to the research of short-term evolution, the ΔC_{20} potential coefficients show the most significant variation when compared to ΔC_{21} , ΔC_{22} , ΔS_{21} and ΔS_{22} . In next step, ΔC_{20} evolution over long-term timescales is studied. The numerical variation of ΔC_{20} are plotted in Figs.7.16,7.17 and 7.18 over the interval from 0 to 100, from 0 to 1000 year with a daily step and from -1000 to 0 with a yearly step where t_0 corresponds to $J2000$, respectively for the eight planets, Pluto and the Moon.

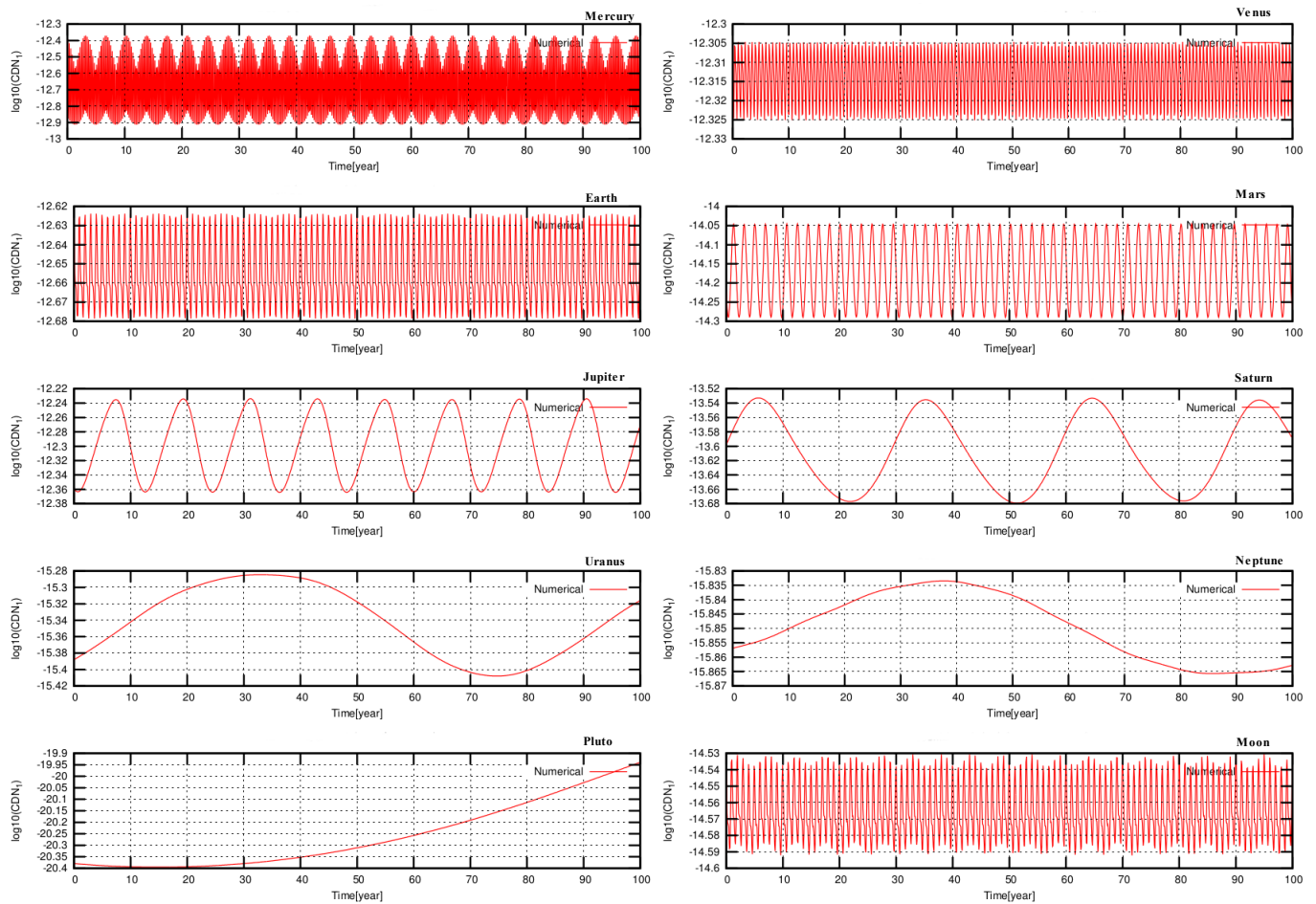


Figure 7.16 – Numerical deformation coefficient ΔC_{20} (noted as $\log_{10}(\text{CDN}_1)$ in logarithmic scale) using Eq.7.11 for the corresponding eight planets including Pluto and the Moon covering an 100 year interval.

7.5. SEMI-ANALYTICAL AND NUMERICAL ESTIMATION OF THE DEFORMATION COEFFICIENTS

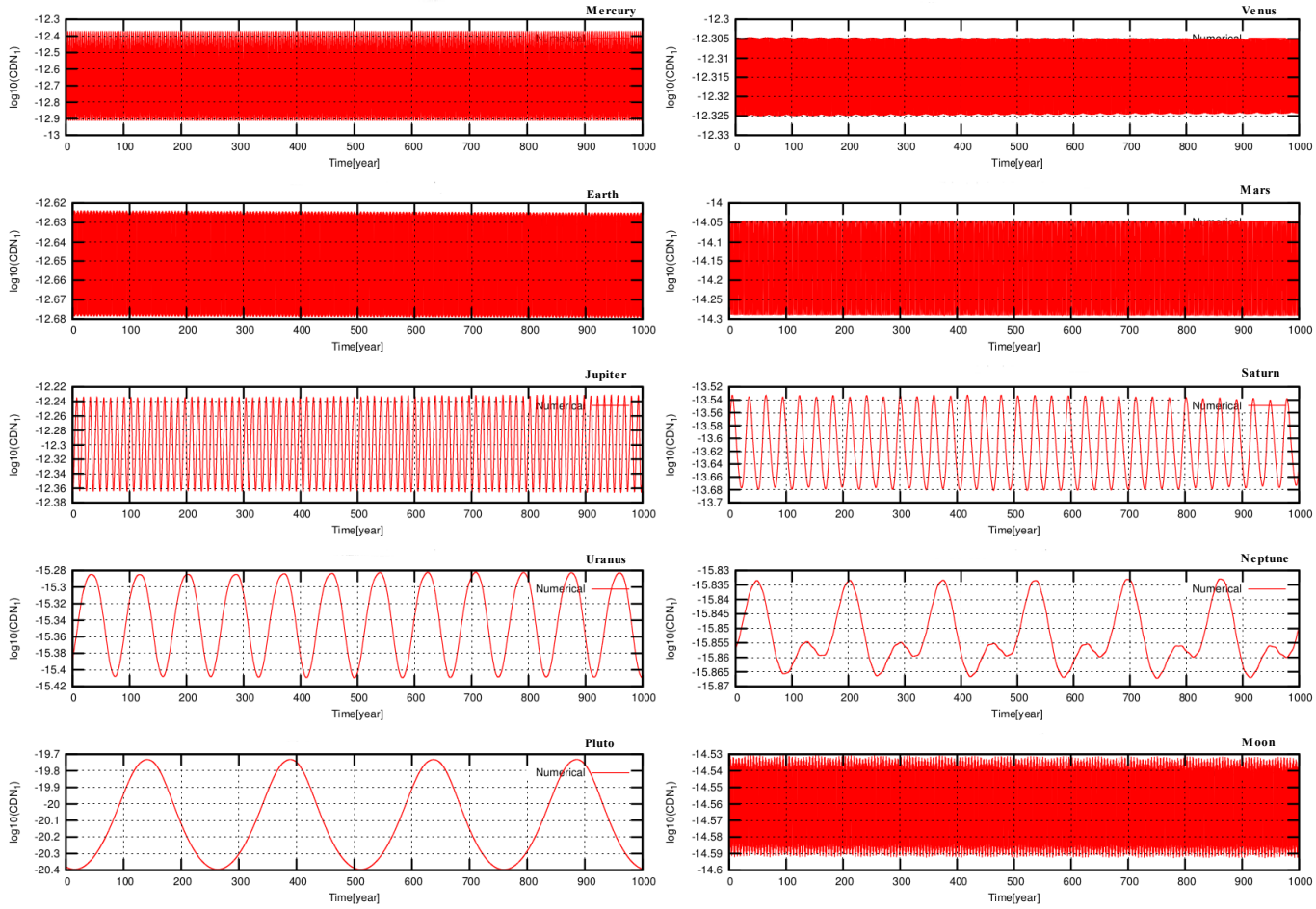


Figure 7.17 – Numerical deformation coefficient ΔC_{20} (noted as $\log_{10}(\text{CDN}_1)$ in logarithmic scale) using Eq.7.11 for the corresponding eight planets including Pluto and the Moon covering an 1000 year interval.

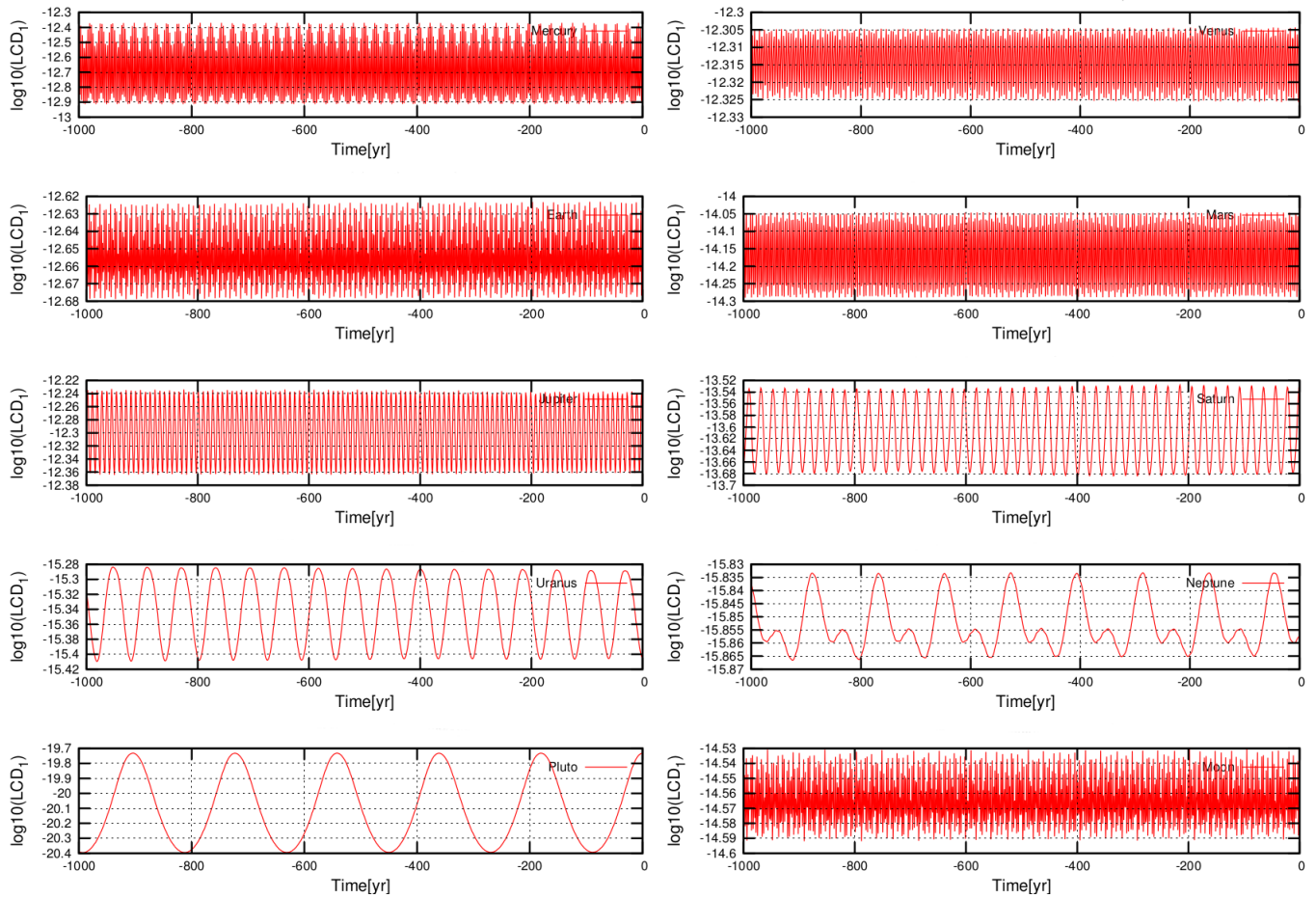


Figure 7.18 – Numerical deformation coefficient ΔC_{20} (noted as $\log_{10}(\text{LCD}_1)$ in logarithmic scale) using Eq.7.11 for the corresponding eight planets including Pluto and Moon covering an 1000 year of interval from 1000AD to 2000AD.

7.5. SEMI-ANALYTICAL AND NUMERICAL ESTIMATION OF THE DEFORMATION COEFFICIENTS

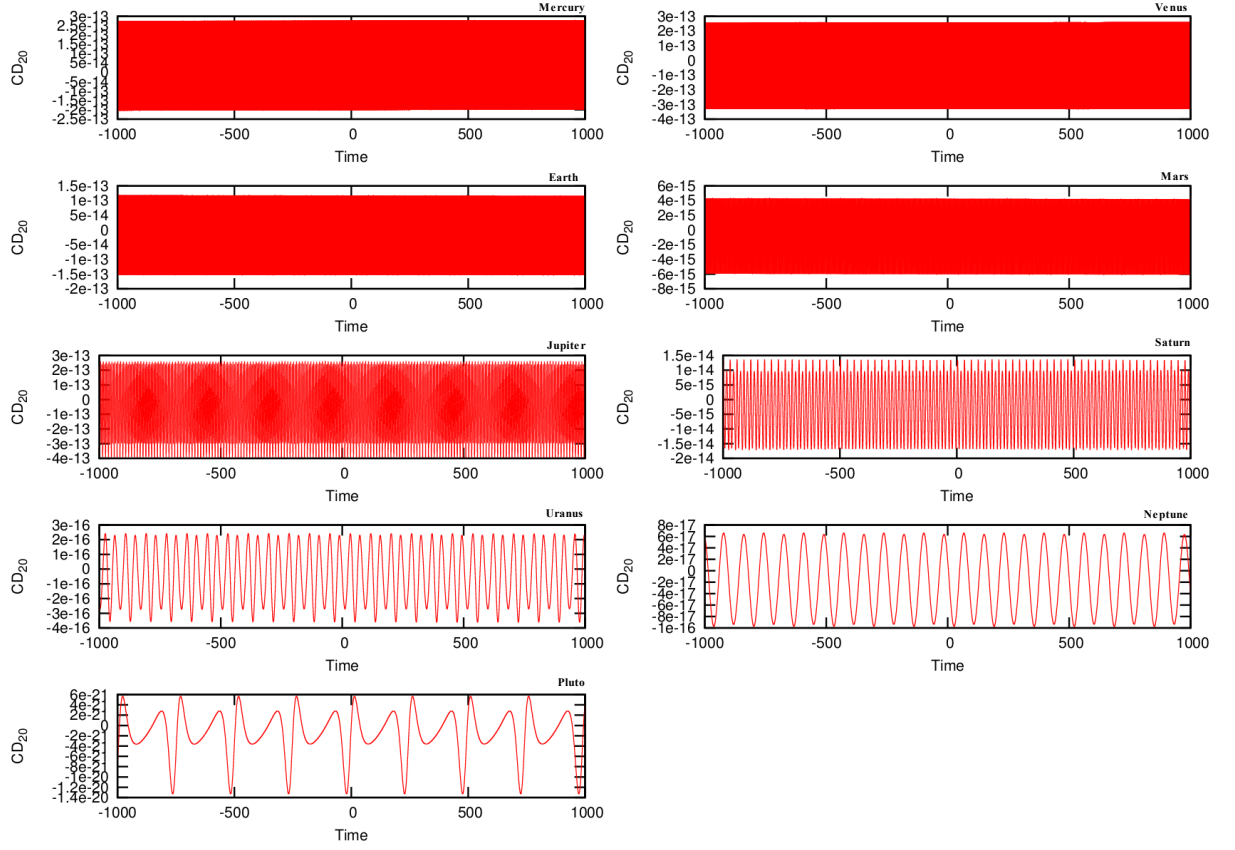


Figure 7.19 – Numerical deformation coefficient ΔC_{20} (noted as CD_{20}) using Eq.7.11 for the corresponding eight planets including Pluto covering the 2000 year interval from 1000AD to 3000AD .

From these figures the orbital periods of each planet are well identified. The most dominate planets are Jupiter, Mercury, Venus and the Earth as expected from the analytical expressions (see Eq.7.16) and also corresponds to the results shown in Fig.7.11 and 7.10. The ephemerides of the planets from INPOP are given for the interval of 1000AD to 3000A.D. after J2000, where t_0 corresponds to the 1st of January 2000 at mid night. The numerical variation of ΔC_{20} for this interval is shown in Fig.7.19, for the eight planets and Pluto. ΔC_{20} corresponds to zonal coefficient $-J_2$ which is the most significant coefficient when compared to the other ΔC_{21} , ΔC_{22} , ΔS_{21} and ΔS_{22} coefficients, as shown in the previous section.

Multi-millennial evolution of the potential coefficients. The sum of each ΔC_{20} , ΔC_{21} , ΔC_{22} , ΔS_{21} and ΔS_{22} deformation coefficients of all the planets for the interval of 10 Myr shows a small but not negligible values such as $\Delta C_{20} = 10^{-11.9}$, $\Delta C_{21} = 10^{-13.9}$, $\Delta C_{22} = 10^{-12.2}$, $\Delta S_{21} = 10^{-13.2}$ and $\Delta S_{22} = 10^{-12.2}$, see Fig.7.20. Here was used the La2004 ephemerides of planets (Laskar et al., 2004). This data covers 250 Myr of planetary ephemerides with steps of 1000 years.

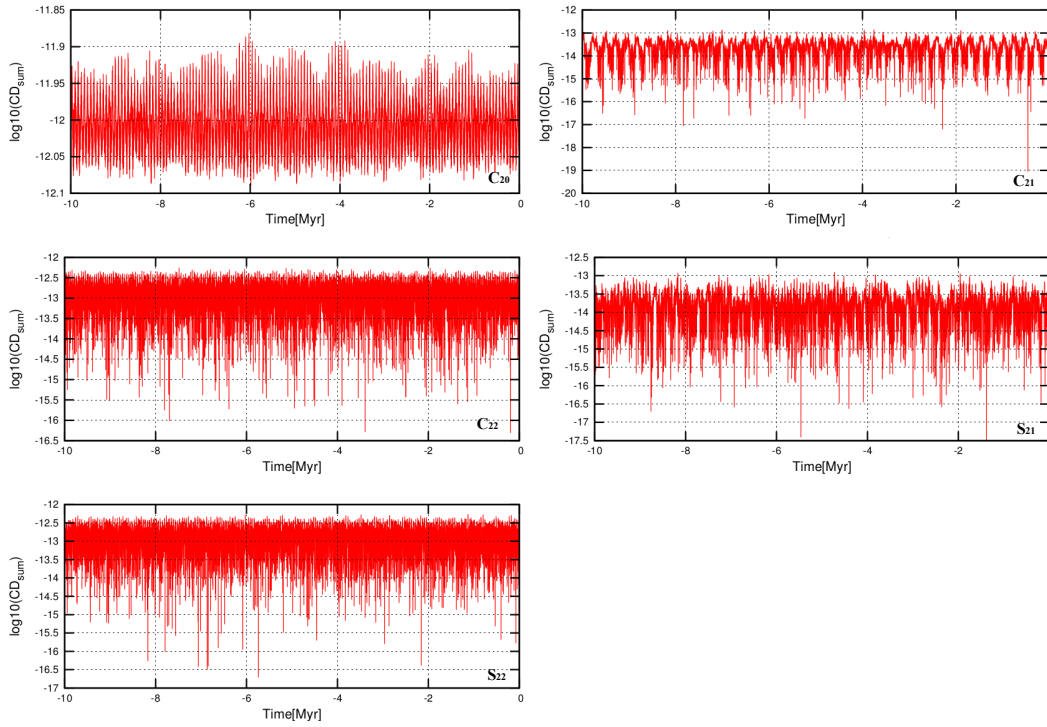


Figure 7.20 – The figure shows the sum of the deformation coefficients of all the planets covering a 10 Myr interval. The gravity field coefficients of ΔC_{20} , ΔC_{21} , ΔC_{22} , ΔS_{21} and ΔS_{22} are shown on the bottom right.

The millennial variation of ΔC_{20} corresponding to the eight planets including Pluto and the Moon shows the secular variation of each planet. The deformation coefficients due to Jupiter has a maximum value as shown in Fig.7.10. In the next step, we need to search for common periodicities between the observed solar activity records and the calculated Sun's deformation coefficients due to the planets.

7.5.2 Periodicities of ΔC_{20}

The periodicities of potential coefficients due to the perturbation of the planets are shown here. In Tabs.7.1 and 7.2 are presented the frequency analysis of the decadal and yearly computed ΔC_{20} deformation coefficients as the sum of all planets.

Table 7.1 – Frequency analysis of the ΔC_{20} deformation coefficient. The columns show 1: The frequency number, 2: The frequency, 3: The period, 4: Modulus of the amplitude, 5: The phase.

k	ν_k [rad/year]	P [year]	$\log_{10}(\alpha_k)$	φ_k [°]
0	0.008457	742.983761	-12.622	125.303
1	0.007787	806.910659	-12.490	29.488
2	0.198252	31.692856	-12.526	74.969
3	0.306667	20.488609	-12.563	-41.610
4	0.000000	inf	-12.684	180.000
5	0.298410	21.055538	-12.978	119.402
6	0.020055	313.300883	-13.225	-86.694

Table 7.2 – Frequency analysis of ΔC_{20} as the sum of deformation coefficients all the planets. The columns show 1: The frequency number, 2: The frequency, 3: The period, 4: Modulus of the amplitude, 5: The phase.

k	ν_k [rad/yr]	P [yr]	$\log_{10}(\alpha_k)$	φ_k [°]
0	1.059370	5.931056	-12.835	171.615
1	1.563977	4.017441	-12.540	-120.011
2	0.000000	inf	-12.710	180.000
3	1.875899	3.349426	-12.894	-85.621
4	0.008921	704.325810	-12.907	34.462
5	2.813812	2.232980	-13.030	-107.995
6	1.589099	3.953930	-13.289	-33.111
7	2.535769	2.477823	-13.330	-3.845
8	1.597793	3.932415	-13.707	24.798
9	1.566188	4.011768	-13.719	-9.591
10	0.937977	6.698654	-13.817	118.827
11	0.000000	inf	-13.838	177.708
12	0.426598	14.728597	-13.863	-8.714
13	1.562115	4.022229	-13.929	-88.106
14	0.659901	9.521411	-14.126	45.341
15	0.007133	880.839370	-14.162	-105.744
16	0.797562	7.877990	-14.167	177.441
17	2.118687	2.965603	-14.238	142.575
18	0.003625	1733.127607	-14.331	126.786
19	1.588195	3.956181	-14.616	176.124

In Tab.7.1 are identified the principal periods of 742.98 and 806.91 years. The mean motion resonances between solar planets are mentioned in the literature, such as the resonances 5 : 2 for the Jupiter-Saturn system, 2 : 1 for the Uranus-Neptune system, 3 : 1 for the Saturn-Uranus system and 3 : 2 for the Neptune-Pluto system (Peale, 1976). The Jupiter-Saturn mean motion resonance is ~ 846 years which is closer to principal determined periods of 806.91 and 880.83 years. The 21.06 and 20.49 year periods are due to the well known reversal magnetic, Hale cycle (Hale, 1929), while the 31.69 period may correspond to the solar origin of the 35 years Bruckner climatic periodicity (Raspopov et al., 2000), finally the period of 313.3 years would be closer to the Link cycle (Link, 1964) and also the significant periodicities of ~ 350 and ~ 710 years mentioned in the study of radionuclide proxies (Steinhilber et al., 2012) which may be closer to the determined period of 742.98 and 704.32 years. In (Ryabov, 2015) was studied the Wolf number in the northern and southern hemispheres during cycles 23 – 24 (1992 – 2013), by obtaining a pattern of development of the "northern" and "southern" solar cycles in detail. They adopt the formation of each of the cycles which is determined by the joint effect of long-period processes lasting from 3 to 7 years and short-period processes lasting less than 2 years. In Tab.7.1 are also determined the periods from 2.47 to 6.70 years.

7.5.3 Comparison of potential coefficients of the Sun with solar activity records

In the previous sections we have attempted to analyse the available observed and physical based reconstructed series of solar activity indicators. The QP properties are then used to reconstruct these series. The analytical expressions of the deformation coefficients have shown multi-secular and millennial behavior of the deformation coefficients of the Sun by tracing the orbital periods of the planets. A long-term series of solar data is required to study its correlation with semi-analytical and numerical calculation of planetary tidal effects. For this purpose, here we have used the daily SSN and yearly GSN observed QP reconstruction series, the physical-based estimation of GSN (S04, U14, U03) and the observational estimation of GSN (L16, U16, C16, H98 and Hd98), finally the IntCal13 radiocarbon calibration curve ^{14}C .

7.5.3.1 QP reconstruction of SSN vs ΔC_{20}

The deformation coefficients and the observed data can be studied in order to search for their possible correlation. The observed decadal reconstruction series are based on the QP approximation (see for more 6.3.1). The calculated deformation coefficient ΔC_{20} is estimated as the sum of the contributions from all the planets (see for more 7.5.1.2). In Fig.7.21 and Fig.7.22 are represented the comparison of ΔC_{20} with the daily DSN and yearly YSN observed (WDC-SILSO, Frédéric et al. (2015)) reconstruction series RDSN and RYSN respectively. The multi-millennial yearly YSN and daily DSN observed decadal QP reconstruction of the SSN series are presented for the interval of 1000 to 3000 years. The DSN, YSN and ΔC_{20} decadal series are averaged for 10 years, which represents a purely secular variation of these series. Here ΔC_{20} is the deformation coefficient summed for all the planets. The variation of the presented patterns shows some similarity which may be random for the two series. The QP approximation based RDSN reconstruction series of DSN (daily observed data) during the given interval of 1000 – 3000 years show three multi secular cycles which are also peculiar to ΔC_{20} as displayed in Fig.7.21. Although, the reconstruction series RYSN of yearly observed

data shown in Fig.7.22 represents different variations when compared to ΔC_{20} . The reconstruction of the long-term timescales of DSN, YSN and ΔC_{20} are RDSN, RYSN and RC_{20} respectively and are displayed in Fig.7.23 and Fig.7.24 with their QP based reconstruction series. It should be noted that in all the figures DSN, YSN and ΔC_{20} are normalized for the purpose of a quantitative view.

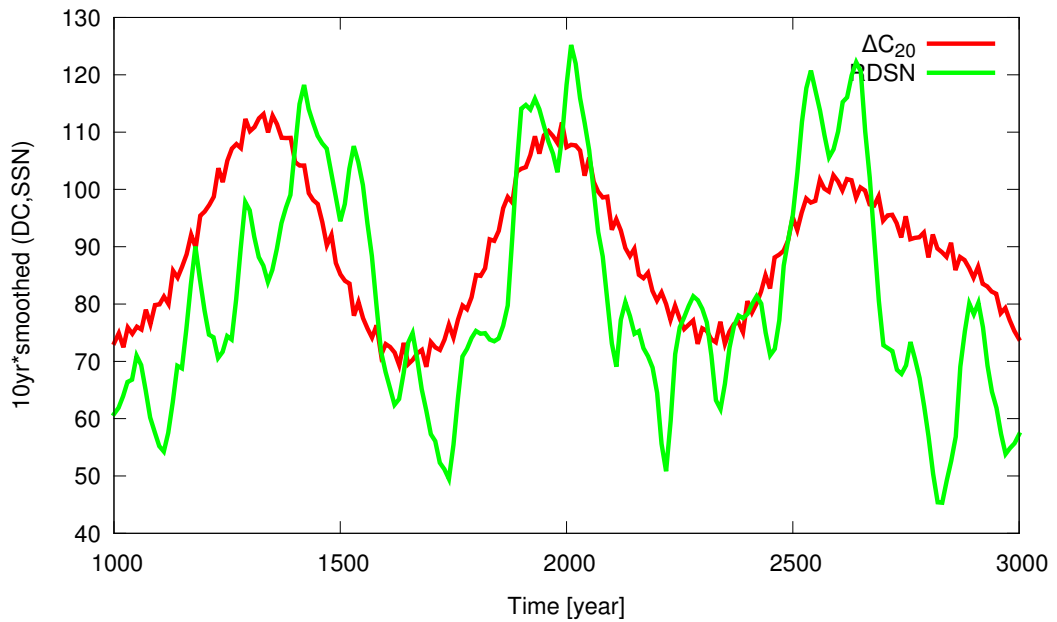


Figure 7.21 – The SSN daily observed (Frédéric et al., 2015, WDC-SILSO) QP based reconstruction RDSN compared to the sum of all the planets ΔC_{20} . Both series are averaged over 10 years and have a decadal variation, covering the interval between 1000 to 3000 years.

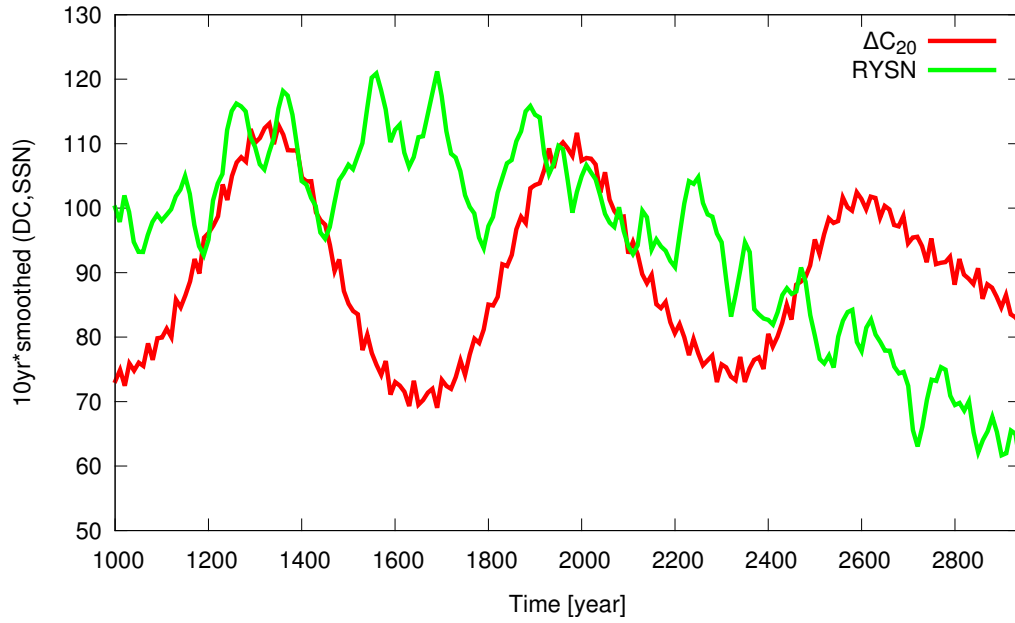


Figure 7.22 – The SSN yearly observed (Frédéric et al., 2015, WDC-SILSO) QP based reconstruction RYSN compared to the sum of all the planets ΔC_{20} . Both series are averaged to 10 years and have a decadal variation, covering the interval between 1000 to 3000 years.

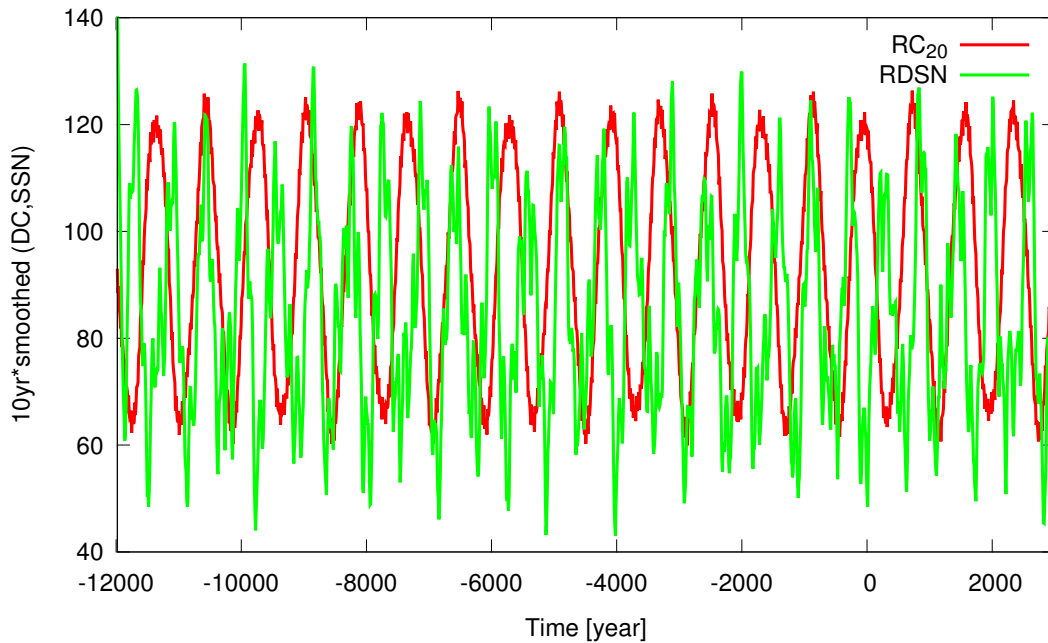


Figure 7.23 – The SSN daily observed (Frédéric et al., 2015, WDC-SILSO) QP based RDSN reconstruction compared to the QP based reconstruction of the sum of all planets RC_{20} . Both series are averaged to 10 years and present the decadal variation, covering the interval 12,000B.C. to 3000A.D.

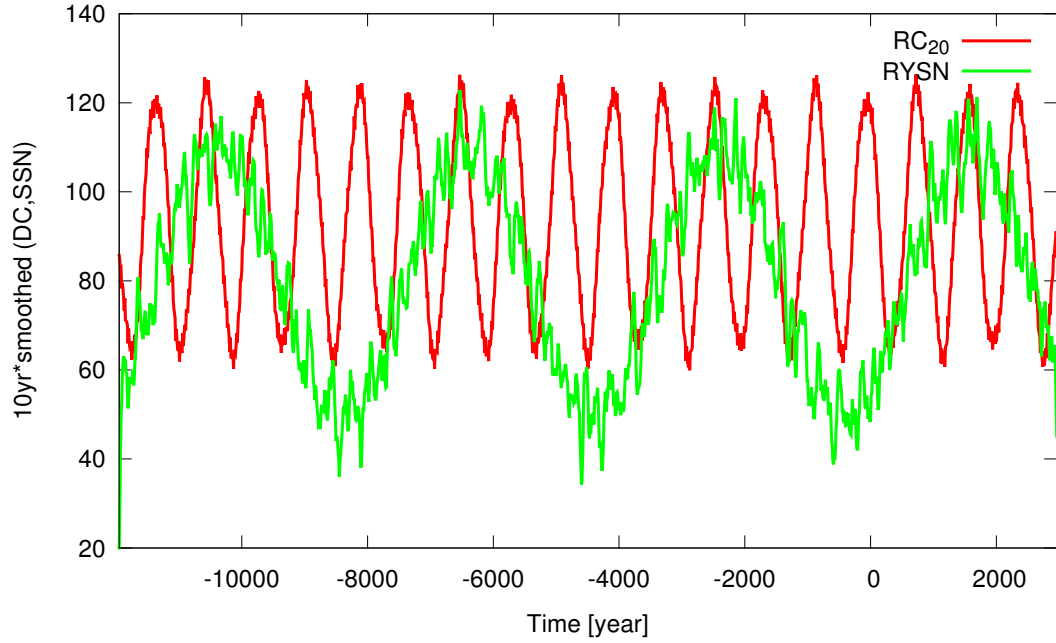


Figure 7.24 – The SSN yearly observed (Frédéric et al., 2015, WDC-SILSO) QP based RYSN reconstruction compared to the QP based reconstruction of the sum of all planets RC_{20} . Both series are averaged to 10 years and present the decadal variation, covering the interval 12,000B.C. to 3000A.D.

According to the above presented results, the reconstructed DSN and ΔC_{20} series in Figs.7.21 and 7.23 have excellent matching periodicities. In Fig.7.21 for both series we can identify three peaks with periods of about 500 years. The long-term duration in Fig.7.23 has a continuation of these periodicities presenting both in and out phase variations. When compared with the ΔC_{20} series its yearly observed QP based reconstruction shows a different pattern as shown in Fig.7.22 and Fig.7.24.

7.5.3.2 QP reconstruction of estimated GSN vs ΔC_{20}

The GSN decadal estimation of the reconstructed RU16, RC16, RL16, RH98 and RHd98 series can be used to search for the common periodicities on the variation of ΔC_{20} . The multi-millennial variation of the decadal QP based reconstruction of the GSN series is presented in Fig.7.25 for the data of L16 (Svalgaard & Schatten, 2016), Fig.7.26 for the data of U16 (Usoskin et al., 2016c), Fig.7.27 and Fig.7.28 for the daily H98d and yearly H98 data (Hoyt & Schatten, 1998), finally Fig.7.29 for the data of C16 (Frédéric et al., 2015) (see for more 6.3.2). These results show the decadal variation of GSN compared with the sum of all the planets deformation coefficients ΔC_{20} for the interval of 1000 to 3000 years. Both series are the decadal 10 year smoothed variation. It should be noted that in all the series of RU16, RC16, RL16, RH98, RHd98 and ΔC_{20} are normalized for the purpose of quantitative view.

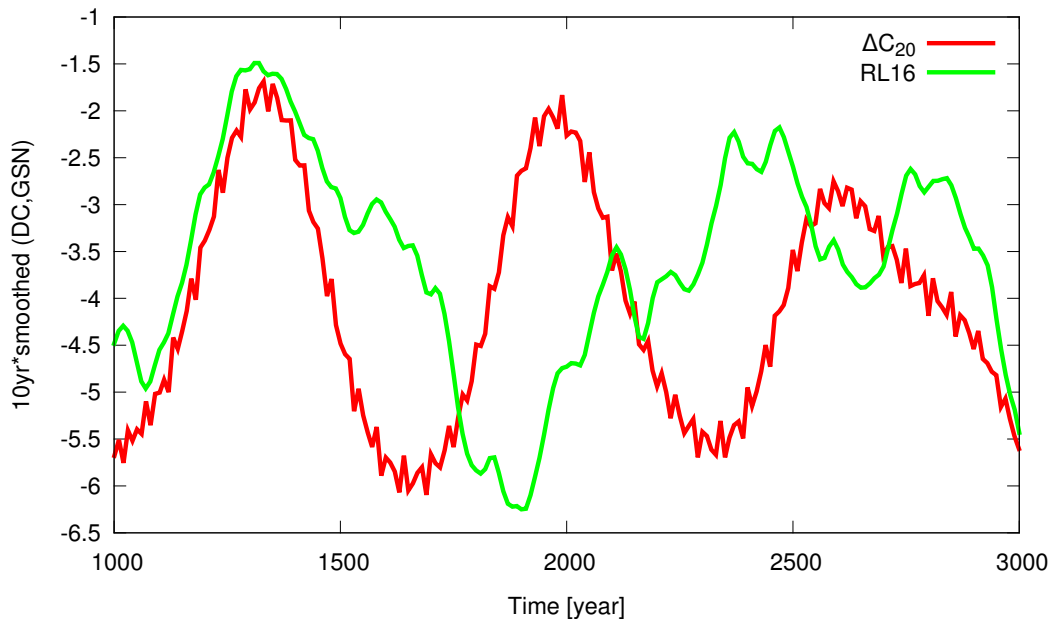


Figure 7.25 – The GSN yearly estimated decadal reconstruction RL16 based on QP approximation compared to the sum of all planets ΔC_{20} . Both series are averaged to 10 years covering the interval between 1000 to 3000 years.

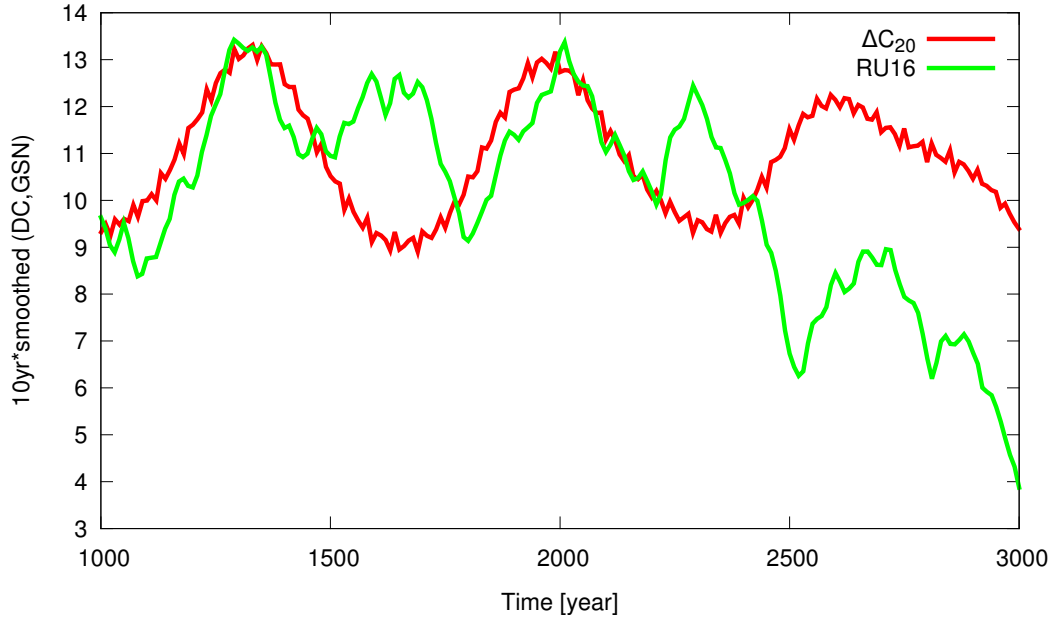


Figure 7.26 – The GSN yearly estimated decadal reconstruction RU16 based on QP approximation compared to the sum of all planets ΔC_{20} . Both series are averaged to 10 years covering the interval between 1000 to 3000 years.

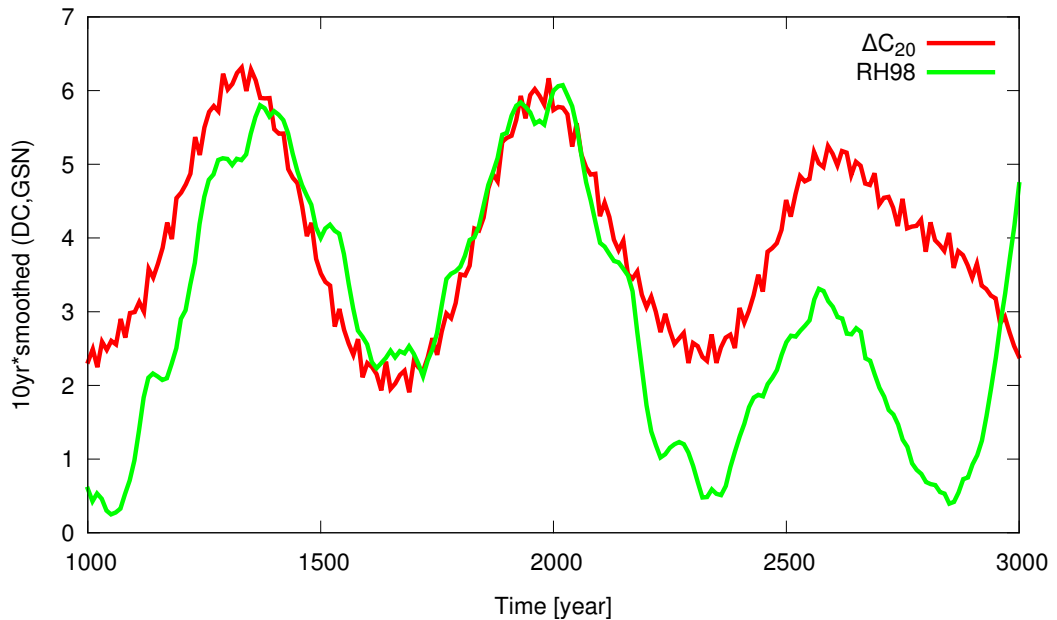


Figure 7.27 – The GSN yearly estimated decadal reconstruction RH98 based on QP approximation compared to the sum of all planets ΔC_{20} . Both series are averaged to 10 years covering the interval between 1000 to 3000 years.

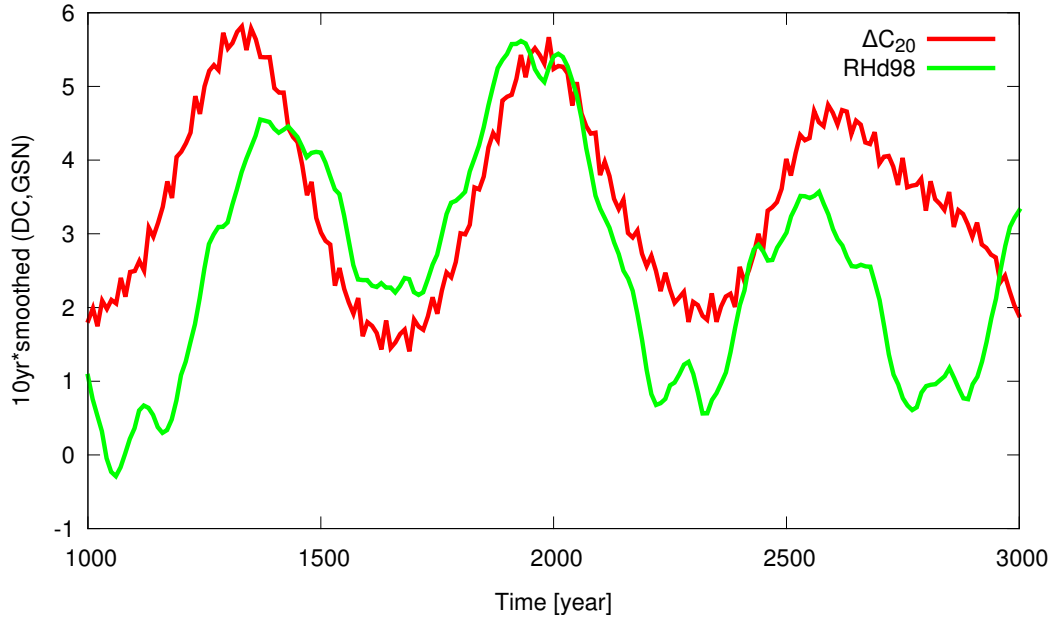


Figure 7.28 – The GSN yearly estimated decadal reconstruction RHD98 based on QP approximation compared to the sum of all planets ΔC_{20} . Both series are averaged to 10 years covering the interval between 1000 to 3000 years.

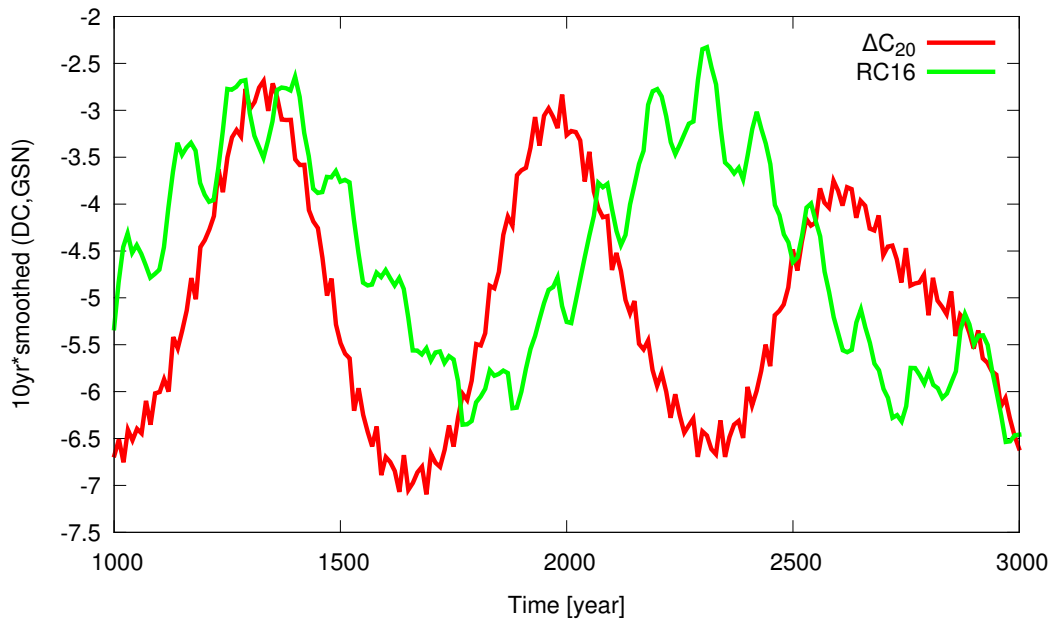


Figure 7.29 – The GSN yearly estimated decadal reconstruction RC16 based on QP approximation compared to the sum of all planets ΔC_{20} . Both series are averaged to 10 years covering the interval between 1000 to 3000 years.

7.5. SEMI-ANALYTICAL AND NUMERICAL ESTIMATION OF THE DEFORMATION COEFFICIENTS

According to presented results, the comparison of GSN and ΔC_{20} series shows the closest correlation between the Hd98 daily and H98 yearly observed records. This data has been intensively used as the only available and reliable solar activity GSN record until the year 2016. Then in the same year there appeared other new GSN records such as L16, U16 and C16, however these records are also based on the H98 records. Some correlations of the GSN yearly H98 and daily Hd98 reconstructions also might be coincidences of the data's reconstructions. Thus its needs long-term verification of the reconstructed series. For this purpose in Figs.7.23,7.24,7.30,7.31,7.32,7.33 and 7.34 has been presented the decadal reconstructed long-term variation of GSN and ΔC_{20} gravity coefficients. The QP based reconstruction series of deformation coefficient RC_{20} is the sum of all the planets with 10 year averages for the interval of 12,000B.C. to 3000A.D. years.

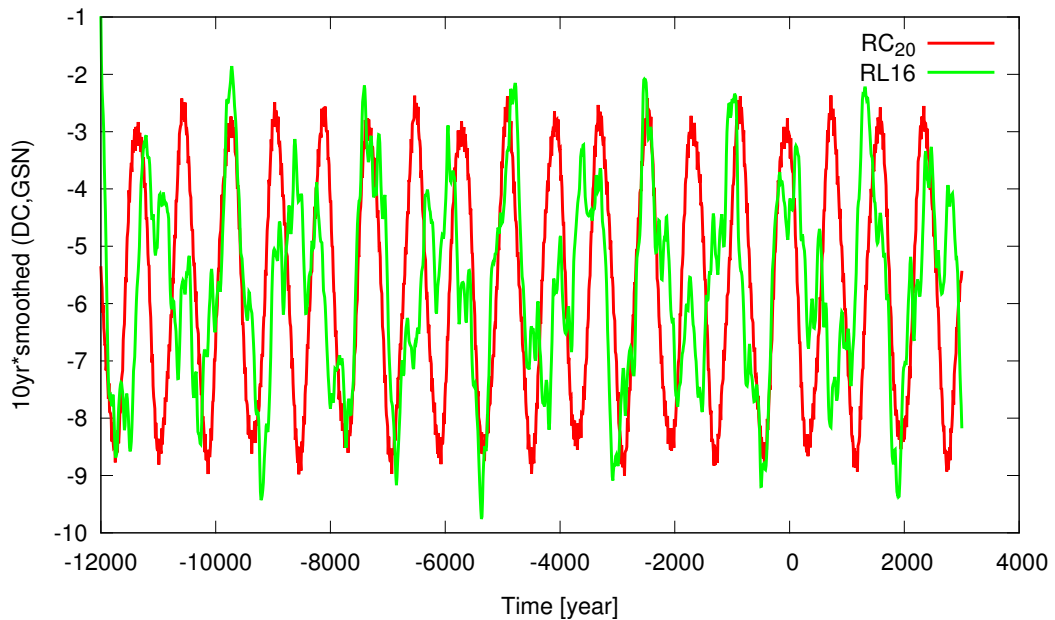


Figure 7.30 – The GSN estimated reconstruction RL16 compared to the reconstruction of the sum of all the planets ΔC_{20} . Both series are averaged to 10 years and their reconstructions are based on QP approximation, covering the interval between 12,000B.C. to 3000A.D.

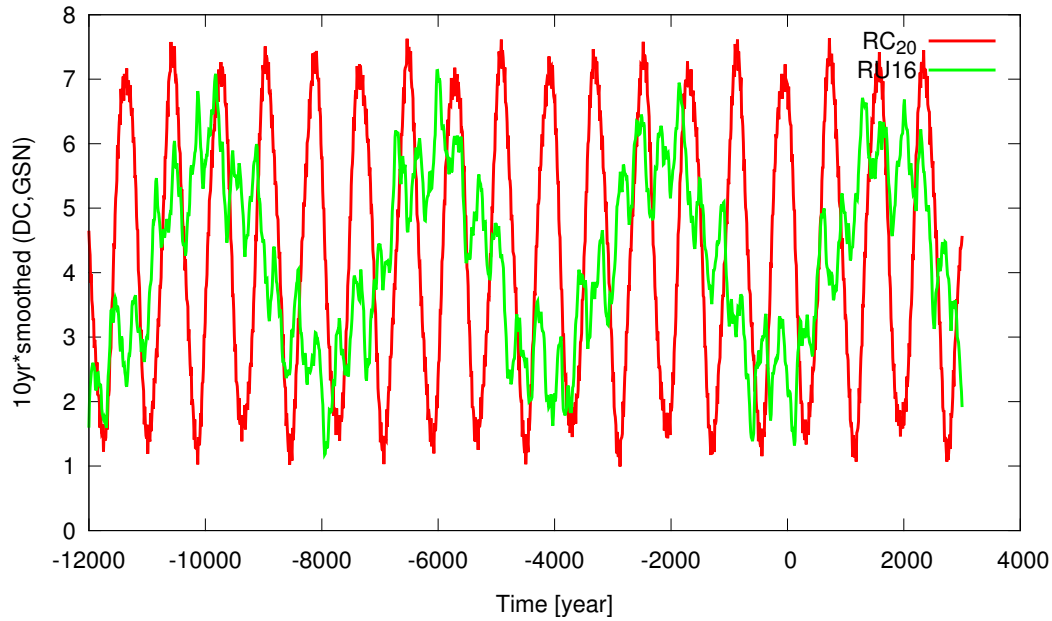


Figure 7.31 – The GSN estimated reconstruction RU16 compared to the reconstruction of the sum of all the planets ΔC_{20} . Both series are averaged to 10 years and their reconstructions are based on QP approximation, covering the interval between 12,000B.C. to 3000A.D.

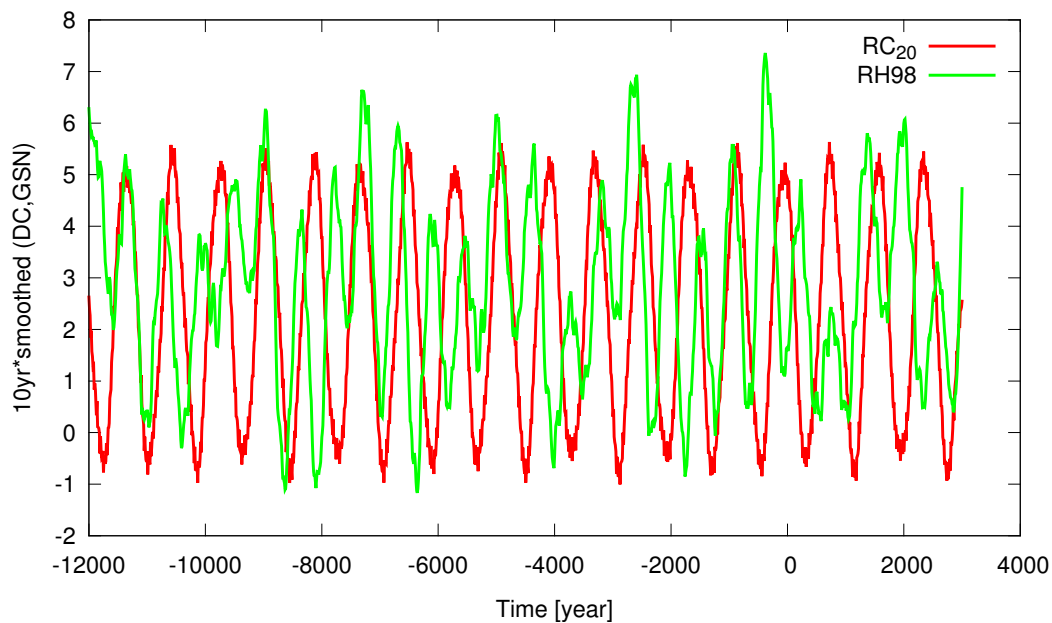


Figure 7.32 – The GSN estimated reconstruction RH98 compared to the reconstruction of the sum of all the planets ΔC_{20} . Both series are averaged to 10 years and their reconstructions are based on QP approximation, covering the interval between 12,000B.C. to 3000A.D.

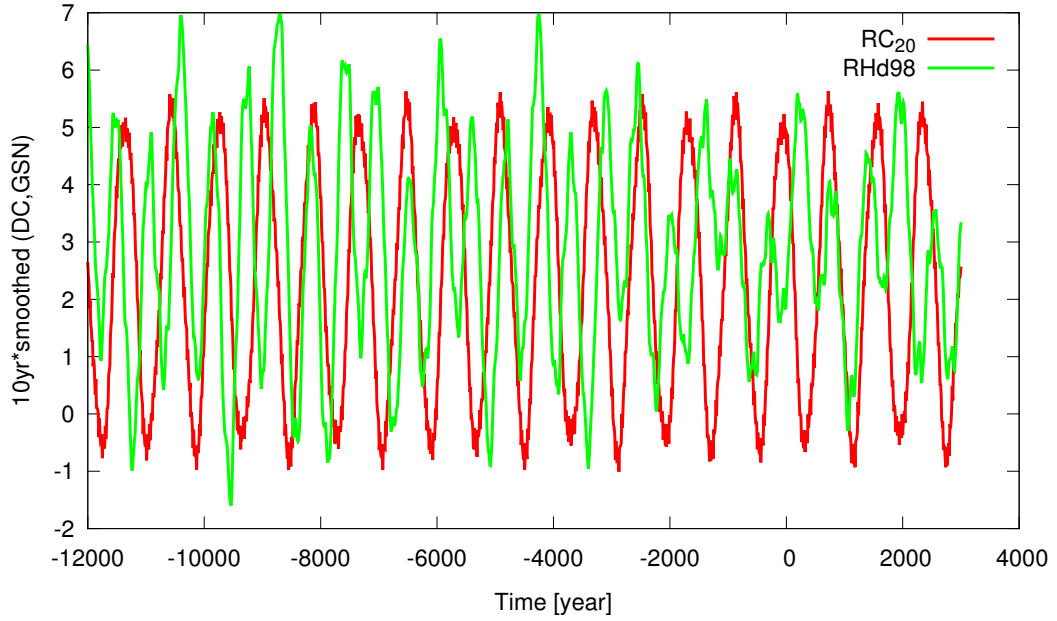


Figure 7.33 – The GSN estimated reconstruction RHd98 compared to the reconstruction of the sum of all the planets ΔC_{20} . Both series are averaged to 10 years and their reconstructions are based on QP approximation, covering the interval between 12,000B.C. to 3000A.D.

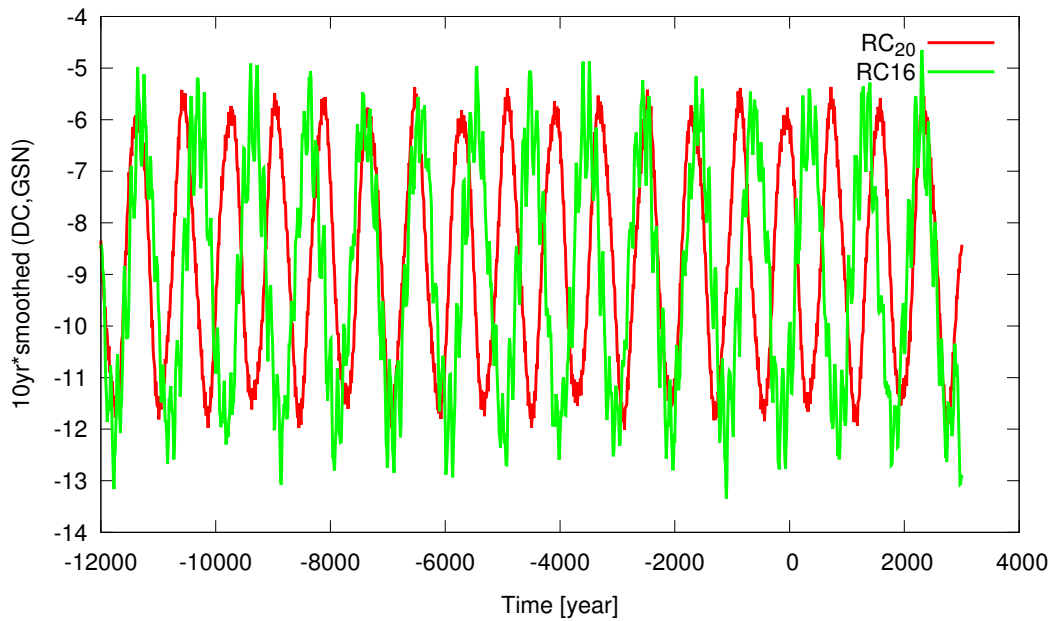


Figure 7.34 – The GSN estimated reconstruction RC16 compared to the reconstruction of the sum of all the planets ΔC_{20} . Both series are averaged to 10 years and their reconstructions are based on QP approximation, covering the interval between 12,000B.C. to 3000A.D.

The above presented results of the GSN and ΔC_{20} series tend to have some secular periodicities. The RH98, RH98d and RDSN series have some similar periodicities with the ΔC_{20} series, while the RYSN and RU16 series present some different variations. The other reconstructed RC16 and RL16 shows hardly any correlated behavior with the ΔC_{20} series. The presented correlations between solar activity and the deformations of the Sun due to the tidal perturbation of planets do not eliminate the likelihood that these correlations are random coincidences.

7.5.3.3 Physical based reconstruction of GSN vs ΔC_{20}

The radio nuclides of physical-based S04 (see for more Sec. 6.4.3, Solanki et al. (2004b)), U03 (see for more Sec. 6.4.2, Usoskin et al. (2003)) and U14 (see for more Sec. 6.4.3, Usoskin et al. (2014)) decadal series of the GSN proxies are used to search for the common periodicities on the variation of ΔC_{20} . Fig. 7.35 and Fig.7.36 represent the proxies of S04 compared with the sum of the reconstructed deformation coefficients of all the planets RC_{20} for the interval of 1000 – 1895 and 9450B.C. to 1895A.D. respectively. Both the S04 and RC_{20} series have decadal steps and are averaged for 10 years representing their secular variations. The curves of S04 and RC_{20} in Fig.7.35 have an excellent correlation representing the similar secular periodicities, while in Fig.7.36 S04 shows a more chaotic variation and the RC_{20} curve represents a regular periodicity. Although, some periodicities between the S04 and RC_{20} series are well distinguished.

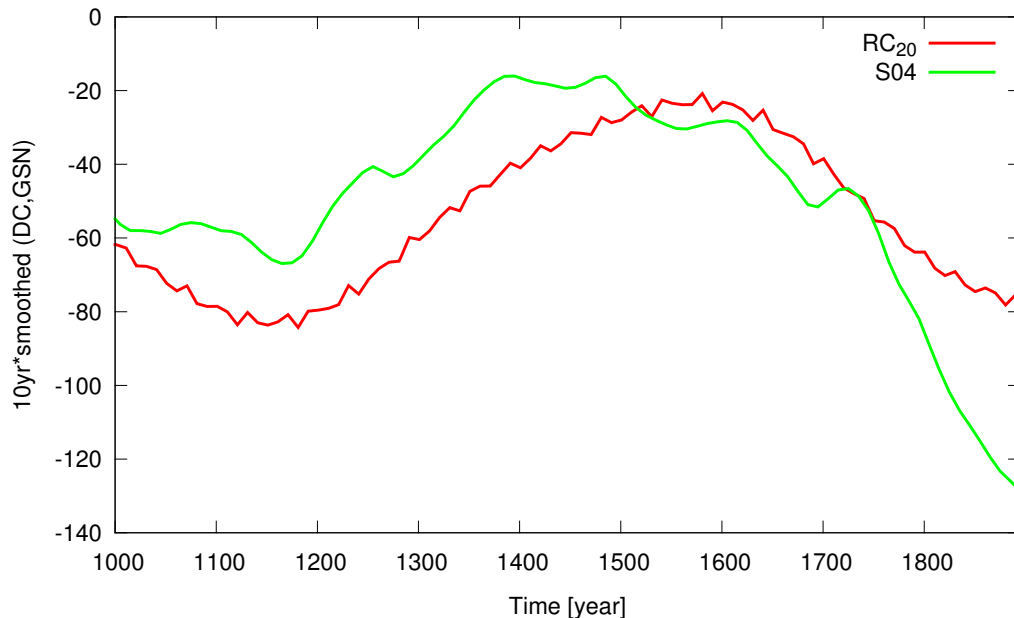


Figure 7.35 – The radioisotope based GSN decadal proxies of S04 compared to the sum of all the planets RC_{20} reconstructed deformation coefficient. Both series are averaged to 10 years with decadal variation, covering the interval between 1000 to 1895 years.

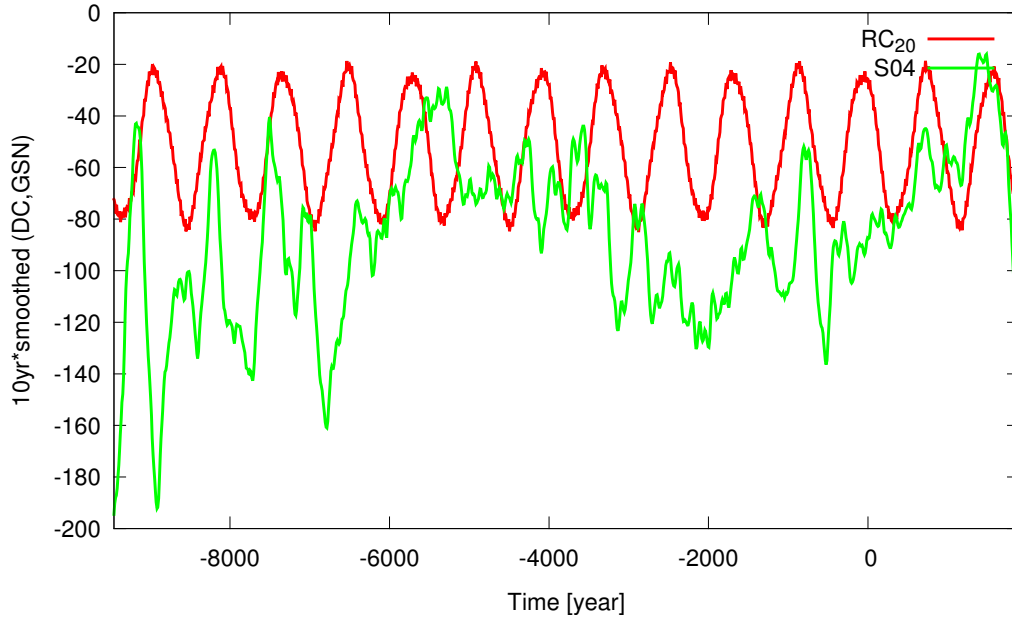


Figure 7.36 – The radioisotope based GSN decadal proxies of S04 compared to the sum of reconstructed all the planets RC_{20} deformation coefficient. Both series are averaged to 10 years with decadal variation, covering the interval between 9450B.C. to 1895A.D. years.

In Fig.7.36 the correlations have some interesting features which can not be explained by the planetary perturbation mechanism. In some periods the gravitational effect of planets is reversed in comparison to the SSN series.

In the same way, in Fig.7.37 and Fig.7.38 are displayed the radio nuclides based GSN series of U03, U14 and the reconstructed potential coefficient RC_{20} for the interval of 855 – 1975 and 1145B.C. to 1945A.D respectively. All the series have decadal steps with an average of 10 years which represent their secular variations.

The comparison of U03 and U14 with the RC_{20} series shows a lack of correlation representing their long-term evolution. The variations of GSN proxies and the reconstructed RC_{20} deformation coefficient series during the given period present some correlation e.g. as shown in Fig.7.37 and Fig.7.38. This may also be due to randomness.

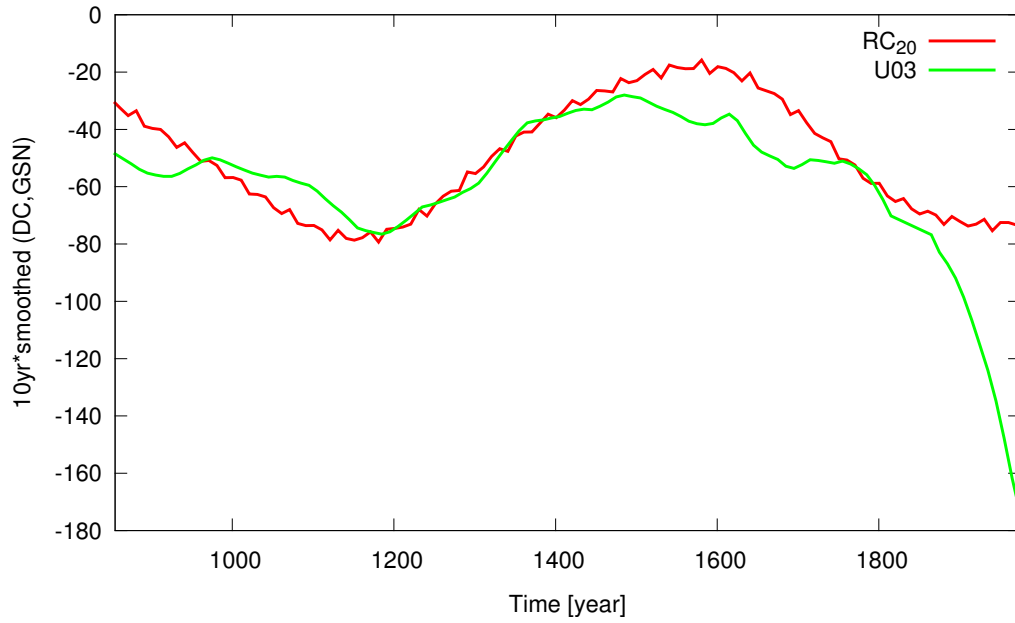


Figure 7.37 – The radioisotope based GSN decadal proxies of U03 compared to the sum of all the planets RC_{20} reconstructed deformation coefficient. Both series are averaged to 10 years with decadal variation, covering the interval between 855A.D. to 1975A.D. years.

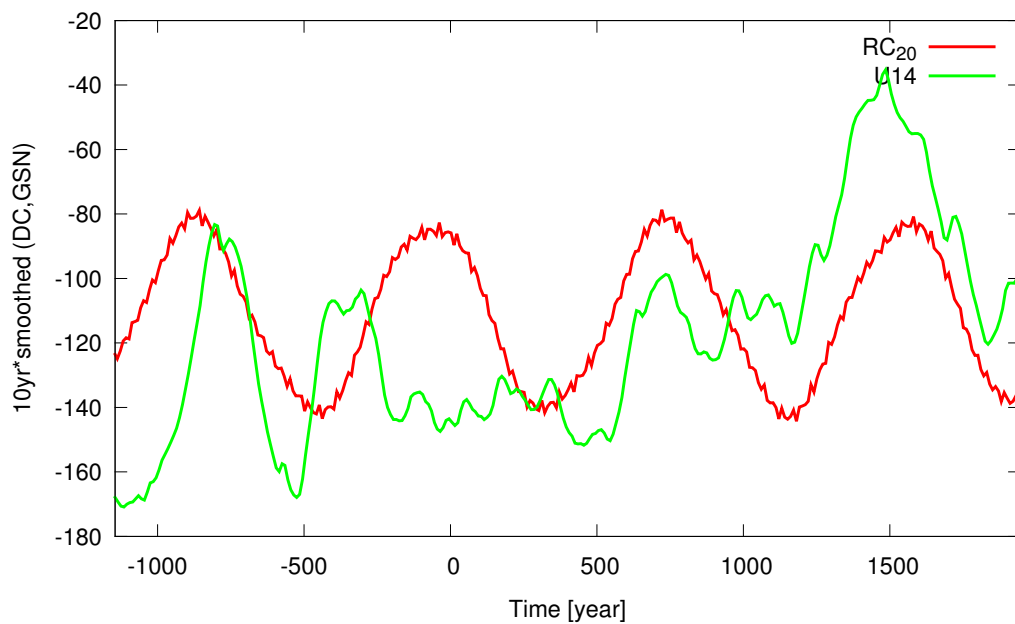


Figure 7.38 – The radioisotope based GSN decadal proxies of U14 compared to the sum of all the planets ΔC_{20} reconstructed deformation coefficient. Both series are averaged to 10 years with decadal variation, covering the interval between 1145B.C. to 1945A.D. years.

7.5.3.4 IntCal13 radiocarbon calibration curve ^{14}C vs ΔC_{20}

The measurement of IntCal98 and IntCal13 from the Northern hemisphere atmospheric radiocarbon calibration curve ^{14}C (see for more 6.4.1, Reimer, 2013) compared with the ΔC_{20} deformation coefficients of the sum of all the planets including Pluto. The decadal series are smoothed with a 10 year variation.

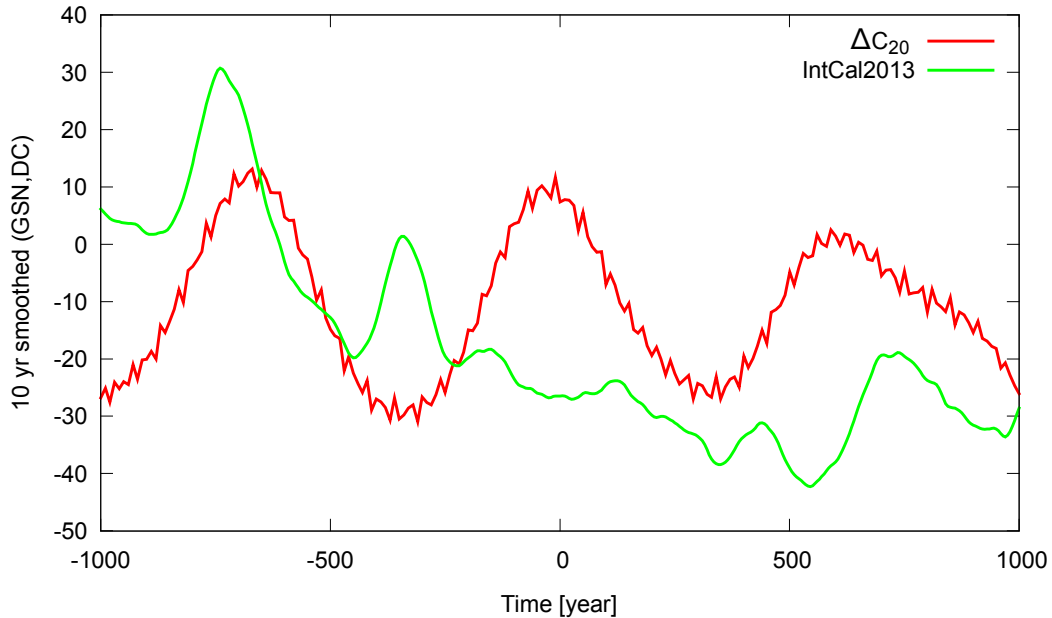


Figure 7.39 – IntCal2013 decadal smoothed variation for the sum of all planets ΔC_{20} are compared. Both decadal series are averaged to 10 years, covering the interval between 1000B.C. to 1000A.D.

According to Fig.7.39, the variations of ^{14}C and ΔC_{20} at the given interval of 1000B.C. to 1000A.D shows some correlated peaks. Here we do not exclude that it might be caused by purely chaotic or stochastic effects. It does not appear possible to use such a period match statistically to imply that planetary tides affect sunspots without either a physical justification or a much closer period match than can be obtained with current sunspot data. The periodicities of the two series are well matched repeating the same maxi and mini peaks. It should be noted that the above presented results do not conclude the influences of tidal forces of the planets on the cyclic period of solar activity. On the other hand, the observed SSN/GSN and computed potential coefficients should represent a haphazardly coherence of both series because they are not linked with each other. The variations of the pattern show some coincidence which might be due to appearance at random of the two series. The SSN cycle has a non-random nature and the variation of the SSN might be consistent with a planetary tidal driven mechanism. The convection of hot plasma of the Sun rises up from the interior of the Sun. It then spreads out across the surface of the Sun, which cools and sinks inward in a random process. That is why random processes can not result in a non-random process. There is an assumption: the SSN is not originated from and is not related to random plasma convection of the Sun. From Fig.7.20 we see that the quantitative maximum value of gravity coefficients is $\Delta C_{20} = 10^{-11.9}$. Even if planetary influences are too small to produce no more than a small modulation of the solar cycle, we do not exclude the possibility that

the long-term combined action of the planets may induce small internal motions in the Sun, which may indirectly have an effect on the solar dynamo. That is why we not conclude that the variation of SSN are not partially related by planetary hypotheses.

Our purpose was the research of a relationship between the solar activity indices and the planetary tidal force. The reconstructed series of solar indices were adopted for a more precise method of frequency analysis of the temporal data of observation.

The presented results and estimations might be summarized with the following conclusions: All of the equations of deformation coefficients were expressed in equatorial coordinates of the Sun, and the data in La2004 is in nearly ecliptic reference of the Sun, INPOP being the reference of ICRF. Our model is based on tide theory. This is based on the consideration of the dynamics of planets without taking account the physical processes of the Sun and planets. The interior physics of the bodies, i.e. the loss of the mass, order, magnitude, convection, angular momentum, evolution of the rotation, spin-orbit coupling mechanism etc. were not taken into account. All the calculations and estimations in this section are not sufficient to assume planetary evidence on the Sun cyclic periodicities. We have been interested just in dynamical effects of the planets on the Sun, where the mass of the Sun is constant without rotation and the planets are material points. The model is based on the assumption that each gravitational effect of the planets modified separately or together the orbits of solar system bodies. This results in deformation of Sun's surface then impact flux or inertial motion on the Sun. Garai (2001) studied the model of evaporation of projectiles hitting the Sun that produces a shock wave which disturbs the up welling of the plasma resulting in a sunspot formation. Wolf (in 1877) discovered that the periodicity of the sunspots is related to the periods of Jupiter and Saturn. This discovery lead to many possible planetary hypothesizes, with still just empirical evidence. It needs such investigations to study an assumption and to understand the long-term solar cycles which is still a big unsolved problem.

Chapter 8

Conclusion and Perspectives

In this thesis historical and current observation techniques were described complete with data. Instruments (see Sec. 2) and methods of treatments of analysis with events (see Secs. 4 and 3) were detailed. The overview of solar activity, its impact to the terrestrial climate and a review of this topic were discussed in Sec.5. We used for our research the revised observational data such as daily DSN, yearly YSN sunspot numbers, and observational estimated GSN data (L16, C16, U16, H98 and Hd98), as well as reconstructed proxies from radionuclides. By comparing the different sources of observational records of past solar activity changes we selected data which is verified with the long-term historical/observed data and cosmogenic proxies. This is because cosmogenic radionuclides are considered one of the possibilities of obtaining an alternative and completely independent record of solar variability. This observational data was taken as a basis for the quantitative solar activity reconstructions far back into the past using the method of frequency analysis. We compared the quasi-periodic reconstruction series to the observed sunspot records. It was shown that the reconstruction series is based on a quasi-periodic approximation using the various solar activity records that have good quantitative agreements (as shown in Sec.6) with the observed sunspot data, in particular with H98 and Hd98 data. These quasi-periodic based reconstructions of the observed records identified historically known grand maxima and minima events. Although, we note that these long-term reconstruction series might have some agreements because of a stochastic process. That leads for the need of a critical assessment and comparisons with other independent proxies. For this propose we used physical based radionuclide reconstructions of solar variability proxies such as U03, U14 and S04 to verify the reconstructed data series. The results presented in Sec.6 show good correlation before 1000B.C., but less so after 1000B.C. These uncertainties after 1000B.C. would be potentially due to identifying remaining non-solar processes in the radionuclide based solar activity reconstructions. These two completely independent series exhibit a linear correlation compared to the radionuclide based solar modulation records.

Especially in the long-term reconstruction records of H98, Hd98, C16 and revised DSN show very good correlation with the radionuclide based proxies. In particular, focusing on all grand events they show a reasonable agreement except the Sporer minima in the series of DSN, H98, Hd98 and U16. Until 1600 A.D., the ^{14}C -based record agrees better with all the reconstructed solar activity series, while after 1600 A.D. there is some additional short-term disagreement represented by anti-phased amplitudes, that might be caused by chaotic variation of the solar records. Comparing our long-term reconstructed series to the radionuclide based reconstruction results using normalization after 1000B.C. leads to some systematically anti-phased variations. This might be caused by the limited terms of the extrapolation methods.

The main goal of this work was to estimate the tidal effects of the planets and their impact and role on solar activity evolution. The final aim was devoted to researching the possible correlation between the reconstructed long-term series of solar activity data with the variation of the deformation coefficients of the Sun. Methods we developed here provide a more realistic dynamical model for describing the tidal effect exerted by planets on the deformation of the non-spherical homogenic Sun's surface. This was compared to the corresponding short, mid and long timescale reconstructed solar proxies. The analytical and numerical calculated deformation coefficients were compared to verify accuracy. We investigated the deformation coefficients to test the mid and long-term variability during the last, and only directly observed, grand solar events. Sec.7 shows the quasi-periodic and physical based reconstructions of the sunspots in comparison with the potential coefficients calculated in this study. The results present the comparison of the reconstructed DSN, H98, Hd98 and C16 series which have variations connected to secular changes. It is notable that most of the 704 – 880 decadal variability is determined in the deformation coefficients variations (see 7.5.2) and that the periodicities are mostly synchronous with the reconstructed sunspot proxies such as U03 and S04 (see 6.4.2). The 704 – 880 years of period is may be the motion of the Jupiter-Saturn planetary system near the 5 : 2 mean-motion resonance. Reconstructed series of SSN and GSN during 2000 years shows some coherences with ΔC_{20} variations with periods of 743 and 807 years, as well S04, U03, U14 and InCal2013 proxies. The yearly variation of the deformation coefficients have identified the periodicities from 2 to 10, as well from 20 to 31 (for more see, Sec.7.5.2). These periodicities have appeared in the observed solar activity data (see 6.3.2).

We have shown that planetary tides produce major cycles with proprieties of ~ 10 year periods, which correspond to the cycles observed in the sunspot number data. There is an assumption that the cycles with periods of 10, and 12 years might be directly related to Jupiter and Saturn orbits, while the 11-year cycle is the average between the 10 and 12 year Jupiter-Saturn cycles, and it is also reproduced by the recurrent tidal patterns generated by the fast tidal cycles related to Mercury, Venus and Earth. The tidal perturbation may be generated by the two planetary subsystems (terrestrial and Jovian planets). Hence, terrestrial and Jovian planets are possibly both important to determine solar dynamics over multiple timescales. The variation of the deformation coefficients ΔC_{20} also have identified the known solar cycles such as the northern and southern hemisphere leading cycle (~ 5 and ~ 3 years respectively) (Zolotova et al., 2010; Ryabov, 2015), the Schwabe (8–15 years) (Schwabe, 1844), the polar/Hale cycles (22 – 23 years) (Hale & Ellerman, 1918), the Bruckner cycle (30 – 50 years) (Bruckner, 1890) (for more see, Sec.7.5.2). The frequency analysis of the observed series have identified the Gleissberg ($\sim 65 – 110$ years) (Gleissberg, 1967b), the DeVaris/Suess ($\sim 150 – 210$ years) (Suess, 1980), the Schove (55 – 160, 160 – 270 years) (Schove, 1983b), the Link cycle (380 – 420) (Link, 1964), except the Bray/Hallstatt (~ 2200 years) (Bray, 1967) and Eddy (~ 970 years) (Eddy, 1976) cycles (see Sec. 7). Although, it is hard to quantify and conclude the planetary influences produce more than a small modulation of the solar cycle and can deform the solar surface only insignificantly e.g., for total planets $\Delta C_{20}=10^{-12}$.

We also note that some apparent differences in the quasi-periodic based series, variations of the deformation coefficients and radionuclide based reconstruction may lead to disagreeing conclusions about planetary theory on solar activity levels. In general, variation of the potential coefficients lead to similar solar activity reconstructions, where radionuclide records agree well. The radionuclide based proxies S04, U03 and U14 show an excellent correlation with the deformation variations, lending strong support to these revisions. Here we do not exclude

the possibility that the long-term variability combined with action of the planets may induce small internal motions in the Sun, which may indirectly have an effect on the solar dynamo. Here we also conclude that the formation of sunspots might be partially related by planetary hypotheses. Although most of the recent research argues that solar cyclic phenomena is originated by the Sun's interior (Augustson et al., 2015; Strugarek et al., 2017). First, in the future our proposed dynamical model will be developed considering more detailed physical processes of the Sun. Application of this proposed model to solar like stars with short activity cycles may give another image on planetary theory. As these solar like stars have a short differential period this gives more reliable long-term observed data and its hosting planets have short orbital periods. Second, taking account the rotational spin of the Sun and its interior physical processes of solar dynamo theory based on the SSM. This approach could allow an estimate on a quantitative level of the planetary tides theory influences to the solar activity variation.

Appendix A

Expression of the potential

Here we used the following notations:

G -constant of the gravitation;

M -mass of the deformable body with R mean equatorial radii, in our case the Sun

m_g -mass of the generative body, in our case the planets

$r_g = \|\mathbf{r}_g\| = \sqrt{(x_g^2 + y_g^2 + z_g^2)}$ coordinates of the generative body expressed in a linked reference frame of an extended body.

In the spherical (r, φ, λ) and $(\rho, \varphi', \lambda')$ coordinates the expressions of a body's motion are defined by the follow equations:

$$\begin{aligned} x &= r \cos \varphi \cos \lambda & x' &= \rho \cos \varphi' \cos \lambda' \\ y &= r \cos \varphi \sin \lambda & y' &= \rho \cos \varphi' \sin \lambda' \\ z &= r \sin \varphi & z' &= \rho' \sin \varphi' \end{aligned}$$

and are shown in Fig.A.1. Thus we have:

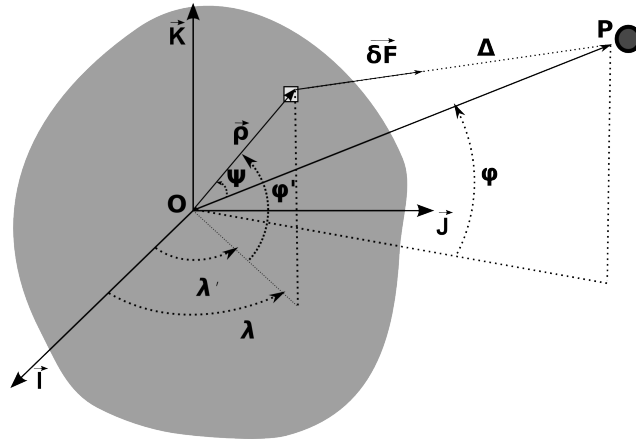


Figure A.1 – Scheme and notations for correlations between a solid body and a punctual mass.

$$\cos \psi = \frac{\mathbf{r} \cdot \boldsymbol{\rho}}{\|\mathbf{r}\| \|\boldsymbol{\rho}\|} = \sin \varphi \sin \varphi' + \cos \varphi \cos \varphi' \cos (\lambda - \lambda'). \quad (\text{A.1})$$

Legendre associate functions using the additional Legendre polynomials are introduced as in (Lambeck, 1988) $(P_{nm})_{0 \leq n, 0 \leq m \leq n}$:

$$P_{n0}(\cos \psi) = \sum_{m=0}^n (2 - \delta_{0m}) \frac{(n-m)!}{(n+m)!} P_{nm}(\sin \varphi) P_{nm}(\sin \varphi') \cdot (\cos m\lambda \cos m\lambda' + \sin m\lambda \sin m\lambda'). \quad (\text{A.2})$$

In this expression, δ_{0m} represents the symbol of Kronecker by:

$$\delta_{0m} = \begin{cases} 0 & \text{if } m \neq 0 \\ 1 & \text{if } m = 0 \end{cases}$$

The potential at a point P due to an extended body is calculated by integration of δU on the volume of body:

$$U(P) = \iiint_V \frac{G}{\Delta} dm. \quad (\text{A.3})$$

Let M be the mass of the extended body and R its average equatorial radius, then the Stokes coefficients can be determined as in Lambeck (1988, eq. 2.2.14a):

$$\begin{pmatrix} C_{nm} \\ S_{nm} \end{pmatrix} = (2 - \delta_{0m}) \frac{1}{MR^n} \frac{(n-m)!}{(n+m)!} \iiint_V (\rho)^n P_{nm} \cdot (\sin \varphi') \begin{pmatrix} \cos m\lambda' \\ \sin m\lambda' \end{pmatrix} dm. \quad (\text{A.4})$$

Due to an extended body the development in spherical harmonics of the potential at a point P of spherical coordinates (r, φ, λ) :

$$U(r, \varphi, \lambda) = -\frac{GM}{r} \sum_{n=0}^{+\infty} \sum_{m=0}^n \left(\frac{R}{r}\right)^n P_{nm}(\sin \varphi) (C_{nm} \cos m\lambda + S_{nm} \sin m\lambda). \quad (\text{A.5})$$

Appendix B

The deformation coefficients

By limiting to the 2nd degree in Eq.A.5 (P_{nm}) $_{0 \leq n, 0 \leq m \leq n}$ the expression of the polynomials of Legendre in the spherical coordinates will be:

$$\begin{aligned}
 r^2 P_{20}(\sin \varphi) &= z^2 - \frac{1}{2}(x^2 + y^2) \\
 r^2 P_{21}(\sin \varphi) \cos(\lambda) &= 3xz \\
 r^2 P_{21}(\sin \varphi) \sin(\lambda) &= 3yz \\
 r^2 P_{22}(\sin \varphi) \cos(2\lambda) &= 3(x^2 - y^2) \\
 r^2 P_{22}(\sin \varphi) \sin(2\lambda) &= 6xy
 \end{aligned} \tag{B.1}$$

According to expression Eq.A.4, the coefficients of potential of the 2nd degree are given:

$$\begin{aligned}
 MR^2 C_{20} &= \iiint_V r'^2 P_{20}(\sin \varphi') dm \\
 MR^2 C_{21} &= \frac{1}{3} \iiint_V r'^2 P_{21}(\sin \varphi') \cos(\lambda') dm \\
 MR^2 C_{22} &= \frac{1}{12} \iiint_V r'^2 P_{22}(\sin \varphi') \cos(2\lambda') dm \\
 MR^2 S_{21} &= \frac{1}{3} \iiint_V r'^2 P_{21}(\sin \varphi') \sin(\lambda') dm \\
 MR^2 S_{22} &= \frac{1}{12} \iiint_V r'^2 P_{22}(\sin \varphi') \sin(\lambda') dm.
 \end{aligned} \tag{B.2}$$

The polynomial values in the cartesian coordinates are expressed using Eq.B.1 on Eq.B.2 as follows:

$$\begin{aligned}
 MR^2 C_{20} &= \frac{1}{2} \iiint_V 2z'^2 - x'^2 - y'^2 dm \\
 MR^2 C_{21} &= \iiint_V z'x' dm, & MR^2 S_{21} &= \iiint_V z'y' dm \\
 MR^2 C_{22} &= \frac{1}{4} \iiint_V x'^2 - y'^2 dm, & MR^2 S_{22} &= \frac{1}{2} \iiint_V x'y' dm.
 \end{aligned} \tag{B.3}$$

The matrix of inertia of a non-punctual body is defined by

$$I = \begin{pmatrix} I_{11} & I_{12} & I_{13} \\ I_{12} & I_{22} & I_{23} \\ I_{13} & I_{23} & I_{33} \end{pmatrix} \quad (\text{B.4})$$

where

$$\begin{aligned} I_{11} &= \iiint_V (y^2 + z^2) \, dm, & I_{12} &= I_{21} = - \iiint_V yx \, dm \\ I_{22} &= \iiint_V (x^2 + z^2) \, dm, & I_{13} &= I_{31} = - \iiint_V xz \, dm \\ I_{33} &= \iiint_V (y^2 + x^2) \, dm, & I_{32} &= I_{23} = - \iiint_V yz \, dm. \end{aligned}$$

Appendix C

The inertia matrix of the extended body

Let \mathcal{I} be the matrix of inertia of an extended body expressed in the reference \mathcal{R}_E as in Eq.B.4. \mathcal{I} is expressed as:

$$\mathcal{I} = \iiint_V \begin{pmatrix} y^2 + z^2 & -xy & -xz \\ -yx & x^2 + z^2 & -yz \\ -zx & -zy & y^2 + x^2 \end{pmatrix} dm. \quad (\text{C.1})$$

It is also possible to transform the ICRF and La2004 coordinates to the mean ecliptic reference of the Sun, then to the equatorial coordinates of the Sun. The deformational coefficients of the Sun are given in the equatorial coordinates of the Sun. The matrix of inertia also can be expressed with the coefficients of the deformation in Eq.B.3. Let I' be the matrix of inertia of the extended body as it undergoes deformation:

$$\begin{aligned} I' &= \begin{pmatrix} I'_{33} & 0 & 0 \\ 0 & I'_{33} & 0 \\ 0 & 0 & I'_{33} \end{pmatrix} + MR^2 \begin{pmatrix} C'_{20} - 2C'_{22} & -2S'_{22} & -C'_{21} \\ -2S'_{22} & C'_{20} + 2C'_{22} & -S'_{21} \\ -C'_{21} & -2S'_{21} & 0 \end{pmatrix} \\ &= \begin{pmatrix} I'_{33} & 0 & 0 \\ 0 & I'_{33} & 0 \\ 0 & 0 & I'_{33} \end{pmatrix} + MR^2 \begin{pmatrix} C_{20} - 2C_{22} & -2S_{22} & -C_{21} \\ -2S_{22} & C_{20} + 2C_{22} & -S_{21} \\ -C_{21} & -2S_{21} & 0 \end{pmatrix} \\ &\quad + MR^2 \begin{pmatrix} \Delta C_{20} - 2\Delta C_{22} & -2\Delta S_{22} & -\Delta C_{21} \\ -2\Delta S_{22} & \Delta C_{20} + 2\Delta C_{22} & -\Delta S_{21} \\ -\Delta C_{21} & -2\Delta S_{21} & 0 \end{pmatrix}. \end{aligned} \quad (\text{C.2})$$

The five coefficients are the potential of the extended body in the 2nd degree. According to Rochester and Smylie(1974), the effects of tide inducing redistribution of masses on the surface of a body is given as follows:

$$3I'^{33} + MR^2 (2C_{20} + 2\Delta C_{20}) = 3I_{33} + 2MR^2 C_{20}, \quad (\text{C.3})$$

then:

$$I'_{33} = I_{33} - \frac{2}{3}MR^2 \Delta C_{20}. \quad (\text{C.4})$$

Finally, will be expressed as follows:

$$I' = I + MR^2 \begin{pmatrix} \frac{1}{3}\Delta C_{20} - 2\Delta C_{22} & -2\Delta S_{22} & -\Delta C_{21} \\ -2\Delta S_{22} & \frac{1}{3}\Delta C_{20} + 2\Delta C_{22} & -\Delta S_{21} \\ -\Delta C_{21} & -\Delta S_{21} & -\frac{2}{3}\Delta C_{20} \end{pmatrix} \quad (\text{C.5})$$

where I is the matrix of the extended body, which is not yet deformed due to a tide or its spin. I is given as follows:

$$I = \begin{pmatrix} I_{33} & 0 & 0 \\ 0 & I_{33} & 0 \\ 0 & 0 & I_{33} \end{pmatrix} + MR^2 \begin{pmatrix} C_{20} - 2C_{22} & -2S_{22} & -C_{21} \\ -2S_{22} & C_{20} + 2C_{22} & -S_{21} \\ -C_{21} & -2S_{21} & 0 \end{pmatrix} \quad (\text{C.6})$$

Appendix D

Analytical expression of the deformation coefficients

The orbital elements of the generative body are:

e – eccentricity;

a – semimajor axis;

i – inclination;

ω – argument of periapsis;

Ω – longitude of the ascending node;

ν – true anomaly;

E – eccentric anomaly;

n – mean motion;

r – radius vector.

Using the orbital elements the transformation of coordinates with rotation matrices in a reference frame is associated the direction of the perihelion and can be expressed:

$$\begin{aligned} X &= r \cos \nu & \dot{X} &= -\frac{na}{\sqrt{1-e^2}} \sin \nu \\ Y &= r \sin \nu & \dot{Y} &= -\frac{na}{\sqrt{1-e^2}} (e + \cos \nu) \end{aligned} \quad (\text{D.1})$$

with

$$r = a(1 - e \cos E) \quad n = \mu^{1/2} a^{-3/2} \quad \mu = G(M + m_g).$$

In the spatial reference frame, thus:

$$\begin{pmatrix} x & \dot{x} \\ y & \dot{y} \\ z & \dot{z} \end{pmatrix} = \mathcal{R}_3(\Omega) \times \mathcal{R}_1(i) \times \mathcal{R}_3(\omega) \times \begin{pmatrix} X & \dot{X} \\ Y & \dot{Y} \\ 0 & \dot{0} \end{pmatrix} \quad (\text{D.2})$$

with

$$\mathcal{R}_3(\phi) = \begin{pmatrix} \cos \phi & -\sin \phi & 0 \\ \sin \phi & \cos \phi & 0 \\ 0 & 0 & 1 \end{pmatrix} \quad \mathcal{R}_1(\phi) = \begin{pmatrix} 1 & 0 & 0 \\ 0 & \cos \phi & -\sin \phi \\ 0 & \sin \phi & \cos \phi \end{pmatrix}. \quad (\text{D.3})$$

The coordinates Eq.D.2 with the orbital elements then can be written as:

$$\begin{cases} x = r (\cos u \cos \Omega - \sin u \sin \Omega \cos i) \\ y = r (\cos u \sin \Omega + \sin u \cos \Omega \cos i) \\ z = r \sin u \sin i \end{cases} \quad (\text{D.4})$$

with $u = \omega + v$. Considering the following known series, up to the 5th degree in eccentricity:

$$\begin{aligned} \left(\frac{a}{r}\right)^3 \epsilon^{i2v} &= \sum_{k=-5}^{+5} X_k^{-3,2} \epsilon^{ikM} \\ \left(\frac{a}{r}\right)^3 \sin 2u &= \sum_{k=1}^{+5} S_k^{-3,2} \sin(kM + 2\omega) \\ \left(\frac{a}{r}\right)^3 &= \sum_{k=0}^{+5} C_k^{-3,2} \cos(kM) \\ \left(\frac{a}{r}\right)^3 \cos 2u &= \sum_{k=0}^{+5} C_k^{-3,2} \cos(kM + 2\omega) \end{aligned} \quad (\text{D.5})$$

where the Stock coefficients $C_k^{m,n}$ can be expressed in terms of usual Hansen coefficients $X_k^{m,n}$, as:

$$\begin{aligned} C_0^{-3,2} &= X_0^{-3,2} \\ C_k^{-3,2} &= X_k^{-3,2} + X_{-k}^{-3,2} \\ S_k^{-3,2} &= X_k^{-3,2} - X_{-k}^{-3,2} \\ k &= 1, 2..5 \end{aligned}$$

By taking into account Eq.D.4 the components of the extended body's (App.C.3) in orbital elements are expressed as:

$$\begin{aligned} (xz) &= r (\cos u \cos \Omega - \sin u \sin \Omega \cos i) \cdot r \sin u \sin i \\ &= \frac{r^2}{2} \left(\sin 2u \cos \Omega \sin i - \sin 2i \sin \Omega \left(\frac{1 - \cos 2u}{2} \right) \right) \\ (x^2 - y^2) &= (r \cos u \cos \Omega - r \sin u \sin \Omega \cos i)^2 \\ &\quad - (r \cos u \sin \Omega + r \sin u \cos \Omega \cos i)^2 \\ &= r^2 \left(\frac{\cos 2\Omega}{2} (\cos 2u (1 + \cos^2 i) + 1 - \cos^2 i) \right. \\ &\quad \left. - \sin 2\Omega \sin 2u \cos i \right) \\ (xy) &= (r \cos u \cos \Omega - r \sin u \sin \Omega \cos i) \\ &\quad \cdot (r \cos u \sin \Omega + r \sin u \cos \Omega \cos i) \\ &= \frac{r^2}{2} \left(\frac{1}{2} \sin 2\Omega (\cos 2u (1 + \cos^2 i) + 1 - \cos^2 i) \right. \\ &\quad \left. + \sin 2u \cos i \cos 2\Omega \right) \\ (zy) &= r^2 \sin i \sin u (\sin \Omega \cos u + \cos \Omega \cos i \sin u) \\ &= \frac{r^2}{2} \left(\sin 2u \sin \Omega \sin i + \sin 2i \cos \Omega \left(\frac{1 - \cos 2u}{2} \right) \right) \end{aligned} \quad (\text{D.6})$$

Hence Eq.B.3 in Keplerian elements can be expressed as:

$$\begin{aligned}
\Delta C_{20} &= P \left(\frac{a}{r}\right)^3 \frac{k_{20}}{2} \left[\frac{3}{2} \sin^2 i (1 - \cos 2u) - 1 \right] \\
\Delta C_{21} &= P \left(\frac{a}{r}\right)^3 \frac{k_{21}}{2} \left[\sin 2u \cos \Omega \sin i - \frac{1}{2} \sin 2i \sin \Omega (1 - \cos 2u) \right] \\
\Delta C_{22} &= P \left(\frac{a}{r}\right)^3 \frac{k_{22}}{4} \left[\frac{\cos 2\Omega}{2} (\cos 2u (1 + \cos^2 i) + \sin^2 i) - \sin 2\Omega \sin 2u \cos i \right] \\
\Delta S_{21} &= P \left(\frac{a}{r}\right)^3 \frac{k_{21}}{2} \left[\sin 2u \sin \Omega \sin i + \frac{1}{2} \sin 2i \cos \Omega (1 - \cos 2u) \right] \\
\Delta S_{22} &= P \left(\frac{a}{r}\right)^3 \frac{k_{22}}{4} \left[\frac{1}{2} \sin 2\Omega (\cos 2u (1 + \cos^2 i) + \sin^2 i) + \sin 2u \cos i \cos 2\Omega \right].
\end{aligned} \tag{D.7}$$

Eq.D.7 using Eq.D.5 with an infinity degrees of eccentricity can be expressed as follows:

$$\begin{aligned}
\Delta C_{20} &= P \frac{k_{20}}{2} \left(\left(\frac{3 \sin^2 i}{2} - 1 \right) \sum_{k=0}^{\infty} C_k^{-3,0} \cos kM \right. \\
&\quad \left. - \frac{3 \sin^2 i}{2} \sum_{k=0}^{\infty} C_k^{-3,2} \cos (kM + 2\omega) \right) \\
\Delta C_{21} &= P \frac{k_{21}}{2} \left(\cos \Omega \sin i \sum_{k=1}^{\infty} S_k^{-3,2} \sin (kM + 2\omega) \right. \\
&\quad \left. - \frac{1}{2} \sin 2i \sin \Omega \sum_{k=0}^{\infty} (C_k^{-3,0} \cos kM + C_k^{-3,2} \cos (kM + 2\omega)) \right) \\
\Delta C_{22} &= P \frac{k_{22}}{4} \left(\frac{\cos 2\Omega}{2} \sum_{k=0}^{\infty} ((1 + \cos^2 i) C_k^{-3,2} \cos (kM + 2\omega) \right. \\
&\quad \left. + \sin^2 i C_k^{-3,0} \cos kM) + \sin 2\Omega \cos i \sum_{k=1}^{\infty} S_k^{-3,2} \sin (kM + 2\omega) \right) \\
\Delta S_{21} &= P \frac{k_{21}}{2} \left(\sin \Omega \sin i \sum_{k=1}^{\infty} S_k^{-3,2} \sin (kM + 2\omega) \right. \\
&\quad \left. + \frac{1}{2} \sin 2i \cos \Omega \sum_{k=0}^{\infty} (C_k^{-3,0} \cos kM - C_k^{-3,2} \cos (kM + 2\omega)) \right) \\
\Delta S_{22} &= P \frac{k_{22}}{4} \left(\frac{1}{2} \sin 2\Omega \sum_{k=0}^{\infty} ((1 + \cos^2 i) C_k^{-3,2} \cos (kM + 2\omega) \right. \\
&\quad \left. - \sin^2 i C_k^{-3,0} \cos kM) + \cos i \cos 2\Omega \sum_{k=1}^{\infty} S_k^{-3,2} \sin (kM + 2\omega) \right).
\end{aligned} \tag{D.8}$$

The analytic development of the Hansen $C_k^{-3,0}(e)$, $C_k^{-3,2}(e)$, $S_k^{-3,2}(e)$ coefficients in eccentricity up to the 5th order are given in next table:

k	$C_k^{-3,0}(e)$	$C_k^{-3,2}(e)$	$S_k^{-3,2}(e)$
0	$2 + 3e^2 + \frac{15}{4}e^4$	0	0
1	$3e + \frac{27}{8}e^3 + \frac{261}{64}e^5$	$-\frac{1}{2}e + \frac{1}{12}e^3 + \frac{1}{768}e^5$	$-\frac{1}{2}e + \frac{1}{24}e^3 - \frac{7}{256}e^5$
2	$\frac{9}{2}e^2 + \frac{7}{2}e^4$	$1 - \frac{5}{2}e^2 + \frac{41}{48}e^4$	$1 - \frac{5}{2}e^2 + \frac{37}{48}e^4$
3	$\frac{53}{8}e^3 + \frac{393}{128}e^5$	$\frac{7}{2}e + \frac{123}{16}e^3 + \frac{4971}{1280}e^5$	$\frac{7}{2}e - \frac{123}{16}e^3 - \frac{4809}{1280}e^5$
4	$\frac{77}{8}e^4$	$\frac{17}{2}e^2 - \frac{115}{6}e^4$	$\frac{17}{2}e^2 - \frac{115}{6}e^4$
5	$\frac{1773}{128}e^5$	$\frac{845}{48}e^3 - \frac{32525}{768}e^5$	$\frac{845}{48}e^3 - \frac{32525}{768}e^5$

Appendix E

Reference frame

The purpose here is to choose the reference frame of the solution in which will be expressed the vector position and velocity of celestial bodies. In the origin of integration $t = 0$, the geometry of the system (initial conditions) is given in an inertial reference frame, noted \mathcal{R}_E . The objective is to find a particular reference \mathcal{R}_0 , in uniform translation in comparison with \mathcal{R}_E (therefore inertial), better adapted to the study of the evolution of the system. Such change of reference frame is made by changing the initial conditions of bodies, in translating their positions of the same vector \mathbf{r} and their velocity of the same vector $\dot{\mathbf{r}}$ in the geometry of the system, that is means relative positions and velocities are well conserved.

E.1 Transformation of references

The expressions of the deformation coefficients in Eq.D.7 and D.8 are expressed in the reference frame linked to the extended body, the position of the perturbation in the punctual body, as well as the coefficients of the potential C_{nm} and S_{nm} that are expressed in $\mathcal{R}_E = (O_E, \mathbf{I}, \mathbf{J}, \mathbf{K})$. Hence it is necessary to pass from the fixed reference frame \mathcal{R}_0 to the mobile reference \mathcal{R}_E , and thus to know the coordinates of the vectors \mathbf{I} , \mathbf{J} and \mathbf{K} in the basis $\mathcal{B}_0 = (\mathbf{i}, \mathbf{j}, \mathbf{k})$ associated to \mathcal{R}_0 . It is possible by injecting a model of orientation which is already known, or by integrating in the direction of extended body at the same time as the position and velocity of the bodies. In Eq.E.1 the part of $\mathcal{R}(\mathbf{K}, \psi)$ is equal to one. Thus, by the rotation of the axis \mathbf{K} the extended body remains being spherical in structure thus is not deformable.

E.2 Integration of direction

The direction of a body in space can be determined by its Euler angles ϕ, θ and ψ , defined in the following way:

- θ - nutation angle is the angle between the vectors \mathbf{K} and \mathbf{k} , positive or zero;
- Ω -the ascending node ($\theta \geq 0$)
- ϕ - procession angle, is the angle $(\mathbf{i}, \overrightarrow{O\Omega})$
- ψ -own rotation angle is the angle $(\overrightarrow{O\Omega}, \mathbf{I})$

The basis $\mathcal{B}_E = (\mathbf{I}, \mathbf{J}, \mathbf{K})$ is an image of \mathcal{B}_0 by the successive rotations $\mathcal{R}(\mathbf{k}, \phi)$, $\mathcal{R}(\overrightarrow{O\Omega}, \theta)$ and $\mathcal{R}(\mathbf{K}, \psi)$. The coordinates of a vector \mathbf{r} in \mathcal{R}_E deduct from those in \mathcal{R}_0 :

$$\mathbf{r}_{\mathcal{R}_E} = P_{\mathcal{R}_E \rightarrow \mathcal{R}_0} \mathbf{r}_{\mathcal{R}_0} = \begin{pmatrix} \cos \psi & \sin \psi & 0 \\ -\sin \psi & \cos \psi & 0 \\ 0 & 0 & 1 \end{pmatrix} \begin{pmatrix} 1 & 0 & 0 \\ 0 & \cos \theta & \sin \theta \\ 0 & -\sin \theta & \cos \theta \end{pmatrix} \begin{pmatrix} \cos \varphi & \sin \varphi & 0 \\ -\sin \varphi & \cos \varphi & 0 \\ 0 & 0 & 1 \end{pmatrix} \mathbf{r}_{\mathcal{R}_0} \quad (\text{E.1})$$

The position and the velocity of a body expressed using the Euler angles of the extended body on the given system reference frame. The above expression will be used for the transformation of the coordinates from the ICRF (The International Celestial Reference Frame) which corresponds to \mathcal{R}_0 and to the equator $J2000$ reference frame which corresponds to \mathcal{R}_E .

Bibliography

2015, Lunarplanner.com

Abhyankar, K. 1977, A survey of the solar atmospheric models, *Bulletin of the Astronomical Society of India*, 5, 40

Abreu, J. A., Beer, J., Ferriz-Mas, A., McCracken, K. G., & Steinhilber, F. 2012, Is there a planetary influence on solar activity?, *A&A*, 548, A88

Acton, L., Tsuneta, S., Ogawara, Y., et al. 1992, The YOHKOH mission for high-energy solar physics, *Science*, 258, 618

Acuña, M. H., Ogilvie, K. W., Baker, D. N., et al. 1995, The Global Geospace Science Program and its investigations, *Space Science Reviews*, 71, 5

Aguirre, L. A., Letellier, C., & Maquet, J. 2008, Forecasting the Time Series of Sunspot Numbers, *Sol. Phys.*, 249, 103

Ahluwalia, H. S. 1998a, The predicted size of cycle 23 based on the inferred three-cycle quasi-periodicity of the planetary index Ap, *J. Geophys. Res.*, 103, 12103

Ahluwalia, H. S. 1998b, The predicted size of cycle 23 based on the inferred three-cycle quasi-periodicity of the planetary index Ap, *J. Geophys. Res.*, 103, 12103

Ahluwalia, H. S. & Ygbuhay, R. C. 2009, Preliminary forecast for the peak of solar activity cycle 24, *Advances in Space Research*, 44, 611

Antia, H. & A. Bhatnagar, P. U. 2003, *Lectures on Solar Physics (Lecture Notes in Physics) (Vol 619) (Springer)*

Arlt, R. 2011, The sunspot observations by Samuel Heinrich Schwabe, cite arxiv:1110.3620Comment: 10 pages, 6 figures

Asvestari, E. & Usoskin, I. G. 2016, An empirical model of heliospheric cosmic ray modulation on long-term time scale, *Journal of Space Weather and Space Climate*, 6, A15

Athay, R. G. 1976, *The solar chromosphere and corona quiet sun (Dordrecht; Reidel)*

Augustson, K., Brun, A. S., Miesch, M., & Toomre, J. 2015, Grand Minima and Equatorward Propagation in a Cycling Stellar Convective Dynamo, *The Astrophysical Journal*, 809, 149

- Babcock, H. W. 1961, The Topology of the Sun's Magnetic Field and the 22-YEAR Cycle., *ApJ*, 133, 572
- Bahcall, J. N., Serenelli, A. M., & Basu, S. 2006, 10,000 standard solar models: a Monte Carlo simulation, *The Astrophysical Journal Supplement Series*, 165, 400
- Bahng, J. & Schwarzschild, M. 1961, Lifetime of Solar Granules., *The Astrophysical Journal*, 134, 312
- Bai, T. & Cliver, E. W. 1990, A 154 day periodicity in the occurrence rate of proton flares, *ApJ*, 363, 299
- Ball, W. T., Unruh, Y. C., Krivova, N. A., et al. 2012, Reconstruction of total solar irradiance 1974-2009, *A&A*, 541, A27
- Ballester, J. L., Oliver, R., & Carbonell, M. 2002, The Near 160 Day Periodicity in the Photospheric Magnetic Flux, *ApJ*, 566, 505
- Balthasar, H. & Schuessler, M. 1983, Preferred longitudes of sunspot groups and high-speed solar wind streams - Evidence for a 'solar memory', *Sol. Phys.*, 87, 23
- Bard, E., Baroni, M., & Aster Team. 2015, Solar activity and climate change during the 1750 A.D. solar minimum, 17, 7459
- Bard, E. & Frank, M. 2006, Climate change and solar variability: What's new under the sun?, *Earth and Planetary Science Letters*, 248, 1
- Bard, E. & Frank, M. 2006, Climate change and solar variability: What's new under the sun?, *Earth and Planetary Science Letters*, 248, 1
- Bard, E., Raisbeck, G., Yiou, F., & Jouzel, J. 2000, Solar irradiance during the last 1200 years based on cosmogenic nuclides, *Tellus B*, 52
- Bard, E., Raisbeck, G. M., Yiou, F., & Jouzel, J. 1997, Solar modulation of cosmogenic nuclide production over the last millennium: comparison between ^{14}C and ^{10}Be records, *Earth and Planetary Science Letters*, 150, 453
- Bazilevskaya, G. A., Krainev, M. B., Makhmutov, V. S., et al. 2000, Structure of the maximum phase of solar cycles 21 and 22, *Sol. Phys.*, 197, 157
- Becker, U. 1954, Die Eigenbewegung der Sonnenflecken in Breite, *Z. Astrophys.*, 34, 129
- Beer, J. 2000, Long-term indirect indices of solar variability, *Space Science Reviews*, 94, 53
- Beer, J., Blinov, A., Bonani, G., et al. 1990, Use of ^{10}Be in polar ice to trace the 11-year cycle of solar activity
- Beer, J., McCracken, K., & Abreu, J. 2012, Long-term solar activity: improvements and predictions, 39, 120
- Beer, J., McCracken, K., et al. 2012, *Cosmogenic radionuclides: theory and applications in the terrestrial and space environments* (Springer Science & Business Media)

- Beer, J., McCracken, K. G., Abreu, J., Heikkilä, U., & Steinhilber, F. 2013, Cosmogenic Radionuclides as an Extension of the Neutron Monitor Era into the Past: Potential and Limitations, *Space Science Reviews*, 176, 89
- Bendandi, R. 1931, Un principio fondamentale dell'universo ...
- Benestad, R. E. 2002, *Solar activity and earth's climate* (London ; Springer ; c2002.)
- Benevolenskaya, E. E. 1995, Double Magnetic Cycle of Solar Activity, *Sol. Phys.*, 161, 1
- Bhatt, N. J., Jain, R., & Aggarwal, M. 2009, Prediction of the Maximum Amplitude and Timing of Sunspot Cycle 24, *Sol. Phys.*, 260, 225
- Bianchini, A., Milani, F., Scafetta, N., & Ortolani, S. 2016, Phase correlation between the 20 and 60 year modulations of global temperatures and the equivalent harmonic components of the Sun velocity about the barycenter of the planetary system., 18, 9861
- Bigg, E. 1967a, Influence of the planet Mercury on sunspots, *AJ*, 72, 463
- Bigg, E. K. 1967b, Influence of the planet Mercury on sunspots, *AJ*, 72, 463
- Bigg, E. K. & Mulhall, P. S. 1967, Planetary modulation of solar activity, *Proceedings of the Astronomical Society of Australia*, 1, 53
- Blizard, J. B. 1968, Long-Range Solar-Flare Prediction., *The Astronomical Journal Supplement*, 73, 55
- Blizard, J. B. 1981, in *Bulletin of the American Astronomical Society*, Vol. 13, *Bulletin of the American Astronomical Society*, 876
- Bond, G., Kromer, B., Beer, J., et al. 2001, Persistent Solar Influence on North Atlantic Climate During the Holocene, *Science*, 294, 2130
- Box, G. E., Jenkins, G. M., Reinsel, G. C., & Ljung, G. M. 2015, *Time series analysis: forecasting and control* (John Wiley & Sons)
- Bradley W. Carroll, D. A. O. 2001, *Generalized Linear Models and Extensions* (College Station, Texas: Stata Press), 245
- Brajivia, R., Verbanac, G., Sudar, D., et al. 2015, A comparison between the observed and predicted amplitude of the 24th solar cycle, *Central European Astrophysical Bulletin*, 39, 135
- Brajivia, R., Wöhl, H., Hanslmeier, A., et al. 2009a, On solar cycle predictions and reconstructions, *A&A*, 496, 855
- Brajivia, R., Wohl, H., Hanslmeier, A., et al. 2009b, On solar cycle predictions and reconstructions, *A&A*, 496, 855
- Bray, R. J. & Loughhead, R. E. 1979, *Sunspots*. (New York, NY (USA): Dover Publications)
- Bray, W. 1967, Radio Relay Systems, *Electronics and Power*, 13, 130

- Brown, E. W. 1900, A possible explanation of the sun-spot period, *MNRAS*, 60, 599
- Brown, G. M. 1976, What determines sunspot maximum, *MNRAS*, 174, 185
- Bruckner, E. 1890, *Klimaschwankungen seit 1700 nebst Bemerkungen uber die Klimaschwankungen der Diluvialzeit* (E. Holzels)
- C. J. Durrant. 1988, *The atmosphere of the sun* (Bristol ; A. Hilger, c1988.)
- Callebaut, D. K., de Jager, C., & Duhau, S. 2012, The influence of planetary attractions on the solar tachocline, *Journal of Atmospheric and Solar-Terrestrial Physics*, 80, 73
- Cameron, R. & Schüssler, M. 2007, Solar Cycle Prediction Using Precursors and Flux Transport Models, *The Astrophysical Journal*, 659, 801
- Cameron, R. & Schüssler, M. 2007, Solar Cycle Prediction Using Precursors and Flux Transport Models, *ApJ*, 659, 801
- Cameron, R. H., Jiang, J., & Schüssler, M. 2016, Solar Cycle 25: Another Moderate Cycle?, *ApJ*, 823, L22
- Cameron, R. H. & Schüssler, M. 2013, No evidence for planetary influence on solar activity, *A&A*, 557, A83
- Canto Martins, B. L., Das Chagas, M. L., Alves, S., et al. 2011, Chromospheric activity of stars with planets, *A&A*, 530, A73
- Carrasco, V. M. S., Álvarez, J. V., & Vaquero, J. M. 2015, Sunspots During the Maunder Minimum from *Machina Coelestis* by Hevelius, *Sol. Phys.*, 290, 2719
- Carrington, R. C. 1858, On the distribution of the solar spots in latitudes since the beginning of the year 1854, with a map, *Monthly Notices of the Royal Astronomical Society*, 19, 1
- Carrington, R. C. 1859, On certain phenomena in the motions of solar spots, *Monthly Notices of the Royal Astronomical Society*, 19, 81
- Cartwright, D. E. 1999, *Tides : a scientific history* (The Pitt Building, Trumpington Street, Cambridge CB2 1RP, United Kingdom: Cambridge University Press)
- Cash, M. D., Biesecker, D. A., & Reinard, A. A. 2012, The DSCOVR Solar Wind Mission and Future Space Weather Products, *AGU Fall Meeting Abstracts*
- Cauquoin, A., Raisbeck, G., Jouzel, J., Bard, E., & Aster Team. 2013, Extended record of ^{10}Be at EPICA Dome C during the last 800 000 years and its synchronization with geomagnetic paleointensity variations from marine sediments, 15, *EGU2013*
- Cauquoin, A., Raisbeck, G. M., Jouzel, J., & Bard, E. 2014, No evidence for planetary influence on solar activity 330 000 years ago, *A&A*, 561, A132
- Charbonneau, P. 2002, The rise and fall of the first solar cycle model, *Journal for the History of Astronomy*, 33, 351

- Charbonneau, P. 2005, Dynamo models of the solar cycle, *Living Reviews in Solar Physics*, 2, 1
- Charbonneau, P. 2010, Dynamo Models of the Solar Cycle, *Living Rev. Solar Phys*, 7,3, 1
- Charbonneau, P. 2013a, Magnetohydrodynamics, *Solar and Stellar Dynamos*, Saas-Fee Advanced Courses, Volume 39. ISBN 978-3-642-32092-7. Springer-Verlag Berlin Heidelberg, 2013, p. 1, 39, 1
- Charbonneau, P. 2013b, Where is the solar dynamo?, *Journal of Physics: Conference Series*, 440, 12014
- Charbonneau, P., Christensen-Dalsgaard, J., Henning, R., et al. 1999, Helioseismic Constraints on the Structure of the Solar Tachocline, *ApJ*, 527, 445
- Charvatova, I. & Hejda, P. 2013, Responses of the basic cycle of 178.7 and 2402 yr in solar-terrestrial phenomena during Holocene, *Pattern Recogn. Phys*
- Charvatova, I. & Strestik, J. 1991, Long-term variations in duration of solar cycles, *Bulletin of the Astronomical Institutes of Czechoslovakia*, 42, 90
- Chistyakov, V. F. 1983, A Forecast of the Solar Activity till the Year 2030, *Byulletin Solnechnye Dannye Akademii Nauk SSSR*, 1, 97
- Choudhary, D. P., Lawrence, J. K., Norris, M., & Cadavid, A. C. 2014, Different Periodicities in the Sunspot Area and the Occurrence of Solar Flares and Coronal Mass Ejections in Solar Cycle 23 - 24, *Sol. Phys.*, 289, 649
- Choudhuri, A. R., Chatterjee, P., & Jiang, J. 2007a, Predicting Solar Cycle 24 With a Solar Dynamo Model, *Physical Review Letters*, 98, 131103
- Choudhuri, A. R., Chatterjee, P., & Jiang, J. 2007b, Predicting Solar Cycle 24 With a Solar Dynamo Model, *Physical Review Letters*, 98, 131103
- Choudhuri, A. R., Chatterjee, P., & Jiang, J. 2007c, Predicting Solar Cycle 24 With a Solar Dynamo Model, *Physical Review Letters*, 98, 131103
- Chowdhury, P., Gokhale, M. H., Singh, J., & Moon, Y.-J. 2016, Mid-term quasi-periodicities in the CaII-K plage index of the Sun and their implications, *Ap&SS*, 361, 54
- Cionco, R. G. & Compagnucci, R. H. 2012, Dynamical characterization of the last prolonged solar minima, *Advances in Space Research*, 50, 1434
- Cionco, R. G. & Soon, W. 2015, A phenomenological study of the timing of solar activity minima of the last millennium through a physical modeling of the Sun-Planets Interaction, *New A*, 34, 164
- Clark, D. H. & Stephenson, F. R. 1978, An interpretation of the pre-telescopic sunspot records from the orient, *Quarterly Journal of the Royal Astronomical Society*, 19, 387
- Clegg, J. A. 1958, Remanent Magnetism of the Rajmahal Traps of North-Eastern India, *Nature*, 181, 830

- Clette, F., Lefèvre, L., Cagnotti, M., Cortesi, S., & Bulling, A. 2016, The Revised Brussels-Locarno Sunspot Number (1981 - 2015), *Sol. Phys.*
- Clette, F., Svalgaard, L., Vaquero, J. M., & Cliver, E. W. 2014, Revisiting the Sunspot Number. A 400-Year Perspective on the Solar Cycle, *Space Sci. Rev.*, 186, 35
- Clette, F., Svalgaard, L., Vaquero, J. M., & Cliver, E. W. 2015, in *The Solar Activity Cycle* (Springer), 35–103
- Cliver, E. W. 2015, The Extended Cycle of Solar Activity and the Sun 22-Year Magnetic Cycle, 169
- Cliver, E. W. 2016, Comparison of New and Old Sunspot Number Time Series, *Sol. Phys.*
- Cliver, E. W. & Ling, A. G. 2016, The Discontinuity Circa 1885 in the Group Sunspot Number, *Sol. Phys.*
- Clúa de Gonzalez, A. L., Gonzalez, W. D., Dutra, S. L., & Tsurutani, B. T. 1993, Periodic variation in the geomagnetic activity: A study based on the Ap index, *Journal of Geophysical Research: Space Physics* (1978–2012), 98, 9215
- Cohen, O., Drake, J. J., Kashyap, V. L., et al. 2009, Interactions of the Magnetospheres of Stars and Close-In Giant Planets, *ApJ*, 704, L85
- Cole, T. W. 1973, Periodicities in Solar Activity, *Sol. Phys.*, 30, 103
- Cowling, T. G. 1933, The magnetic field of sunspots, *Monthly Notices of the Royal Astronomical Society*, 94, 39
- Crosson, I. J. & Binder, P.-M. 2009, Chaos-based forecast of sunspot cycle 24, *Journal of Geophysical Research (Space Physics)*, 114, A01108
- Culhane, J. L., Harra, L. K., James, A. M., et al. 2007, The EUV Imaging Spectrometer for Hinode, *Solar Physics*, 243, 19
- Cuntz, M., Saar, S. H., & Musielak, Z. E. 2000, On Stellar Activity Enhancement Due to Interactions with Extrasolar Giant Planets, *ApJ*, 533, L151
- Damon, P. E. & Laut, P. 2004a, Pattern of Strange Errors Plagues Solar Activity and Terrestrial Climate Data, *EOS Transactions*, 85, 370
- Damon, P. E. & Laut, P. 2004b, Pattern of Strange Errors Plagues Solar Activity and Terrestrial Climate Data, *EOS Transactions*, 85, 370
- De Jong, T. & van Soldt, W. 1989, The earliest known solar eclipse record redated
- De Meyer, F. 1998, Modulation of the Solar Magnetic Cycle, *Solar Physics*, 181, 201
- De Pontieu, B., Title, A. M., Lemen, J. R., et al. 2014, The Interface Region Imaging Spectrograph (IRIS), *Solar Physics*, 289, 2733
- Dergachev, V. A., Raspopov, O. M., & Vasiliev, S. S. 2000, Long-term Variability of Solar Activity during the Holocene, 463, 489

- Desmoulins, J.-P. 1995, Sunspots, Sunspot cycles are they caused by Venus, Earth and Jupiter syzygies ?
- Dikpati, M. 2008, Predicting cycle 24 using various dynamo-based tools, *Annales Geophysicae*, 26, 259
- Dikpati, M., de Toma, G., & Gilman, P. A. 2008, Polar Flux, Cross-equatorial Flux, and Dynamo-generated Tachocline Toroidal Flux as Predictors of Solar Cycles, *ApJ*, 675, 920
- Dikpati, M. & Gilman, P. A. 2001a, Flux-transport Dynamos Driven by a Tachocline α -effect; a Solution to Magnetic Parity Selection in the Sun, AGU Spring Meeting Abstracts, 31
- Dikpati, M. & Gilman, P. A. 2001b, Prolateness of the Solar Tachocline Inferred from Latitudinal Force Balance in a Magnetohydrodynamic Shallow-Water Model, *ApJ*, 552, 348
- Dikpati, M. & Gilman, P. A. 2006, Simulating and Predicting Solar Cycles Using a Flux-Transport Dynamo, *ApJ*, 649, 498
- Dikpati, M. & Gilman, P. A. 2009, Flux-Transport Solar Dynamos, *Space Sci. Rev.*, 144, 67
- Dingle, L. A., van Hoven, G., & Sturrock, P. A. 1973, Test for Planetary Influences on Solar Activity, *Sol. Phys.*, 31, 243
- Domingo, V., Fleck, B., & Poland, A. I. 1995, The SOHO mission: An overview, *Solar Physics*, 162, 1
- Donnelly, R. F., Puga, L. C., & Busby, W. S. 1986, Temporal characteristics of solar EUV, UV and 10830-A full-disk fluxes, NASA STI/Recon Technical Report N, 87
- Donner, R. & Thiel, M. 2007, Scale-resolved phase coherence analysis of hemispheric sunspot activity: a new look at the north-south asymmetry, *A&A*, 475, L33
- Drake, S. 1957, Discoveries and opinions of Galileo (Doubleday New York)
- Drake, S. 2001, Galileo: a very short introduction (Oxford University Press)
- Du, Z. & Du, S. 2006, The Relationship Between the Amplitude and Descending Time of a Solar Activity Cycle, *Sol. Phys.*, 238, 431
- Du, Z. L. 2006, Relationship Between Solar Maximum Amplitude and Max-Max Cycle Length, *AJ*, 132, 1485
- Dwivedi, B. N. & Parker, E. N. 2003, Dynamic sun (Cambridge, UK ; Cambridge University Press, 2003.)
- Echer, E., Rigozo, N., Echer, M. S., Vieira, L., & Nordemann, D. 2004, Reconstruction of the aa index on the basis of spectral characteristics, *Geofísica Internacional*, 43, 103
- Eddy, J. A. 1976, The maunder minimum (publisher not identified)

- Eddy, J. A. 1980, in *The Ancient Sun: Fossil Record in the Earth, Moon and Meteorites*, Vol. 1, 119–134
- Eddy, J. A. 1983, *The Maunder Minimum: A reappraisal*, *Solar Physics*, 89, 195
- Eddy, J. A. 1994, *Solar history and human affairs*, *Human Ecology*, 22, 23
- Eddy, J. A., Gilman, P. A., & Trotter, D. E. 1976, *Solar rotation during the Maunder Minimum*, *Solar Physics*, 46, 3
- Eddy, J. A., Stephenson, F. R., & Yau, K. K. 1989, *On pre-telescopic sunspot records*, *Quarterly Journal of the Royal Astronomical Society*, 30, 65
- Edmonds, I. 2015, *Evidence of a planetary influence on solar activity: Phase coherence of the variation in sunspot area with the tidal effect of Mercury*, ArXiv e-prints
- Fairbridge, R. W. & Shirley, J. H. 1987, *Prolonged minima and the 179-yr cycle of the solar inertial motion*, *Sol. Phys.*, 110, 191
- Feynman, J. 1982, *Geomagnetic and solar wind cycles, 1900-1975*, *J. Geophys. Res.*, 87, 6153
- Fienga, A., Laskar, J., Exertier, P., Manche, H., & Gastineau, M. 2015, *Numerical estimation of the sensitivity of INPOP planetary ephemerides to general relativity parameters*, *Celestial Mechanics and Dynamical Astronomy*, 123, 325
- Figueira, P., Santerne, A., Suárez Mascareño, A., et al. 2016, *Is the activity level of HD 80606 influenced by its eccentric planet?*, *A&A*, 592, A143
- Fineschi, S. & Gummin, G. 2003, *Telescopes and instrumentation for solar astrophysics: 7-8 August 2003, San Diego, California, USA (Bellingham, Washington : SPIE, c2004.)*
- Foukal, P. 1996, *The Behavior of solar magnetic plages measured from Mt. Wilson observations between 1915-1984*, *Geophys. Res. Lett.*, 23, 2169
- Fox, N. J., Velli, M. C., Bale, S. D., et al. 2015, *The Solar Probe Plus Mission: Humanity's First Visit to Our Star*, *Space Science Reviews*, 1
- Frédéric, Clette, & Lefèvre, L. 2015, *The new Sunspot Number: assembling all corrections*, ArXiv e-prints
- Frick, P., Galyagin, D., Hoyt, D. V., et al. 1997a, *Wavelet analysis of solar activity recorded by sunspot groups*, *A&A*, 328, 670
- Frick, P., Galyagin, D., Hoyt, D. V., et al. 1997b, *Wavelet analysis of solar activity recorded by sunspot groups*, *A&A*, 328, 670
- Fröhlich, C. 2003, in *ESA Special Publication, Vol. 535, Solar Variability as an Input to the Earth's Environment*, ed. A. Wilson, 183–193
- Fröhlich, C. 2006, *Solar Irradiance Variability Since 1978. Revision of the PMOD Composite during Solar Cycle 21*, *Space Sci. Rev.*, 125, 53

- Frohlich, C., Crommelynck, D., Wehrli, C., et al. 1997, In-Flight Performance of the Virgo Solar Irradiance Instruments on SOHO., *Solphys*, 175, 267
- Galilei, G. & Drake, S. 1990a, Discoveries and opinions of Galileo : including The starry messenger (1610), Letter to the Grand Duchess Christina (1615), and excerpts from Letters on sunspots (1613), The assayer (1623)
- Galilei, G. & Drake, S. 1990b, Discoveries and opinions of Galileo : including The starry messenger (1610), Letter to the Grand Duchess Christina (1615), and excerpts from Letters on sunspots (1613), The assayer (1623)
- Gandorfer, A., Solanki, S. K., Woch, J., et al. 2011, The Solar Orbiter Mission and its Polarimetric and Helioseismic Imager (SO/PHI), *Journal of Physics Conference Series*, 271, 012086
- Garai, J. 2001, Cometary Impact Origin of Sunspots as Indicated by the Correlation Between the Orbiting Positions of Jupiter and Saturn and the Distributions of the Sunspots, *AGU Spring Meeting Abstracts*
- García, R. A., Turck-Chièze, S., Jiménez-Reyes, S. J., et al. 2007, Tracking Solar Gravity Modes: The Dynamics of the Solar Core, *Science*, 316, 1591
- Gelfreikh, G. B., Nagovitsyn, Y. A., & Nagovitsyna, E. Y. 2006, Quasi-periodic oscillations of microwave emission in solar active regions, *Publications of the Astronomical Society of Japan*, 58, 29
- Georgieva, K., Kirov, B., & Nagovitsyn, Y. A. 2013, Long-term variations of solar magnetic fields derived from geomagnetic data, *Geomagnetism and Aeronomy*, 53, 852
- Gleissberg, W. 1939a, A long-periodic fluctuation of the sun-spot numbers, *The Observatory*, 62, 158
- Gleissberg, W. 1939b, A long-periodic fluctuation of the sun-spot numbers, *The Observatory*, 62, 158
- Gleissberg, W. 1944, A table of secular variations of the solar cycle, *Terrestrial Magnetism and Atmospheric Electricity*, 49, 243
- Gleissberg, W. 1967a, Secularly Smoothed Data on the Minima and Maxima of Sunspot Frequency, *Sol. Phys.*, 2, 231
- Gleissberg, W. 1967b, Secularly smoothed data on the minima and maxima of sunspot frequency, *Solar Physics*, 2, 231
- Gleissberg, W. 1971, The Probable Behaviour of Sunspot Cycle 21, *Sol. Phys.*, 21, 240
- Gnevyshev, M. & Ohl, A. 1948, On the 22-year cycle of solar activity, *Astron.ZH*, 18
- Goldreich, P. & Nicholson, P. D. 1989, Tidal friction in early-type stars, *ApJ*, 342, 1079
- Golub, L., Cirtain, J. W., Kobayashi, K., et al. 2010, The Marshall Grazing Incidence X-ray Spectrometer (MaGIXS), *AGU Fall Meeting Abstracts*

- Golub, L., DeLuca, E., Austin, G., et al. 2007, The X-Ray Telescope (XRT) for the Hinode Mission, *Solar Physics*, 243, 63
- Grandpierre, A. 1996, On the origin of solar cycle periodicity, *Ap&SS*, 243, 393
- Grant, S. B. . D. 1979, *Sunspots: an exploration of solar energy through fact and fiction* (Seattle : Cloudburst Press, 1979.)
- Gray, L. J., Beer, J., Geller, M., et al. 2010, Solar Influences on Climate, *Reviews of Geophysics*, 48, 4001
- Hagenaar, H. & Cheung, M. 2008, Magnetic Flux Emergence on Different Scales, 12, 2.53
- Hagenaar, H. J., Schrijver, C. J., & Title, A. M. 2003, The Properties of Small Magnetic Regions on the Solar Surface and the Implications for the Solar Dynamo(s), *ApJ*, 584, 1107
- Haigh, J. D. 2007, The Sun and the Earth's climate, *Living Reviews in Solar Physics*, 4, 1
- Hale, G. E. 1929, The spectrohelioscope and its work, *The Astrophysical Journal*, 70, 265
- Hale, G. E. & Ellerman, F. 1918, in *Publications of the American Astronomical Society*, Vol. 3, *Publications of the American Astronomical Society*, 81
- Handy, B., Acton, L., Kankelborg, C., et al. 1999, The transition region and coronal explorer, *Solar Physics*, 187, 229
- Hansteen, V., Leer, E., & Holzer, T. 1997a, The role of helium in the outer solar atmosphere, *The Astrophysical Journal*, 482, 498
- Hansteen, V., Leer, E., & Holzer, T. 1997b, The role of helium in the outer solar atmosphere, *The Astrophysical Journal*, 482, 498
- Hathaway, D. H. 2009, Solar Cycle Forecasting, *Space Sci. Rev.*, 144, 401
- Hathaway, D. H. 2010, The Solar Cycle, *Living Reviews in Solar Physics*, 7
- Hathaway, D. H. 2011, A Standard Law for the Equatorward Drift of the Sunspot Zones
- Hathaway, D. H. 2015, The Solar Cycle, *Living Reviews in Solar Physics*
- Hathaway, D. H. & Upton, L. 2016a, Predicting the Amplitude and Hemispheric Asymmetry of Solar Cycle 25 with Surface Flux Transport, 47, #10.06
- Hathaway, D. H. & Upton, L. 2016b, Predicting the Amplitude and Hemispheric Asymmetry of Solar Cycle 25 with Surface Flux Transport, 47, #10.06
- Hathaway, D. H. & Wilson, R. M. 2006, Geomagnetic activity indicates large amplitude for sunspot cycle 24, *Geophys. Res. Lett.*, 33, L18101
- Hathaway, D. H., Wilson, R. M., & Reichmann, E. J. 1994, The Shape of the Sunspot Cycle, *Solar Phys.*, 151, 177

- Hathaway, D. H., Wilson, R. M., & Reichmann, E. J. 1999, A synthesis of solar cycle prediction techniques, *J. Geophys. Res.*, 104, 22,375
- Hathaway, D. H., Wilson, R. M., & Reichmann, E. J. 1999, A Synthesis of Solar Cycle Prediction Techniques, *J. Geophys. Res.*, 104, 22
- Hays, J. D., Imbrie, J., & Shackleton, N. J. 1976, Variations in the Earth's Orbit: Pacemaker of the Ice Ages, *Science*, 194, 1121
- Heath, T. L. 2014, *Greek Astronomy*
- Helal, H. R. & Galal, A. A. 2013, An early prediction of the maximum amplitude of the solar cycle 25, *Journal of Advanced Research*, 4, 275
- Hellwege, K. H. & Madelung, O., eds. 1975, *Landolt-Börnstein: Numerical Data and Functional Relationships in Science and Technology – New Series, Vol. III/7B1/II.1.1* (Berlin, Heidelberg, New York: Springer)
- Herschel, W. 1801, Observations Tending to Investigate the Nature of the Sun, in Order to Find the Causes or Symptoms of Its Variable Emission of Light and Heat; With Remarks on the Use That May Possibly Be Drawn from Solar Observations, *Philosophical Transactions of the Royal Society of London Series I*, 91, 265
- Herschel, W. 1811, *Astronomical Observations relating to the Construction of the Heavens, arranged for the Purpose of a critical Examination, the Result of which appears to throw some new Light upon the Organization of the celestial Bodies*, *Philosophical Transactions of the Royal Society of London*, 101, 269
- Hiremath, K. M. 2008a, Prediction of solar cycle 24 and beyond, *Ap&SS*, 314, 45
- Hiremath, K. M. 2008b, Prediction of solar cycle 24 and beyond, *Ap&SS*, 314, 45
- Howe, R., Christensen-Dalsgaard, J., Hill, F., et al. 2007, Temporal variations in solar rotation at the bottom of the convection zone: The current status, *Advances in Space Research*, 40, 915
- Hoyt, D. V., Kyle, H. L., Hickey, J. R., & Maschhoff, R. H. 1992, The NIMBUS 7 solar total irradiance - A new algorithm for its derivation, *J. Geophys. Res.*, 97, 51
- Hoyt, D. V. & Schatten, K. H. 1997, The role of the sun in climate change
- Hoyt, D. V. & Schatten, K. H. 1998, Group Sunspot Numbers: A New Solar Activity Reconstruction, *Sol. Phys.*, 181, 491
- Hoyt, D. V. & Schatten, K. H. 1998, Group Sunspot Numbers: A New Solar Activity Reconstruction, *Solar Physics*, 181, 491
- Hung, C., C. 2007, *Apparent Relations Between Solar Activity and Solar Tides Caused by the Planets*, NASA/TM
- Hurford, G., Schmahl, E., Schwartz, R., et al. 2002, The RHESSI Imaging Concept, *Solar Physics*, 210, 61

- Inceoglu, F., Simoniello, R., Faurschou Knudsen, M., et al. 2016a, On the Current Solar Magnetic Activity using Its Behavior During the Holocene, 41
- Inceoglu, F., Simoniello, R., Knudsen, M. F., et al. 2016b, On the Current Solar Magnetic Activity in the Light of Its Behaviour During the Holocene, *Sol. Phys.*, 291, 303
- Inceoglu, F., Simoniello, R., Knudsen, M. F., et al. 2015, Grand solar minima and maxima deduced from ^{10}Be and ^{14}C : magnetic dynamo configuration and polarity reversal, *A&A*, 577, A20
- Ivanov, V. G. & Miletsky, E. V. 2016, Characteristics of latitude distribution of sunspots and their links to solar activity in pre-Greenwich data, ArXiv e-prints
- Jager, C. & Versteegh, G. J. M. 2005, Do Planetary Motions Drive Solar Variability?, *Sol. Phys.*, 229, 175
- Javaraiah, J. 2005, Sun's retrograde motion and violation of even-odd cycle rule in sunspot activity, *MNRAS*, 362, 1311
- Javaraiah, J. 2007, North-south asymmetry in solar activity: predicting the amplitude of the next solar cycle, *MNRAS*, 377, L34
- Javaraiah, J. 2015, Long-term variations in the north–south asymmetry of solar activity and solar cycle prediction, III: Prediction for the amplitude of solar cycle 25 , *New Astronomy*, 34, 54
- Javaraiah, J. 2015, Long-term variations in the north-south asymmetry of solar activity and solar cycle prediction, III: Prediction for the amplitude of solar cycle 25, *New A*, 34, 54
- Javaraiah, J. 2016, North-south asymmetry in small and large sunspot group activity and violation of even-odd solar cycle rule, *Ap&SS*, 361, #208
- Jiang, J., Chatterjee, P., & Choudhuri, A. R. 2007a, Solar activity forecast with a dynamo model, *MNRAS*, 381, 1527
- Jiang, J., Chatterjee, P., & Choudhuri, A. R. 2007b, Solar activity forecast with a dynamo model, *MNRAS*, 381, 1527
- Jones, C. A., Thompson, M. J., & Tobias, S. M. 2010, The Solar Dynamo, *Space Science Reviews*, 152, 591
- Jose, P. D. 1965, Sun's motion and sunspots, *AJ*, 70, 193
- Juckett, D. 2003, Temporal variations of low-order spherical harmonic representations of sunspot group patterns: Evidence for solar spin-orbit coupling, *A&A*, 399, 731
- Judit Brody. 2002, *The enigma of sunspots: a story of discovery and scientific revolution* (Edinburgh : Floris Books, 2002.)
- Kaiser, M. L., Kucera, T. A., Davila, J. M., et al. 2008, The STEREO Mission: An Introduction, *Space Science Reviews*, 136, 5

- KANDA, S. 1933, Ancient Records of Sunspots and Auroras in the Far East and the Variation of the Period of Solar Activity, Proc. Imp. Academy of Tokyo, 9, 293
- Kane, R. P. 2007, Solar Cycle Predictions Based on Extrapolation of Spectral Components: An Update, Sol. Phys., 246, 487
- Kane, R. P. 2008, Prediction of Solar Cycle Maximum Using Solar Cycle Lengths, Sol. Phys., 248, 203
- Kashyap, V. L., Drake, J. J., & Saar, S. H. 2008, Extrasolar Giant Planets and X-Ray Activity, ApJ, 687, 1339
- Keil, L. & Avakyan, S. 2003, Innovative telescopes and instrumentation for solar astrophysics: 24-28 August 2002, Waikoloa, Hawaii, USA (Bellingham, Wash. : SPIE, c2003.)
- Kilcik, A., Anderson, C. N. K., Rozelot, J. P., et al. 2009, Nonlinear Prediction of Solar Cycle 24, ApJ, 693, 1173
- Kilcik, A., Özgüç, A., Rozelot, J. P., & Ataç, T. 2010, Periodicities in Solar Flare Index for Cycles 21 - 23 Revisited, Sol. Phys., 264, 255
- Kitiashvili, I. & Kosovichev, A. G. 2008, Application of Data Assimilation Method for Predicting Solar Cycles, ApJ, 688, L49
- Koestler, A. & Dürrenmatt, F. 2008, Dynamo models of the solar cycle
- Komitov, B., Sello, S., Duchlev, P., et al. 2010, The sub- and quasi-centennial cycles in solar and geomagnetic activity data series/v.3
- Kontor, N. N., Lyubimov, G. P., Pereslegina, N. V., & Khotilovskaya, T. G. 1984, A prediction of the sunspot maxima for solar cycles NN 22-44., Byulletin Solnechnye Dannye Akademii Nauk SSSR, 1983, 74
- Kopp, G., Lawrence, G., & Rottman, G. 2005, The Total Irradiance Monitor (TIM): Science Results, Sol. Phys., 230, 129
- Kosugi, T., Matsuzaki, K., Sakao, T., et al. 2007, The Hinode (Solar-B) Mission: An Overview, Sol. Phys., 243, 3
- Krivova, N., Solanki, S. K., Dasi Espuig, M., Leng Yeo, K., & Wu, C.-J. 2016, Long-term solar irradiance variability: knowns and unknowns, 41
- Kudryavtsev, I. V., Dergachev, V. A., Nagovitsyn, Y. A., Ogurtsov, M. G., & Jungner, H. 2013, Influence of climatic factors on the past atmospheric content of the C-14 isotope, Geomagnetism and Aeronomy, 53, 927
- Kunitomo, S. 1980, The Solar Activity in the Time of Galileo, Journal for the History of Astronomy, 11, 164
- Kuzanyan, K., Obridko, V. N., Kotlyarov, O. L., Loskutov, A. Y., & Istomin, I. A. 2008, in European Solar Physics Meeting, Vol. 12, European Solar Physics Meeting, ed. H. Peter, 2.69

- Lambeck, K. 1988, Geophysical geodesy - The slow deformations of the earth
- Landscheidt, T. 1999, Extrema in Sunspot Cycle Linked to Sun's Motion, *Sol. Phys.*, 189, 413
- Lanza, A. F. 2009, Stellar coronal magnetic fields and star-planet interaction, *A&A*, 505, 339
- Lanza, A. F. 2012, Star-planet magnetic interaction and activity in late-type stars with close-in planets, *A&A*, 544, A23
- Larmor, J. 1919, How could a Rotating Body such as the Sun Become a Magnet?, *Concrete Mine Timbers, Scientific American*, 88, 287
- Laskar, J. 1994, Large-scale chaos in the solar system, *A&A*, 287, L9
- Laskar, J. 1999, *Introduction to Frequency Map Analysis* (Springer)
- Laskar, J. 2003, Frequency map analysis and quasiperiodic decompositions, arXiv preprint math/0305364
- Laskar, J., Fienga, A., Gastineau, M., & Manche, H. 2011, La2010: a new orbital solution for the long-term motion of the Earth, *A&A*, 532, A89
- Laskar, J., Robutel, P., Joutel, F., et al. 2004, A long-term numerical solution for the insolation quantities of the Earth, *A&A*, 428, 261
- Latyshev, S. V. & Olemskoy, S. V. 2016, Relationship between the north-south asymmetry of sunspot formation and the amplitude of 11-year solar activity cycles, *Astronomy Letters*, 42, 488
- Le, G.-M. & Wang, J.-L. 2003, Wavelet Analysis of Several Important Periodic Properties in the Relative Sunspot Numbers, *Chinese J. Astron. Astrophys.*, 3, 391
- Leal-Silva, M. & Herrera, V. V. 2012, Solar forcing on the ice winter severity index in the western Baltic region, *Journal of Atmospheric and Solar-Terrestrial Physics*, 89, 98
- Lean, J. 1990, Evolution of the 155 day periodicity in sunspot areas during solar cycles 12 to 21, *ApJ*, 363, 718
- Lean, J. & Rind, D. 1998a, Climate Forcing by Changing Solar Radiation., *Journal of Climate*, 11, 3069
- Lean, J. & Rind, D. 1998b, Climate Forcing by Changing Solar Radiation., *Journal of Climate*, 11, 3069
- Lee, III, R. B., Gibson, M. A., Wilson, R. S., & Thomas, S. 1995, Long-term total solar irradiance variability during sunspot cycle 22, *J. Geophys. Res.*, 100, 1667
- Leighton, R. B., Noyes, R. W., & Simon, G. W. 1962, Velocity Fields in the Solar Atmosphere. I. Preliminary Report., *The Astrophysical Journal*, 135, 474
- Leussu, R. & Ilya G. Usoskin¹, Rainer Arlt, M. K. 2016, Properties of sunspot cycles and hemispheric wings since the 19th century, *Astronomy and Astrophysics*, 592, 1

- Li, K., Wang, J., Zhan, L., et al. 2003, On the Latitudinal Distribution of Sunspot Groups over a Solar Cycle, *Solar Physics*, 215, 99
- Li, K. J., Feng, W., & Li, F. Y. 2015, Predicting the maximum amplitude of solar cycle 25 and its timing, *Journal of Atmospheric and Solar-Terrestrial Physics*, 135, 72
- Li, K. J., Yun, H. S., & Gu, X. M. 2001, On long-term predictions of the maximum sunspot numbers of solar cycles 21 to 23, *A&A*, 368, 285
- Lin, R., Dennis, B., Hurford, G., et al. 2002, The Reuven Ramaty High-Energy Solar Spectroscopic Imager (RHESSI), *Solar Physics*, 210, 3
- Link, F. 1964, Manifestations de l'activité solaire dans le passé historique, *Planet. Space Sci.*, 12, 333
- Link, F. 1977, L'activité solaire au 17e siècle, *l'Astronomie*, 91, 191
- Lo, M. W., Williams, B. G., Bollman, W. E., et al. 2001, Genesis mission design, *Journal of the Astronautical Sciences*, 49, 169
- Lockwood, M., Owens, M., & Barnard, L. 2014, Centennial variations in sunspot number, open solar flux, and streamer belt width: 2. Comparison with the geomagnetic data, *Journal of Geophysical Research: Space Physics*, 119, 5183
- Lockwood, M., Owens, M. J., Barnard, L., et al. 2016, Tests of Sunspot Number Sequences: 2. Using Geomagnetic and Auroral Data, *Sol. Phys.*
- Loskutov, A. Y., Istomin, I. A., Kotlyarov, O. L., & Kuzanyan, K. M. 2001, A Study of the Regularities in Solar Magnetic Activity by Singular Spectral Analysis, *Astronomy Letters*, 27, 745
- Ma, L. 2015, The 27-day variation in the Mg II index of solar activity, *Solar System Research*, 49, 205
- Ma, L. H. & Vaquero, J. M. 2009, Is the Suess cycle present in historical naked-eye observations of sunspots?, *New A*, 14, 307
- Maggio, A., Pillitteri, I., Scandariato, G., et al. 2015, Coordinated X-Ray and Optical Observations of Star, Planet Interaction in HD 17156, *ApJ*, 811, L2
- Malville, J. M. & Singh, R. P. B. 1995, Visual Astronomy in the Mythology and Ritual of India: The Sun Temples of Varanasi, *Vistas in Astronomy*, 39, 431
- Manoharan, P. K., Ananthakrishnan, S., Dryer, M., et al. 1995, Solar wind velocity and normalized scintillation index from single-station IPS observations, *Sol. Phys.*, 156, 377
- Maris, G. & Oncica, A. 2006a, Solar Cycle 24 Forecasts, *Sun and Geosphere*, 1, 8
- Maris, G. & Oncica, A. 2006b, Solar Cycle 24 Forecasts, *Sun and Geosphere*, 1, 8

- Matter, A., Labadie, L., Augereau, J. C., et al. 2016, Inner disk clearing around the Herbig Ae star HD 139614: Evidence for a planet-induced gap?, *A&A*, 586, A11
- Matthiä, D., Herbst, K., Heber, B., Berger, T., & Reitz, G. 2013, ^{10}Be Production in the Atmosphere by Galactic Cosmic Rays, *Space Sci. Rev.*, 176, 333
- Maunder, E. W. 1894, Connection between Solar Activity and Magnetic Disturbances, etc, on the Earth, *PASP*, 6, 125
- Maunder, E. W. 1904, Sunspot Variation in Latitude, *Popular Astronomy*, 12, 616
- Mavromichalaki, H., Petropoulos, B., Plainaki, C., Dionatos, O., & Zouganelis, I. 2005, Coronal index as a solar activity index applied to space weather, *Advances in Space Research*, 35, 410
- McCracken, K. G., Beer, J., & Steinhilber, F. 2014, Evidence for Planetary Forcing of the Cosmic Ray Intensity and Solar Activity Throughout the Past 9400 Years, *Sol. Phys.*, 289, 3207
- Meftah, M. et al. 2014, PICARD SODISM, a space telescope to study the Sun from the middle ultraviolet to the near infrared, *Solar Phys.*, 289, 1043
- Meyer-Vernet, N. 2007, *Basics of the solar wind* (Cambridge University Press)
- Milankovitch, J. 1920, *heorie Mathematique des Phenomenes Thermiques produits par la Radiation Solaire*
- Miller, B., Gallo, E., & Wright, J. T. 2015, A Comprehensive Statistical Assessment of Star-Planet Interaction, *IAU General Assembly*, 22, 2258384
- Minasyants, G. S. & Minasyants, T. M. 2013, *Solar active regions and space weather* (Almaty, Kazakhstan; Lambert, 2013.)
- Mitalas, R. & Sills, K. R. 1992, On the photon diffusion time scale for the sun, *ApJ*, 401, 759
- Moreno-Insertis, F. 1992, in *NATO Advanced Science Institutes (ASI) Series C, Vol. 375*, NATO Advanced Science Institutes (ASI) Series C, ed. J. H. Thomas & N. O. Weiss, 385–410
- Mörner, N., Tattersall, R., Solheim, J., et al. 2013, General conclusions regarding the planetary-solar-terrestrial interaction, *Pattern Recognition in Physics*, 1, 205
- Mörner, N.-A. 2012, Planetary beat, solar wind and terrestrial climate, 47–66, cited By 0
- Mörner, N.-A. 2015, The approaching new grand solar minimum and little ice age climate conditions, 7, 510
- Muraközy, J. 2016, Phase Relationships of Solar Hemispheric Toroidal and Poloidal Cycles, *ApJ*, 826, 145
- Nagovitsyn, Y. A. 1997, A nonlinear mathematical model for the solar cyclicity and prospects for reconstructing the solar activity in the past, *Astronomy Letters*, 23, 742

- Nagovitsyn, Y. A. 1997, A nonlinear mathematical model for the solar cyclicity and prospects for reconstructing the solar activity in the past, *Astronomy Letters*, 23, 742
- Nagovitsyn, Y. A. & Kuleshova, A. I. 2015, North-South asymmetry of solar activity on a long timescale, *Geomagnetism and Aeronomy*, 55, 887
- Narayanan, A. S. 2012, *An Introduction to Waves and Oscillations in the Sun* (Springer Science & Business Media)
- Navarro, R. & Prieto, E. 2012, Modern technologies in space- and ground-based telescopes and instrumentation III-6 July 2012, Amsterdam, Netherlands (BELLINGHAM; INTL SOC OF OPTICAL ENG)
- Neuhäuser, R. & Neuhäuser, D. L. 2016, Studying the start of the Maunder Minimum to understand the current situation, 18, 11910
- Noyes, R. W. 1982, *The sun, our star*, Cambridge, MA, Harvard University Press, 1982. 268 p, 1
- Ochadlick, Jr., A. R., Kritikos, H. N., & Giegengack, R. 1993, Variations in the period of the sunspot cycle, *Geophys. Res. Lett.*, 20, 1471
- Ogawara, Y., Takano, T., Kato, T., et al. 1991, The SOLAR-A mission: An overview, *Solar Physics*, 136, 1
- Oggusc, A., A. T. R. J. 2003, Temporal variability of the flare index (1966-2001), *Sol. Phys.*, 214, 375
- Ogurtsov, M., Lindholm, M., Jalkanen, R., & Veretenenko, S. 2015, Evidence for the Gleissberg solar cycle at the high-latitudes of the Northern Hemisphere, *Advances in Space Research*, 55, 1285
- Ogurtsov, M., Nagovitsyn, Y. A., Kocharov, G., & Jungner, H. 2002, Long-period cycles of the Sun's activity recorded in direct solar data and proxies, *Solar Physics*, 211, 371
- Ogurtsov, M. G. 2012, Missing solar cycle hypothesis and basic statistical regularities of solar cycles, *Geomagnetism and Aeronomy*, 52, 977
- Ogurtsov, M. G., Kocharov, G. E., Jungner, H., Lindholm, M., & Eronen, M. 2003, On the connection between the solar cycle length and terrestrial climate
- Ogurtsov, M. G., Nagovitsyn, Y. A., Kocharov, G. E., & Jungner, H. 2002, Long-Period Cycles of the Sun's Activity Recorded in Direct Solar Data and Proxies, *Sol. Phys.*, 211, 371
- Okal, E. & Anderson, D. L. 1975, On the planetary theory of sunspots, *Nature*, 253, 511
- Okhlopkov, V. 2014, 11 -year planetary index of solar activity, 40
- Ol', A. I. 1978, Forecast of solar and geomagnetic activity for solar cycle No. 21., *Byulletin Solnechnye Dannye Akademii Nauk SSSR*, 1977, 87

- Otaola, J. A. & Zenteno, G. 1983, On the existence of long-term periodicities in solar activity, *Sol. Phys.*, 89, 209
- Patterson, C. 1956, Age of meteorites and the earth, *Geochimica et Cosmochimica Acta*, 10, 230
- Peale, S. J. 1976, Orbital resonances in the solar system, *ARA&A*, 14, 215
- Perryman, M. & Schulze-Hartung, T. 2011, The barycentric motion of exoplanet host stars: tests of solar spin-orbit coupling, *Astron.Astrophys.*, 525, 65
- Pesnell, W. D. 2008, Predictions of Solar Cycle 24, *Sol. Phys.*, 252, 209
- Pesnell, W. D. 2012a, Solar Cycle Predictions (Invited Review), *Sol. Phys.*, 281, 507
- Pesnell, W. D. 2012b, Solar cycle predictions (invited review), *Solar Physics*, 281, 507
- Pesnell, W. D., Thompson, B. J., & Chamberlin, P. C. 2012, The Solar Dynamics Observatory (SDO), *Solar Physics*, 275, 3
- Peter Foukal. 1990, *Solar astrophysics* (New York : Wiley, c1990.)
- Petrovay, K. 2010, Solar Cycle Prediction, *Living Rev. Solar Phys.*
- Pillitteri, I., Maggio, A., Micela, G., et al. 2015, FUV Variability of HD 189733. Is the Star Accreting Material From Its Hot Jupiter?, *ApJ*, 805, 52
- Pishkalo, M. I. 2008, Preliminary prediction of solar cycles 24 and 25 based on the correlation between cycle parameters, *Kinematics and Physics of Celestial Bodies*, 24, 242
- Pittock, A. B. 1978, A critical look at long-term sun-weather relationship., *Reviews of Geophysics and Space Physics*, 16, 400
- Polunianov, S. & Usoskin, I. 2014, Critical Analysis of a Hypothesis of the Planetary Tidal Influence on Solar Activity, *Sol. Phys.*, 289, 2333
- Poppenhaeager, K. 2015, Stellar magnetic activity - Star-Planet Interactions, 101, 05002
- Poppenhaeager, K. & Schmitt, J. H. M. M. 2011, A Correlation Between Host Star Activity and Planet Mass for Close-in Extrasolar Planets?, *ApJ*, 735, 59
- Poppenhaeager, K. & Wolk, S. J. 2014, Indications for an influence of hot Jupiters on the rotation and activity of their host stars, *A&A*, 565, L1
- Prša, A., Harmanec, P., Torres, G., et al. 2016, Nominal Values for Selected Solar and Planetary Quantities: IAU 2015 Resolution B3, *AJ*, 152, 41
- Pulkkinen, A. A., Pirjola, R., & Viljanen, A. 2007, Statistical coupling between solar wind conditions and extreme geomagnetically induced current events, *AGU Fall Meeting Abstracts*

- Quassim, M. S., Attia, A.-F., & Elminir, H. K. 2007, Forecasting the Peak Amplitude of the 24th and 25th Sunspot Cycles and Accompanying Geomagnetic Activity, *Sol. Phys.*, 243, 253
- Raspopov, O., Shumilov, O., Kasatkina, E., Turunen, E., & Lindholm, M. 2000, in *The solar cycle and terrestrial climate, Solar and space weather*, Vol. 463, 517
- Reimer, P.J., B. E. e. a. 2013, IntCal04 atmospheric radiocarbon age calibration 26-0 BP, *A*
- Richard Stephenson, F., M Willis, D., & J Hallinan, T. 2004, The earliest datable observation of the aurora borealis, *Astronomy & Geophysics*, 45, 615
- Rigozo, N., Nordemann, D., Echer, E., Echer, M., & Silva, H. 2010, Prediction of solar minimum and maximum epochs on the basis of spectral characteristics for the next millennium, *Planetary and Space Science*, 58, 1971
- Rigozo, N. R., Echer, E., Vieira, L., & Nordemann, D. J. R. 2001, Reconstruction of Wolf sunspot numbers on the basis of spectral characteristics and estimates of associated radio flux and solar wind parameters for the last millennium, *Solar Physics*, 203, 179
- Rigozo, N. R., Souza Echer, M. P., Evangelista, H., Nordemann, D. J. R., & Echer, E. 2011, Prediction of sunspot number amplitude and solar cycle length for cycles 24 and 25, *Journal of Atmospheric and Solar-Terrestrial Physics*, 73, 1294
- RiOUSset, J., Motschmann, U., Reiners, A., & Marvin, C. 2015, Towards theoretical modeling of planet-induced stellar activity using A.I.K.E.F. simulations, 17, 14287
- Roe, G. 2006, In defense of Milankovitch, *Geophys. Res. Lett.*, 33, L24703
- Rosen, E. 1984, *Copernicus and the scientific revolution* (Malabar, Fla. : Krieger, 1984.)
- Roshchina, E. M. & Sarychev, A. P. 2015, Approximation of periodicity in sunspot formation of and prediction of the 25th cycle, *Geomagnetism and Aeronomy*, 55, 892
- Rubio, L. R. B. 2010, *The Evershed Flow and the Brightness of the Penumbra* (Springer)
- Russell, C. 2001, Solar wind and interplanetary magnetic field: A tutorial, *Space Weather*, 73
- Ryabov, M. I. 2015, Activity of the northern and southern hemispheres as a basis of the solar cycle manifestation, *Geomagnetism and Aeronomy*, 55, 1089
- Rybansky, M., Rušin, V., Minarovjeh, M., Klocok, L., & Cliver, E. W. 2005, Reexamination of the coronal index of solar activity, *Journal of Geophysical Research (Space Physics)*, 110, A08106
- Salvador, R. 2013, A mathematical model of the sunspot cycle for the past 1000yr, *Pattern Recogn. Phys*, 1, 117
- Sankarasubramanian, K. 2013, in *Astronomical Society of India Conference Series*, Vol. 9, *Astronomical Society of India Conference Series*
- Satya Narayanan, A. 2013, *An Introduction to Waves and Oscillations in the Sun*

- Scafetta, N. 2009, Total solar irradiance satellite composites and their phenomenological effect on climate, arXiv preprint arXiv:0908.0792
- Scafetta, N. 2010a, Empirical evidence for a celestial origin of the climate oscillations and its implications, *Journal of Atmospheric and Solar*
- Scafetta, N. 2010b, Empirical evidence for a celestial origin of the climate oscillations and its implications, *Journal of Atmospheric and Solar-Terrestrial Physics*, 72, 951
- Scafetta, N. 2012a, Does the Sun work as a nuclear fusion amplifier of planetary tidal forcing? A proposal for a physical mechanism based on the mass-luminosity relation, 81
- Scafetta, N. 2012b, Does the Sun work as a nuclear fusion amplifier of planetary tidal forcing? A proposal for a physical mechanism based on the mass-luminosity relation, *Journal of Atmospheric and Solar-Terrestrial Physics*, 81, 27
- Scafetta, N. 2012, Does the Sun work as a nuclear fusion amplifier of planetary tidal forcing? A proposal for a physical mechanism based on the mass-luminosity relation, *Journal of Atmospheric and Solar-Terrestrial Physics*, 81, 27
- Scafetta, N. 2012, Multi-scale harmonic model for solar and climate cyclical variation throughout the Holocene based on Jupiter-Saturn tidal frequencies plus the 11-year solar dynamo cycle, *Journal of Atmospheric and Solar-Terrestrial Physics*, 80, 296
- Scafetta, N. 2012, Multi-scale harmonic model for solar and climate cyclical variation throughout the Holocene based on Jupiter-Saturn tidal frequencies plus the 11-year solar dynamo cycle
- Scafetta, N. 2014, Discussion on the spectral coherence between planetary, solar and climate oscillations: a reply to some critiques, *Astrophysics and Space Science*, 354, 275
- Scafetta, N. 2014a, Discussion on the spectral coherence between planetary, solar and climate oscillations: a reply to some critiques, *Ap&SS*, 354, 275
- Scafetta, N. 2014b, The complex planetary synchronization structure of the solar system, *Pattern Recognition in Physics*, 2, 1
- Scafetta, N. 2014, The complex planetary synchronization structure of the solar system, arXiv preprint arXiv:1405.0193
- Scafetta, N. 2016a, High resolution coherence analysis between planetary and climate oscillations, *Advances in Space Research*, 57, 2121
- Scafetta, N. 2016b, Hindcast and forecast of grand solar minima and maxima using a three-frequency dynamo model based on Jupiter-Saturn tidal frequencies modulating the 11-year sunspot cycle, 18, 13513
- Scafetta, N. 2016c, Hindcast and forecast of grand solar minima and maxima using a three-frequency dynamo model based on Jupiter-Saturn tidal frequencies modulating the 11-year sunspot cycle, 18, 13513

- Scafetta, N. & Willson, R. C. 2013, Empirical evidences for a planetary modulation of total solar irradiance and the TSI signature of the 1.09-year Earth-Jupiter conjunction cycle, *Astrophys.Space Sci.*, 348, 25
- Scafetta, N. & Willson, R. C. 2014, ACRIM total solar irradiance satellite composite validation versus TSI proxy models, *Ap&SS*, 350, 421
- Scandariato, G., Maggio, A., Lanza, A. F., et al. 2013a, A coordinated optical and X-ray spectroscopic campaign on HD 179949: searching for planet-induced chromospheric and coronal activity, *A&A*, 552, A7
- Scandariato, G., Maggio, A., Lanza, A. F., et al. 2013b, A coordinated optical and X-ray spectroscopic campaign on HD 179949: searching for planet-induced chromospheric and coronal activity, *A&A*, 552, A7
- Scharf, C. A. 2010a, Possible Constraints on Exoplanet Magnetic Field Strengths from Planet-star Interaction, *ApJ*, 722, 1547
- Scharf, C. A. 2010b, Possible Constraints on Exoplanet Magnetic Field Strengths from Planet-star Interaction, *ApJ*, 722, 1547
- Schatten, K. 2002, Solar activity prediction: Timing predictors and cycle 24, *Journal of Geophysical Research (Space Physics)*, 107, 1377
- Schatten, K. 2005, Fair space weather for solar cycle 24, *Geophys. Res. Lett.*, 32, L21106
- Schatten, K. & Sofia, S. 1996, Forecasting Solar Activity and Cycle 23 Outlook, 28, 1347
- Schlesinger, M. E. & Ramankutty, N. 1994, Have solar-irradiance variations influenced climate ?, 493
- Schmidt, H. U. 1991, Sunspots, *Geophysical and Astrophysical Fluid Dynamics*, 62, 249
- Schmidt, W. 2000, Solar telescopes and instruments: Ground, *Encyclopedia of Astronomy and Astrophysics*, 1, 1987
- Schmidt, W. 2008, Solar telescopes., *Scholarpedia*, 3, 4333
- Schmidtke, G., Fröhlich, C., & Thuillier, G. 2006, ISS-SOLAR: Total (TSI) and spectral (SSI) irradiance measurements, *Advances in Space Research*, 37, 255
- Schmieder, B. 1997, Advances in the physics of sunspots. Poster contributions. 1st ASPE Meeting, Puerto de la Cruz, Tenerife (Spain), 2 - 6 Oct 1996., 47
- Schmutz, W., Fehlmann, A., Finsterle, W., Kopp, G., & Thuillier, G. 2013, Total solar irradiance measurements with PREMOS/PICARD, *AIP Conference Proceedings*, 1531, 624
- Schove, D. J. 1955, The sunspot cycle, 649 BC to AD 2000, *Journal of Geophysical Research*, 60, 127
- Schove, D. J. 1979, Sunspot Turning-Points and Aurorae Since A. D. 1510, *Sol. Phys.*, 63, 423

- Schove, D. J. 1983a, Sunspot, auroral, radiocarbon and climatic fluctuations since 7000 BC., *Annales Geophysicae*, 1, 391
- Schove, D. J. 1983b, Sunspot cycles (Stroudsburg, Pa. : Hutchinson Ross Pub. Co. ; c1983.)
- Schove, D. J. 1983c, Sunspot cycles, Stroudsburg, PA, Hutchinson Ross Publishing Co.(Benchmark Papers in Geology. Volume 68), 1983, 410 p., 1
- Schove, J. 1983d, Sunspot cycles (Stroudsburg, Pa. : Hutchinson Ross Pub. Co. ; c1983.)
- Schröder, W. 2009, Johann Fabricius and the discovery of sunspots, *Acta Geodaetica et Geophysica Hungarica*, 44, 255
- Schulz, N. S. 2012, The Formation and early evolution of stars: from dust to stars and planets (Springer Science & Business Media)
- Schuster, A. 1911, The Influence of Planets on the Formation of Sun-Spots, *Proceedings of the Royal Society of London Series A*, 85, 309
- Schwabe, M. 1844, Sonnenbeobachtungen im Jahre 1843. Von Herrn Hofrath Schwabe in Dessau, *Astronomische Nachrichten*, 21, 233
- Seltman, M. & Robert Goulding. 2007, Thomas Harriot's *Artis analyticae praxis*: an English translation with commentary (New York : Springer, 2007.)
- Shaltout, M., Shaltout, M., Ramy Mawad, R., & Youssef, M. 2008, The Solar Radio Flux on 10.7cm as the best index for Space Weather long-term Prediction, 37, 2827
- Shapiro, A. I., Schmutz, W., Rozanov, E., et al. 2011, A new approach to the long-term reconstruction of the solar irradiance leads to large historical solar forcing, *A&A*, 529, A67
- Shepherd, S. J., Zharkov, S. I., & Zharkova, V. V. 2014, Prediction of Solar Activity from Solar Background Magnetic Field Variations in Cycles 21-23, *ApJ*, 795, 46
- Shirley, J. H. 2006, Axial rotation, orbital revolution and solar spin-orbit coupling, *MNRAS*, 368, 280
- Shkolnik, E. 2005, Chromospheric Activity Induced by Short-Period Planets: A Search for Modulation of Ca ii H, K Emission, *JRASC*, 99, 23
- Shkolnik, E. 2010, Star-Planet Interactions: The Tidal and Magnetic Influence of Hot Jupiters, 12, 13591
- Simon, J. I., Hutcheon, I. D., Simon, S. B., et al. 2011, Oxygen isotope variations at the margin of a CAI records circulation within the solar nebula, *Science*, 331, 1175
- Sivaraman, K. R., Gupta, S. S., & Howard, R. F. 1999, Measurement of Kodaikanal white-light images - IV. Axial Tilt Angles of Sunspot Groups, *Sol. Phys.*, 189, 69
- Smythe, C. M. & Eddy, J. A. 1977, Planetary tides during the Maunder Sunspot minimum

- Snow, M., McClintock, W. E., Woods, T. N., et al. 2005, The Mg II Index from SORCE, *Sol. Phys.*, 230, 325
- Solanki, S., Livingston, W., Ayres, T., et al. 1994, New light on the heart of darkness of the solar chromosphere, *Science-AAAS-Weekly Paper Edition-including Guide to Scientific Information*, 263, 64
- Solanki, S., Schüssler, M., & Fligge, M. 2000, Evolution of the Sun's large-scale magnetic field since the Maunder minimum, *Nature*, 408, 445
- Solanki, S. K. 2003, Sunspots: An overview, *The Astronomy and Astrophysics Review*, 11, 153
- Solanki, S. K., Krivova, N. A., Schussler, M., & Fligge, M. 2002, Search for a relationship between solar cycle amplitude and length, *ASTRONOMY AND ASTROPHYSICS -BERLIN-*, 396, 1029
- Solanki, S. K., Usoskin, I. G., Kromer, B., Schüssler, M., & Beer, J. 2004a, Unusual activity of the Sun during recent decades compared to the previous 11,000 years, *Nature*, 431, 1084
- Solanki, S. K., Usoskin, I. G., Kromer, B., Schüssler, M., & Beer, J. 2004b, Unusual activity of the Sun during recent decades compared to the previous 11,000 years, *Nature*, 431, 1084
- Sonett, C. P. & Finney, S. A. 1990, The Spectrum of Radiocarbon, *Philosophical Transactions of the Royal Society of London Series A*, 330, 413
- Spiegel, E. A. & Zahn, J.-P. 1992, The solar tachocline, *A&A*, 265, 106
- Steele, J., Stephenson, F., & Morrison, L. 1997, The accuracy of eclipse times measured by the Babylonians, *Journal for the History of Astronomy*, 28, 337
- Steinhilber, F., Abreu, J. A., & Beer, J. 2008, Solar modulation during the Holocene, *Astrophysics and Space Sciences Transactions*, 4, 1
- Steinhilber, F., Abreu, J. A., Beer, J., et al. 2012, 9,400 years of cosmic radiation and solar activity from ice cores and tree rings, *Proceedings of the National Academy of Science*, 109, 5967
- Steinhilber, F., Abreu, J. A., Beer, J., et al. 2012a, 9,400 years of cosmic radiation and solar activity from ice cores and tree rings, *Proceedings of the National Academy of Sciences*, 109, 5967
- Steinhilber, F., Abreu, J. A., Beer, J., et al. 2012b, 9,400 years of cosmic radiation and solar activity from ice cores and tree rings, *Proceedings of the National Academy of Sciences*, 109, 5967
- Steinhilber, F., Beer, J., & Frohlich, C. 2009, Total Solar Irradiance during the past 9300 Years inferred from the Cosmogenic Radionuclide Beryllium-10, *AGU Fall Meeting Abstracts*

- Steinhilber, F. & Jurg, B. 2011, Solar activity—the past 1200 years, *PAGES news*, 19, 5
- Stenflo, J. O. & Kosovichev, A. G. 2012, Bipolar Magnetic Regions on the Sun: Global Analysis of the SOHO/MDI Data Set, *ApJ*, 745, 129
- Stephenson, F. 1978, in *Tidal Friction and the Earth's Rotation* (Springer), 5–21
- Stephenson, F. 1990, Historical evidence concerning the Sun: interpretation of sunspot records during the telescopic and pretelescopic eras, *Philosophical Transactions of the Royal Society of London A: Mathematical, Physical and Engineering Sciences*, 330, 499
- Stephenson, F. R. 1982, Historical eclipses, *Scientific American*, 247, 170
- Stephenson, F. R. 2008, How Reliable Are Archaic Records of Large Solar Eclipses?, *Journal for the History of Astronomy*, 39, 229
- Stix, M. 2003, On the time scale of energy transport in the sun, *Sol. Phys.*, 212, 3
- Stone, E., Frandsen, A., Mewaldt, R., et al. 1998, The Advanced Composition Explorer, *Space Science Reviews*, 86, 1
- Strassmeier, K. G. 2002, Doppler images of starspots, *Astronomische Nachrichten*, 323, 309
- Strugarek, A., Beaudoin, P., Charbonneau, P., Brun, A. S., & do Nascimento, J.-D. 2017, Reconciling solar and stellar magnetic cycles with nonlinear dynamo simulations, *Science*, 357, 185
- Strugarek, A., B.-P. C. P. B. A. S. N. J.-D. 2017, Reconciling solar and stellar magnetic cycles with nonlinear dynamo simulations, *Science*, 357, 185
- Stuiver, M. 1980, Solar variability and climatic change during the current millennium, *Nature*, 286, 868
- Stuiver, M. & Quay, P. D. 1980, Changes in atmospheric Carbon-14 attributed to a variable sun, *Science*, 207, 11
- Suess, H. E. 1980, The Radiocarbon Record in Tree Rings of the Last 8000 Years, *Radiocarbon*, 22, 200
- Svalgaard, L. & Cliver, E. 2007, Long-term geomagnetic indices and their use in inferring solar wind parameters in the past, *Advances in Space Research*, 40, 1112
- Svalgaard, L., Cliver, E. W., & Kamide, Y. 2005a, Sunspot cycle 24: Smallest cycle in 100 years?, *Geophys. Res. Lett.*, 32, L01104
- Svalgaard, L., Cliver, E. W., & Kamide, Y. 2005b, Sunspot cycle 24: Smallest cycle in 100 years?, *Geophys. Res. Lett.*, 32, L01104
- Svalgaard, L. & Schatten, K. H. 2008, Predicting Solar Cycle 24, *AGU Fall Meeting Abstracts*
- Svalgaard, L. & Schatten, K. H. 2016, Reconstruction of the Sunspot Group Number: The Backbone Method, *Sol. Phys.*

- Svensmark, H. & Friis-Christensen, E. 1997, Variation of cosmic ray flux and global cloud coverage—a missing link in solar-climate relationships, *Journal of Atmospheric and Solar-Terrestrial Physics*, 59, 1225
- Takahashi, K. 1968, On the Relation between the Solar Activity Cycle and the Solar Tidal Force induced by the Planets, *Sol. Phys.*, 3, 598
- Tan, B. 2011, Multi-timescale solar cycles and the possible implications, *Ap&SS*, 332, 65
- Tan, B. & Cheng, Z. 2012, The Mid-term and Long-term Solar Quasi-periodic Cycles and the Possible Relationship with Planetary Motions, *Astrophysics and Space Science*
- Tan, B. & Cheng, Z. 2013, The Mid-term and Long-term Solar Quasi-periodic Cycles and the Possible Relationship with Planetary Motions, *Astrophys.Space Sci.*, 343, 511
- Tapping, K. F. & Charrois, D. P. 1994, Limits to the accuracy of the 10.7 CM flux, *Sol. Phys.*, 150, 305
- Tebabal, A. & Damtie, B., N.-M. B. A. Y. E. 2015, Modeling total solar irradiance from PMOD composite using feed-forward neural networks, *Journal of Atmospheric and Solar-Terrestrial Physics*, 135, 64
- Tebabal Yirdaw, A., Damtie, B., Nigussie, M., Bires, A., & Yizengaw, E. 2015, Total solar irradiance reconstruction using artificial neural networks, *IAU General Assembly*, 22, 2237766
- Thomas, J. H. & Weiss, N. O., eds. 1992, *NATO Advanced Science Institutes (ASI) Series C, Vol. 375, Sunspots: Theory and observations; Proceedings of the NATO Advanced Research Workshop on the Theory of Sunspots*, Cambridge, United Kingdom, Sept. 22-27, 1991
- Thomas, J. H. & Weiss, N. O. 2008, *Sunspots and starspots* (Cambridge, UK ; Cambridge University Press, 2008.)
- Thompson, R. J. 1993, A Technique for Predicting the Amplitude of the Solar Cycle, *Sol. Phys.*, 148, 383
- Tlatov, A. G. 2009, The Minimum Activity Epoch as a Precursor of the Solar Activity, *Sol. Phys.*, 260, 465
- Tobias, S. M. 2002, The solar dynamo, *Philosophical Transactions of the Royal Society of London Series A*, 360, 2741
- Tong, H. 1990, *Non-linear time series: a dynamical system approach* (Oxford U.P., 1990.)
- Trellis, M. 1966, Marees solaires d origine planetaire, *C.R. Acad. Sci. Paris*, 262, 221
- Tsuneta, S. 2008, The Solar Optical Telescope for the Hinode Mission: An Overview
- Usoskin, I. 2011, Solar modulation of cosmic rays since 1936: Neutron monitors and balloon-borne data, *International Cosmic Ray Conference*, 11, 39

- Usoskin, I., Schüssler, M., Solanki, S., & Mursula, K. 2005, Solar activity, cosmic rays, and Earth's temperature: A millennium-scale comparison, *Journal of Geophysical Research: Space Physics* (1978–2012), 110
- Usoskin, I. G. 2013, A History of Solar Activity over Millennia, *Usoskin*
- Usoskin, I. G., Arlt, R., Asvestari, E., et al. 2015, The Maunder minimum (1645-1715) was indeed a grand minimum: A reassessment of multiple datasets, *A&A*, 581, A95
- Usoskin, I. G., Gallet, Y., Lopes, F., Kovaltsov, G. A., & Hulot, G. 2016a, Solar activity during the Holocene: the Hallstatt cycle and its consequence for grand minima and maxima, *A&A*, 587, A150
- Usoskin, I. G., Gallet, Y., Lopes, F., Kovaltsov, G. A., & Hulot, G. 2016b, *VizieR Online Data Catalog: Solar activity during the Holocene (Usoskin+, 2016)*, *VizieR Online Data Catalog*, 358
- Usoskin, I. G., Horiuchi, K., Solanki, S., Kovaltsov, G. A., & Bard, E. 2009, On the common solar signal in different cosmogenic isotope data sets, *Journal of Geophysical Research (Space Physics)*, 114, A03112
- Usoskin, I. G., Hulot, G., Gallet, Y., et al. 2014, *VizieR Online Data Catalog: Solar activity reconstructed for 3 millennia (Usoskin+, 2014)*, *VizieR Online Data Catalog*, 356
- Usoskin, I. G., Kovaltsov, G. A., Lockwood, M., et al. 2016c, A New Calibrated Sunspot Group Series Since 1749: Statistics of Active Day Fractions, *Sol. Phys.*
- Usoskin, I. G. & Mursula, K., S.-S. S. M. A. K. 2004, Reconstruction of solar activity for the last millennium using ^{10}Be data, *Astron.Astrophys.*, 413, 745
- Usoskin, I. G., Solanki, S. K., & Kovaltsov, G. A. 2007, Grand minima and maxima of solar activity: new observational constraints, *Astronomy & Astrophysics*, 471, 301
- Usoskin, I. G., Solanki, S. K., Schuessler, M., Mursula, K., & Alanko, K. 2003, A Millennium Scale Sunspot Number Reconstruction: Evidence For an Unusually Active Sun Since the 1940's, *Phys.Rev.Lett.*, 91, 211101
- Uwamahoro, J., McKinnell, L.-A., & Cilliers, P. J. 2009a, Forecasting solar cycle 24 using neural networks, *Journal of Atmospheric and Solar-Terrestrial Physics*, 71, 569
- Uwamahoro, J., McKinnell, L.-A., & Cilliers, P. J. 2009b, Forecasting solar cycle 24 using neural networks, *Journal of Atmospheric and Solar-Terrestrial Physics*, 71, 569
- Vaquero, J. M. 2007, Historical sunspot observations: A review, *Advances in Space Research*, 40, 929
- Vaquero, J. M. 2007, Historical Sunspot Observations: A Review, cite arxiv:astro-ph/0702068Comment: 19 pages, 6 figures, to be published in *Adv. Space Res*
- Vaquero, J. M., Svalgaard, L., Carrasco, V. M. S., et al. 2016, A Revised Collection of Sunspot Group Numbers, *Sol. Phys.*

- Vaquero, J. M. & Vázquez, M. 2009, *The Sun Recorded Through History*, Vol. 361 (Springer Science & Business Media)
- Vázquez, M. & Hanslmeier, A. 2005, *Ultraviolet radiation in the solar system*, Vol. 331 (Springer Science & Business Media)
- Velasco Herrera, V. M., Mendoza, B., & Velasco Herrera, G. 2015, Reconstruction and prediction of the total solar irradiance: From the Medieval Warm Period to the 21st century, *New A*, 34, 221
- Vieira, L. A., Dudok de Wit, T., & Da Silva, L. A. 2011a, The role of energy exchange between the eddies and the mean flow for the long-term modulation of the solar activity, *AGU Fall Meeting Abstracts*, B1946
- Vieira, L. E. A., Solanki, S. K., Krivova, N. A., & Usoskin, I. 2011b, Evolution of the solar irradiance during the Holocene, *A&A*, 531, A6
- Vitinskij, Y. I. 1973, Recurrence and forecast of solar activity.
- Vitinskij, Y. I., Kuklin, G. V., & Obridko, V. N. 1986, On principal phases of the solar cycle., *Byulletin Solnechnye Dannye Akademii Nauk SSSR*, 1986, 53
- Vonmoos, M., Beer, J., & Muscheler, R. 2006, Large variations in Holocene solar activity: Constraints from ^{10}Be in the Greenland Ice Core Project ice core, *Journal of Geophysical Research: Space Physics* (1978–2012), 111
- Wagner, G., Laj, C., Beer, J., et al. 2001, Reconstruction of the paleoaccumulation rate of central Greenland during the last 75 kyr using the cosmogenic radionuclides ^{36}Cl and ^{10}Be and geomagnetic field intensity data, *EARTH AND PLANETARY SCIENCE LETTERS*, 193, 515
- Waldmeier, M. 1939, Die Zonenwanderung der Sonnenflecken, *Astronomische Mitteilungen der Eidgenössischen Sternwarte Zurich*, 14, 470
- Waldmeier, M. 1955, *Ergebnisse und Probleme der Sonnenforschung*, 2nd edn. (Leipzig: Geest & Portig)
- Wang, H.-B., Xiong, J.-N., & Zhao, C.-Y. 2015, The Mid-term Forecast Method of Solar Radiation Index, *Chinese Astron. Astrophys.*, 39, 198
- Wang, Y.-M. & Sheeley, N. R. 2009a, Understanding the Geomagnetic Precursor of the Solar Cycle, *ApJ*, 694, L11
- Wang, Y.-M. & Sheeley, N. R. 2009b, Understanding the Geomagnetic Precursor of the Solar Cycle, *ApJ*, 694, L11
- Wang, Y.-M. & Sheeley, Jr., N. R. 2003, On the Fluctuating Component of the Sun's Large-Scale Magnetic Field, *ApJ*, 590, 1111
- Webb, D. F. & Howard, T. A. 2012, Coronal Mass Ejections: Observations, *Living Reviews in Solar Physics*, 9, 3

- Wei, W. 2005, Time series analysis: univariate and multivariate methods (Redwood City, CA , Addison Wesley Pub., 1990.)
- Wenzel, K., Marsden, R., Page, D., & Smith, E. 1992, The ULYSSES mission, *Astronomy and Astrophysics Supplement Series*, 92, 207
- Willson, R. C. 1997, Total solar irradiance trend during solar cycles 21 and 22., *Science*, 277, 1963
- Willson, R. C. 2014, ACRIM3 and the Total Solar Irradiance database, *ASTROPHYSICS AND SPACE SCIENCE -DORDRECHT-*, 352, 341
- Willson, R. C. & Hudson, H. S. 1991, The sun's luminosity over a complete solar cycle, *Nature*, 351, 42
- Willson, R. C. & Mordvinov, A. V. 2003, Composite total solar irradiance time series show a secular 0.04 %/decade trend, *AGU Fall Meeting Abstracts*
- Wilson, I. R. G. 2013, The Venus-Earth-Jupiter spin-orbit coupling model, *Pattern Recognition in Physics*, 1, 147
- Wilson, P. R. 1994, *Solar and stellar activity cycles* (Cambridge ; Cambridge University Press, 1994.)
- Wilson, R. M. 1987, On the distribution of sunspot cycle periods, *J. Geophys. Res.*, 92, 10
- Wilson, R. M. 1988a, On the long-term secular increase in sunspot number, *Sol. Phys.*, 115, 397
- Wilson, R. M. 1988b, On the long-term secular increase in sunspot number, *Sol. Phys.*, 115, 397
- Wilson, R. M., Hathaway, D. H., & Reichmann, E. J. 1998, An estimate for the size of cycle 23 based on near minimum conditions, *J. Geophys. Res.*, 103, 6595
- Wittmann, A. 1978, The Sunspot Cycle before the Maunder Minimum, *A&A*, 66, 93
- Wittmann, A. & Xu, Z. 1987, A catalogue of sunspot observations from 165 BC to AD 1684, *Astronomy and Astrophysics Supplement Series*, 70, 83
- Wittmann, A. & Xu, Z. 1987, A catalogue of sunspot observations from 165 BC to AD 1684, *Astronomy and Astrophysics Supplement Series*, 70, 83
- Wittmann, A. D. & Xu, Z. T. 1988, in *Secular Solar and Geomagnetic Variations in the Last 10,000 Years.*, ed. F. R. Stephenson & A. W. Wolfendale, 131–139
- Woch, J. & Gizon, L. 2007, The Solar Orbiter mission and its prospects for helioseismology, *Astronomische Nachrichten*, 328, 362
- Wolf, R. 1859a, Extract of a Letter to Mr. Carrington, *MNRAS*, 19, 85
- Wolf, R. 1859b, Extract of a Letter to Mr. Carrington, *MNRAS*, 19, 85

- Wolff, C. L. & Patrone, P. N. 2010, A New Way that Planets Can Affect the Sun, *Sol. Phys.*, 266, 227
- Wood, Jr., A. T. 1972a, PhD thesis, HARVARD UNIVERSITY.
- Wood, K. D. 1972b, Physical Sciences: Sunspots and Planets, *Nature*, 240, 91
- Wood, R. M. 1965, Solar Motion and Sunspot Comparison, *Nature*, 208, 129
- Wu, C.-J., Usoskin, I., Krivova, N., & Solanki, S. K. 2016, Solar total and spectral irradiance reconstruction over last 9000 years, 41
- Yang, S., Zhang, J., Jiang, F., & Xiang, Y. 2015, Oscillating Light Wall Above a Sunspot Light Bridge, *ApJ*, 804, L27
- Yau, K. K. C. & Stephenson, F. R. 1988, A revised catalogue of Far Eastern observations of sunspots (165 BC to AD 1918), *QJRAS*, 29, 175
- Yndestad, H. & Solheim, J.-E. 2016, ({The) Solar System Large Planets influence on a new Maunder Mini μ m}, 18, 2839
- Zaqarashvili, T. V. 1997a, On a Possible Generation Mechanism for the Solar Cycle, *ApJ*, 487, 930
- Zaqarashvili, T. V. 1997b, On a Possible Generation Mechanism for the Solar Cycle, *ApJ*, 487, 930
- Zolotova, N., Ponyavin, D., Arlt, R., & Tuominen, I. 2010, Secular variation of hemispheric phase differences in the solar cycle, *Astronomische Nachrichten*, 331, 765
- Zolotova, N. V. & Ponyavin, D. I. 2016, How Deep Was the Maunder Minimum?, *Sol. Phys.*
- Zwaan, C. 1981, Empirical sunspot models - Statement of the problem, 123

